THE UNIVERSITY OF HULL

Molecular Electrochemistry

being a Thesis submitted for the Degree of

Doctor of Philosophy

in the University of Hull

by

Yan Zhou BSc (Hons)

December 2012

ABSTRACT

The research contained within this thesis probes different aspects of molecular electrochemistry including electrochemically induced ion release, protonation, catalytic processes, mass transport in lyotropic liquid crystals and computer simulation studies of redox batteries.

Chapter 3 reports finding on some electrochemically induced catalytic reactions. Chlorpromazine was used as a mediator in EC′ reactions to monitor the concentration of L-cysteine and glutathione in both buffered and un-buffered solutions. Interference experiments were also carried out for analytical purposes. The detection limits for L-cysteine and glutathione were found to be 6.30 ± 0.03 μM and 4.06 ± 0.07 μM respectively. In addition, lactic acid concentrations were determined *via* the photo-current responses of chlorpromazine. The limit of detection was found to be 5.85 ± 0.05 mM, but could be varied by altering the concentration of chlorpromazine used. The photo-activity of chlorpromazine was studied using a channel-flow electrode combined with an external light source, and in this way the photo reaction mechanisms determined. Finally, 2,4,6-trihydroxybenzoic acid (THBA) was employed as a redox catalyst for the detection of melamine. The detection limit could be altered by changing the concentration of THBA used (the melamine concentration must be slightly higher than THBA), which is indicative of a 1:1 THBA:melamine complex, as anticipated from earlier X-ray crystallographic studies. Other modified electrodes examined include the functionalisation of glassy carbon electrodes with variamine blue B (a diazonic salt) and 6-(ferrocenyl)hexanethiol.

Three separate studies on electrochemically induced protonation/deprotonation were completed. Firstly, the electrochemically catalysed Birch reduction was studied in detail. It was found that an electrochemically induced protonation offers several advantages over conventional Birch reduction conditions, these include: synthesis at room temperature, insensitive to trace water contamination in solvents and

accessibility to reaction intermediates. Secondly, the redox chemistry of lipid-supported vitamin K_1 (VK_1) was studied. It was found that the presence of lipids afforded apparently higher electrochemical sensitivity than without it. The reduction of VK_1 involves both electron and proton transfer and thus is pH dependent. Below pH 6, it was found that a two-electron, two-proton transfer occurred, which changed to a two-electron, one-proton transfer at pH 8 and above. Finally, Sudan III, a diazo dye, was investigated. It was found that the oxidation of Sudan III involves a deprotonation step that is pH dependent. The reaction mechanisms were characterised in this work.

Electrochemically induced ion release was investigated using nitroprusside. In non-aqueous solution, electrochemically triggered release of cyanide was observed. It was found that an increase in electrolyte concentration resulted in an increase in the rate of $[Fe(CN)_5NO_3]^-$ formation. The apparent decrease in the number of electrons transferred when the concentration of electrolyte increased (characteristic of the kinetic salt effect) was subsequently found to be because of a viscosity change in the solution, which also shifted the peak potential, therefore, no evidence for the kinetic salt effect was found. Additionally, iodo-nitrobenzene was also studied and the iodide ion release observed. Experiments studying bromide ion triggering processes experiments were also undertaken by modifying the electrode surface with bromobenzene diazonium salt. The electrode surface was successfully functionalised and the triggering process was performed successfully.

Electrochemistry of organometallic lyotropic chromonic liquid crystals and molecular wires was performed, and the resulting the mass transport profiles were studied. Two types of lyotropic liquid crystals composed of copper(II) and nickel(II) phthalocyanine tetrasulfonic acid tetrasodium salt have been studied. Two-dimensional diffusion was found in this system with D_z found to be quicker than D_r (*i.e.* the mass transport perpendicular to the electrode surface is faster than that of parallel to the electrode).

In the final chapter, computer simulations of cerium-zinc redox batteries were undertaken for several forms of renewable energy such as solar, wind, tidal and the burning of biomass. Under reasonable assumptions, the mathematical model developed enables the observation that the performance characteristics of cells charged with a constant power input differentiate between the various current charge waveshapes, with cell geometry and electrode kinetics playing subtle, but significant, roles; in particular, high efficiency is observed for sunlight-charged batteries which are the thin and suffer no corrosion of the sacrificial electrode, and which have already experienced a charge-discharge cycle. The performance characteristics of the systems are interpreted in the light of consequences for smart grid realisation.

ACKNOWLEDGEMENTS

First, I would like to thank Dr J. D. Wadhawan and Dr. J. Eames for supervising this project. I thank Dr J. D. Wadhawan for giving me the opportunity to do a Ph.D. and assisting me throughout.

I thank Dr. T. Varley for helping me with the electrochemistry both experimentally and theoretically in my second year and third year. I would also like to thank Dr. P. He and Dr. Y. Dou for giving me assistance and advice, not only in area of chemistry, but also in other aspects of my PhD career throughout the three years. I thank K. J. Wright, A. A. Altalhi, L. Partington and all the people working in our lab for providing friendly and helpful discussions during my project. Additionally, as all the people in the Analytical Group have been very friendly to me, providing a very productive and supportive environment for experiments and work; I would like to acknowledge them all.

I would also like to specially include my Mum and Dad in this acknowledgement, for their help and supporting both mentally and financially. I could not do this without them.

Finally, the project cannot be carried out without funding. Therefore I would like to thank EPSRC for funding my studentship and for partially covering my fees and University of Hull for covering the remaining fees.

CONTENTS

LIST OF SYMBOLS

Latin symbols

A	frequency/probability factor
a_i	activity coefficient of species i
k_B	Boltzmann constant (1.3806 x 10^{-23} J K^{-1})
c_i	molar concentration of species i (mol dm^{-3})
c^0	standard molar concentration (1 mol dm^{-3})
D	diffusion coefficient (m^2 s^{-1})
e	electronic charge
E	equilibrium potential of the electrode / applied electrode potential (V)
E_A	activiation energy (J mol^{-1})
E^θ	standard electrode potential of the reaction (V)
$E^{\theta'}$	formal potential (V)
$\Delta E^\ddagger$	energy required to form an activated complex (J mol^{-1})
F	Faraday's constant (96484.6 C mol^{-1})
ΔG	Gibbs free energy (J mol^{-1})
$\Delta G_a^\ddagger$	Gibbs free energy at anode (J mol^{-1})
$\Delta G_c^\ddagger$	Gibbs free energy at cathode (J mol^{-1})
$\Delta G_{0a}^\ddagger$	standard Gibbs free energy at anode (J mol^{-1})
$\Delta G_{0c}^\ddagger$	standard Gibbs free energy at cathode (J mol^{-1})
$\Delta G(\dagger)$	Gibbs free energy at transition state (J mol^{-1})
$\Delta H^{\ominus}$	standard enthalpy change (J mol^{-1})
$\Delta H^\ddagger$	standard enthalpy of activation (J mol^{-1})
i	current (A)
i_a	current at anode (A)
i_c	current at cathode (A)

I_p	peak current (A)
j	flux of reaction
K	equilibrium constant
k	rate constant
k^0	standard rate constant
k_f	rate constant of forward reaction
k_b	rate constant of backward reaction
M	number of moles of molecule reacted (mol)
n	number of electrons
Q	charge (C)
R	universal gas constant (8.314 J K^{-1} mol^{-1})
R_i	resistance (Ω)
r_D	Debye length (m)
S	electrode area (m^2)
$\Delta S^{\ddagger}$	standard entropy change (J mol^{-1})
T	temperature (K)
t	time (s)
t_i	transport number
u_i	mobility of species i (m s^{-1})
V_f	rate of forward reaction
V_b	rate of backward reaction
V_{net}	net rate of reaction
v	scan rate (V s^{-1})
v_f	volume flow rate (cm^3 s^{-1})
v_x	velocity at x-axis (m s^{-1})
v_y	velocity at y-axis (m s^{-1})
v_z	velocity at z-axis (m s^{-1})
ΔX	change in reaction coordiate
Z_i	charge of ion i

Greek symbols

α	transfer coefficient
γ	dimensionless activity coefficient
ε_0	electric constant / vacuum permittivity (F m^{-1})
ε_{op}	optical dielectric constant (F m^{-1})
ε_s	static dielectric constant (F m^{-1})
η	over potential (V)
κ_j	force constant of the *j*th vibrational coordinate
λ	reorganisation energy (eV)
λ_0	solvent reorganisation energy (eV)
λ_i	reorganisation energy for a redox active material (eV)
ρ	density (g dm^{-3})
τ	dimensionless time
ψ	dimensionless current
$\Delta\Phi$	potential difference between electrode and solution (V)
Φ_M	potential at metal electrode (V)
Φ_O	potential at outer Helmoholtz plane (V)
Φ_S	solution potential (V)
$\Delta\Phi_{diff}$	potential drop of diffusion layer / Zata-potential (V)
Φ_i	Coulomb potential (V)
φ_p	dimensionless peak current

Other symbols

$\hbar$	Planck constant (4.1357 x 10^{-15} eV s)
∇	Laplacian operator

ABBREVIATIONS

AM	Air mass
BPGE	Basal plane graphite electrode
CE	Counter electrode
CPZ	Chlorpromazine
CV	Cyclic voltammetry
GCE	Glassy carbon electrode
HPLC	High performance liquid chromatography
IHP	Inner Helmholtz plane
MS	Mass spectrometry
OHP	Outer Helmholtz plane
RE	Reference electrode
SCE	Saturated calomel electrode
SPA	Spiro-bis-anil
SWV	Square wave voltammetry
TBABF	Tetrabutylammonium tetrafluoroborate
TBANP	Tetrabutylammonium nitroprusside
TBAP	Tetrabutylammonium perchlorate
THBA	2,4,6-trihydroxybenzoic acid
TMPD	*N,N,N',N'*-tetramethyl-*p*-phenylenediamine
VBB	Variamine blue B
VK_1	Vitamine K_1
WE	Working electrode

1. INTRODUCTION

Fundamental and experimental theories of dynamic electrochemistry relevant to the experiments presented in this thesis are discussed with in this chapter.

1.1. Background

Electrochemistry is a branch of chemistry, which is concerned with chemical reactions that occurs at the surface of a conductor (electrode), immersed in an electrolyte solution or the electron transfer between liquid/liquid interface. In this thesis, dynamic electrochemistry is concerned with electron transfer process that occurs at the solution/electrode interface.

In the last few decades electrochemistry has become an important research area within chemistry, examples include the development of voltammetric reaction mechanism determination[1, 2], understanding the corrosion of metals[3, 4], the construction of electrochemical sensors[5, 6], *etc*. In addition, electrochemistry also offers a lot of benefits for chemical synthesis such as a green process, since electricity maybe employed as a reactant, under mild conditions, since experiments can be carried out at room temperature. However, there are also some disadvantages: separation of synthetically useful product from the necessary supporting electrolyte can be difficult.

1.2. Faraday's Law

There are three types of electrochemical cells: a galvanic cell or primary cell (Fig. 1.1a), electrolytic cell (Fig. 1.1b) and "supergalvanic" cell. The galvanic cell can autonomously generate potential, which allows current to flow. Whereas the

electrolytic cell can only be forced by an external potential to flow a current. The third type known as “supergalvanic” cell, which may be employed for Joule heating through electric discharge in the SG region, i^2R_i loss is used to heat the system.

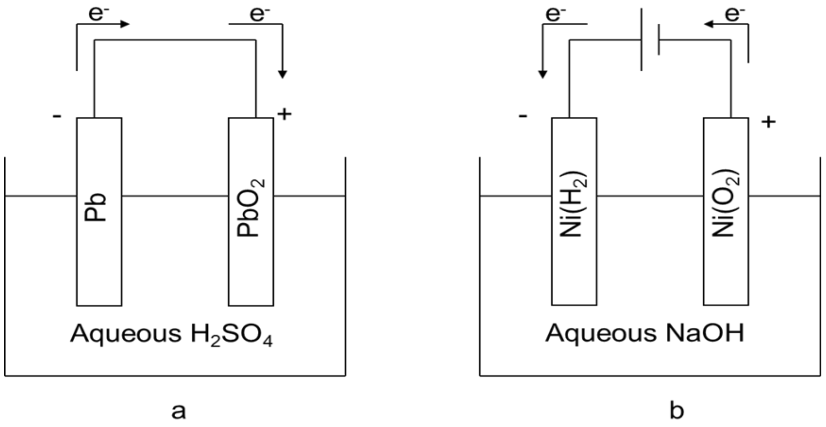

Fig. 1.1. Schematic examples of a galvanic cell (a) and an electrolytic cell (b).

An electrolytic cell operates by allowing current to flow from on electrode to the other. The electrode that passes electrons into the solution is the cathode and the electrode that accepts electrons from solution is the anode. Whereas, in a galvanic cell, the reduction happens at an anode or *vice versa*, this is because reduction of the species takes electron from the electrode causing it to become more positive.

The extent of electrolysis is related to the charge that is passed through the electrodes. Since the charge carried by each electron is known as -1.602 x 10^{-19} C, the passage of one mole of electrons (6.022 x 10^{23} electrons), flowing into a cathode can be determined to be 96484.6 C. This number is known as the Faraday constant. Faraday’s Law is illustrated in Eqn. 1.1.

$$Q = nM\mathrm{F} \qquad \text{(Eqn. 1.1)}$$

Where Q is the charge passed in C, n is the number of moles of electron transferred, M is the number of moles of molecule reacted and F is the Faraday constant.

1.3. Dynamic electrochemistry

Electron transfer processes can be explained by two major concepts: thermodynamics and kinetics. Thermodynamics describes the change in enthalpy and entropy during a reaction, and kinetics describes the rate of a reaction. Electrode reactions are interfacial processes; accordingly, material transport effects must be considered as well.

1.3.1. Electrical double layer

In dynamic electrochemistry, it is essential to understand the electron transfer between electrode surface and the analyte in solution. The structure of the electrode/solution interfacial region has been extensively studied.[7, 8] Helmoltz[9] first proposed a "double layer" model. The modern double layer model was described by Gouy and Chapman[9] who, worked independently, and, was followed by Stern[10], who combined Helmoltz and Goup-Chapman models. Further work was carried out by Grahame[11], with one layer of specifically adsorbed ions, one layer of non-specifically adsorbed ions, and a diffusion layer region expanding to the bulk electrolyte solution phase. Modern treatments of the double layer were studied in various of areas by numerous of researchers such as Bockris, Devanathan and Müller.[12]

As shown in Fig. 1.2, the solution component near the electrode surface can be separated into several layers. The inner layer consists of adsorbed solvent molecules and sometimes other specifically adsorbed species, the edge of this layer is defined by locus of the center of the largest specifically adsorbed species, and is called the inner Helmholtz plane (IHP). The closest distance a solvated ion can get to the electrode surface, x_2, denotes the edge of the second layer of the double layer, and is called the

outer Helmholtz plane (OHP).

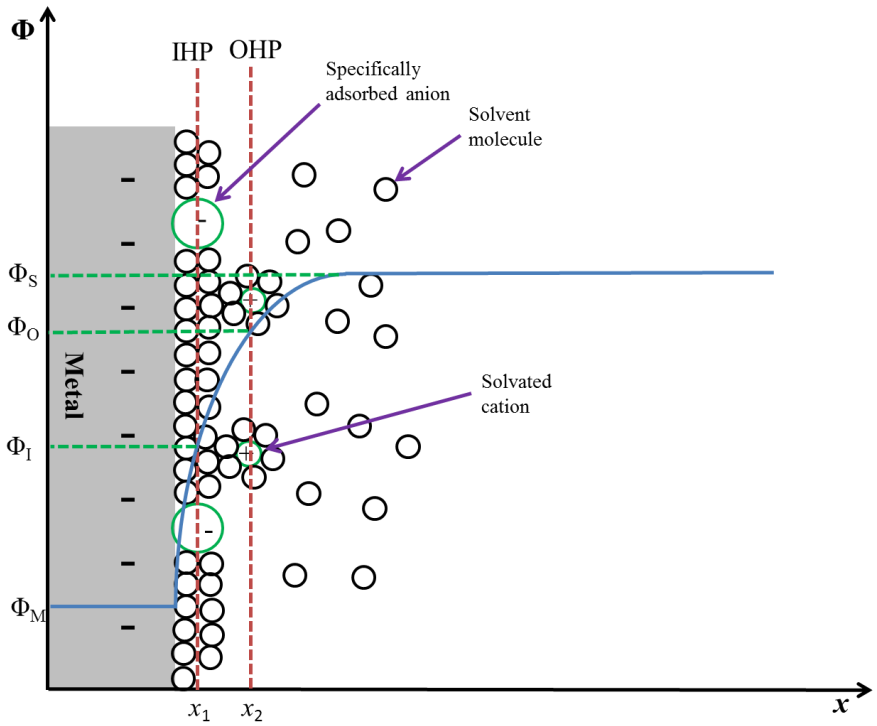

Fig. 1.2. A schematic diagram of an electric double layer between solution and metal with negative charge. x is the distance and Φ is potential, respectively. The subscripts of Φ, S, O, I, M are solution, outer Helmoholtz plane (OHP), inner Helmoholtz plane (IHP) and electrode, respectively. Note that Φ is negative potential.

The structure of electric double layer can affect the rate of electrode process. If the electroactive species that are of interested is not specifically adsorbed, then the nearest position where it can travel to the electrode surface is OHP, as shown in Fig. 1.2, there is a potential drop from electrode surface to the solvated molecules, therefore the overall potential of electroactive species experienced is less than the potential which is applied on the electrode. According to Fig. 1.2, the potential difference between electrode and solution can be described by:

$$\Delta\Phi = (\Phi_M - \Phi_O) + (\Phi_O - \Phi_S) = \Delta\Phi_H + \Delta\Phi_{diff} \qquad \text{(Eqn. 1.2)}$$

where $\Delta\Phi_H$ is the potential drop of Helmoholtz Double Layer and $\Delta\Phi_{diff}$ is the

potential drop of diffusion layer, the latter was also known as Zeta-potential. The position at that the potential in diffusion layer equals to 1/e of $\Delta\Phi_H$ is defined as the double layer thickness. The double layer thickness depends on ionic strength of the solution. In dilute solutions, the diffusion double layer can be as thick as 10 nm, whereas in the presence of large concentration of electrolyte (*i.e.* concentration greater than 0.1 mol dm^{-3}), the thickness of diffusion double layer can be negligible and the all the potential drop can be treat as same as $\Delta\Phi_H$. In addition, Debye length needs to be mentioned here as it is essential for the double layer structure. It describes the distance over which large separation of charge can occur. The Debye length, r_D, can be written as:

$$r_D = -\frac{\ell}{\ln(\frac{\Phi_i \ell}{Z_i})} \qquad \text{(Eqn. 1.3)}$$

where ℓ is the distance of Coulomb potential (Φ_i) from an isolated ion of charge (Z_i).

1.3.2. Thermodynamics

Consider a general electrochemical reaction,

$$A + ne^- \rightleftarrows B \qquad \text{(Scheme 1.1)}$$

where A is the oxidized species and B is the reduced species, *n* represents the number of electrons transferred in the reaction, respectively. When controlling the potential of a metallic electrode, the Fermi level will rise, provided negative potential is applied, which energetically favours the electron transfer from metal to the solution, *i.e.* A. As the electrons are transferred from electrode to the solution, the energy level of electrode will decrease whereas the energy level of solution will increase, until equilibrium is reached. A schematic diagram is shown in Fig. 1.3 to depict this phenomenon.

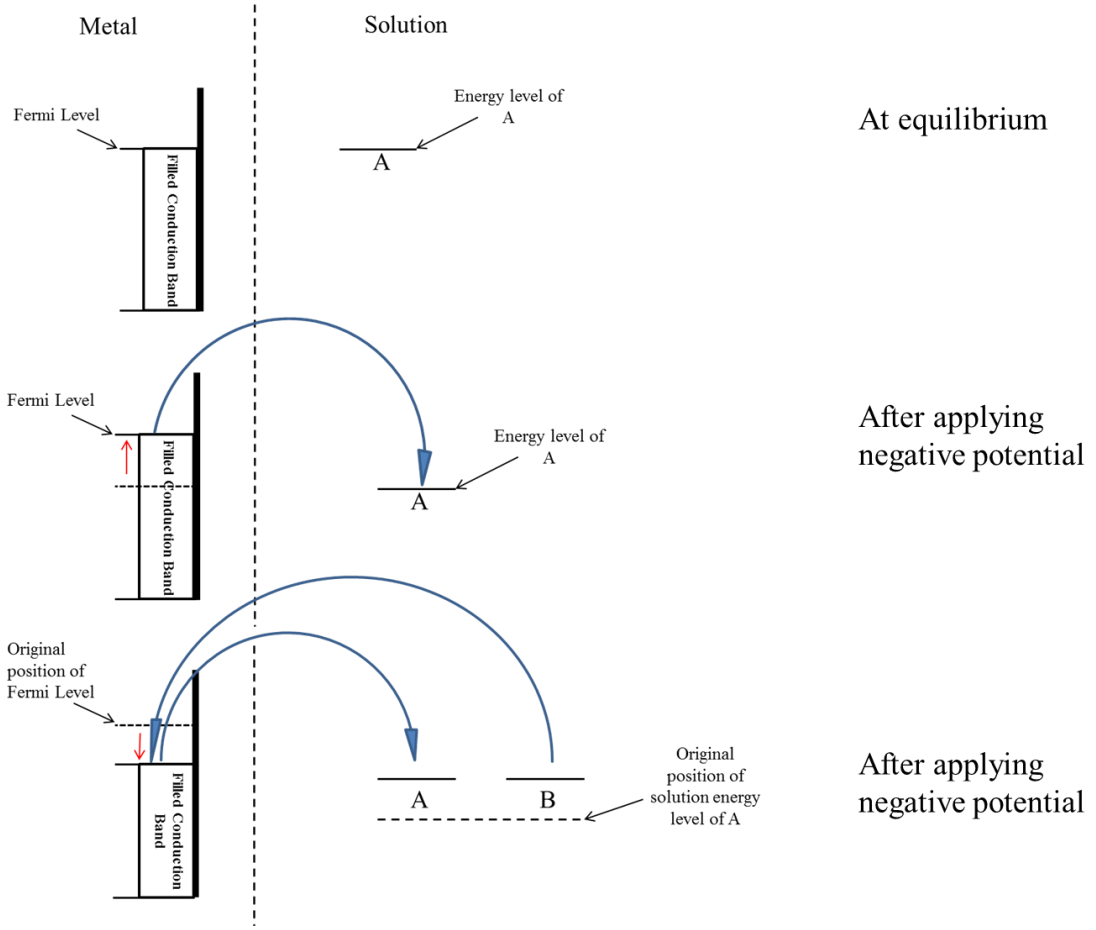

Fig. 1.3. Fermi energy change of electrode before and after applying electric potential.

At equilibrium, there is no net current flow, as the rate of the forward reaction is equal to that of the backward reaction (*i.e.* A and B). Nernst described this relationship in terms of potential and gave an equation:

$$E = E^{\theta} + \frac{RT}{nF} ln \frac{a_A}{a_B} \qquad \text{(Eqn. 1.3)}$$

where E^{θ} is the standard potential of the A/B redox couple and a_i is the activity of species *i*. Determining activities is challenging, especially at high concentrations, therefore formal potential, $E^{\theta\prime}$ is often used. In order to substitute a standard potential with a formal potential, activity coefficients must be converted. In thermodynamics, activity of a solution can be written as dimensionless activity coefficient, γ, multiply by the ratio of concentration, c, over standard concentration, c^0, *viz.*, 1 mol L^{-1}.

Therefore the Nernst equation can be written as:

$$\mathrm{E} = E^{\theta} + \frac{RT}{nF} ln \frac{c_A}{c_B} + \frac{RT}{nF} ln \frac{\gamma_A}{\gamma_B} \qquad \text{(Eqn. 1.4)}$$

As formal potential equals to the sum of standard potential and the term involving the activity coefficients in Equation 1.3, the Nernst equation, with respect to concentration can be written:

$$\mathrm{E} = E^{\theta\prime} + \frac{RT}{nF} ln \frac{c_A}{c_B} \qquad \text{(Eqn. 1.5)}$$

Therefore the formal potential can be worked out in practice, when the *concentrations* of each species are known.

1.3.3. Kinetics

Thermodynamics explains electrochemical reactions at equilibrium, it does not provide information on the rate of the reaction. Electrochemists are often interested in the rate of an electron, or ion, transfer. Therefore, kinetics studies are essential for understanding an electrochemical reaction process.

In kinetics, if consider a uni-molecular elementary reaction:

$$\mathrm{A_{(aq)}} \underset{k_b}{\overset{k_f}{\rightleftharpoons}} \mathrm{B_{(aq)}} \qquad \text{(Scheme 1.2)}$$

then the rate of forward reaction is:

$$\mathrm{v}_f = k_f c_A \qquad \text{(Eqn. 1.6)}$$

and the rate of backward reaction can be written as:

$$\mathrm{v}_b = k_b c_B \qquad \text{(Eqn. 1.7)}$$

therefore the net rate is:

$$v_{net} = k_f c_A - k_b c_B \quad \text{(Eqn. 1.8)}$$

At equilibrium, the net rate becomes zero, and therefore the relationship of rate constant and concentration can be given as:

$$K = \frac{k_f}{k_b} = \frac{c_B}{c_A} \quad \text{(Eqn. 1.9)}$$

It was found that the rate constant changes with changing temperature, natural logarithm of rate constant is linear with 1/*T*. This relationship was firstly discovered by van't Hoff[13], and described this isochore as:

$$\frac{\partial \ln K}{\partial T} = \frac{\Delta H^{\ominus}}{RT^2} \quad \text{(Eqn. 1.10)}$$

where K is the equilibrium constant, *T* is temperature, R is the molar gas constant and $\Delta H^{\ominus}$ represents the standard enthalpy change.

Arrhenius[14] employed van't Hoff's relationship to introduce an equation to explain the phenomenon of the dependence of the reaction rate constant on temperature:

$$k = A\mathrm{e}^{-E_A/\mathrm{R}T} \quad \text{(Eqn. 1.10)}$$

where E_A is an energy unit which known as activation energy, and *A* is the frequency and probability factor. As shown in Eqn. 1.10, the exponential factor indicates that the activation energy can be surmounted by thermal energy, which relates the thermodynamics and kinetic together. The derivation of the Arrhenius equation from the van't Hoff's relationship is detailed in Appendix 10.1.

Fig. 1.4 shows the energy change along a reaction coordinate. In order to form a product from a reactant, the potential energy must raise to the maximum level, E_A; and the energy required from reactant to E_A is described as E_f, whereas the energy required

from product back to react is E_b.

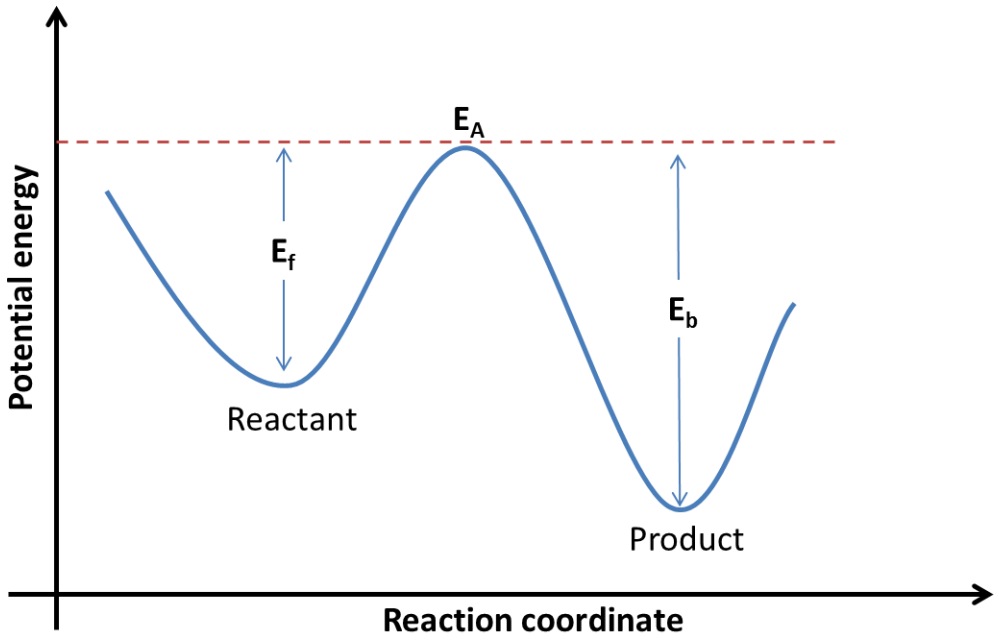

Fig. 1.4. The change of potential energy during a reaction.

The energy of reactant and product occupy two minimum levels which indicate that both the reactant and product are energetically stable.

In transition state theory, the reactants combine to form an activated complex or transition state requires energy $\Delta E^{\ddagger}$. In a condensed-phase reaction, the change of pressure and volume can be negligible, and therefore the standard enthalpy of activation, $\Delta H^{\ddagger}$, is approximately equal to $\Delta E^{\ddagger}$. Therefore Eqn. 1.10 can be written as:

$$k = \mathrm{A}e^{-\Delta H^{\ddagger}/RT} \qquad \text{(Eqn. 1.11)}$$

And the equation can also be presented in terms of standard free energy of activation or standard Gibbs energy:

$$k = \mathrm{A}'e^{-\Delta G^{\ddagger}/RT} \qquad \text{(Eqn. 1.12)}$$

Where A' equals to $\exp(\Delta S^{\ddagger}/\mathrm{R})$ with $\Delta S^{\ddagger}$ is standard entropy and R is the molar gas

constant, respectively.

Consequently, Fig. 1.4 can also be presented by standard free energy instead of potential energy. By introducing the Boltzmann constant, k_B, and the Planck constant, $\hbar$, Eqn. 1.12 can be rearranged, to afford the enquired form,

$$k = \kappa \frac{k_B T}{\hbar} e^{-\Delta G^{\ddagger}/RT} \qquad \text{(Eqn. 1.13)}$$

If the electrochemical reaction is considered:

$$A + ne^- \underset{k_b}{\overset{k_f}{\rightleftharpoons}} B \qquad \text{(Scheme1.3)}$$

the rate of forward reaction at the cathode surface can be described as:

$$v_f = k_f c_A = \frac{i_c}{nFS} \qquad \text{(Eqn. 1.14)}$$

and the rate of backward reaction at anode can be presented as:

$$v_f = k_b c_B = \frac{i_a}{nFS} \qquad \text{(Eqn. 1.15)}$$

where n is the molar number of electrons transferred in the reaction, F is the Farady's constant and *S* is the area of electrode. The net current at electrode surface can be then described as:

$$i = i_c - i_a = nFS(k_f c_A - k_b c_B) \qquad \text{(Eqn. 1.16)}$$

Conventionally, IUPAC describes the oxidation current to be positive and reduction current to be negative.

1.3.3.1. Bulter-Volmer Kinetics

In electrochemistry, Bulter-Volmer kinetics is one of several theories, which describe the relationship between applied potential and the rate of electron transfer. If the reaction in Scheme 1.1 is considered and a single electron transfer process is assumed, the standard free energy change *via* a reaction coordinate is shown in Fig. 1.5.

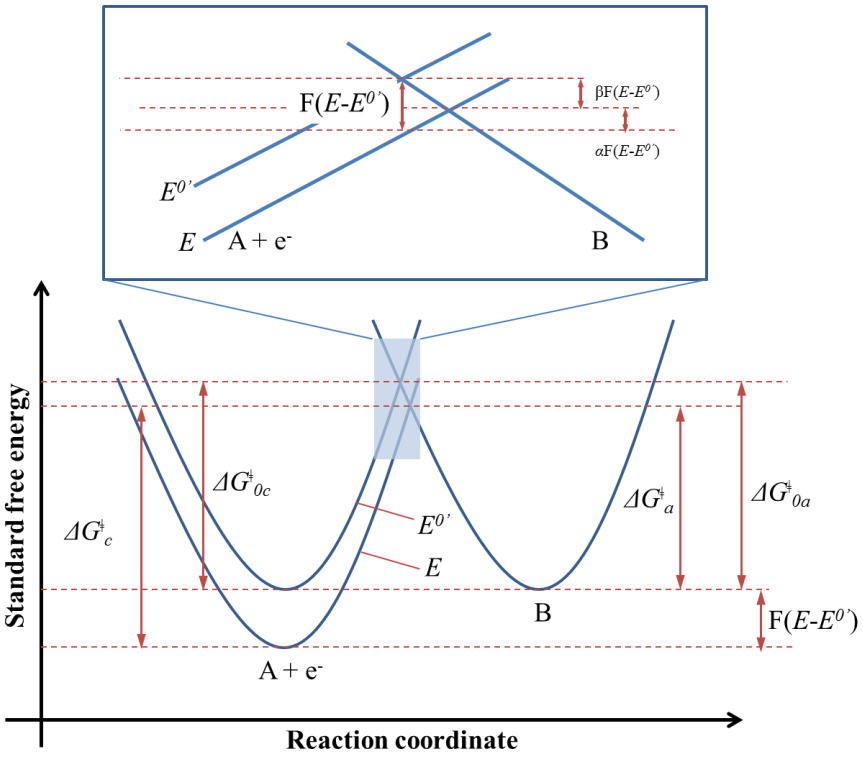

Figure 1.5. A schematic diagram of Bulter-Volmer Kinetics.

As indicated in Fig. 1.5, the potential of the electrode starts at a reference point, $E^{0'}$, and the oxidation potential is E, the energy of electron change can be then described as $-F(E-E^{0'})$. Note that the energy change in transition state is smaller than $-F(E-E^{0'})$, therefore the energy change in transition state is a fraction of $-F(E-E^{0'})$, and can be described as $\beta F(E-E^{0'})$, where $\beta=(1-\alpha)$, and α is known as transfer coefficient. The transfer coefficient indicates essentially the measure of the symmetry of the energy barrier. Therefore the change of Gibbs free energy can be described as:

$$\Delta G_{\mathrm{a}}^{\ddagger} = \Delta G_{0\mathrm{a}}^{\ddagger} - \beta \mathrm{F}(E - E^{0\prime}) \qquad \text{(Eqn. 1.17)}$$

and,

$$\Delta G_{c}^{\ddagger} = \Delta G_{0c}^{\ddagger} + \alpha \mathrm{F}(E - E^{0\prime}) \qquad \text{(Eqn. 1.18)}$$

where $\Delta G^{\neq}_{0a}$ and $\Delta G^{\neq}_{0b}$ are the changes in Gibbs free energy at anode and cathode, respectively. By applying the Arrhenius equation, the rate constants for the forward reaction can be presented as:

$$k_f = A_f e^{-\Delta G_{0c}^{\ddagger}/\mathrm{R}T} e^{-\alpha f(E-E^{0\prime})} \qquad \text{(Eqn. 1.19)}$$

and backward reaction can be written as:

$$k_b = A_b e^{-\Delta G_{0\mathrm{a}}^{\ddagger}/\mathrm{R}T} e^{\beta f(E-E^{0\prime})} \qquad \text{(Eqn. 1.20)}$$

where f = F/RT. At equilibrium, $\Delta G^{\ddagger}_{0a}$=$\Delta G^{\ddagger}_{0c}$, and the term $\mathrm{A}_f e^{-\Delta G_{0c}^{\ddagger}/\mathrm{R}T}$ equals to $\mathrm{A}_b e^{-\Delta G_{0\mathrm{a}}^{\ddagger}/\mathrm{R}T}$, which can be substituted by k^0. By combining with Eqn. 1.16, the relationship between current and potential can be shown as:

$$i = \mathrm{F}\mathrm{A}k^0\{c_A \exp[-\alpha f(E - E^{0\prime})] - c_B \exp[\beta f(E - E^{0\prime})]\} \qquad \text{(Eqn. 1.21)}$$

1.3.3.2. Marcus Theory

The Marcus theory was developed by Rudolph A. Marcus following earlier work by Libby.[15] The reaction occurs by thermal activation, the bond lengths and angles of reactant species become compressed, stretched or distorted, as well as the solvation shells of species changes. At its heart is the notion that electron tunnelling can only occur when the reactant reaches the energy of the transition state *via* vibrations of the thermally excited reactants and the energy of the product matches that of the transition

state. It also states that the activation barrier is low when reactant and product are close in molecular geometry and *vice versa*. As shown in Fig. 1.6, the greater change in reaction coordinate, Δx, the higher the activation energy required to reach transition state. In other words, the change of reaction coordinate represents the similarity of product and reactant in geometry.

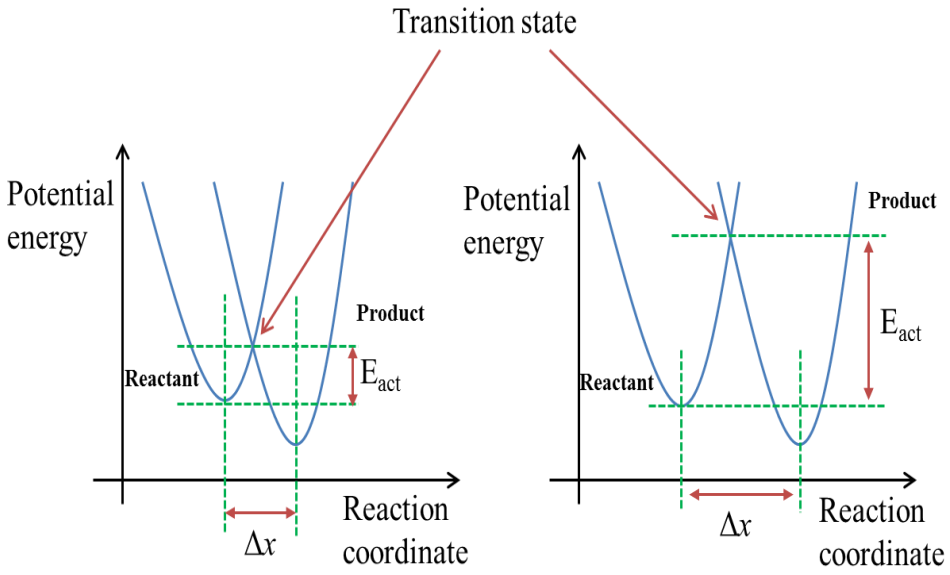

Fig. 1.6. The change in reaction coordinate changes the transition state.

The electron transfer process also refers to be either adiabatic or nonadiabatic. The extent of interaction or electronic coupling between reactants is often described in terms of adiabaticity. As shown in Fig. 1.7, when the interaction is strong, there is the usual splitting of the two surfaces at their intersection, then the extent of the reaction will continue on the surface toward right on the abscissa, to form the product (green arrow), which is known as adiabatic process. On the other hand, when the interaction between two reactants is very weak, then the split at the intersection of the two surfaces is negligible, then the extent of the reaction will follow the continuous reactant surface (red arrow) and remains on the reactant surface, then is known as nonadiabatic process. In the latter, there is a reduced probability of electron transfer.

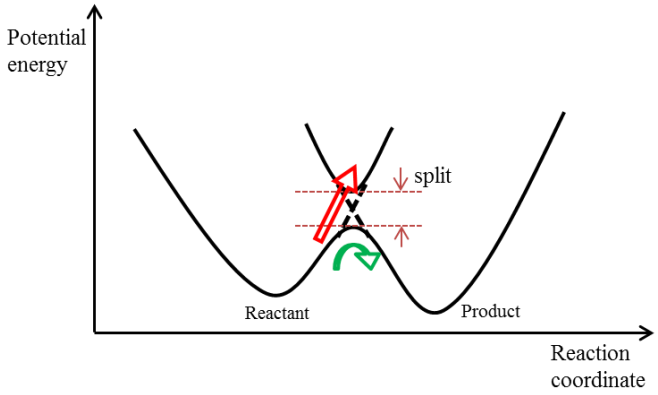

Fig. 1.7. Potential energy surface for the reactants and the products.

In addition, the different spin in reactant and product affect the activation energy. For instance, the redox couple, $Co(NH_3)_6^{3+}/Co(NH_3)_6^{2+}$, the electrons in Co(II) is an octahedral d^7 high spin whereas the Co(III) has d^6 low spin. Therefore, it is less possible for the electron to "jump" from a high spin orbital to a low spin orbital, unless the spin flips, making the kinetics very slow[16].

The electron transfer in Marcus theory can be separated into inner and outer sphere electron transfer. The outer sphere electron transfer denotes a reaction between two species in which the original coordination spheres are maintained in the activated complex, whereas, the inner sphere electron transfer process denotes the two species shared with one common solvation molecule.

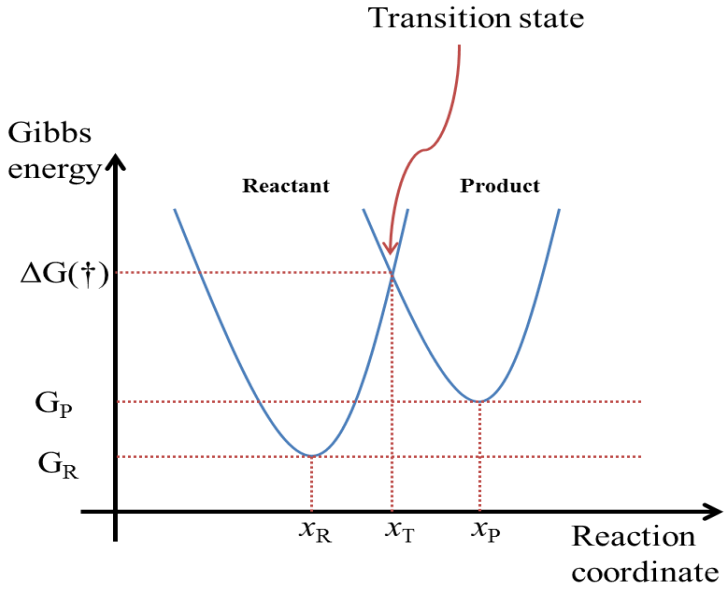

Fig. 1.8. A plot of Gibbs energy change along reaction coordinate.

As shown in Fig. 1.8, the Gibbs energy at transition state can be given by:

$$\Delta G(\dagger) = \frac{(\lambda+\Delta G)^2}{4\lambda} \quad \text{(Eqn. 1.22)}$$

where

$$\lambda = \frac{1}{2}k(x_R - x_P)^2 \quad \text{(Eqn. 1.23)}$$

and

$$\Delta \mathrm{G} = G_P - G_R \quad \text{(Eqn. 1.24)}$$

There are two contributions to the reorganization energy, λ:

$$\lambda = \lambda_i + \lambda_0 \quad \text{(Eqn. 1.25)}$$

where λ_0 is the solvent reorganization energy and λ_i is the reorganization energy for a redox active material. Because the reaction coordinate is "the pathway of least resistance" in a multidimensional potential hyper surface, it translates the reactants to products, λ_i is a function of the sum of distribution of geometric properties such as bond angle and length, therefore according to Fig. 1.8,

$$\lambda_i = \sum \frac{1}{2}k(x_R - x_P)^2 \quad \text{(Eqn. 1.26)}$$

where x_R and x_P are the reaction coordinates of reactant and product in their stable atomic structure. In terms of geometry, λ_i can be also defined based on bond stretch and bond bending:

$$\lambda_i = \sum_j \frac{\kappa_j^R \kappa_j^P}{\kappa_j^R + \kappa_j^P}(x_R^j - x_P^j)^2 \quad \text{(Eqn. 1.27)}$$

where κ_j^R and κ_j^P are the normal mode force constants for the *j*th vibrational coordinate in the reactants and products, respectively. The term $(x_R^j - x_P^j)$ can be substituted by geometry change such as bond angle and length, for instance, the oxidation of nitrogen dioxide (example obtained from *Understanding Voltammetry*, R.G. Compon and C. E. Banks):

$$NO_2 \rightleftarrows NO_2^+ + e^-(m) \qquad \text{(Eqn. 1.28)}$$

This reaction involves changes of both bond lengths and bond angles, which the N-O bond stretches and O-N-O bends to 180°, therefore Equation 1.27 can be re-written as:

$$\lambda_i = \frac{2\kappa_{str}^R \kappa_{Str}^P}{\kappa_{str}^R + \kappa_{str}^P}(\ell_R - \ell_P)^2 + \frac{\kappa_{bend}^R \kappa_{bend}^P}{\kappa_{bend}^R + \kappa_{bend}^P}(\theta_R - \theta_P)^2 \qquad \text{(Eqn. 1.29)}$$

where κ_{str}^R represents the force constant of bond stretch of reactant and κ_{bend}^P represents the force constant of bond bending of the products.

In addition, for an electrode reaction, the solvent reorganization energy is given by:

$$\lambda_0 = \frac{e^2}{8\pi\varepsilon_0}\left(\frac{1}{\text{ϒ}} - \frac{1}{2d}\right)\left(\frac{1}{\varepsilon_{op}} - \frac{1}{\varepsilon_s}\right) \qquad \text{(Eqn. 1.30)}$$

where e is the electronic charge, ϒ is the radius of reactant, d is the distance from the reactant to the electrode surface, ε_0 is the vacuum permittivity (or electric constant), ε_{op} is the optical dielectric constant and ε_s is the static dielectric constant, respectively.

The Marcus theory can be related by Butler-Volmer kinetics and according to Butler-Vomler kinetics:

$$k_f = k^0 \exp(\frac{-\alpha\eta}{2k_BT}) \quad \text{(Eqn. 1.31)}$$

$$k_b = k^0 \exp(\frac{(1-\alpha)\eta}{2k_BT}) \quad \text{(Eqn. 1.32)}$$

where k_f and k_b are the forward and reverse reaction rate constant in Scheme 1.3. η is the overpotential which equals to $E - E^{0'}$, k_B is the Boltzmann constant, T is the temperature, k_0 is the standard heterogeneous rate constant and α is the transfer coefficient. The analogous Marcus relations[17] can be written as:

$$k_f = k^0 \exp(\frac{-\alpha\eta}{2k_BT} - \frac{\eta^2}{4\lambda k_BT}) \quad \text{(Eqn. 1.33)}$$

$$k_b = k^0 \exp(\frac{(1-\alpha)\eta}{2k_BT} - \frac{\eta^2}{4\lambda k_BT}) \quad \text{(Eqn. 1.34)}$$

As it can be seen from Eqn. 1.33 and Eqn. 1.34 that when $\eta/\lambda \ll 1$, the equations can be reduced to Butler-Volmer equations. Whereas the Marcus theory predicts that, as η increases and approaches λ, the rate constants no longer increase exponentially with overpotential and reaches maximum when $\eta = \pm\lambda$ and start to decrease at larger η, which is known as Marucs "inverted" region.

1.3.3.3. Tafel law

For an electrochemical process in Scheme 1.3, according to Bulter-Volmer kinetics, the net rate or flux of reaction, j, is given by:

$$j = k_f^0 exp\left[\frac{-\alpha F(E-E_f^0)}{RT}\right] c_A - k_b^0 exp\left[\frac{\beta F(E-E_f^0)}{RT}\right] c_B \quad \text{(Eqn. 1.35)}$$

where k_f^0 and k_b^0 are the standard rate constants for forward and backward reaction, α and β are the transfer coefficient with $\alpha+\beta=1$, E is the electrode potential, E_f^0 is the standard potential for A/B couple and c_A and c_B are concentrations of A and B in bulk

solution. At equilibrium, *j* equals to zero. However at extreme potentials (oxidation or reduction), such as $E \gg E^0_f$ or $E \ll E^0_f$, then it is possible to neglect one term or another in Eqn. 1.35. Therefore for an oxidation process:

$$j = k_b^0 exp\left[\frac{\beta F(E-E_f^0)}{RT}\right] c_B \qquad \text{(Eqn. 1.36)}$$

and for a reduction process:

$$j = k_f^0 exp\left[\frac{-\alpha F(E-E_f^0)}{RT}\right] c_A \qquad \text{(Eqn. 1.37)}$$

In electrochemistry (single electron transfer),

$$I = \mathrm{F}Sj \qquad \text{(Eqn. 1.38)}$$

as E^0_f is a fixed number, the overpotential, η (where $\eta = E - E_f^0$) is the function of potential change, then Eqn. 1.36 and 1.37 can be rearranged:

$$\ln|i_{red}| = \frac{-\alpha F\eta}{RT} + \ln(\mathrm{F}Sk_f^0 c_A) \qquad \text{(Eqn. 1.39)}$$

and

$$\ln|i_{ox}| = \frac{\beta F\eta}{RT} + \ln(\mathrm{F}Sk_b^0 c_B) \qquad \text{(Eqn. 1.40)}$$

where the latter term on the right-hand-side of the equations can be shorten by constant. Therefore according to Eqn. 1.35 and Eqn. 1.36, a plot of ln|*i*| *vs. E* can provide information about electron transfer coefficient, α. This plot is known as a Tafel plot (Fig. 1.9). The transfer coefficient can then be worked out from the slope of the linear region of the graph.

As shown in Fig. 1.9, i_0 is the exchange current (see Butler-Volmer kinetics). The value of slope is unaffected by the formal potential as the slope donates a ratio rather than an exact number. At equilibrium, the current tends to small and the logarithm of

current tends to infinity.

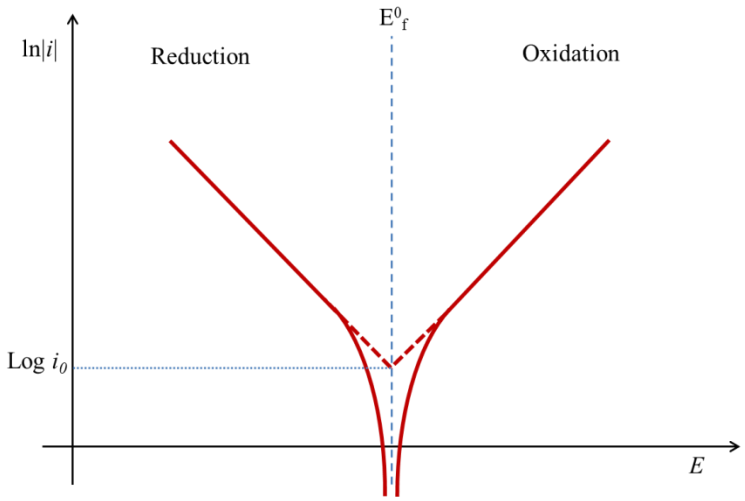

Fig. 1.9 An example of Tafel plots

1.3.4. Electrodes

A three electrode system needs to be used in order to study the electrode kinetics quantitatively as two electrodes system normally cannot offer a stable reference potential. The three electrodes are: working electrode (WE), reference electrode (RE) and counter electrode (CE).

1.3.4.1. Working Electrode

Working electrode is the electrode often made of unreactive metal or carbon, which reactants can undergo electron transfer process at its surface. Electrons can be transferred either from the electrode to the reactant or *vice versa*. The WE is normally designed for a disc shape, with a well-defined area. Other geometries are also used for different purpose, *e.g.* a square shape WE is designed for a hydrodynamic flow system, as mass transport under laminar flow can be simulated relatively easier than that of disc shape.

1.3.4.2. Reference Electrode

The reference electrode provides a stable reference potential to the working electrode under normal pressure and temperature (*i.e.* 1 atmosphere and 298 K). It is made from a highly reversible redox system that small passage of current is ineffective to its potential. A saturated calomel reference electrode and silver/silver chloride reference electrode are the common reference electrodes used in research.

1.3.4.3. Counter Electrode

In order for a current to flow a circuit must be made, between the working electrode and the counter electrode. The counter electrode is made from an unreactive conducting material that has high surface area in order to ensure that the current passed through the CE is sufficient. Commonly used materials are platinum or nickel wires. Electro-active species can undergo reaction at the CE surface, therefore it is necessary to keep WE and CE apart from each other since the chemicals produced at CE surface could interfere with the reactions that occurring at WE surface.

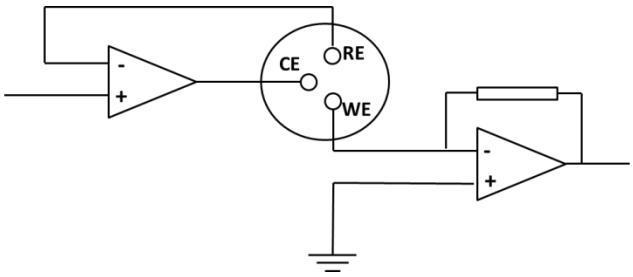

Fig. 1.10. A schematic diagram of potentiostat. RE is reference, CE is counter electrode and WE is working electrode.

Fig. 1.10 illustrates the basic design of a potentialstat, the operational amplifier is the key component as the feedback circuit drives the current between the working and counter electrode, while ensuring that there is no current passes through the reference

electrode circuit, with the working electrode at virtual earth.

The potential, *E*, is applied to the working electrode, which is relative to the constant potential provided by the reference electrode:

$$E = (\Phi_M - \Phi_S)_{working} - (\Phi_M - \Phi_S)_{reference} \quad \text{(Eqn. 1.41)}$$

Because the potential of reference electrode is constant, changing *E* gives the same change of $(\phi_M - \phi_S)_{\text{working}}$. The counter electrode completes the circuit, allowing current to flow. This can be measured, allowing the current through the electrode-solution interface as a function of potential to be evaluated. The counter electrode will give whatever voltage is required (normally ±10 V or ±1000 V) to drive the electrode reaction, as the bulk solution gives resistance, R_i. As E=iR_i, therefore for Eqn. 1.41, the term of iR_i should be introduced to the equation:

$$E = (\Phi_M - \Phi_S)_{working} - (\Phi_M - \Phi_S)_{reference} + iR_i \quad \text{(Eqn. 1.42)}$$

In order to minimise iR_i drop, a large concentration of electrolyte (*e.g.* 0.1 mol dm^{-3} potassium chloride in water) is added into the solution to reduce the resistance of the solution (see Section 1.41). In addition, chemists also use electrode with small area (microelectrodes) to encounter the iR_i loss as the current is small.

1.4. Mass transport

At equilibrium, exchange current, i_0, can be given as:

$$i_0 = \mathrm{F}Sk^0 {c_{A\ bulk}}^{(1-\alpha)} {c_{B\ bulk}}^{\alpha} \quad \text{(Eqn. 1.43)}$$

By dividing Eqn. 1.40 by Eqn. 1.43, net current can be presented in terms of exchange current:

$$i = i_0[\frac{c_{A\ surface}}{c_{A\ bulk}}\exp(-\alpha f\eta) - \frac{c_{B\ surface}}{c_{B\ bulk}}\exp(\beta f\eta)] \quad \text{(Eqn. 1.45)}$$

where η is the overpotential, which equals to E-$E_{equilibrium}$. The current increases exponentially with the increase of η. The current increase dramatically in the beginning and tends to stable when overpotential becomes extreme. The stable current is then caused not by the kinetics but the rate of mass transport.

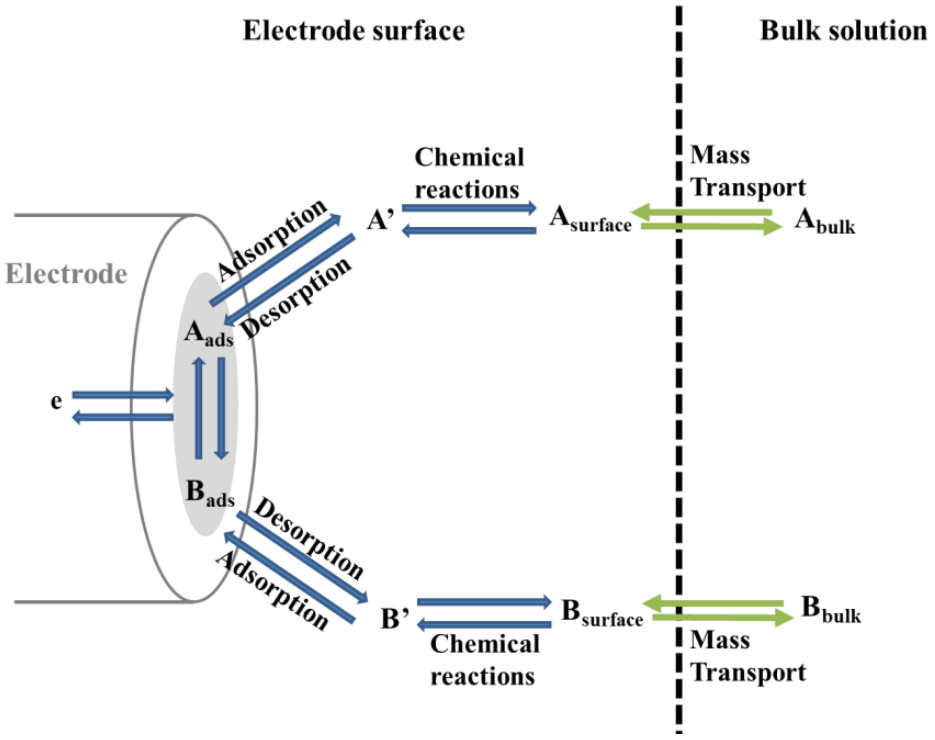

Fig. 1.11. A schematic diagram of material transport at electrode surface.

Fig. 1.11 illustrates the transfer of an electro-active species travel from bulk solution to an electrode surface. The chemical reaction, adsorption and desorption processes occur close to the electrode surface, whereas a solution dissolved species must travel from bulk solution to this region to react, therefore mass transport is essential. There are three major types of mass transport: diffusion, migration and convection. The flux of mass transport, j_i, can be described by equation:

$$j_i = -D_i \nabla c_i - \frac{z_i F}{RT} D_i c_i \nabla \phi + c_j v \qquad \text{(Eqn. 1.46)}$$

Eqn. 1.46 indicates that the flux of material *i* can be described by three terms, the first term describes the contribution of diffusion, middle term represents the migration distribution and the latter term is contributed by convection. The contribution of each of these terms is discussed.

1.4.1. Migration

Electromigration in solution is caused by an electric field that results the movement of charged species. For example, a negatively charged species can be attracted by a positively charged electrode and causes the species to move towards to the electrode in the solution. The transport number, t_i, of ion *i* in solution which contains both ion *i* and *j*, can be described by Eqn. 1.47.

$$t_i = \frac{|z_i| u_i c_i}{\sum_{j=1}^{n} |z_j| u_j c_j} \qquad \text{(Eqn. 1.47)}$$

where *z*, *u*, *c* represent charge, mobility and concentration, respectively. In addition, mobility of ion *i* can be written as:

$$u_i = \frac{|z_i| F D_i}{RT} \qquad \text{(Eqn. 1.48)}$$

Therefore from Eqn. 1.48, it is shown that the transport number is proportional to the mobility ratio of ion *i* and *j*, *e.g.* in HCl solution, if $u_{H^+} \approx 4u_{Cl^-}$, then $t_{H^+}=0.8$ and $t_{Cl^-}=0.2$. Additionally, in the near-electrode-range, the current is contributed by both migration and diffusion, which leads to Eqn. 1.44:

$$i_{total} = i_m + i_d \qquad \text{(Eqn. 1.49)}$$

where i_m and i_d represent the current contribution by migration and diffusion, respectively.

The migration flux of the electroactive ions can be decreased or even eliminated by adding excessive indifferent inert electrolyte, since $t_i \to 0$ leading $i_m \to 0$.

1.4.2. Diffusion

Diffusion is an entropically driven process which describes the random movement of species to the homogenization due to thermodynamics. The species move *via* a concentration gradient (a chemical potential gradient). Therefore the rate of diffusion at a certain point in the solution is dependent on the concentration gradient. The rate of diffusion can be described as flux in $mol^{-1}\ s^{-1}\ cm^{-2}$. The relationship between flux and concentration gradient for species A at position *x* and time *t* (*x*,*t*) can be explained by Fick's first law:

$$j_A(x,t) = -D_A \frac{\partial c_A(x,t)}{\partial x} \qquad \text{(Eqn. 1.50)}$$

The relationship between concentration gradient and time in one dimension can be described by Fick's second law:

$$\frac{\partial c_A(x,t)}{\partial t} = D_A \left[\frac{\partial^2 c_A(x,t)}{\partial x^2}\right] \qquad \text{(Eqn. 1.51)}$$

For any spatial geometry, Fick's second law can be generalized:

$$\frac{\partial c_A}{\partial t} = D_A \nabla^2 [A] \qquad \text{(Eqn. 1.52)}$$

Where ∇^2 is the Laplacian operator.

1.4.3. Convection

There are two forms of convections: natural and forced. Natural convection is caused by the presence of density gradients, thermal gradients, *etc.* in a solution. It causes the material to flow from dense to less dense region. Because electrolysis can cause changes in solution density, which leads to a convection effect, therefore the time duration of voltammetric measurements are often controlled within 10 seconds in order to minimise the convection effect. Forced convection is caused by an external force that agitates the solution, normally by mechanical means. In this case, convection normally dominates the mass transport in the system. Because convection is deliberately induced to the system, therefore its hydrodynamic behaviour is well defined. Consequently, there are several convection controlled experiments, such as rotation disc voltammetry, sono-voltammetry and channel flow voltammetry. Convection can be simply treated based on a diffusion layer approach. Based on Fick's first law in one dimension, the flux of convection for species A can be shown in Eqn.1.53.

$$j_{convection} = [\mathrm{A}]V(x) \qquad \text{(Eqn. 1.53)}$$

where $V(x)$ is the local fluid velocity at point x in cm s^{-1}. The relationship between concentration, time and position is then given by:

$$\frac{\partial[A]}{\partial t} = -\mathrm{V}(x)\frac{\partial[A]}{\partial x} \qquad \text{(Eqn. 1.54)}$$

1.5. Electrochemical measurements

There are several major methods for electrochemical measurement and two of them were used in this thesis: potential controlled measurement and current controlled measurement. Cyclic voltammetry (CV), square wave voltammetry (SWV),

polography, chronoamperometry *etc.* are examples of voltage controlled method. Chronopontentiometry is an example of current controlled method.

1.5.1. Cyclic voltammetry

Cyclic voltammetry (CV) is one of the most widely used electroanalytical method for studying electroactive species.[18] CV can be used for analysing solids[19], polymers[20], liquid/liquid systems[21], biological systems[22, 23] and most commonly liquid solutions. A potentiostat (Fig. 1.10) controls the whole system. A modern potentiostat (controlled by a modern computer through an operation software or manually controlled through an oscilloscope) usually has the capability of carrying out a range of different voltammetric measurements such as cyclic voltammetry, chronoamperometry, and linear sweep voltammetry. Cyclic voltammetry is the predominate method employed within this thesis.

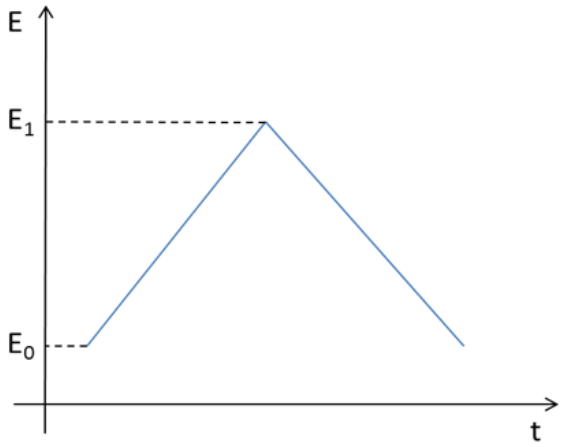

Fig. 1.12. A typical plot of potential against time for a cyclic voltammetry experiment.

Cyclic voltammetry is a potential controlled method, also known as the sweep potential method. A potential is scanned from E_0 to E_1 and normally back to E_0 (Fig. 1.12) or other potentials other than E_0 in a certain timescale. E_1 normally needs to be higher or lower than the standard potential, E^0 in order for a redox reaction to occur.

With the change of potential, the current passed through the electrode changes due to oxidation or reduction processes, therefore normally a cyclic voltammogram is a plot of current against potential. An example of a cyclic voltammetry at macroelectrode is shown in Fig. 1.13.

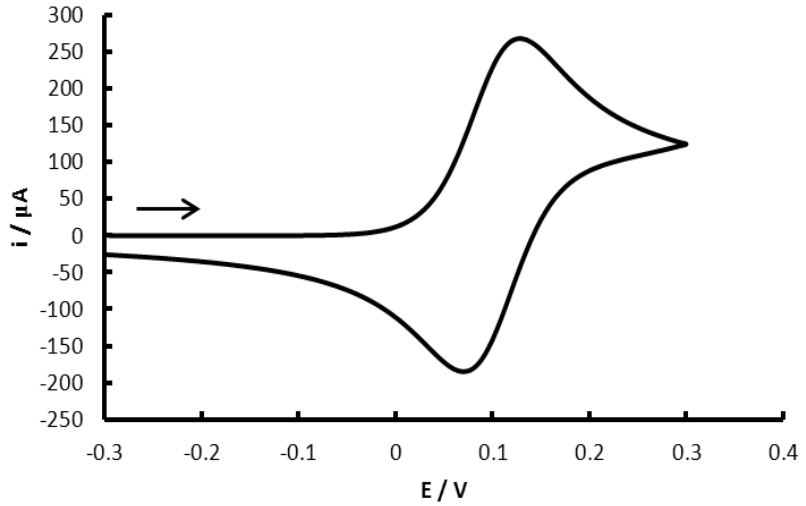

Fig. 1.13. An example of cyclic voltammetry created using DigiSim® with an A + e = B mechanism. Parameters: E_{start}: -0.3 V; E_{switch}: -0.3 V; E_{end}: -0.3 V; E^0 = +0.1 V; T = 298.2 K; planar electrode geometry = 10 cm^2; initial concentration of A = 0.001 mol dm^{-3}; E_0 = 0.1 V; using the semi-finite diffusion model.

1.5.1.1. Reversibility

Based on the different electrode kinetics, the electrochemical reactions can be described as reversible, quasi-reversible and irreversible. An electrochemically reversible process occurs when the rate of electrode reaction is faster than that of the mass transport. Conversely, if the rate of electrochemical reaction is slower than the rate of mass transport, then the reactant is electrochemically irreversible. Normally with D = 10^{-5} cm^2 s^{-1} and at 298 K, the reversibility can be described by a standard heterogeneous rate constant, k^0. Matsuda and Ayabe[24] suggested that, for a reversible case, $k^0 > 0.3v^{1/2}$ cm s^{-1}, for a quasi-reversible case, k^0 in range of less than $0.3v^{1/2}$ cm s^{-1} and greater than 2 x $10^{-5}v^{1/2}$ cm s^{-1}, and for a totally irreversible case, $k^0 < 2$ x $10^{-5}v^{1/2}$ cm s^{-1}, where v is the scan rate, respectively.

If consider a simple one electron transfer process (Scheme 1.1, with n = 1), the process can be described as E_r, where the E stands for electron transfer and the subscript, r, stands for reversible process.

For a reversible limit case, the sweep peak current can be given by the Randles-Sevčik equation[25, 26]:

$$i_p = 0.4463nFA\left[\frac{nF}{RT}\right]^{1/2} cD^{1/2}v^{1/2} \qquad \text{(Eqn. 1.55)}$$

For a reversible CV, the rate of electron transfer is controlled by diffusion. The separation of cathodic and anodic peak potentials is around 56/n mV. In real cases, the separation in range 60-70 mV can be considered as reversible. The peak potential in reversible process is independent of scan rate. The ratio of cathodic to anodic currents is unity at all different scan rates. As shown in Eqn. 1.55, the peak current is proportional to the square root of the scan rate, therefore graph of log i_p *vs.* log v is normally plotted in order to distinguish between a diffusion controlled process and an adsorbed process. In practical cases, the slope equals to 0.5 indicates the process is under diffusion controlled; a slope of unity indicates the electroacitve material is adsorbed on the electrode.

For an irreversible case, E_{irr}, the Randles-Sevčik equation is modified to be:

$$i_p = 0.496nFA\left[\frac{\alpha nF}{RT}\right]^{1/2} cD^{1/2}v^{1/2} \qquad \text{(Eqn. 1.56)}$$

As it can be seen from Eqn. 1.56, the peak current is still proportional to the square root of scan rate due to the diffusion controlled process. An extra term, the symmetry coefficient of the electron transfer process, is introduced in the Randles-Sevčik equation for irreversible case. For a single electron irreversible electrochemical process, the separation of peak potential varies with the change of scan rate at 298 K is given by:

$$\Delta E_p = \frac{59.4}{\alpha} + \text{constant} \qquad \text{(Eqn. 1.57)}$$

where ΔE_p is the potential difference between oxidative and reductive peaks. It is also known as approximately 30 mV shift per decade change in scan rate.

A quasi-reversible process sits in between reversible limit and irreversible limit. In practice, quasi-reversible processes appear reversible at slow scan rate and afforts irreversible behaviour at high scan rate as the limits which are described by Matsuda and Ayabe[24]. Normally a plot of peak potential versus $\log_{10} v$ is used to find the reversible limit. The peak potential initially independent on increasing scan rate and the peak potential starts to shift in high scan rates, therefore reversible limit equations can be applied in the reversible regime and irreversible limit equations can be applied in the irreversible regime.

In addition, the transit between reversible to quasi-reversible and on to irreversible process can be described by plotting peak current against square root of scan rates (Fig. 1.14).

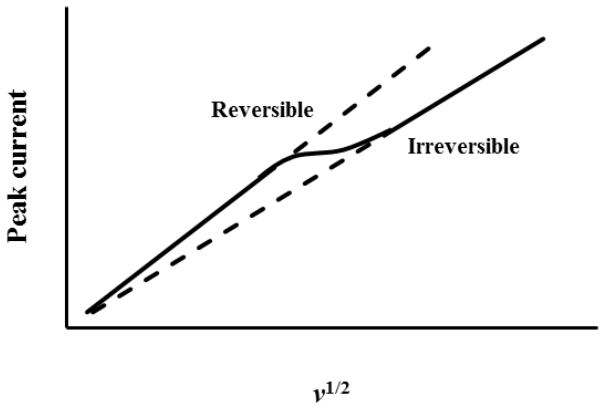

Fig. 1.14. Plot of peak current against square root of scan rates corresponding to reversibility changes.

1.5.1.2. Coupled homogeneous reactions

1.5.1.2.1. EC process

A reversible heterogeneous electron transfer process sometimes can be coupled with an irreversible homogeneous chemical process, the latter followed by the former, and this process is normally termed as an $E_{rev}C_{irrev}$ process. A general illustration can be given by:

$$A + e^- \rightleftarrows B \quad (E) \qquad \text{(Scheme 1.4)}$$

$$B \rightarrow C \quad (C) \qquad \text{(Scheme 1.5)}$$

The most obvious indicator of an $E_{rev}C_{irrev}$ process is losing a reverse peak in the cyclic voltammetry as the homogeneous chemical reaction consumes the product, which is generated by the electrochemical process and a shift on the peak potential. Alternatively, the reverse peak may change shape (*i.e.* decrease in peak current) as the homogeneous chemical reaction consumes certain amount of product but not significant enough to loss the reverse peak.

In a typical $E_{rev}C_{irrev}$ process, the ratio of forward peak current and reverse peak current is less than 1. The peak potential shifts ~30/n mV at 298 K per decade change in scan rate. The shape of voltammogram appears more reversible at fast scan rate (*e.g.* 1000 V s^{-1}).

In some cases, the homogeneous chemical reaction is reversible. The general equation is given by:

$$A + e^- \rightleftarrows B \quad (E) \qquad \text{(Scheme 1.6)}$$

$$B \rightleftarrows C \quad (C) \qquad \text{(Scheme 1.7)}$$

The diagnostics of an $E_{rev}C_{rev}$ process are similar to the characteristics of an $E_{rev}C_{irrev}$ process except a decrease in the reverse peak can be observed at high scan rate and tends to more reversible at slow scan rate (*e.g.* 0.01 V s^{-1}).

There is another important case of EC process, which is known as catalytic or EC′. The redox couple acts as a mediator. The general equations are given by:

$$A + e^- \rightleftarrows B \quad (E) \qquad \text{(Scheme 1.8)}$$

$$B + C \rightleftarrows A + D \quad (C) \qquad \text{(Scheme 1.9)}$$

As shown in Scheme 1.9, the chemical reaction forms A and D, and A "feeds back" into the electrode reaction, and as a result, the current response of electron transfer process is increased. When the concentration of chemical B is high enough, the shape of voltammgram starts to trends to a sigmoidal shape which similar to a steady state voltammogram. The increase concentration of B causes the increase of concentration of A at electrode surface. This leads to the change of the ratio of diffusion and reaction layer thickness, λ. With λ less than 0.1, the diffusion is faster than the chemical reaction, on the other hand, with λ greater than 1, the process becomes independent on diffusion and the shape of voltammogram tends to sigmoidal. An example of a typical cyclic voltammetry response of EC′ process is shown in Fig. 1.15.

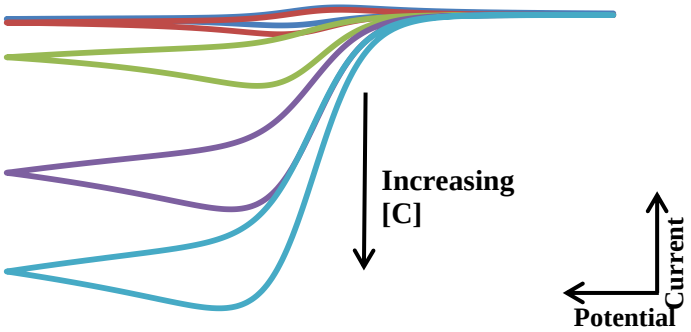

Fig. 1.15. Simulated example of EC′ reaction

As shown in Fig. 1.15, there is an enhancement in the reduction peak by the addition of C. The corresponding reduction peak decrease by the addition of C due to the consumption of B. When a large amount of C added to the solution, the shape of wave transformed from a conventional “duck shape” to a sigmoidal shape and the current becomes limiting current.

The mass transport near electrode is described in Fig. 1.16. As it can be seen that in Fig. 1.16, the current response on the electrode can be depended on:

- concentration of A,
- concentration of C,
- rate of mass transport of A, and
- rate of mass transport of C.

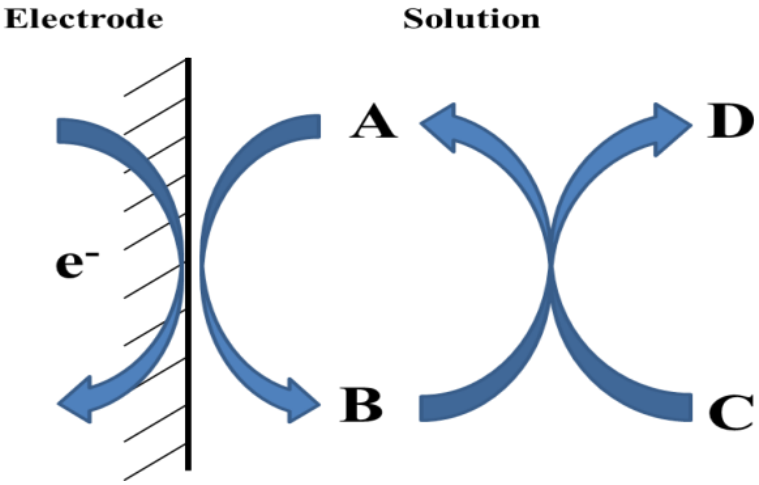

Fig. 1.16. Mass transport of EC′ reaction.

The cyclic voltammetry response corresponding to the first order rate-determine step of A and C can be different governed by only two dimensionless parameters:

- $\log(\frac{RTkc_A}{Fv})$
- $\log\left(\frac{c_C}{c_A}\right)$

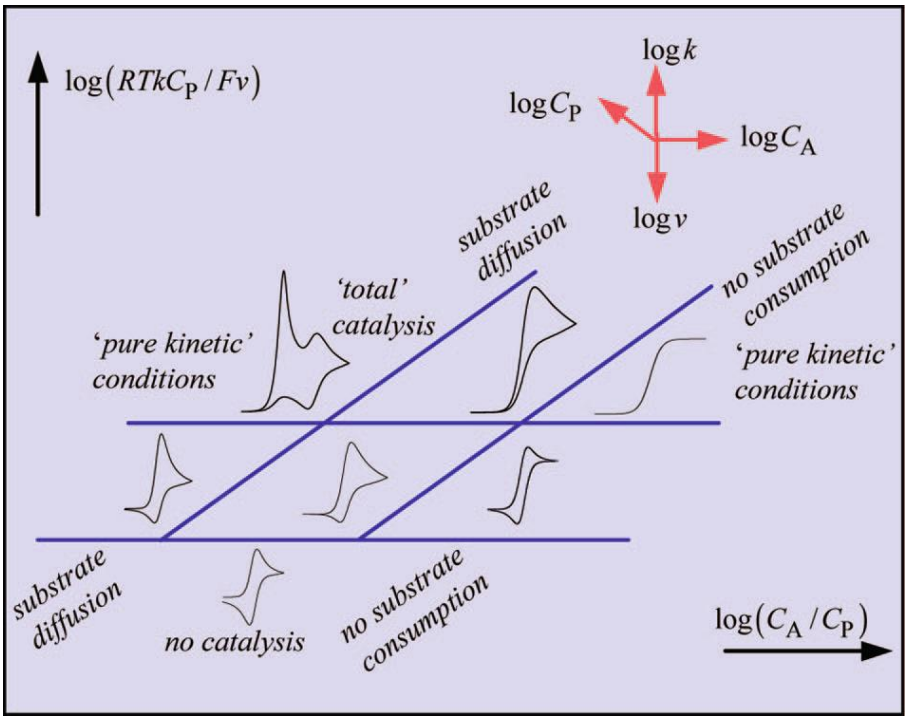

Fig. 1.17. Cyclic voltammetry graphs in kinetic zone of EC′ reaction mechanism. Reprinted with permission from Savéant, J.-M., *Chem. Rev.* **2008,** *108*, 2348-2378.[27] Copyright (2008) American Chemical Society.

As shown in Fig. 1.17, in the "no substrate consumption" zone, the response transferred from a reversible "no catalytic" response (*i.e.* the "the duck shape") to a sigmoidal shape and becomes no dependent on scan rates. The catalytic reaction is faster compared to diffusion. The plateau current, I_p, can be used to measure the rate constant:

$$I_P = \mathrm{F} c_A {D_A}^{1/2} k^{1/2} {c_C}^{1/2} S \qquad \text{(Eqn. 1.58)}$$

where F is Faraday constant, c_A is the concentration of species *A*, D_A is the diffusion coefficient of species A, k is the first order rate constant, c_C is the concentration of species C and *S* is the area of electrode, respectively.

On the other hand, when the system controlled by the diffusion of substrate, C, then the voltammogram looks like the two-wave "total catalysis" response, which consists on the top left of zone diagram (Fig. 1.17). And the peak current of the first wave, I_p',

can be described as:

$$I_P' = 0.609S\mathrm{F}\sqrt{\frac{c_C v}{\mathrm{R}T}} \qquad \text{(Eqn. 1.59)}$$

where R is gas constant and *T* is temperature in K, respectively.

In this case, the rate constant can be worked out by peak potential instead of current:

$$E_p = E^0_{A/B} - 0.409\frac{\mathrm{R}T}{\mathrm{F}} + \frac{\mathrm{R}T}{\mathrm{F}}\ln(\frac{\mathrm{R}Tkc_A{}^2}{\mathrm{F}vc_C}) \qquad \text{(Eqn. 1.60)}$$

In practice, the experimental data normally is used to compare with digital simulated results and analyse the reaction mechanisms.

An example of EC process can be the oxidation of octacyanomolybdate (V)[28], and an example of EC′ reaction can be the oxidation of cysteine which mediated by the oxidation of octacyanomolybdate (V)[28]. In this thesis, the EC′ reaction was studied through the oxidation of thiols using chlorpromazine as mediator.

1.5.1.2.2. ECE and disproportionation process

If there is another heterogeneous electron transfer process followed by an EC process, it can be described as an ECE process. An example of ECE process can be the reduction of p-halonitrobenzene[29]. Assuming both electron transfer process are electrochemical reversible, a general equation of ECE process can be given by:

$$\mathrm{A} + e^- \rightleftarrows B \quad \text{(E)} \qquad \text{(Scheme 1.10)}$$

$$\mathrm{B} \overset{k_1}{\rightarrow} \mathrm{C} \quad \text{(C)} \qquad \text{(Scheme 1.11)}$$

$$\mathrm{C} + e^- \rightleftarrows D \quad \text{(E)} \qquad \text{(Scheme 1.12)}$$

There are a few situations can be considered for an ECE process. First, if the formal potential of A/B couple is more negative than that of C/D couple, there will be only one peak shown in the voltammogram, and the reverse peak can only be seen if k_1 is small compare to the rate of electron transfer, and it will disappear when the chemical reaction is considerably fast (*i.e.* large k_1). Secondly, if the formal potential of A/B couple is less negative than that of C/D couple, then one reversible wave can be seen when chemical reaction is slow. As the chemical reaction becomes faster (*i.e.* k_1 is bigger), the second reversible wave can be seen and the wave corresponding to the first redox couple becomes less reversible, when the chemical reaction is fast enough, the second wave becomes reversible and reaches its maximum peak current at a fixed scan rate, whereas the first redox couple (A/B couple) peak becomes fully irreversible with the disappearance of its reverse peak.

In some coupled phases reaction cases, disproportionation could happen, and the process (DISP process) can be given by equations:

$$\mathrm{A} + e^- \rightleftarrows B \quad \text{(E)} \qquad \text{(Scheme 1.13)}$$

$$\mathrm{B} \rightleftarrows \mathrm{C} \quad \text{(C)} \qquad \text{(Scheme 1.14)}$$

$$\mathrm{B} + \mathrm{C} \rightleftarrows \mathrm{A} + \mathrm{D} \quad \text{(DISP)} \qquad \text{(Scheme 1.15)}$$

There are different types of DISP reaction depending on the rate determining step. If the step of Scheme 1.14 is the rate limiting step, then the reaction can be called as DISP 1 reaction, whereas if the rate determine step is on the step of Scheme 1.15, a second order reaction, then the process can be presented as DISP 2. It is relatively easy to distinguish between DISP 2 and DISP 1 or DISP 2 and ECE as there is a shift of peak potential with changing the concentration of A and the peak potential shifts approximately 20 mV per decade change of scan rate. However, it is hard to

discriminating between DISP 1 and ECE as their voltammetric behaviours are similar. There are several approaches were made to distinguish between DISP 1 and ECE such as by using a double potential step chronoamperometry[30], using a microband channel flow electrode[31], or using a competing homogeneous[31] or heterogeneous[32] processes or even *via* the use of microelectrode waveshape analysis.

1.5.1.2.3. CE process

There is a special case of coupled homogeneous and heterogeneous process known as CE process, which the heterogeneous electron transfer follows a homogeneous chemical reaction. The process is given by:

$$\mathrm{A} \rightleftarrows \mathrm{B} \quad \text{(C)} \qquad \text{(Scheme 1.16)}$$

$$\mathrm{B} + e^- \rightleftarrows C \quad \text{(E)} \qquad \text{(Scheme 1.17)}$$

Because the electron transfer process is followed by the chemical reaction, therefore the faster the chemical reaction, the sharper peak will appear in the voltammogram. There are a few examples of CE process such as reduction of formaldehyde[33] and oxidation of 1,2,3-trimethylhexahydropyridazine in butyronitrile with electrolyte[34]. The peak shape changes with both changing rate of chemical reaction and scan rates.

1.5.2. Square wave voltammetry

Square wave voltammetry (SWV) becomes one of the most important electroanalytical tools in electrochemistry recently due to its well understood theory[35] and extremely high sensitivity, especially to surface-confined electrode reactions. Therefore SWV is used mainly on analytical purposes, specifically on determination of electroactive organic molecules which are adsorbed on the surface of electrode[36].

A schematic diagram is shown in Fig. 1.18 for a potential-time change for a SWV. As shown in Fig. 1.18, the potential changes in a square wave form as increase experimental time. The initial potential starts at E_0, then the potential goes up to E_0+E_{sw}, which E_{sw} is amplitude, and it is held for $\Delta t/2$ (pulse duration) seconds and the potential then goes down to $E_0+(-E_{sw})$. Δt is known as period, and the frequency can be illustrated to be $f = \Delta t^{-1}$. ΔE represents the potential increment of the staircase waveform. The currents are measured at the end of each pulse (both i_f and i_b).

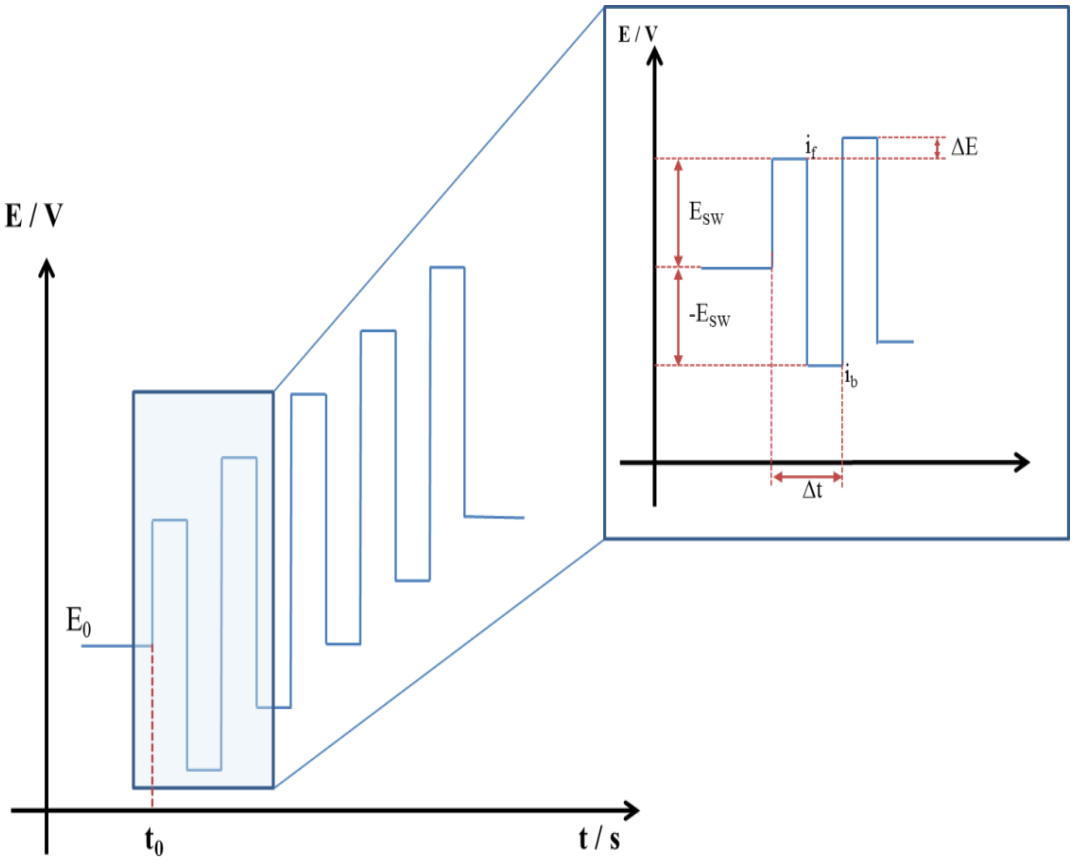

Fig. 1.18 A schematic diagram of the principle square wave voltammetry.

In practice, the net current, which subtracts i_b from i_f is normally shown in the software. Fig. 1.19 shows a typical SWV response.

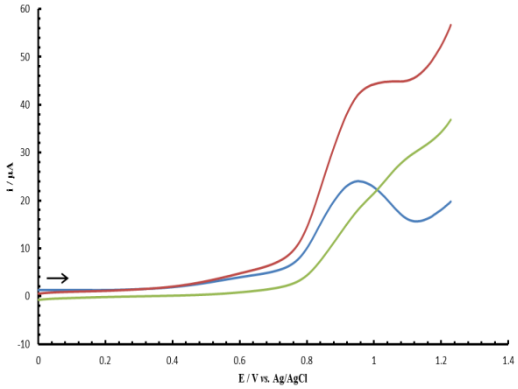

Fig. 1.19. An example of SW voltammogram of oxidation of 1 mM 2,4,6-Trihydroxybenzoic acid in water with 0.1 M KCl. Initial potential = 0 V, end potential = +1.23 V, step potential (ΔE) = 0.005 V, amplitude = 0.02 V and frequency = 25 Hz. Blue line represents the net current, red line represents forward current and green line represents the backward current. Ag/AgCl was used as reference electrode and a nickel wire was used as a counter electrode.

As shown in Fig. 1.19, the net current is usually shown as final view of a SW voltammogram. The charging current in this case can be negligible as the currents are measured after each pulse. Note that the backward current is positive and without a peak is due to small value of E_{SW}. The net peak current i_p has linear dependence on the square root of frequency (f):

$$i_p = n\mathrm{F}SD^{1/2}\varphi_p f^{1/2} c \qquad \text{(Eqn. 1.61)}$$

where φ_p is dimensionless peak current and it depends on nE_{SW} and $n\Delta E$. In an irreversible case, i_p has a linear function of log f, and the slope of the plot is given by:

$$\frac{\partial E_p}{\partial log f} = 2.3\mathrm{R}T/2\alpha n \qquad \text{(Eqn. 1.62)}$$

where α is the kinetic parameter known as symmetry coefficient of the electron transfer process.

1.5.3. Potential step chronoamperometry

Unlike a SWV method, potential step chronoamperometry has a fixed potential and the current response is monitored as a function of time. Fig. 1.20 illustrates the basic

wave-shape and current-time curve of a potential step chronoamperometry.

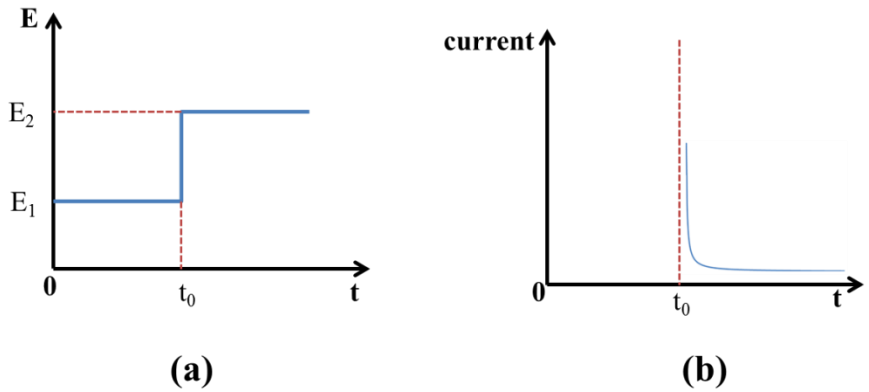

Fig. 1.20. Principle of chronoamperometry. Potential change with time changing (a); current change with changing time (b).

The potential is firstly held at a level, E_1, typically at an energy where no electrolysis can happen. Then at time t_0, the potential is stepped to E_2, a potential that can cause electrolysis or electrochemical reaction of the electroactive species at the electrode surface. Therefore a large current can be seen in Fig. 1.20(b) at t_0. The materials start to deplete and the current drops very fast after t_0. On a macroelectrode, as diffusion profile is linear one-dimensional, the current decays square root of time, whereas on a microelectrode, the current can reach steady state.

A common post-experimental analysis for a potential step chronoamperometry is to fit experimental data to the Shoup-Szabo[37] equation. This method is based on a microelectrode. Briefly, it involves a dimensionless time variable:

$$\tau = \frac{4Dt}{\alpha^2} \qquad \text{(Eqn. 1.63)}$$

and the dimensionless current, ψ_{exp} can be given by:

$$\psi_{\text{exp}} = \frac{i}{4nFDac_{bluk}} \qquad \text{(Eqn. 1.64)}$$

In addition, the theoretical dimensionless current, ψ_{thy}, is given by:

$$\psi_{thy} = 0.7854 + 0.8862\tau^{-0.5} + 0.2146\exp(-0.7823\tau^{-0.5}) \quad \text{(Eqn. 1.65)}$$

with this expression is accurate to 0.6% for all times.

By using these three equations, a fitting can be made by plotting ψ_{exp} and ψ_{thy} against dimensionless time, τ, by varying D and n. Therefore a best fit predicts n and D. A difference minimisation parameter[1], $\wp$, which given by:

$$\wp = \frac{1}{\sum s}\sum_s \frac{|\psi_{exp} - \psi_{thy}|}{\psi_{exp}} \quad \text{(Eqn. 1.66)}$$

Where s is number of data sets, respectively. Therefore the minimal number of $\wp$ indicates the best fitting.

The other common method for analysing chronoamperometry is using Cottrel equation. By applying Fick's second law, the current response under diffusion controlled condition is given by:

$$i = \frac{n\mathrm{F}Ac_{bulk}D^{1/2}}{\pi^{1/2}t^{1/2}} \quad \text{(Eqn. 1.67)}$$

As shown by the Cottrell equation, under diffusion controlled the current decreases exponentially with time (Fig. 1.20b). In practice, the Cottrell equation is normally used to compare theoretical and experimental data, similar to Shoup-Szabo equations. However, in order to use the Cottrell equation, the timescale must be less than 10 s and greater than the charging time of the electrode.

1.5.4. Voltammetry at microelectrodes

The most of the methods mention in previous sections are based on macroelectrode

(apart from the chronoamperometry) that the diffusion profile is linear one-dimension diffusion. However, the diffusion profile at a microelectrode is different from that of on macroelectrodes. This can be explained by flux:

$$j = \mathrm{D}c_{bluk}\left(\frac{1}{\sqrt{D\pi t}} + \frac{1}{r_e}\right) \qquad \text{(Eqn. 1.68)}$$

Where j is flux in mol cm^{-2} s^{-1} and r_e is the radius of electrode, respectively. As it can be seen from Eqn. 1.68, flux is dominated by two terms: $\sqrt{(D\pi t)}$ and r_e. Therefore if the electrode is large and diffusion is linear (one-dimenonional), then r_e is significantly greater than $\sqrt{(\mathrm{D}\pi t)}$, which leads the flux to be dominated by $\sqrt{(D\pi t)}$:

$$j = \frac{c_{bluk}\sqrt{D}}{\sqrt{\pi t}} \qquad \text{(Eqn. 1.69)}$$

Then the flux is proportional to square root of time. Nevertheless, In the case of microelectrode, $\sqrt{(\mathrm{D}\pi t)}$ becomes much greater than the electrode radius, and the flux is then dominated by the radius:

$$j = \frac{Dc_{bluk}}{r_e} \qquad \text{(Eqn. 1.70)}$$

It has been illustrated in Eqn. 1.38 that flux is a function of current, and then the term j can be substituted by current:

$$i = \frac{n\mathrm{F}c_{bluk}AD}{r_e} \qquad \text{(Eqn. 1.71)}$$

where A is the area of electrode. If microelectrode is disc shaped, then:

$$i_{lim} = 4n\mathrm{F}Dr_e c_{bluk} \qquad \text{(Eqn. 1.72)}$$

Comparing with Eqn. 1.71 and Eqn. 1.69, when the radius of electrode is small,

current (flux) becomes independent on time, thus a steady-state current is established.

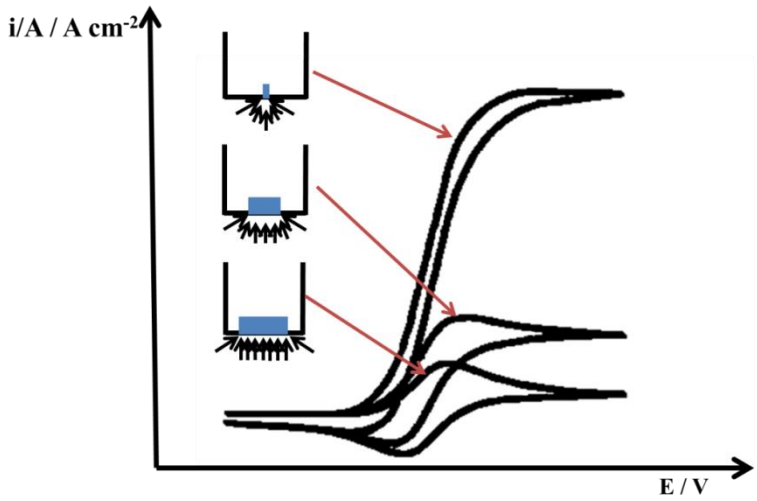

Fig. 1.21. Current density change when electrode size changes at cyclic voltammetry.

At a macroelectrode, diffusion is dominated by planner diffusion profile. As the radius of the disc decreases, the surface to edge ratio decreases, making edge diffusion equally (if not more) important. This brings about an enhanced flux of material and results in a steady-state response, which is shown in Fig. 1.21.

1.5.5. Channel electrodes

In this project, channel flow experiments were carried out and measured by using cyclic voltammetry. Because the solution is flowing through the cell with the working electrode placed in, the electrode process is no longer diffusion controlled; this is similar to the cyclic voltammetry at microelectrodes as mentioned in previous section. Although a steady-state current is established in this circumstance, unlike to the microelectrode, there are two forms of mass transport in this system: convection and diffusion.

In order to understand the mass transport, laminar flow must be established as it

provides a well-defined mass transport over a wide range of flow rates. Therefore under laminar flow steady-state, the components velocities are given by:

$$v_x = \mathrm{V}_0\left(1 - \frac{(y-h)^2}{h^2}\right) \quad \text{(Eqn. 1.73)}$$

$$v_y = 0 \quad \text{(Eqn. 1.74)}$$

$$v_z = 0 \quad \text{(Eqn. 1.75)}$$

where *x*, *y*, *z* are the coordinates and *h* is the half-height of the channel that defined in Fig. 122. V_0 respresents the velocity of the solution at the centre of the channel and can be defined as:

$$v_f = v_0 \int_0^d \int_0^{2h} \left(1 - \frac{(y-h)^2}{h^2}\right) dydz = \frac{4}{3} V_0 hd \quad \text{(Eqn. 1.76)}$$

where V_f is the volume flow rate in $cm^3\ s^{-1}$ and *d* is the width of channel.

In addition, the convective diffusion equation for species A is given by:

$$\frac{\partial[A]}{\partial t} = D_A \nabla^2[A] - \left(V_x \frac{\partial[A]}{\partial x} + V_y \frac{\partial[A]}{\partial y} + V_z \frac{\partial[A]}{\partial z}\right) \quad \text{(Eqn. 1.77)}$$

This equation can be simplified by using laminar flow channel electrode:

- as the height of the channel is relatively small and the laminar flow, the convections on both y and z axis are equal to zero,
- as steady-state measurements are made, the time dependent is removed (*i.e.* $\partial[A]/\partial t = 0$), and
- because the electrode itself is macro-sized, and the flow cell is properly designed, the axial and transverse diffusion can be neglected at relatively high flow rates, given by:

$$v_x \frac{\partial[A]}{\partial x} \gg D_B\left(\frac{\partial^2[B]}{\partial x^2} + \frac{\partial^2[B]}{\partial z^2}\right) \qquad \text{(Eqn. 1.78)}$$

Therefore Eqn. 1.77 becomes:

$$D_B \frac{\partial^2[A]}{\partial y^2} = v_x \frac{\partial[A]}{\partial x} \qquad \text{(Eqn. 1.79)}$$

By applying Lévêque approximation, the limiting current is given by:

$$I_{lim} = 0.925nFc_A w(x_e D_A)^{2/3}\left(\frac{v_f}{h^2 d}\right)^{1/3} \qquad \text{(Eqn. 1.80)}$$

Where I_{lim} is the limiting current measured in the experiment, n is number of moles electrons transferred in the process, F is the Faraday's constant, c_A is the concentration of chemical A in mM, w is width of electrode in meter, x_e is the length of electrode in meter, D_A is the diffusion coefficient in $m^2\ s^{-1}$, V_f is the velocity in $m^2\ s^{-1}$ which is known as flow rate, h is half of the height of the channel and, d is the width of channel (symbols refer to Fig. 1.22).

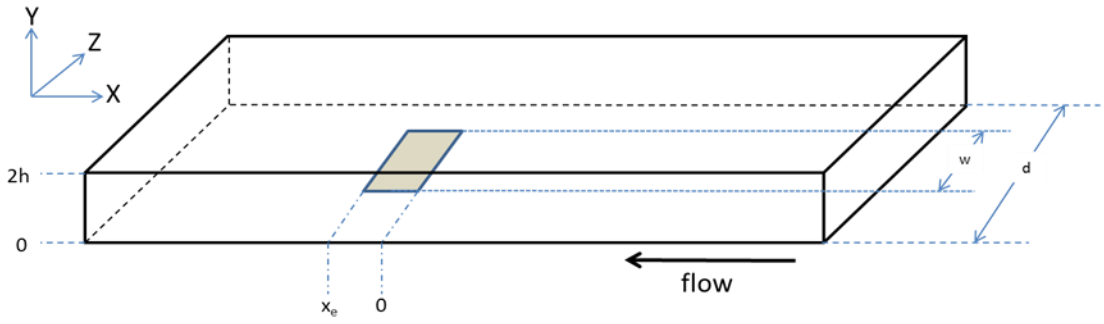

Fig. 1.22. A schematic diagram of typical channel flow cell.

More details of the channel flow setup can be found in experiment section (section 2.2).

1.6. Aims of this thesis

The aims of this thesis are to understand molecular electrochemistry by using several of chemicals, which involves different reaction mechanisms such as single heterogeneous electron transfer, EC, ECE and EC' reactions and the impact of mass transport behaviour in a variety of media such as aqueous, non-aqueous solvents and lyotropic liquid crystals. The study is based on varies of electrochemical analytical techniques such as CV, SWV, chronoamperometry, and also combine with other analytical tools such as UV-vis spectroscopy and X-ray scattering. The results are then analysed and understood by using the theories which are mentioned previously in this chapter and also combined with numerical simulation of transport phenomenon.

2. EXPERIMENTAL

2.1. Instrumentation

2.1.1. Potentiostat

Electrochemical measurements were carried out using conventional three electrode system. Most of the experiments in this thesis were undertaken using a μ-Autolab type III PGSTAT30 potentiostat, Netherland and controlled by an Intel® Core™ 2 processor computer using Window® Vista as operating system. A ModuLab potentiostat (Solarton analytical) which was controlled by an Intel® Core™ 2 processor computer using Window® Vista was used occasionally in this project. The software used to control the Autolab system was GPRS, written by Metrohm Autolab B.V. and the software used to control the ModuLab system was Solarton ModuLab electrochemical Software written by Solarton Analytical.

2.1.2. Electrodes

In all cases, unless otherwise mentioned, the electrochemical measurements were carried out using a three-electrode system. A platinum or nickel wire was serving as the counter electrode. The platinum or nickel wire was coiled in order to increase its surface area.

2.1.2.1. Working electrode

A disc macro-electrode (either made from glassy carbon or gold, BAS), shown in Fig. 2.1, was used as working electrode with 3 mm diameter electro-active area. Working electrodes were polished using increasing finer grades of carburundum paper (P400,

P1200, P2400, P4000 grade, Presi, France) and followed by polishing on a wetted, rayon polishing cloth using 0.3 μm alumina slurry (Presi, France).

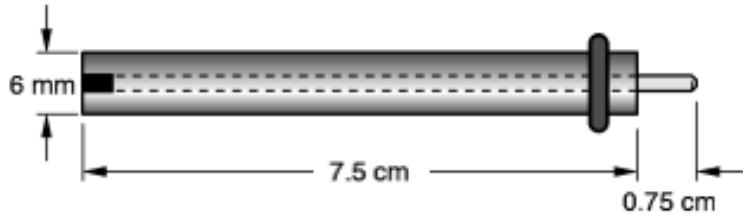

Fig. 2.1. A schematic diagram of the design of a disc macro-electrode. (image taken from the Bio Analytical System Inc. producte catalogue, © BASi)

The micro-working-electrode was made from either gold or carbon fibre and also disc shaped. The gold microelectrode was made in house and calibrated by the redox reaction of ferrocene in acetonitrile, the diameter for gold microelectrodes were found to be 33 μm and 50 μm. The carbon fibre electrode was purchased from BAS with 11 μm diameter electroactive surface area (Fig. 2.2).

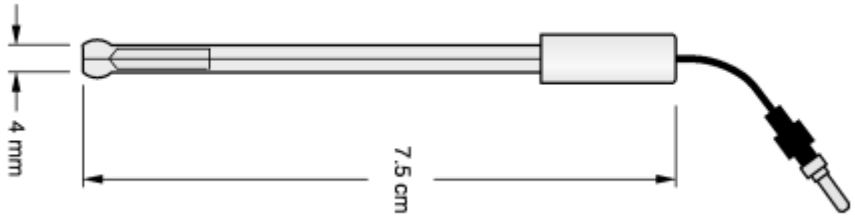

Fig. 2.2. A schematic diagram of the carbon fibre microelectrode used. (image taken from the Bio Analytical System Inc. producte catalogue, © BASi)

2.1.2.2. Reference electrode

A reference electrode were used either a saturated calomel electrode (obtained from BAS) or a siver/silver chloride electrode (obtained from BAS). Fig. 2.3 illustrates the silver/silver chloride reference electrode. The saturated calomel electrode potential is +0.242 V *vs.* standard hydrogen electrode (SHE) and the silver/silver chloride

electrode potential is +0.222 V *vs.* SHE.[38]

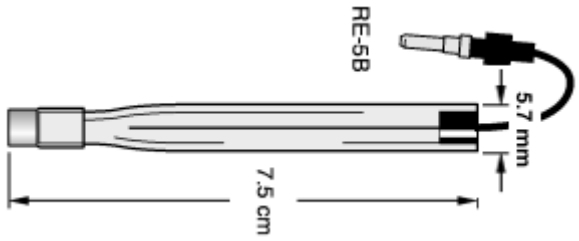

Fig. 2.3. A schematic diagram of the silver/silver chloride reference electrode used (image taken from the Bio Analytical System Inc. producte catalogue, © BASi)

2.1.2.3. Channel electrode

The channel flow electrode is mainly made by two separate parts (Fig. 2.4), the base plate was made of PTFE, and a channel was made in the plate. The plate is covered by an optically pure silica cover plate (Optiglass) in order to seal the channel. The two parts are sealed by super glue (Stick 2, Ever Build). The reason for using silica as cover plate is because photochemistry can be then carried out *in-situ* with this system.

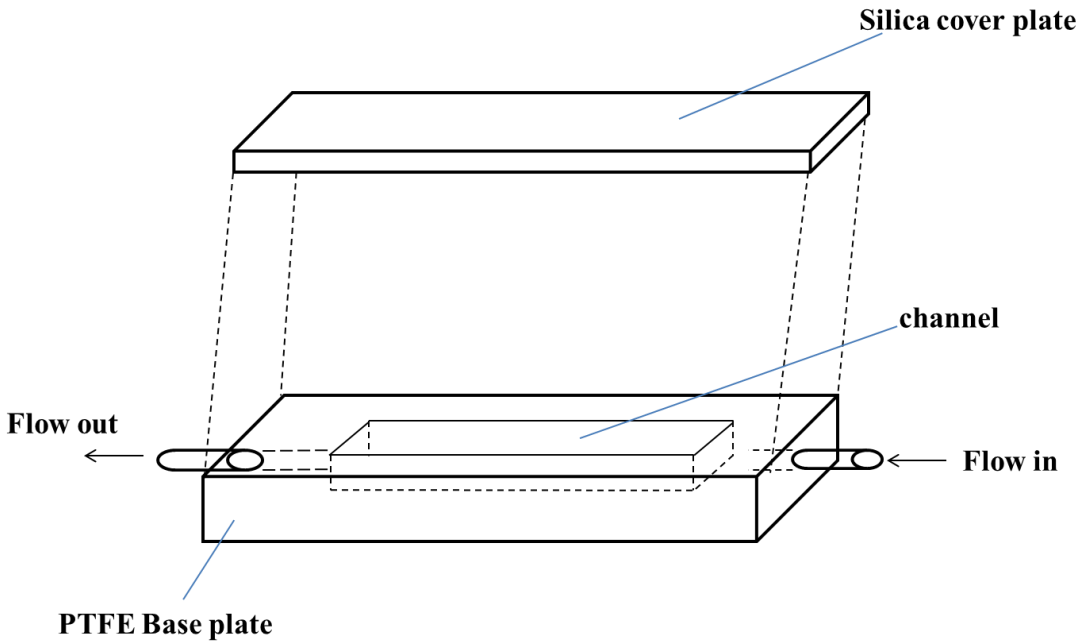

Fig. 2.4. A schematic design for a channel electrode in 3D.

A platinum slide was sat in the channel positioned at 1/3 of the length of channel (Fig.

2.5), to afford sufficient distance to establish laminar flow, the platinum was made in squared shape with 5.5 mm length and 4.5 mm width. The slide was connected *via* a conductive wire through a hole at the bottom of the channel. The squared shape allows a well-defined surface area and flow direction. The long lead-in positioned upstream of the electrode to allow the full development of Poiseuille flow. The electrode was polished by using a cotton swab with 0.3 μm alumina powder.

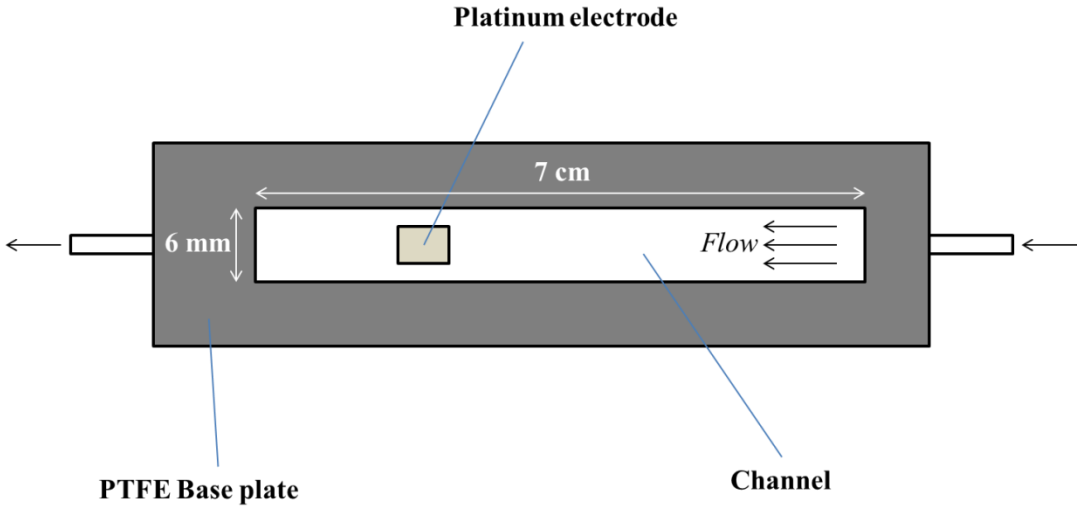

Fig. 2.5. Top view of the base plate with platinum electrode in the channel.

A syringe pump (Fusion 200, CHEMYX, USA) was used to drive the solution to flow in well-defined flow rates. The reference electrode was placed upstream relative to the working channel electrode and counter electrode was placed downstream to the working electrode so that the products formed on the counter electrode would not interfere with the process occurring on the working electrode.

2.1.2.4. Other equipments

The white light source for photo-catalytic electrochemical reactions in this project used was a two spot fiber optic illuminator manufactured by Brunel Microscopes Ltd.

The light source used for channel electrode experiment was an OptoScan monochromator, CAIRN RESEARCH.

Balance used in this project is Denver SI-234 by Denver Instrument.

2.2. Reagents

2.1.1 Chemicals

All the chemicals used in this project were purchased from Sigma-Aldrich unless otherwise mentioned.

Purified water was obtained from Centra-R200 HFV water-purifying system (of resistivity greater than 18.2 MΩ cm), made by GLGA.

2.2.1. Electrolyte

The electrolyte used in organic solvents was mainly either tetrabutylammonium perchlorate (TBAP) or tetrabutylammonium tetrafluoroborate (TBAT). TBAP was purchased from Sigma-Aldrich. TBAT was house synthesised by mixing 130 g tetrabutylammonium bisulfate and 44 g sodium tetrafluoroborate in purified water (800 mL). The precipitate was obtained by filtration and then dissolved in dichloromethane (HPLC grade, purchased from Fisher Scientific). Magnesium sulphate (laboratory reagent grade, purchased from Fisher Scientific) was used to dry the solution. The magnesium sulfate was removed by filtration and the dichloromethane evaporated off. The product was then recrysatllised by 60/40 petrol ether (purchased from Fisher Scientific, reagent grade).

2.3. Experimental preparations

Different coupled homogenous reactions have been studied including electrochemically induced ion release, protonation, catalysis and the study of mass transport in lyotropic liquid crystals.

2.3.1. Electrochemically induced ion release

Electrochemical reduction of nitroprusside ion was investigated in non-aqueous solvent as a typical ECE process with a cyanide ion release[39]. In order to solubilise nitroprusside ion in non-aqueous solvent (*i.e.* acetonitrile), Tetra-*n*-butylammonium nitroprusside (short for TBANP), $[N(C_4H_9)_4]_2Fe(CN)_5NO$, was used in this project. It was prepared by metathesis of sodium nitrprusside and tetra-butylammonium hydrogen sulphate in water with 1:1 molar ratio. The precipitate was then obtained by filtration and washed with water. The powder was then further dried under vacuum and recrystallized from water. The TBANP was slightly wet. The product was verified by HPCL-MS (electron spray ionisation) with m/z = 242 (requires 242.28) for the positive ion and m/z = 108 (requires 107.98) for the negative ion.

The electrochemical analysis was then carried out by dissolving TBANP in acetonitrile (HPLC grade, Fisher Scientific) with supporting electrolyte. A standard three electrode electrochemical cell was used and the electrochemical analysis was controlled by a μ-AutoLab system. A glassy carbon (3 mm diameter, BAS) electrode or a carbon fibre (11 μm diameter, BAS) was used as working electrode, a spiral nickel wire was used as the counter electrode and saturated calomel electrode (Radiometer) was used as the reference electrode.

In addition, electrochemical reduction of iodo-nitrobenzene was studied. 1-iodo-4-nitrobeznene solution was prepared by dissolving 1-5 mM 1-iodo-4-nitrobenzene in acetonitrile (purchased from Fisher Scientific, HPLC grade) with variable concentrations of tetrabutylammonium tetrafluoroborate and tetrabutylammonium iodide in ratios of 10:0, 8:2, 5:5, 2:8 and 0:10, with the fixed ionic strength = 0.1 M.

The cyclic voltammetry was carried out using a glassy carbon macro-electrode (3 mm diameter), or a carbon fibre micro-electrode (11 μm diameter), or a gold

macro-electrode (3 mm diameter), or gold microelectrodes (33 μm and 50 μm diameter). A spiral nickel wire was served as the counter electrode and the reference electrode was a saturated calomel electrode.

2.3.2. Electrochemically induced protonation

An electrochemically induced protontation process was investigated by reducing 2,3-diphenyl-1,4-diazaspiro[4.5]deca-1,3-diene (a spiro-bis-anil, short for SBA). It was prepared by stirring glacial acetic acid (100 mL), benzil (15.80 g), ammonium acetate (40 g) and cyclohexanone (8 mL) for 5 minutes, and followed by refluxing (118 ^{o}C) for 1.5 hours. The heated mixture was then transferred into vigorously stirred cold water (300 mL) and stirred overnight. The yellow spiro-bis-anil precipitate was filtered off and washed with water (4 x 30 mL) and dried under vacuum. with mp = 87–90 ℃; ν_{max} ($CHCl_3$) 1650 cm^{-1} (C═N); δ_H (400 MHz, $CDCl_3$) 7.55–7.45 (4H, m, 4 x C*H*; Ph), 7.52–7.42 (2H, m, 2 x C*H*; Ph),7.30–7.35 (4H, m, 4xC*H*; Ph), 1.92–1.95 (4H, m, 2xCH_2; cyclohexane), 1.80–1.83 (4H, m, 2xCH_2; cyclohexane), 1.71–1.74 (2H, m, CH_2; cyclohexane); δ_C (100 MHz, $CDCl_3$) 164.0 (C═N), 139.2 (2C,2 x *i-C*; Ph), 129.9 (4C, 4 x *C*H; Ph), 128.8 (2C, 2 x *C*H; Ph), 128.2 (4C, 4 x *C*H; Ph), 104.0 (*q-C*; cyclohexane), 34.6 (2C, 2xCH_2; cyclohexane), 25.6 (CH_2; cyclohexane), 24.1 (2C, 2xCH_2; cyclohexane); MS(CI) *m/z* 289.1669 (MH^+), $C_{20}H_{21}N_2^+$ requires 289.1694.

In order to compared the conventional reduction process under Birch condition with electrochemical reduction, conventional Birch condition reduction was performed. The spiro-bis-anil was added into mixture of 112 mL dry-Tetrahydrofuran (THF) and liquid ammonia (112 mL) at -78 ^{o}C with addition of sodium (6.38 g) over 30 minutes. The mixture was followed by 1 hour stirring under nitrogen and quenched by ethanol (100 mL) with stirring for 20 minutes, followed by addition of ammonium chloride (4.86 g) and warmed to 0 ^{o}C. The organic phase was extracted from water (100 mL)

with dichloromethane (3 x 50 mL) and dried over magnesium sulphate. Dichloromethane was then evaporated to afford the product, (2S,3S)-2,3-diphenyl-1,4- diazaspiro[4.5]decane. with mp = 40–43 ℃; δ_H (400 MHz,$CDCl_3$) 7.28–7.24 (10H, m, 10xC*H*; Ph), 5.65 (2H, br, s, 2 x N*H*), 4.10 (2H, s, 2 x C*H*; Ph), 1.80–1.83 (4H, m, 2 x C*H*; cyclohexane), 1.64–1.66 (4H, m, 2xCH_2; cyclohexane), 1.42–1.46 (2H, m, CH_2; cyclohexane); δ_C (100 MHz, $CDCl_3$) 140.5 (2C,2x*i-C*;Ph), 128.4 (4C, 4x*C*H; Ph), 127.4 (2C, 2x*C*H; Ph), 127.1 (4C, 4 x *C*H; Ph), 69.6 (2C, 2x*C*HN), 65.1 (*q-C*; cyclohexane), 39.5 (2C, 2xCH_2; cyclohexane), 25.4 (CH_2;cyclohexane), 23.9 (2C, 2xCH_2; cyclohexane); MS (CI) *m/z* 293.2010 (MH^+), $C_{20}H_{25}N_2^+$ requires 293.2012.

Electrochemical reduction process was conducted by dissolving the synthesised spiro-bis-anil in DMF, THF, acetonitrile and DMF/water mixture with fraction of 9:1 and 8:2 with supporting electrolytes (tetrabutylammonium perchlorate, TBAP and tetrabutylammonium tetrafluoroborate, TBABF). A standard three electrode cell was used and controlled by μ-AutoLab, with a glassy carbon (3 mm diameter, BAS) macroelectrode or a carbon fibre microelectrode (11 μm diameter, BAS) as working electrode, a spiral nickel wire counter electrode and a saturated calomel reference electrode.

Additionally, vitamin K_1 with lipid support and electrochemical oxidation of sudan III were also studied for electrochemically induced protonation, with a protonation process on vitamin K_1 and deprotonation process on sudan III.

Vitamin K_1 (VK1) was purchased from Sigma-Aldrich Co. (UK) and phosphatidylcholine (LC) was purchased from Avanti Polar Lipids Inc, respectively. Chloroform, HCl, boric acid, phosphoric acid, acetic acid and NaOH were ordered from Fisher Sientific, repectively.

The vitamin K_1 solution was prepared by adding 1 mM of vitamin K_1 in chloroform.

The vitamin K_1 with lipid solution was prepared by adding 1 mM of vitamin K_1 and 1.0 mM LC in chloroform. Then a certain amount of aliquot of the solution was pipetted and accumulated on the glassy carbon electrode, GCE, 3.0 mm diameter or a basil plane graphite electrode (BPGE) and waited for the chloroform solvent to be evaporated. The modified electrodes were then dipped into either 1.0 M HCl solution or a Britton-Robinson buffer solution.

The Britton-Robinson buffer (BRS) solution was prepared by dissolving 0.04 M boric acid, 0.04 M phosphoric acid and 0.04 M acetic acid in purified water. The initial pH value for BRS was 2 ± 0.1, measured by a pH meter (pH 210 microprocessor pH meter, HANNA instruments). Then the pH was increased by adding 0.2 M NaOH.

Sudan III was purchased from Sigma-Aldrich and dichloromethane (DCM) was purchased from Fisher Scientific, respectively. All the chemicals were used in the experiment without further purification. K_2HPO_4, KH_2PO_4, KCl, KOH and HCl were purchased from Fisher Scientific.

Phosphate buffer electrolyte solution (PBES) was prepared by adding 0.05 M K_2HPO_4 and 0.05 M KH_2PO_4 in 0.1 M KCl solution. The pH was then adjusted by adding either concentrated KOH or HCl solution.

The oxidation of sudan III experiment was carried out by accumulating 5 μL of 10 mM Sudan III in DCM solution onto a glassy carbon electrode, then waited the DCM solvent to evaporate off and formed a solid layer of Sudan III on the electrode surface. The modified GCE was then dipped into a well-buffered solution (phosphate buffer).

2.3.3. Electrochemically induced catalytic process

The EC′ mechanism was studied in this thesis as an analytical detection method. Thiol compounds and lactic acid can be detected by EC′ process with a mediator of

chlorpromazine hydrochloride. The electrochemical detection of thiol compounds (L-cysteine and glutathione) was carried out by dissolving chlorpromazine (Sigma-Aldrich) in both pH 3.80 acetate buffered and unbuffered aqueous solutions. Variable concentrations of L-cysteine (Sigma) or glutathione (Sigma) was added in the solution. The acetate pH 3.80 buffered solutions was made by mixing 153 mL of 0.1 M sodium acetate and 847 mL of 0.1 M acetic acid with 0.1 M potassium chloride, KCl. The unbuffered solution used was 0.1 M KCl aqueous solution.

The detection of lactic acid was performed using chlorpromazine as mediator and dissolved in 0.1 M KCl aqueous solution. Variable concentrations of sodium acetate (Sigma-Aldrich) were added to the solutions, which contains chlorpromazine. Photochemically induced redox transfer was used in this experiment; therefore a two spot fibre optic illuminator (Brunel Microscopes Ltd.) was used as photo source. A specifically designed cell was used in order to conduct the photocatalysised electrochemistry, as shown in Fig. 2.6. A transparent silica glass was made in the bottom of cell in order to minimise the loss of photo source.

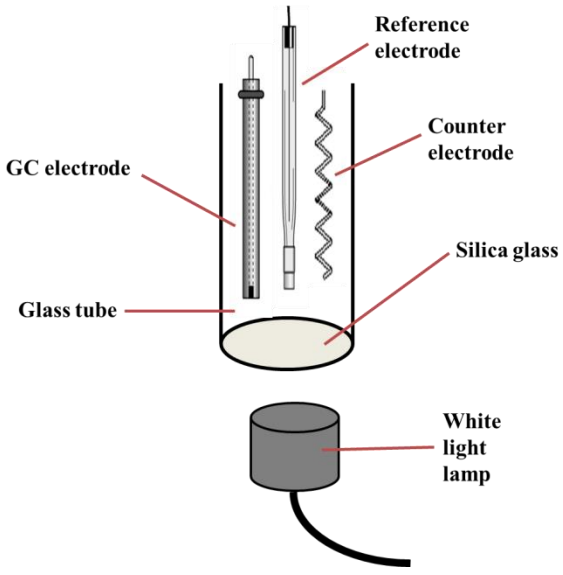

Fig. 2.6. A three electrode photo-electrochemical cell.

A glassy carbon macroelectrode (3 mm diameter, BAS) was used in both experiments, together with a spiral platinum counter electrode and a sliver/sliver chloride reference

electrode.

2.3.4. Mass transport in liquid crystals

Copper(II) phthalocyanine tetrasulfonic acid tetrasodium salt and nickel(II) phthalocyanine tetrasulfonic acid tetrasodium salt were studied electrochemically in order to understand electron transfer process in lyotropic chromonic liquid crystals. Both two organometallic materials were purchased from Sigma-Aldrich in the purest commercially available grade and used as received. Water was obtained from Elgastat system as mentioned before. Nitrogen and argon gas were obtained from BOS Gases, UK.

The chromonic liquid crystal for copper(II) system was prepared by mixing 46 wt.% (0.88 M) with water in a screw capped vial and nickel(II) system was prepared by mixing 20 wt.% (0.27 M) in water. Both samples were heated with stirring at 345 K for between 30 and 60 minutes to obtain sample homogenisation. The samples were then cool down to room temperature (296 ± 2 K) prior to experimentations.

Physical properties were studied preliminary. Conductivities were measured by using CDM210 conductivity meter equipped with a four pole CDC511T conductivity cell (Radiometer) inserted vertically into the sample. Optical properties were studied by using an Olympus BX-51 optical polarising microscope, equipped with a digital camera. UV-Vis spectrometry was carried out using a Perkin-Elmer Lambda 25 Scan UV-Vis instrument, controlled by a Pentium III PC, using a 10 mm path length quartz cell. X-ray scattering measurements were undertaken by filling the capillary tubes with the liquid crystal sample and placed into a MAR345 diffractometer with 2D image plate detector (with copper K_α radiation, graphite monochromator), with λ = 1.54 Å and distance between detector and sample set to 130-300 mm and 30 min exposure time. Both samples were heated between 297 K and 355 K in the presence

of a magnetic field using a home-built cappliary furnace.

Electrochemical measurements were carried out by using a standard three electrode system controlled by a μ-Autolab Type III potentiostat. A sliver/silver chloride reference electrode was employed and a nickel spiral counter electrode was used. Working electrodes used were glassy carbon macroeleectrode (3 mm diameter), platinum microelectrode (10 μm) and carbon fibre microelectrode (11 μm). Samples were degased using nitrogen or argon for reductive electrochemistry experiments. Electrodes were polished prior to all experiment using the procedure described previously.

In general, the temperature of the experiments carried out in this thesis is between 20 and 25 ℃ and under normal atmospheric pressure.

3. BIOSENSORS – ELECTROCHEMICALLY INDUCED CATALYTIC REACTIONS

The work presented in this chapter was undertaken with assistance from M. Hadjieleftheriou, D. Nunes and V. Beilstein. Additionally, this work was also collaborated with J. E. Halls and F. Marken from University of Bath.

3.1. Introduction

Electrochemical biosensors are widely used in varies of areas such as in clinics[40-43], agriculture[44, 45], food industry[46] and for environmental monitoring[47]. Although different measurements have been based on different methodologies, the major way to fabricate the sensor is by modifying the working electrode surface; the latter has been functionalised by a protein, such as antigen or enzyme with a redox active species attached on those[48]. However, the electrode can be hard to be fabricated due to multi-steps fabrication procedures. In most of the cases, especially electrode modified by a biological molecule, the electrode can either easily goes off or has to be stored in low temperature environment in order to maintain the biological molecules active. Therefore the usage can be limited.

Catalytic electrochemistry has been well studied for decades. As mentioned in the Introduction, the EC′ reaction mechanism has been studied systemically. A mediator is used to oxidised/reduce a substrate that of interested, and leads the redox current signal to increase. The catalytic method offers several advantages compared with

surface modification methodologies such as no electrode preparation, can be stored anywhere, rapid analysis and fast sample preparation. In this thesis, catalytic electrochemistry was used as a biosensing method for detection of L-cysteine and glutathione, L-lactic acid, and melamine.

3.2. Electrochemical detection of L-cysteine and glutathione *via* catalytic reactions

L-Cysteine and glutathione (Fig. 3.1) are essential thiols which play important roles in biochemical process[28, 49]. They act as antioxidants in human body to prevent leukaemia and several types of cancer[28], the depletion of cysteine and glutathione can also be a sign of premature arteriosclerosis[50], cervical cancer[51], diabetes, sepsis, cataracts, liver disorder and a few other disorders[52]. On the other hand, the excess concentration of cysteine and glutathione in human bodies can be an indicator for brain disorders[50], Alzheimer's disease, Parkinson's disease and AIDS related dementia[53]. In addition, glutathione has been attracted by numerous of scientists due to its biological functions such as maintain the thiol group in cysteine in reduced state and protect DNA and RNA in cells from free radicals[54]. Therefore analytical detection of thiols in human bodies such as L-cysteine and glutathione becomes an attractive area in analytical chemistry.

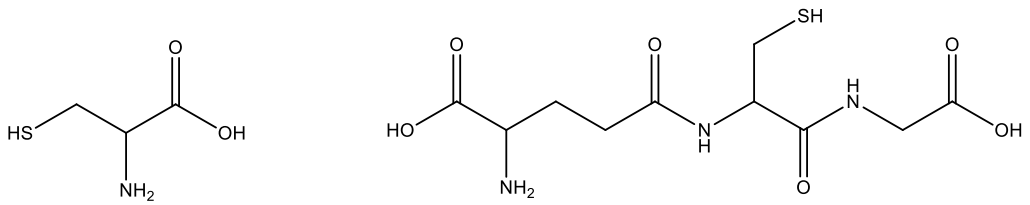

cysteine (a) glutathione (b)

Fig. 3.1. Chemical structures of (a) cysteine and (b) glutathione.

There are numerous of detection methods for thiols using electrochemistry including direct amperometry such as cyclic voltammetry[55-57], differential pulse

voltammetry[58], cathodic stripping voltammetry[59-63] and square wave voltammetry[64], and coupled electrochemical detection method with separation techniques such as liquid chromatography[65-67] and capillary electrophoresis[68-70]. Despite the coupled separation techniques, the direct amperometric/voltammetric detection has already been widely studied. Accordingly, most of the electrochemical detection methodologies of thiols are based on modified electrode, such as using a gold nanorods[71], using a glassy carbon electrode modified by enzymes[72], metal complex films[73], using a platinum electrode modified by organic conducting salt[74]. Because the nature of cysteine and glutathione, the voltammetric responses can be very poor (*vide infra*), and complicated by adsorption phenomena[75], modified electrode is necessary to mediate the oxidation. However, on the other hand, the mediation can also occur in the solution rather than on the electrode surface, and the analysis can be facile. In this thesis, chlorpromazine was used as a catalyst in unbuffered and buffered solutions, and it catalyse the oxidation of oxidation of cysteine and glutathione, in result, the current response increase with increasing concentration of thiols.

3.2.1. Electrochemical behavior of chlorpromazine in the absence of cysteine or its derivatives.

The initial investigation was to examine the oxidation of chlorpromazine hydrochloride in both buffered and unbuffered environments and carried out using cyclic voltammetry. The electrochemical response of 1.13 mM chlorpromazine in 0.1 M KCl aqueous solution is shown in Fig. 3.4. The voltammograms show a well-defined oxidative peak at +0.63 V *vs.* Ag/AgCl due to the single-electron-oxidation of chlorpromazine which forms the chemically stable radical as shown in Scheme 3.1. The pK_a of chlorpromazine is known as 9.3, therefore it is likely to be an ammonium group.

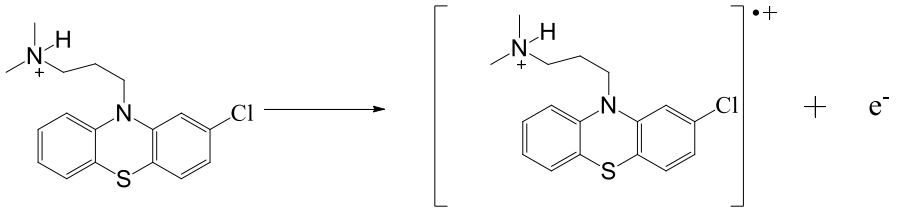

Scheme 3.1. One-electron oxidation of chlorpromazine.

The corresponding reduction peak in Fig. 3.4 was observed at +0.58 V *vs.* Ag/AgCl which leading to the reduction of the cation radical back to chlorpromazine. Three scans were performed and both of the peak potential and peak current remain unchanged for different scans, suggests that no substrates were absorbed on the electrode.

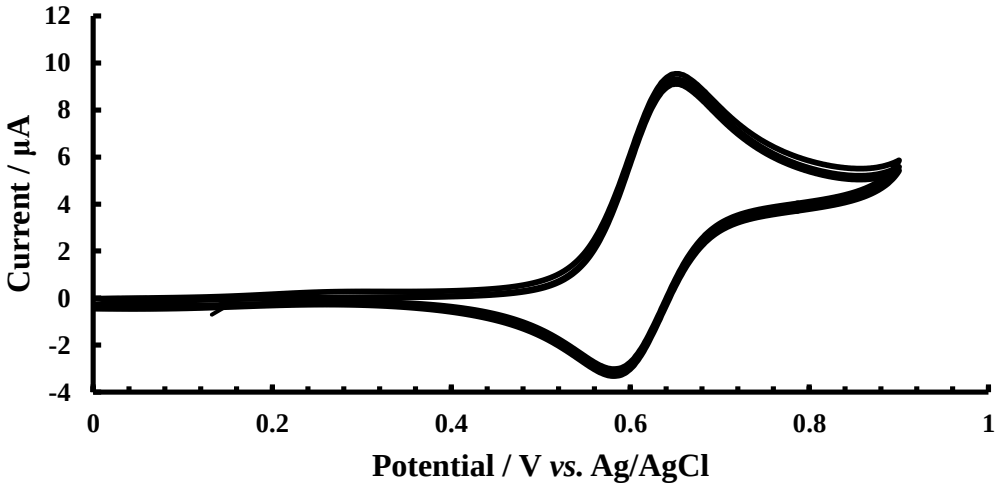

Fig. 3.4. Cyclic voltammograms for the oxidation of 1.26 mM chlorpromazine in 0.1 M KCl at a glassy carbon electrode (BAS, 3 mm diameter). Scan rate = 0.02 V s^{-1}. Ag/AgCl electrode was served as the reference electrode and spiral platinum wire was served as a counter electrode.

Scan rate dependent experiments of chlorpromazine oxidation was undertaken in order to understand the process in more detail. As shown in Fig. 3.5a, 1.13 mM of chlorpromazine was examined; the increase of scan rate leads the both oxidative and reductive peak current to increase. By plotting the peak currents against square root of scan rates (Fig. 3.5b) for both oxidative and reductive wave, the straight line cross the origin suggests that the electrode process is a diffusion-controlled process. The gradient of reduction wave is smaller than that of the oxidation wave, suggests that

there is a loss of material in the diffusion layer. Fig. 3.5c shows the plot of peak potential against logarithm of scan rates. It can be seen that there is a direct porportionation of the oxidative peak whereas there is no dependence on the reductive peak. These suggest that the oxidation process is electrochemically quasi-reversible whereas the reductive process is electrochemically reversible.

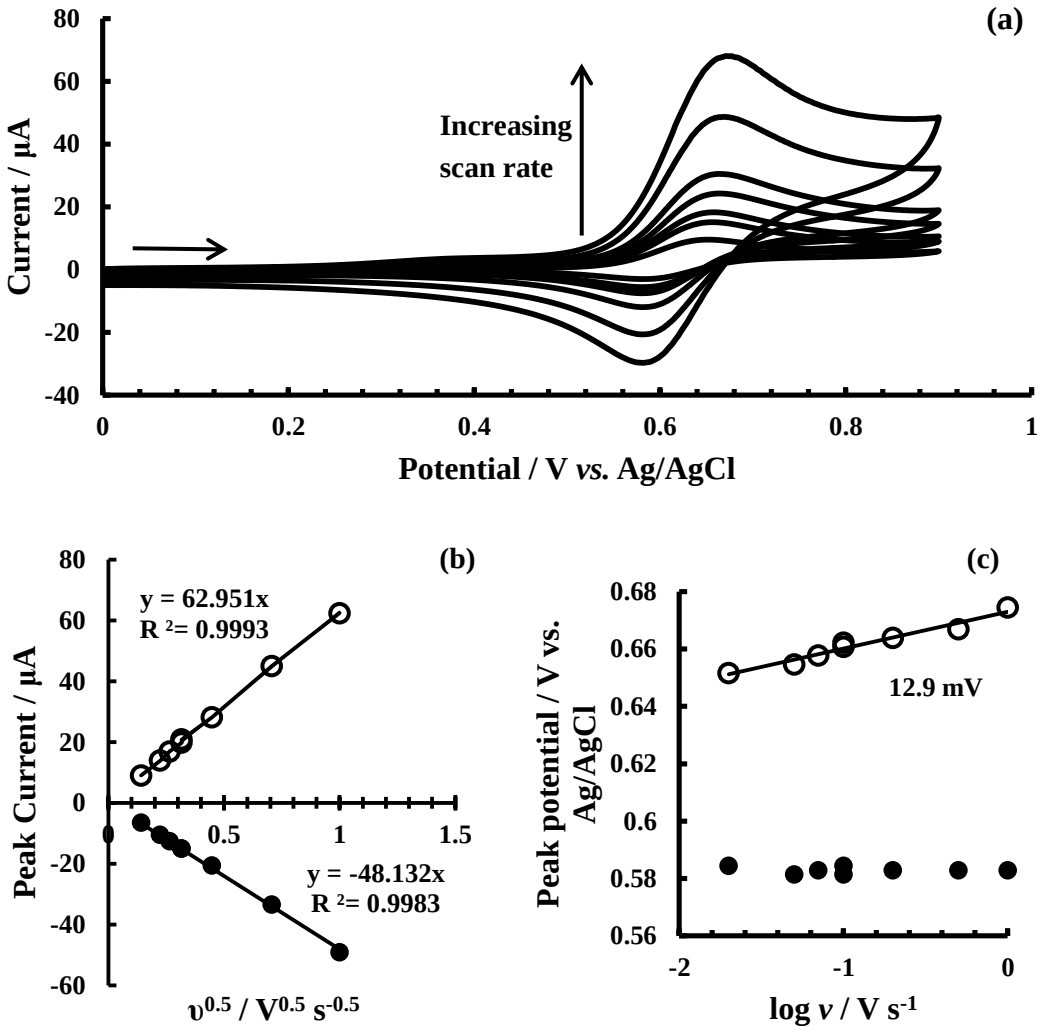

Fig. 3.5. (a) Cyclic voltammograms of the oxidation of 1.13 mM chlorpromazine on glassy carbon electrode (BAS, 3 mm diameter) in 0.1 M KCl at variable scan rates ($0.02 \leq \upsilon$ / V $s^{-1} \leq 1.0$). First scan only. Sliver/Sliver chloride electrode was served as a reference electrode and spiral platinum wire was served as a counter electrode. (b) a corresponding plot of peak current against square root of scan rate of (a) for both oxidation (hollow dots) and reduction (solid dots) peaks.. (c) a corresponding plot of peak potential against logarithm of scan rate of (a) for both oxidation (hollow dots) and reduction (solid dots) peaks.

Higher concentration of chlorpromazine (2.00 mM) has also been carried out and the

results are shown in Fig. 3.6. Similar trends were found as the oxidation of 1.13 mM chlorpromazine. It is worth note that in Fig. 3.6c, the plot of peak potential against logarithm of scan rate for the oxidation peak suggests that the reversible electrochemical oxidation occurs at slow scan rates ($v \leq 0.1$ V s^{-1}) and irreversible electrochemical oxidation process occurs at high scan rates ($v \geq 0.2$ V s^{-1}), concludes that the process is electrochemically quasi-reversible.

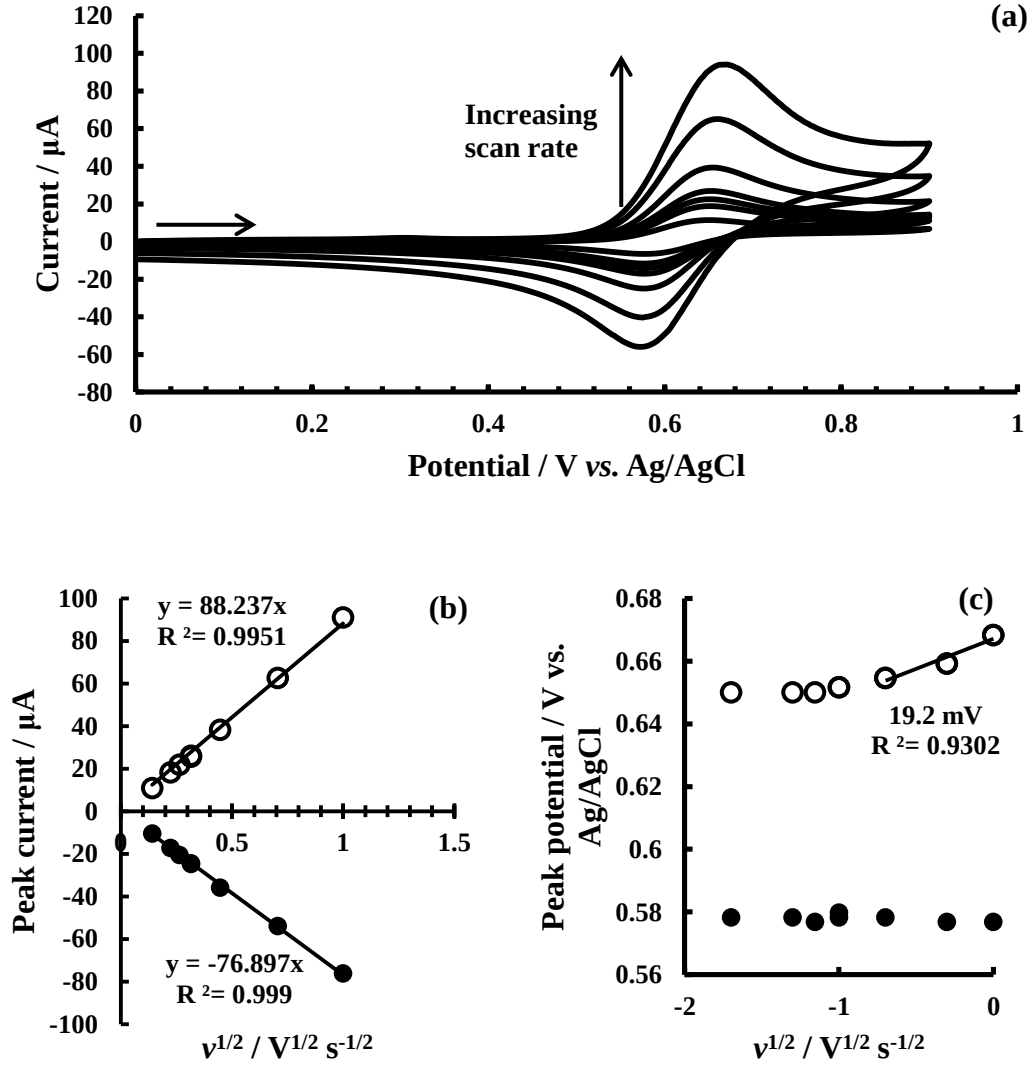

Fig. 3.6. (a) Cyclic voltammograms of the oxidation of 2.00 mM chlorpromazine on glassy carbon electrode (BAS, 3 mm diameter) in 0.1 M KCl at variable scan rates ($0.02 \leq \upsilon$ / V $s^{-1} \leq 1.0$). First scan only. Sliver/Sliver chloride electrode was served as a reference electrode and spiral platinum wire was served as a counter electrode. (b) a corresponding plot of peak current against square root of scan rate of (a) for both oxidation (hollow dots) and reduction (solid dots) peaks. (c) a corresponding plot of peak potential against logarithm of scan rate of (a) for both oxidation (hollow dots) and reduction (solid dots) peaks.

Higher concentration of chlorpromazine (4.90 mM), again, was examined through the same setups (Fig. 3.7). Fig. 3.7a and Fig. 3.7b afford similar trend to that of oxidation of 1.13 mM and 2.00 mM chlorpromazine. However, the plot of peak potential against logarithm of scan rates (Fig. 3.7c) gives different trends from that of 1.13 mM and 2.00 mM chlorpromazine results, as the reduction peak potential has dependence on scan rates, suggests that both of the oxidation and reduction process becomes slower while the concentration of chlorpromazine increases.

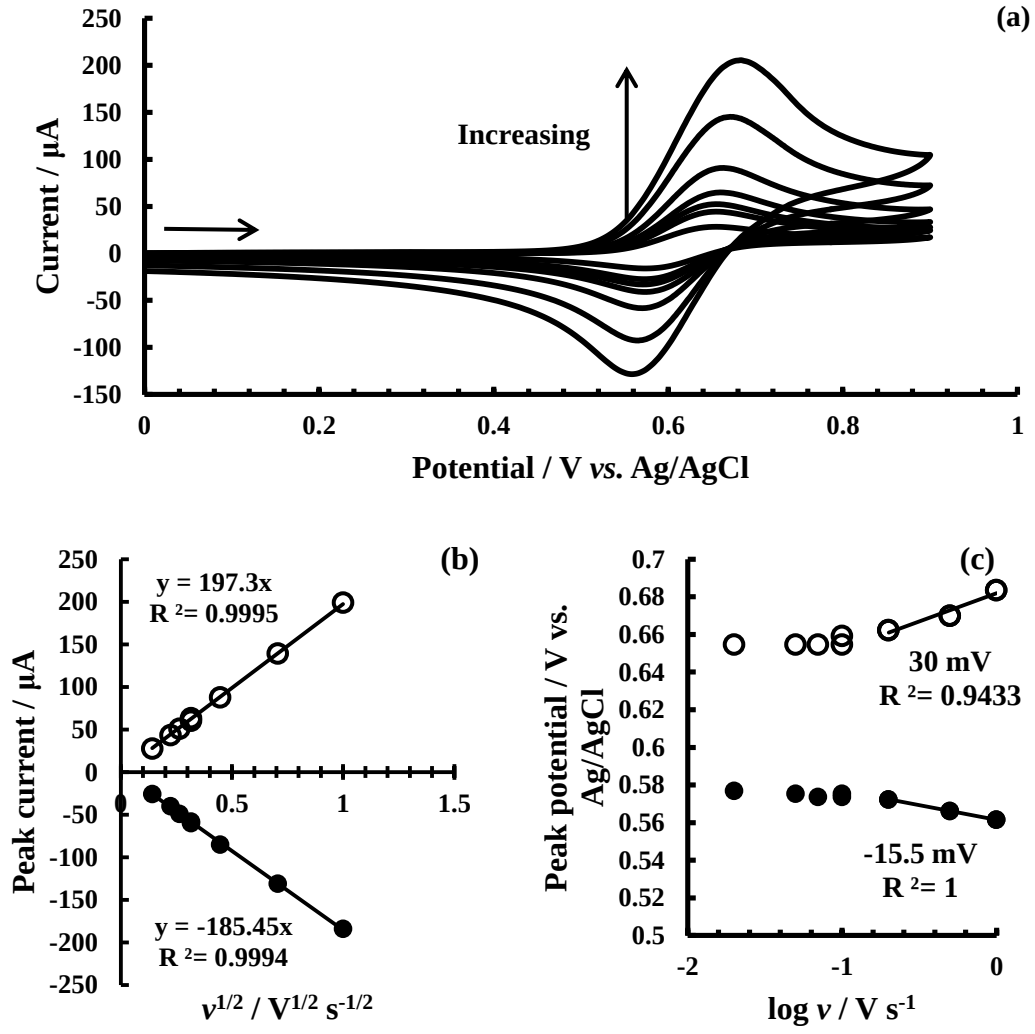

Fig. 3.7. (a) Cyclic voltammograms of the oxidation of 4.90 mM chlorpromazine on glassy carbon electrode (BAS, 3 mm diameter) in 0.1 M KCl at variable scan rates ($0.02 \leq \upsilon$ / V $s^{-1} \leq 1.0$). First scan only. Sliver/Sliver chloride electrode was served as a reference electrode and spiral platinum wire was served as a counter electrode. (b) a corresponding plot of peak current against square root of scan rate of (a) for both oxidation (hollow dots) and reduction (solid dots) peaks. (c) a corresponding plot of peak potential against logarithm of scan rate of (a) for both oxidation (hollow dots) and reduction (solid dots) peaks.

The increase of concentration of chlorpromazine leads the slowed electrode process. In order to understand this phenomenon, the mass transport profile of chlorpromazine was studied. Five different concentrations of chlorpromazine ($1 \leq c_0$ / mM ≤ 100) in 0.1 M KCl were examined by using cyclic voltammetry on a 3 mm diameter glassy carbon electrode. Interestingly, by applying Randles-Sevcik equation, the diffusion coefficient of chlorpromazine was found to be a function of concentration. As shown in Fig. 3.8a, a plot of diffusion coefficient against logarithm of concentration suggests that the diffusion coefficient changes 2.55 x 10^{-10} cm^2 s^{-1} per decade change of concentration. By applying Stokes-Einstein equation, the radius of aggregate can be worked out and a plot aggregate radius against chlorpromazine concentration is shown in Fig. 3.8b.

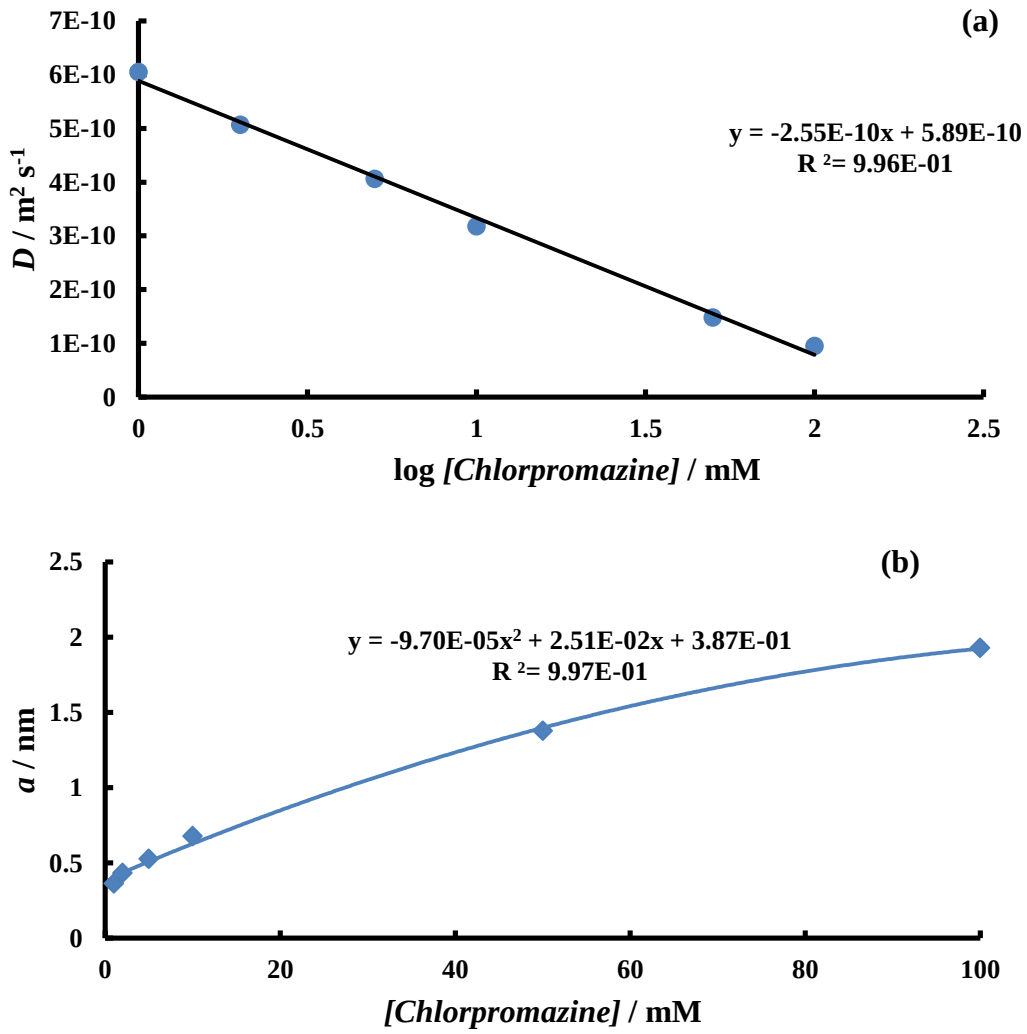

Fig.3.8. (a) A plot of diffusion coefficient of chlorpromazine in 0.1 M KCl against concentration. (b) a plot of molecule radius against chlorpromazine concentration.

By searching the literature, it was found that the aggregation of chlorpromazine can take place. The critical micelle concentration was found to be 28 mM and the micelle structure was suggested to be ellipsoidal (Fig. 3.9)[76]. Therefore, a different diffusion coefficient needs to be applied for different concentrations.

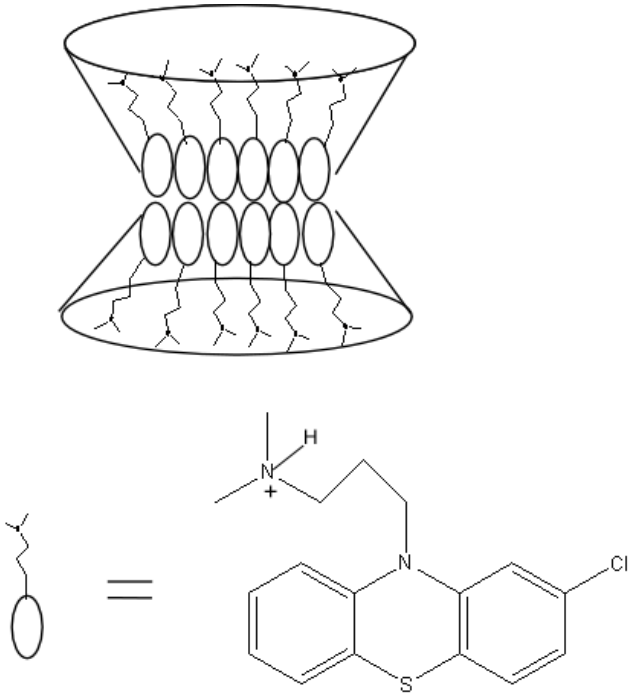

Fig. 3.9. Structure of chlorpromazine micelle.

The experiments of electro-oxidation of chlorpromazine were subsequently carried out in buffered solution (acetate buffer) at pH 3.80. As shown in Fig. 3.10, the cyclic voltammograms of chlorpromazine shows that there is difference between the buffered and unbuffered chlorpromazine at peak potential. The oxidation peak of unbuffered chlorpromazine gives an oxidation peak at +0.63 V *vs.* Ag/AgCl as shown previously and the corresponding reduction peak shows at +0.60 V *vs.* Ag/AgCl, whereas the buffered (pH 3.80) chlorpromazine gives an oxidation peak at +0.61 V and +0.58 V *vs.* Ag/AgCl for the reduction peak. As the pH of buffered solution is lower than the unbuffered solution, the acidic environment favours the oxidation of chlorpromazine.

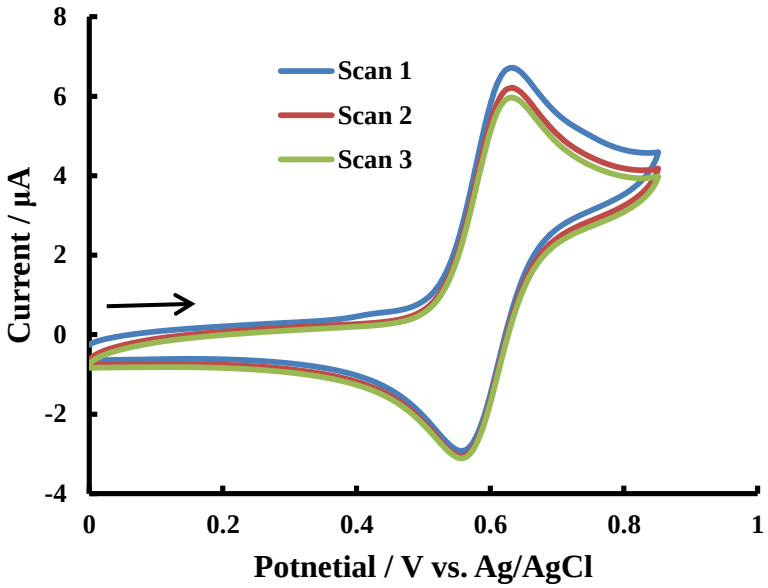

Fig. 3.10. Cyclic voltammograms of the oxidation of chlorpromazine at a glassy carbon electrode (iBAS, 3 mm diameter) in acetate buffer (pH 3.80) with 0.1 M KCl. Scan rate = 0.02 V s^{-1}. Sliver/Sliver chloride electrode was served as a reference electrode and a spiral platinum wire was served as the counter electrode.

The experiments of variable scan rate for the oxidation of buffered chlorpromazine (pH 3.80) was also been carried out. Fig. 3.11a shows the voltammograms of chlorpromazine oxidation in different scan rates. The plot of peak current against square root of scan rate (Fig. 3.11b) gives a straight line, which indicates the process is diffusion controlled. The gradient is similar to the plot of unbuffered chlorpromazine if normalize the concentration, which indicates the diffusion coefficient is similar in buffered and unbuffered solutions. In addition, although a slight shift on peak potential by changing scan rate, 7.6 mV per decade change of scan rate is reasonably small (Fig. 3.11c), moreover, similar trend can be seen from the 1.13 mM chlorpromazine in unbefffered solution (slight oxidative peak potential shift by changing scan rate and no shift on reductive peak potential), suggests that the oxidation processes are identical in both buffered and unbuffered media.

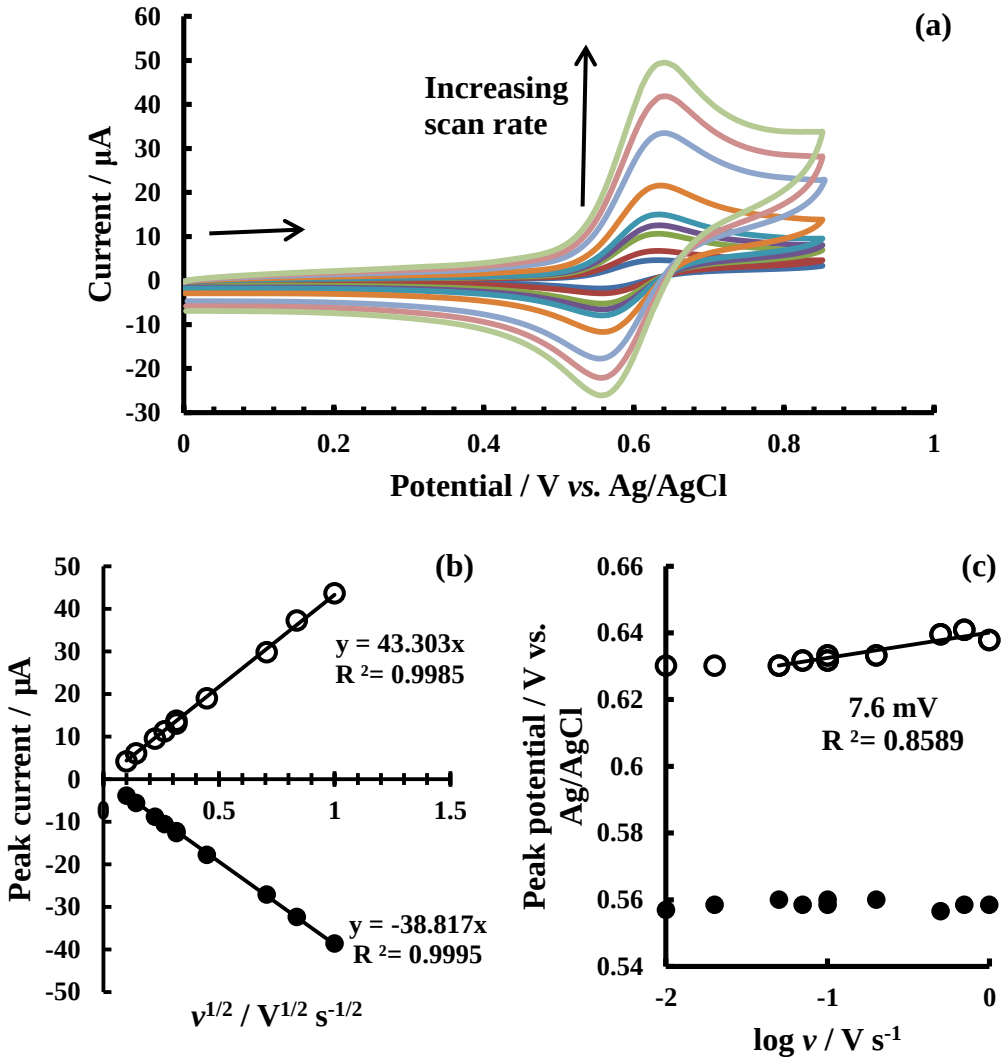

Fig. 3.11. (a) Cyclic voltammograms of the oxidation of 1.35 mM chlorpromazine on glassy carbon electrode (BAS, 3 mm diameter) in acetate buffer (pH 3.80) containing 0.1 M KCl at variable scan rates ($0.01 \leq \upsilon$ / V $s^{-1} \leq 1.0$). First scan only. Sliver/Sliver chloride electrode was served as a reference electrode and spiral platinum wire was served as a counter electrode. (b) a corresponding plot of peak current against square root of scan rate of (a) for both oxidation (hollow dots) and reduction (solid dots) peaks. (c) a corresponding plot of peak potential against logarithm of scan rate of (a) for both oxidation (hollow dots) and reduction (solid dots) peaks.

According to the analysed results, the diffusion coefficient of 1 mM chlorpromazine was found to be 6.9 x 10^{-6} cm^2 s^{-1} in aqueous solution. This value is reasonable as it is similar to other literature[77]. Therefore, the oxidation of chlorpromazine was characterised successfully.

3.2.2. Redox catalysis of the oxidation of L-cysteine and glutathione in unbuffered solution

As the oxidation of L-cysteine in acidic environment requires higher potential (approximately +1.4 V *vs.* Ag/AgCl, *vide infra*), therefore it is necessary to catalyse the oxidation of L-cysteine by using chlorpromazine as a mediator. As shown in Scheme 3.2, the oxidation of chlorpromazine forms a cation radical, which is the same as shown in Scheme 3.1, the chlorpromazine cation radical can be subsequently reduced back to its neutral form homogeneously by L-cysteine, therefore the local concentration of chlorpromazine can be increased by the positive feedback reaction.

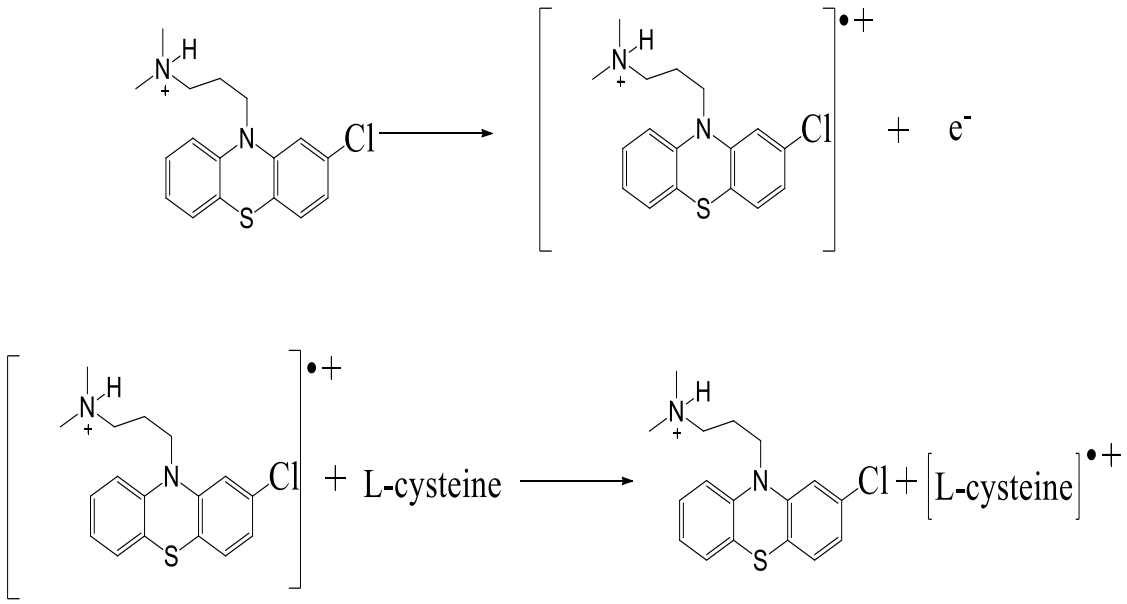

Scheme 3.2. Redox catalytic process of chlorpromazine with L-cysteine as catalyst.

This redox catalysis experiment was firstly carried out in 0.1 M aqueous KCl solution (unbuffered) with 1 mM, chlorpromazine and standard addition of L-cysteine, as shown in Fig.3.12.

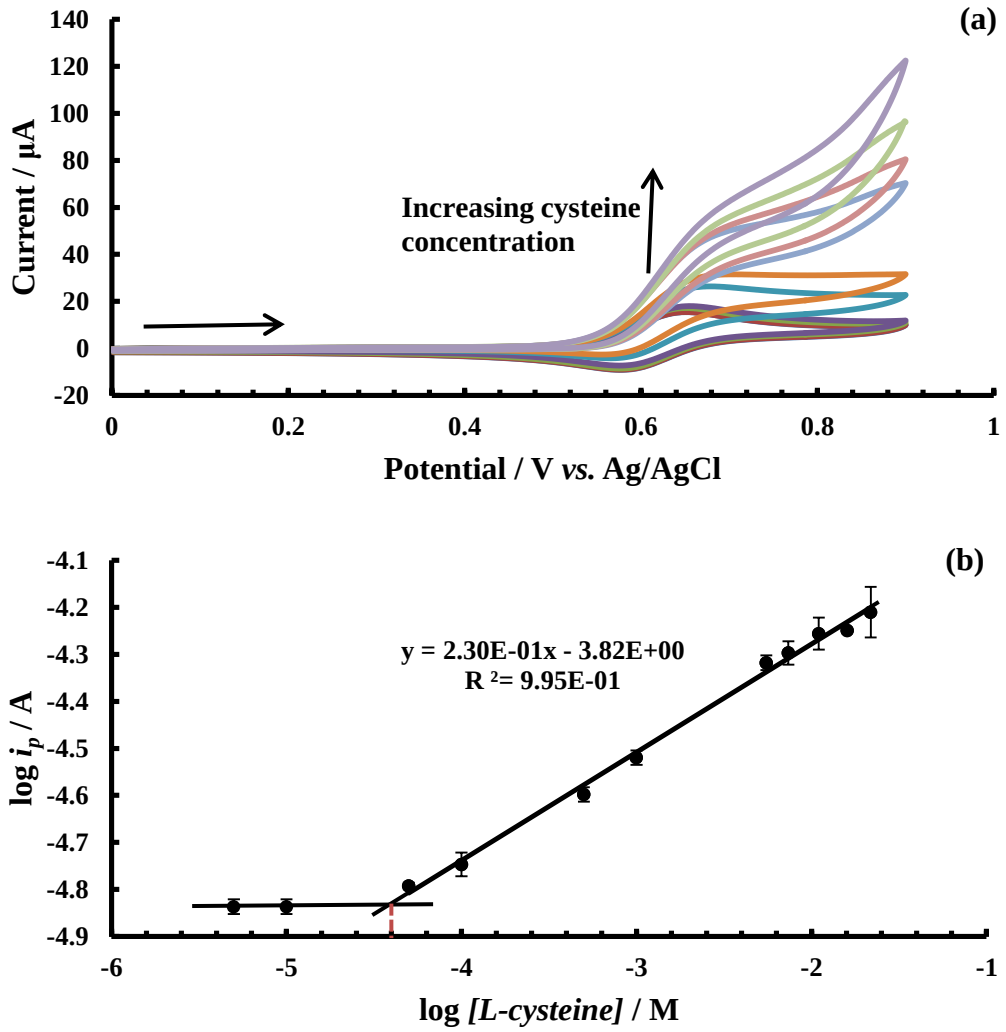

Fig. 3.12. (a) The electro-oxidation of 1 mM chlorpromazine at a glassy carbon electrode (BAS, 3 mm diameter) in 0.1 M KCl aqueous solution with standard addition of L-cysteine. Scan rate = 0.1 V s^{-1}. Silver/Sliver chloride electrode served as a reference electrode and a spiral platinum wire was used for the counter electrode. (b) a plot of logarithm of oxidative peak current against the logarithm of L-cysteine concentration in order to measure the limit of detection. Red dashed line indicates the approximate position of detection limit.

It can be seen that from Fig. 3.12a, the increase cysteine concentration causes the increase of peak current of the oxidation of chlorpromazine. This is due to the positive feedback of chlorpromazine as described above. The shape of the voltammogram of oxidation of chlorpromazine also changes from a conventional waveform to sigmoidal shaped. Fig. 3.12b shows a linear dependence of logarithm of peak current against logarithm of L-cysteine concentration. The peak current has barely changed until the L-cysteine concentration reaches approximately 37.7 µM (where the red dashed line

indicated).

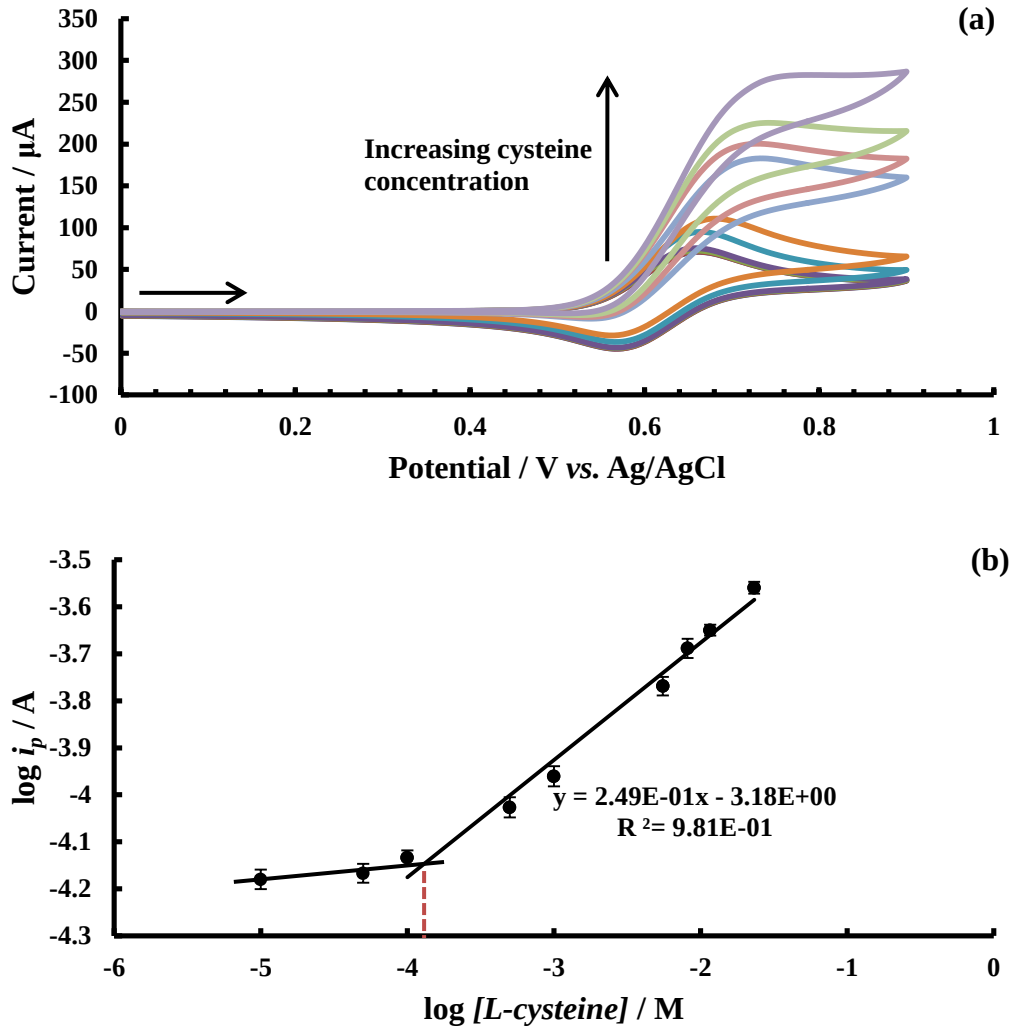

Fig. 3.13. (a) The electro-oxidation of 5.5 mM chlorpromazine at a glassy carbon electrode (BAS, 3 mm diameter) in 0.1 M KCl aqueous solution with standard addition of L-cysteine. Scan rate = 0.1 V s^{-1}. Silver/Sliver chloride electrode served as a reference electrode and a spiral platinum wire was used for the counter electrode. (b) a plot of logarithm of oxidative peak current against the logarithm of L-cysteine concentration in order to measure the limit of detection. Red dashed line indicates the approximate position of detection limit.

5.5 mM chlorpromazine was then used in order to examine the effect of the detection on the change of chlorpromazine concentration. As shown in Fig. 3.13a, the trend of voltammogram of chlorpromazine oxidation with the addition of L-cysteine is similar to that of with 1 mM chlorpromazine with increased peak height as expected. By plotting the logarithm of peak current against logarithm of L-cysteine concentration (Fig. 3.13b), it can be seen that the cross point between the calibration line and the

baseline shifts toward higher L-cysteine concentration, shown as red dashed line.

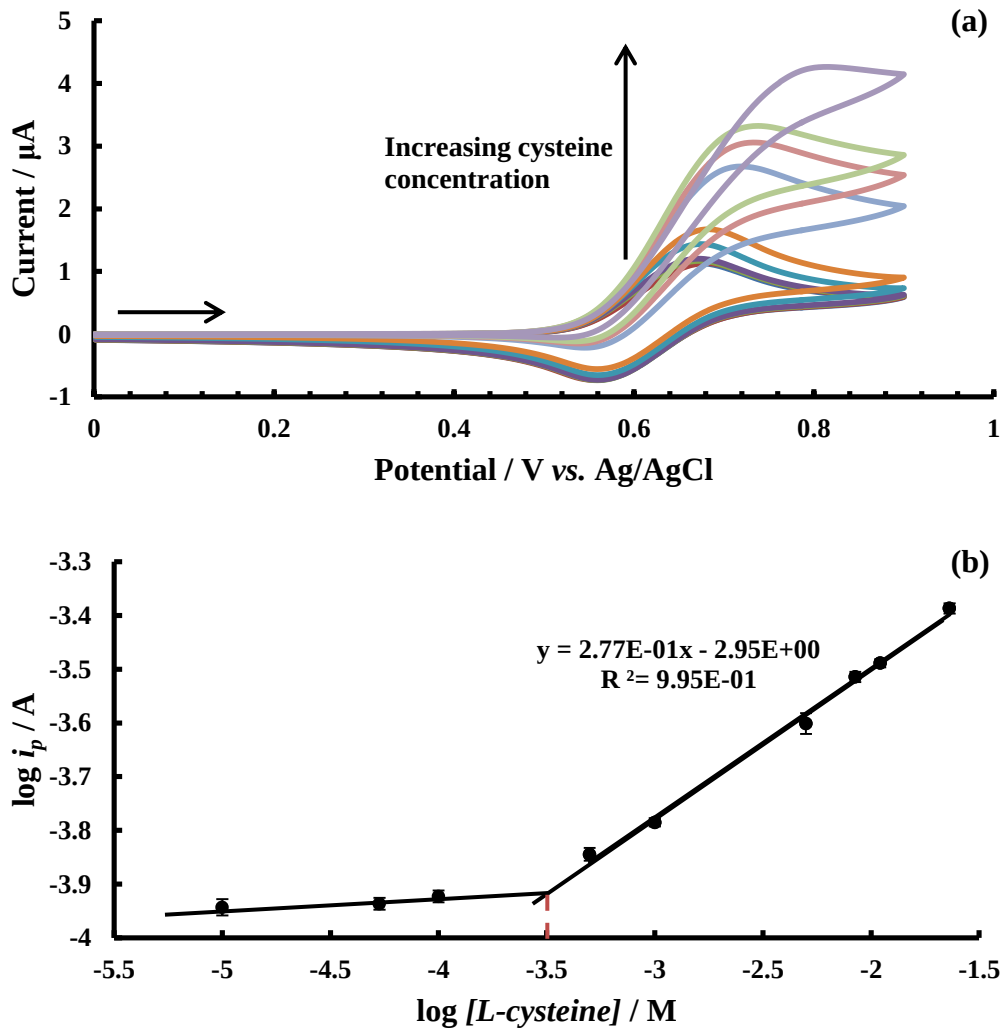

Fig. 3.14. (a) The electro-oxidation of 9.8 mM chlorpromazine at a glassy carbon electrode (BAS, 3 mm diameter) in 0.1 M KCl aqueous solution with standard addition of L-cysteine. Scan rate = 0.1 V s^{-1}. Silver/Sliver chloride electrode served as a reference electrode and a spiral platinum wire was used for the counter electrode. (b) a plot of logarithm of oxidative peak current against the logarithm of L-cysteine concentration in order to measure the limit of detection. Red dashed line indicates the approximate position of detection limit.

As there is effect on the limit of detection with changing concentration of chlorpromazine, a further 9.8 mM chlorpromazine was examined in order to provide a reasonable trend. As shown in Fig. 3.14a, again, the trend of voltammogram while increasing cysteine concentration is similar to 1 and 5.5 mM. Whereas, the calibration graph (Fig. 3.14b) shows shift of detection limit again, as expected. In general, the limit of detection is depended on the chlorpromazine concentration. A summarised

limit of detection change with changing chlorpromazine concentration is shown in Table 3.1.

Table 3.1. The changes of limit of detection of L-cysteine with changing chlorpromazine concentration. The LoD is averaged based on three repeats.

[Chlorpromazine] / mM	LoD / μM[a]
1	37. 7
5. 5	115. 7
9. 8	306. 3

[a] LoD is short for Limit of detection.

Glutathione was also measured by using the same method. Fig. 3.15a shows the voltammogram and corresponding calibration graph for the detection of glutathione with the oxidation of 1 mM chlorpromazine. Although less obvious, the addition of glutathione leads the shape of voltammogram change from convention waveform to sigmoidal shape with the disappearance of reverse peak. As shown in Fig. 3.15b, the red dashed line indicates the cross point of calibration line and baseline, which suggests that the detection limit is approximately 165.96 μM.

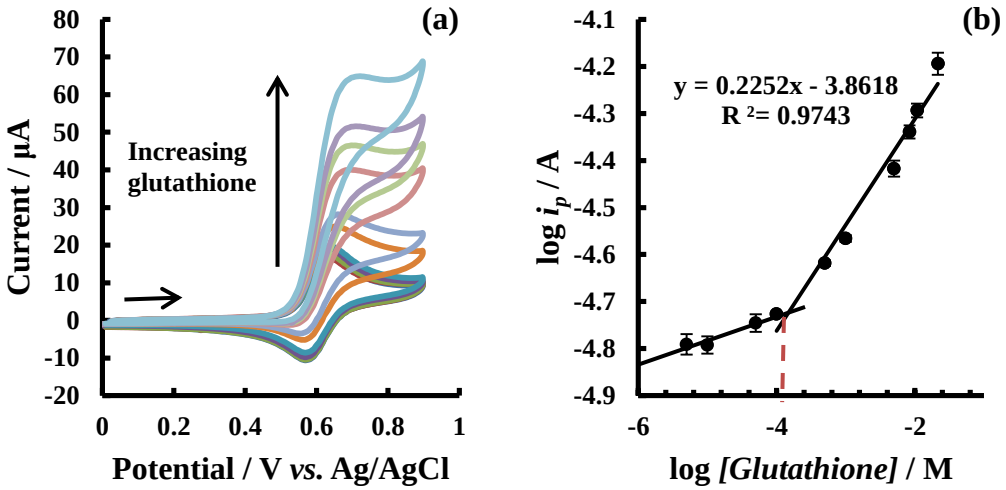

Fig. 3.15. (a) The electro-oxidation of 1 mM chlorpromazine at a glassy carbon electrode (BAS, 3 mm diameter) in 0.1 M KCl aqueous solution with standard addition of glutathione. Scan rate = 0.1 V s^{-1}. Silver/Sliver chloride electrode served as a reference electrode and a spiral platinum wire was used for the counter electrode. (b) a plot of logarithm of oxidative peak current against the logarithm of L-cysteine concentration in order to measure the limit of detection. Red dashed line indicates the approximate position of detection limit.

Two different concentrations of chlorpromazine were also undertaken as the same reason of L-cysteine detection. Fig. 3.16 shows the voltammograms of oxidation of both 5 and 10 mM chlorpromazine with the addition of glutathione. Similar observations can be seen as the 1 mM chlorpromazine. Notably that in the corresponding calibration graphs (Fig. 3.16b and Fig. 3.16d), the cross section of calibration line and baseline shifts toward higher glutathione concentration as the increase of chlorpromazine concentration, which is the same trend as L-cysteine detection discussed above.

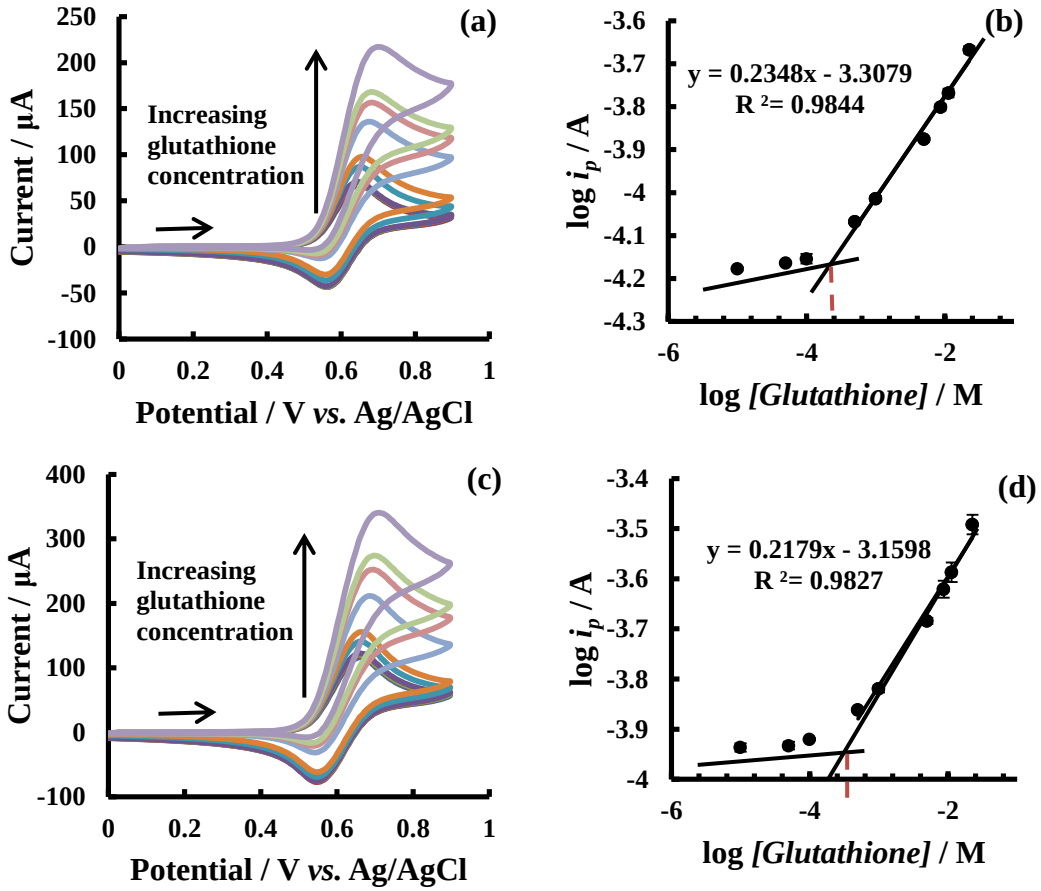

Fig. 3.16. The voltammograms of electro-oxidation of 5 mM (a) and 10 mM (c) chlorpromazine at a glassy carbon electrode (BAS, 3 mm diameter) in 0.1 M KCl aqueous solution with standard addition of glutathione. Scan rate = 0.1 V s^{-1}. Silver/Sliver chloride electrode served as a reference electrode and a spiral platinum wire was used for the counter electrode. (b) and (d) are the plots of logarithm of oxidative peak current against the logarithm of L-cysteine concentration in order to measure the limit of detection. Red dashed line indicates the approximate position of detection limit. With (b) corresponds to the voltammogram (a) and (d) corresponds to the voltammogram (c).

Accordingly, the redox catalysis process can be summarized and shown in Scheme 3.3. The "positive feedback" of CPM in scheme 3.3 causes the increase in the oxidation peak of CPM. The increased L-cysteine or glutathione concentration leads to the increased "feedback", therefore the addition of L-cysteine or glutathione causes the peak current to increase. In addition, as the homogenous chemical step for chlorpromazine cation radical to react with thiols are in the molar ratio of 1:1, therefore the higher concentration of chlorpromazine used, the more thiols are needed in order to perform the catalysis process. This is in agreement that at low concentration of chlorpromazine (*i.e.* 1 mM) and relatively higher concentration of thiols (*i.e.* 50 mM), the shape of voltammogram is sigmoidal whereas at a higher concentration of chlorpromazine (*i.e.* 10 mM) and the same concentration of thiols (50 mM), the shape of voltammogram remains as conventional. Therefore in the following experiments, which carried out in unbuffer solution, 25 μL of chlorpromazine was used in order to achieve low detection limit as well as decent signal.

$$CPM \overset{K_1}{\rightleftharpoons} CPM^{\bullet+} + e^-$$

$$CPM^{\bullet+} + Thiol \underset{K_b}{\overset{K_f}{\rightleftharpoons}} CPM + Thiol^{\bullet+}$$

Scheme 3.3. Where CPM is chlorpromazine and thiol is either L-cysteine or glutathione.

Moreover, the addition of thiols leads the disappearance of back peak. This is due to the chlorpromazine cation radical reacts with thiols, decreased concentration of cation radical while adding thiols, leads the equilibrium towards right. Therefore there is not sufficient chlorpromazine cation radical in the diffusion layer that can be reduced back to its neutral state.

3.2.3. Detection of L-cysteine and glutathione in buffered solution.

As the pK_a of L-cysteine gives 8.30 and the pKa of glutathione gives 8.75 at 25 ℃,

the acidic environment can stabilize these two materials. Although there is some method introduced in the literatures, their experiment needs to be carried out in basic condition in order to deprotonate the L-cysteine or glutathione to make them more reactive. Based on these methods, acidic environment can be limited.

In order to detect L-cysteine and glutathione in low pH environment, the experiments were carried out in acetate buffer (pH 3.8). Additionally, as it was found previously that the lower concentration of chlorpromazine gives lower detection limit, therefore 25 μM of chlorpromazine was used as mediator. As shown in Fig. 3.17, the peak current is increasing with the increase concentration of L-cysteine while there is a small shift on peak potential. The shift of peak potential may due to the slower redox catalysis process compared to one-electron-transferred oxidation on its own. It should be noted that a slower scan rate (0.01 V s^{-1}) was used compared to the experiments did in unbuffered solution (0.1 V s^{-1}). Slower scan rates ensure that there is enough time for L-cysteine to be oxidized while the radical cation of chlorpromazine is formed. The analysed data shows the linear dependence between L-cysteine concentration and peak current. The limit of detection was calculated to be 6.3 ± 0.03 μM.

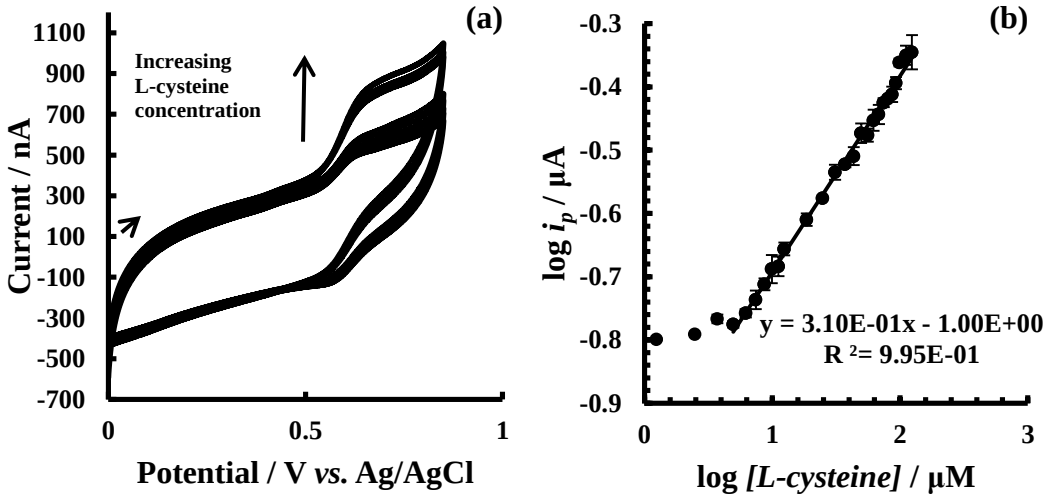

Fig. 3.17. The electro-oxidation of 25 μM chlorpromazine in acetate buffer (pH 3.80) with 0.1 M KCl at a 3 mm diameter glassy carbon disc electrode with standard addition of L-cysteine. Scan rate = 0.01 V s^{-1}. Silver/Sliver chloride electrode served as a reference electrode and a spiral platinum wire was used for the counter electrode. (b) a plot of logarithm of peak current against logarithm of L-cysteine concentration, data obtained from (a).

Similarly, the oxidation addition of glutathione gives linear trend with the logarithm of peak current, the plot of logarithm of peak current against logarithm of glutathione concentration gives similar gradient which indicates the redox catalysis mechanism is same. Notably, the glutathione can be measure in lower concentration than L-cysteine and the detection limit can be down to approximately 4.4 ± 0.07 μM.

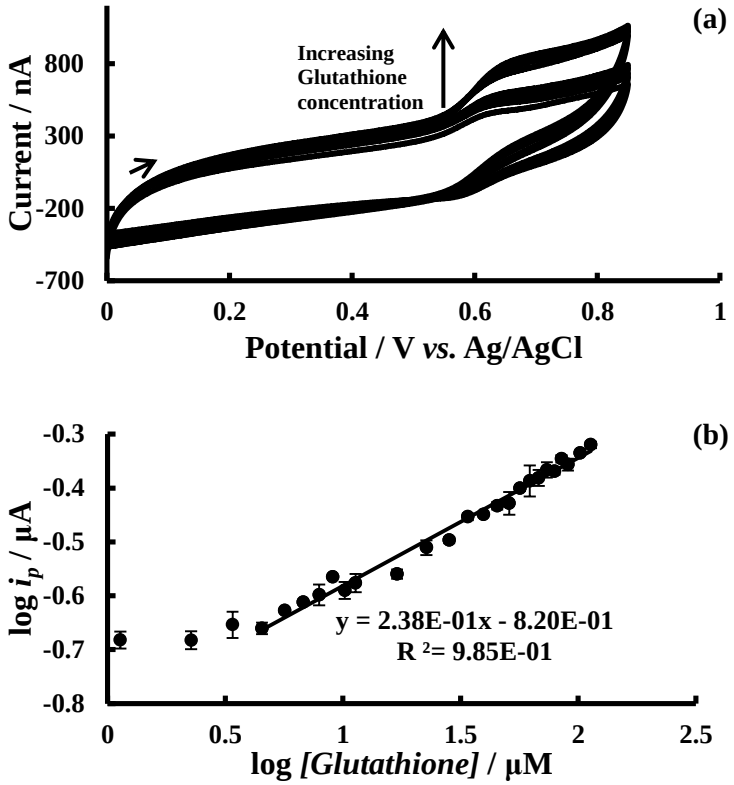

Fig. 3.18. (a)The electro-oxidation of 25 μM chlorpromazine in acetate buffer (pH 3.80) with 0.1 M KCl at a 3 mm diameter glassy carbon disc electrode with standard addition of Glutathione. Scan rate = 0.01 V s^{-1}. Silver/Sliver chloride electrode served as a reference electrode and a spiral platinum wire was used for the counter electrode. (b) a plot of logarithm of peak current against logarithm of glutathione concentration, data obtained from (a).

In summary, it was found that the limit of detection can be lowered by decrease the concentration of chlorpromazine. It was found that 25 μM chlorpromazine is the optimum concentration as the unobvious peak current was found when the concentration of chlorpromazine lower than 25 μM.

3.2.4. Electrochemical oxidation of L-cysteine and glutathione in buffered solution (pH 3.80)

In order to show the redox catalytic method is valuable for the detection of L-cysteine and glutathione, the electrochemical oxidation of L-cysteine and glutathione in buffered solution was carried out. Variable scan rate ($0.01 \leq \upsilon$ / V $s^{-1} \leq 1$) of electrochemical oxidation of L-cysteine is shown in Fig. 3.19. As shown in Fig. 3.19, the oxidation peak potential of L-cysteine is found to be approximately +1.5 V and there is no reverse peak observed. The peak potential shifts while changing the scan rates indicates the oxidation of L-cysteine is electrochemically and chemically irreversible. The plot of peak current against square root of scan rates gives a linear dependence, which leads this process to be under diffusion controlled.

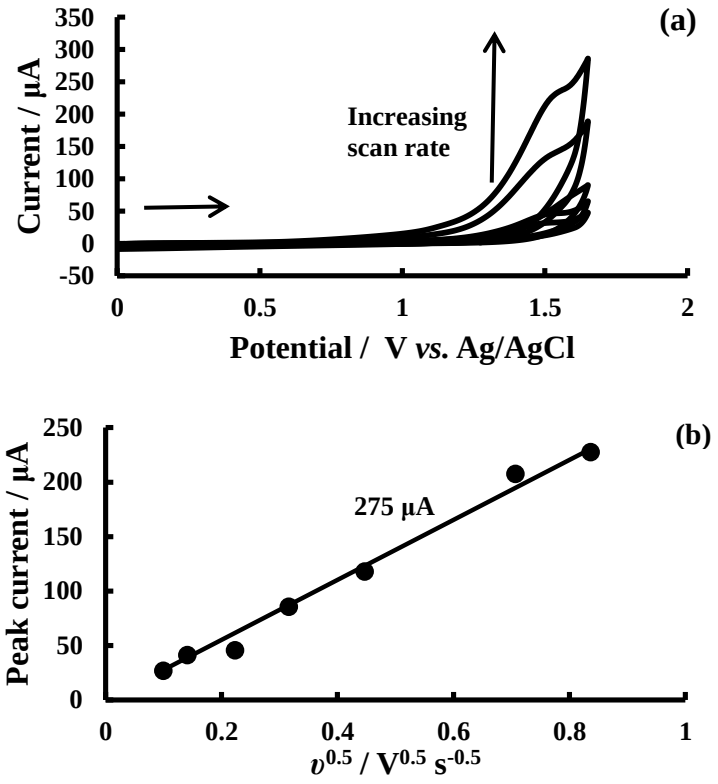

Fig. 3.19. (a) Electrochemical oxidation of 1 mM L-cysteine on glassy carbon disc electrode (3 mm diameter) in acetate buffer (pH 3.80) with 0.1 M KCl. (b) a corresponding plot of peak current against square root of scan rate of (a).

If assuming the oxidation of the L-cysteine is one electron transfer process and the transfer coefficient is 0.5, the diffusion coefficient can be worked out as $3.5(\pm 0.2) \times 10^{-4}$ cm^2 s^{-1}. If the assumptions are turn, this diffusion coefficient indicates that the mass transport of L-cysteine is incredibly fast. This is as expected as the fast mass transfer leads to the faster catalytic process, which lower the limit of detection.

The electrochemical oxidation of glutathione was also attempted. However, the experiment results showing there is no consistent peak with in the aqueous potential window (lower than the potential of hydrogen evolution). These results suggest the oxidation potential of glutathione probably higher than L-cysteine, which makes itself difficult to be measured by using voltammetric method in aqueous environment with low pH. Therefore the redox calatytic detection method can be ideal for detection of L-cysteine and glutathione in acidic aqueous environment.

3.2.5. Interference test for detection of L-cysteine and glutathione

In order to examine the performance of this detection method, interference test was carried out later in the project. Both L-cysteine and glutathione was tested in the presence of either ascorbic acid or Dubacco's Eagle reagent.

The first test was carried in the presence of ascorbic acid or Dubacco's Eagle media for detection of L-cysteine. Small amount of 25 μM of ascorbic acid was added into the buffered solution that gave same concentration of chlorpromazine in order to carry out the ascorbic acid interference test. On the other hand, as Dubacco's eagle's reagent is a simulated biological cell environment, therefore 1 mM L-cysteine was dissolved in DEG solution, and subsequently diluted to 25 μM using the pH 3.8 buffer solution. Fig. 3.20 illustrates the calibration graph for different interference reagents.

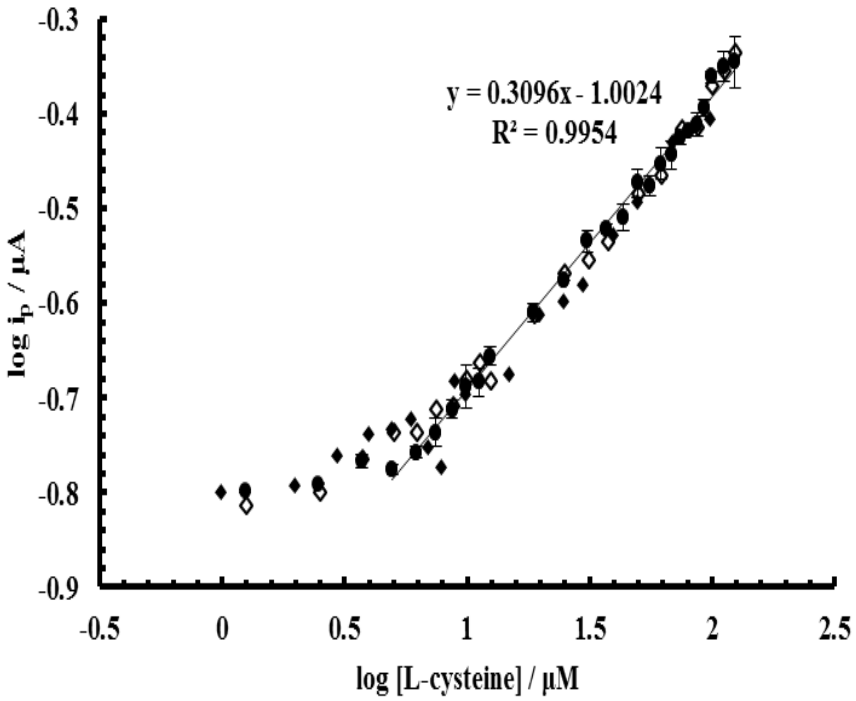

Fig. 3.20. Interference test for L-cysteine detection. Solid circle: 25 µM chlorpromazine in pH 3.8 buffer with standard addition of L-cysteine; solid rhombus: 25 µM chlorpromazine and 25 µM ascorbic acid in pH 3.8 buffer with standard addition of L-cysteine; hollow rhombus: 1 mM L-cysteine dissolved in DEG and standard added to pH 3.8 buffer containing 25 µM chlorpromazine.

As shown in Fig. 3.20, even with the interference present, the trend of the calibration graph remains unchanged. Consequently, the interference test gave reasonable recovery. The average recovery percentage of L-cysteine interfered by ascorbic acid was found to be 97.85% and 98.55% for DEG interfered L-cysteine detection.

Similar trends can be found for glutathione detection, as shown in Fig. 3.21, a calibration graph of detection of glutathione with interference is presented. Compared with L-cysteine test, the data points of standard addition of glutathione scattered larger than that of L-cysteine when at low substrate concentration.

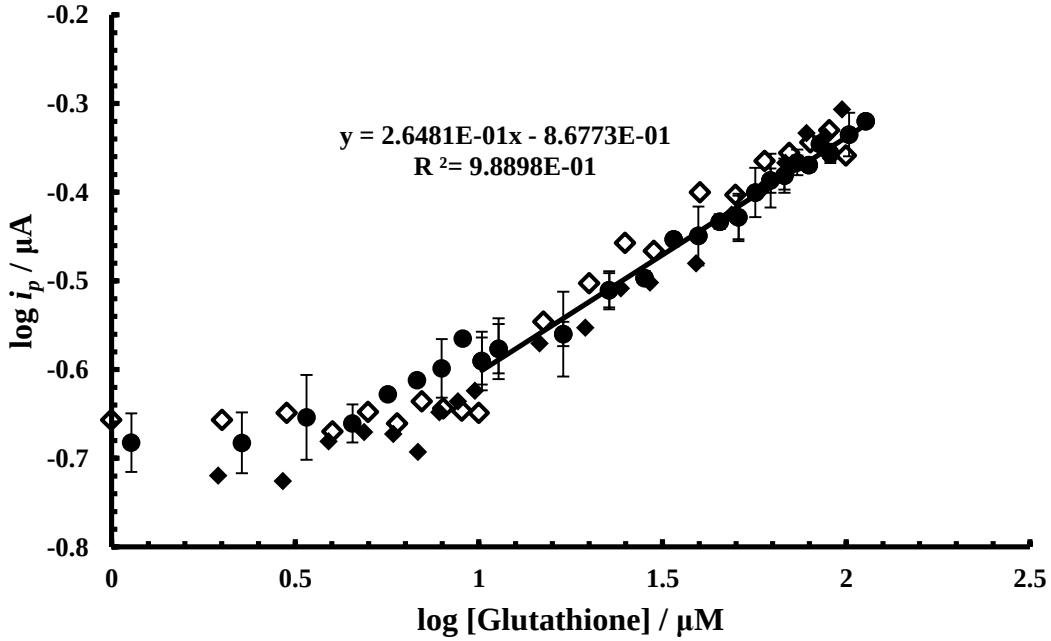

Fig. 3.21. Interference test for glutathione detection. Solid circle: 25 µM chlorpromazine in pH 3.8 buffer with standard addition of glutathione; hollow rhombus: 25 µM chlorpromazine and 25 µM ascorbic acid in pH 3.8 buffer with standard addition of glutathione; solid rhombus: 1 mM glutathione dissolved in DEG and standard added to pH 3.8 buffer containing 25 µM chlorpromazine.

According to the equation shown in Fig. 3.21, the average recovery percentage for ascorbic acid interference test is 99.55% and 98.20% for that of DEG test. Because the recovery percentage is averaged over a wide range of glutathione concentrations, therefore some results gives percentage that more than 100%, therefore even the average recovery percentage of glutathione is higher than that of L-cysteine test, the real detection performance for L-cysteine detection is better than glutathione.

3.3. Photo-catalytic reactions of lactic acid

Lactic acid (Fig. 3.2) is an essential acid in human body which is produced *via* glycolysis and hypoxida metabolism in myocytes. Lactic acid is produce into blood as well as sweat especially during physical actions[78]. Lactic acid is found to be more concentrated in sweat than in the blood or urine and with concentration range from 4 to 40 mM[79]. In addition, in clinic conditions, lactic acid usually measured for

monitoring health status of kidney[80], as well as acts as one of the an indicators for shock (hypovolemia, heart disorder, septic shock *etc.*), infections, insufficient respiratory and several metabolic disoders[81]. Although most researchers measure the lactic acid in blood, the patients necessitates the deployment of an atraumatic treatments, therefore the measurements using sweat instead of blood is interested.

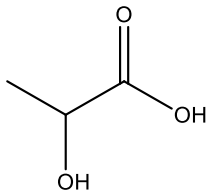

Fig. 3.2. Chemical structure of lactic acid

Due to the importance of lactic acid, several researchers measured the concentration levels of lactic acid in sweat a few decades ago. Michelsen *et al.* measured the sweat lactic acid from range 16 to 42 mM[82] for different skin areas of a man, Dill[83] and van Heyningen[84] suggested that arm sweat offers more concentrated lactic acid to total body sweat. In addition, these workers also found that lactic acid is more concentrated on the skin with acne than a normal skin. Besides, Ottenstein *et al.* found that lactic acid consists less in sweat of women than that of man.[85, 86]

The detection of lactic acid has been studied due to its biological properties. As electrochemical detection methods offers several advantages such as low cost and quick analysis time, therefore detection of lactic acid using electrochemistry become a hot research area. Several detection methods are reported in literatures including electochemiluminescence[80, 87], enzyme-based ZnO nanorods[88] and voltammetry[81, 89]. Due to the nature of lactic acid, direct oxidation of lactic acid is very difficult, and most of authors modified the electrode surface for a voltammetric detection method. Again, because the electrode normally modified by enzyme or other biochemical material, the storage can be difficult. Therefore in this project, again, a catalytic electrochemical method is used for lactic acid detection. Because of the stability of

lactic acid, the catalytic condition needs not only a mediator compared to cysteine or glutathione detection, but also needs photo-excitation.

Due to the inertia of lactic acid, it is difficult to be directly electrolyed or catalysed. Photo EC′ reaction can be utilised which can favour the oxidation. Chlorpromazine was used in this project again as mediator. The investigation of chlorpromazine has been introduced in previous section.

3.3.1. Photo current response of catalysed oxidation of sodium lactate

The initial investigation was to look at the chronoamperometry current response of chlorpromazine in 0.1 M KCl with and without photo excitation. It was known that the oxidation of chlorpromazine occurs at approximately +0.65 V *vs.* Ag/AgCl, therefore the chronoamperometry was set to hold the potential at +0.8 V *vs.* Ag/AgCl. Fig. 3.22 shows the current-time response of chlorpromazine using chronoamperometry on a glassy carbon electrode. A white light source was used for the photo electro-catalysis.

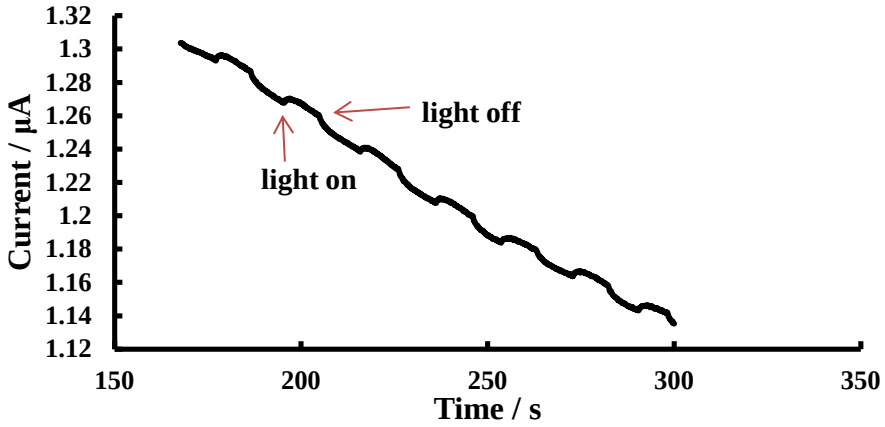

Fig. 3.22. Chronoamperometry of 1 mM Chlorpromazine in 0.1 M KCl with photo catalysis using a 3 mm diameter glassy carbon disc electrode. Potential was held at +0.8 V *vs.* Ag/AgCl. White light source lamp was used.

As it can be seen from Fig. 3.22, current increases when light was on and drop back

after the light was turned off. In this case, chlorpromazine was excited by light and gained more energy, and therefore it leads to an increase signal when doing an oxidation. The average amount of photo-current can be worked out for 5.58 nA.

3.3.2. Photo-catalysis of chlorpromazine oxidation with addition of lactate

With addition of sodium lactate, the electrons in lactate can transfer to the oxidised chlorpromazine and reduce the chlorpromazine cation radical back to chlorpromazine. As the catalytic theory was illustrated in the Introduction, the addition of lactate favours the formation of chlorpromazine and cause the current increase (scheme 3.4).

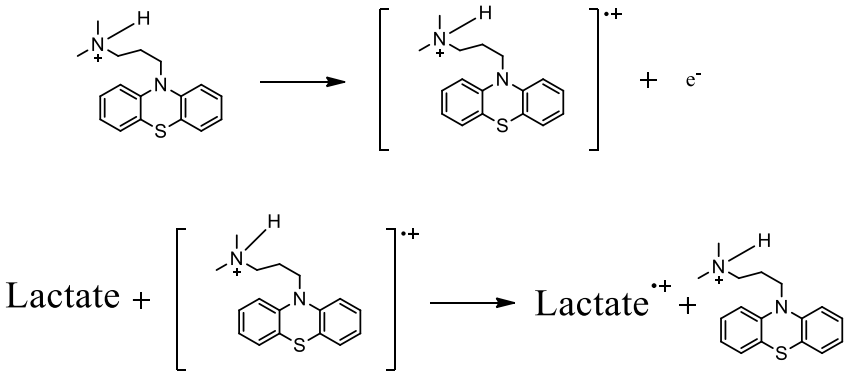

Scheme 3.4 Catalysis lactate oxidation.

The current-time response of chronoamperometry with addition of lactate is increased compare to that of chlorpromazine itself. A plot of photo current against lactate concentration gives a straight line (Fig. 3.23). In addition, in order to show that the increased current is due to the addition of lactate but not due to thermal effect, chronoamperometry experiment was also carried out with holding the potential at 0 V. Clearly from Fig. 3.23, the photo current of chlorpromazine increase with increased concentration of lactate when potential was held at +0.8 V whereas photo current of remains unchanged when potential was held at 0 V, this consequently proved that the increased photo current is due to the photo-catalysis of lactate using the mediator of

chlorpromazine. From the graph, detection limit for lactate was found to be 11.32 mM using 1 mM chlorpromazine.

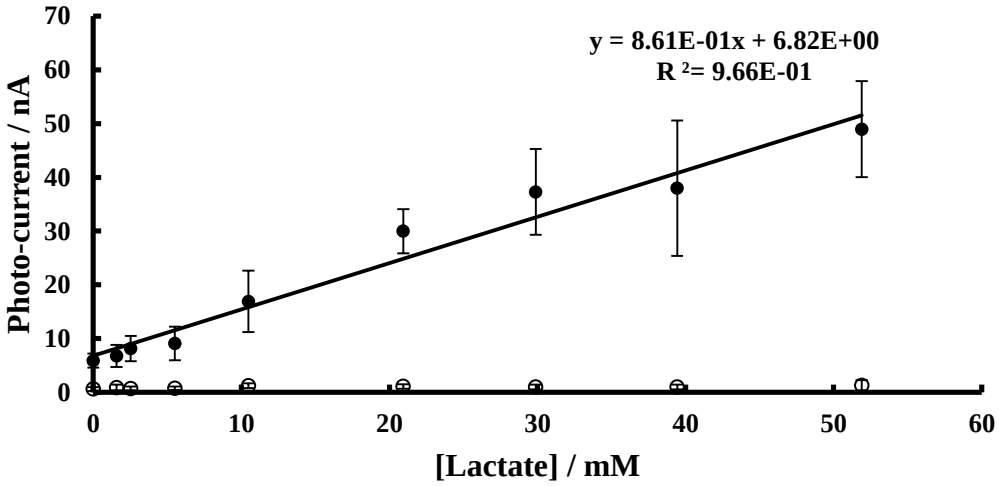

Fig. 3.23. A plot of photo-current of the oxidation of 1 mM chlorpromazine in 0.1 M KCl with addition of lactate against lactate concentration. Solid dots: potential held at +0.8 V *vs.* Ag/AgCl; hollow dots: potential held at 0 V *vs.* Ag/AgCl.

Variable chlorpromazine concentrations were also been carried out. 0.1 mM chlorpromazine (Fig. 3.24a) offered similar trend to that of 1 mM whereas 10 mM chlorpromazine calibration graph appears different from that of 1 mM and 0.1 mM (Fig. 3.24b) and the photo-current response reaches maximum after 30 mM lactate acid addition. The limit of detection with different concentrations of chlorpromazine is shown in Table 3.2.

Table 3.2. Limit of detection of lactate with different chlorpromazine concentration. LoD is limit of detection.

[Chlorpromazine] / mM	LoD* of lacate / mM	Standard error / nA
0.1	5.85	0.33
1.0	11.32	3.25
10.0	23.26	22.00

*LoD refers to the limit of detection.

It is shown that higher concentration of chlorpromazine gives higher LoD of lacate. This can be due to the catalytic reaction mechanism that the catalysis of lactate to chlorpromazine is in a ratio of 1:1. Therefore larger concentration difference can offer

more sensitive results.

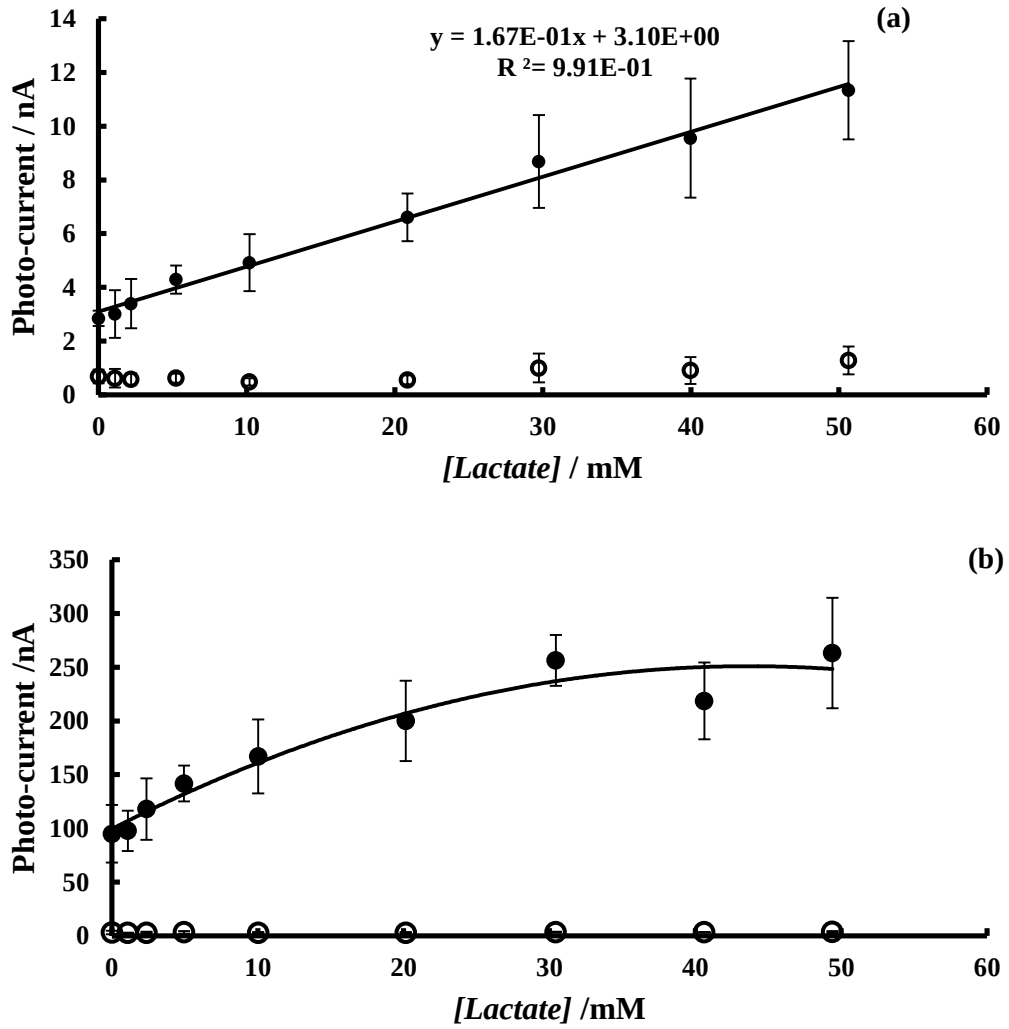

Fig. 3.24. Calibration graphs for photo-catalysis of chlorpromazine by lactate. a: concentration of chlorpromazine used is 0.1 mM; b: concentration of chlorpromazine used is 10 mM.

In addition, in order to understand the photo-catalytical process, a plot of logarithm of photo-current against logarithm of lactate concentration was plotted for 0.1 M chlorpromazine experiment. As shown in Fig. 3.25, the photo-current reaches steady-state after 30 mM addition of lactate. Other concentrations were analysed but only 0.1 mM chlorpromazine reaches steady-state, indicates that the steady-state limit only occurs when the concentration ratio of chlorpromazine and lactate is very large.

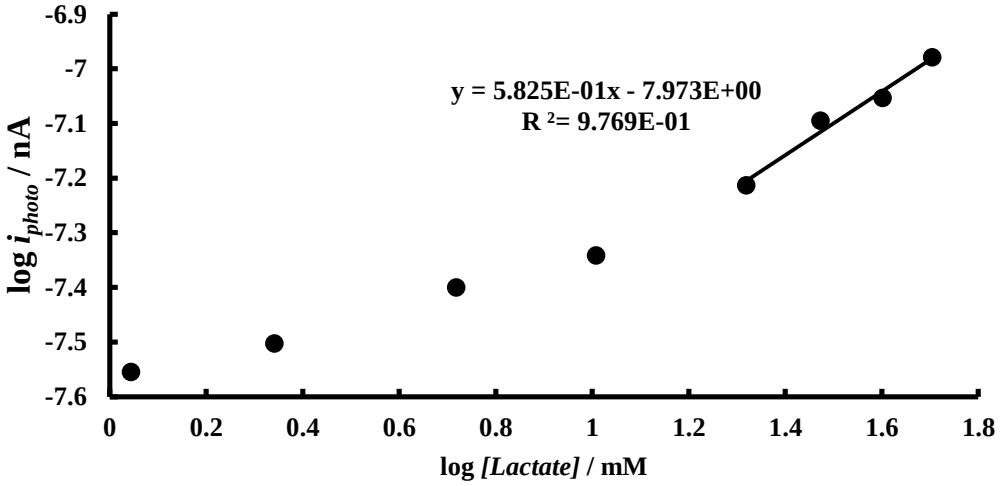

Fig. 3.25. A plot of logarithm of photo-current against logarithm of lactate concentration of 0.1 mM chlorpromazine in 0.1 M KCl. 3 mm diameter glassy carbon electrode was served as working electrode and silver/silver chloride reference electrode and a spiral platinum wire were used as reference and counter electrode, respectively.

In conclusion to the analytical purposes, the photo-catalytic detection of lactate acid was successfully carried out, the detection limit can be as low as 5.85 ± 0.05mM, which is a reasonable range in sweat as the lactate contends in sweat is 4-40 mM as mentioned in the introduction.

3.4. Electrode modification with variamine blue B and 6-(ferrocenyl)hexanethiol

In order to fabricate a decent sensor, modification of electrode surface is required as it affords that no contaminations from the mediator to the analyte. Diazonium salt is a well-known molecular wire to be used to modify the electrode surface.[90] Variamine blue B (VBB) was used to functionalise the electrode (glassy carbon disc), so that a ferrocene derivative, 6-(ferrocenyl) hexanethiol, can be graft onto the electrode surface, so that the ferrocene acts as a mediator in a redox catalytic reaction.

The grafting process was undertaken by dipping a 3 mm diameter glassy carbon disc

electrode in 1 mM VBB in acetonitrile with 0.1 M TBAP and scan from +0.5 V to -0.5 V and back to +0.5 V *vs.* SCE at 0.1 V s^{-1} scan rate. Fig. 3.26 shows the voltammogram of grafting process.

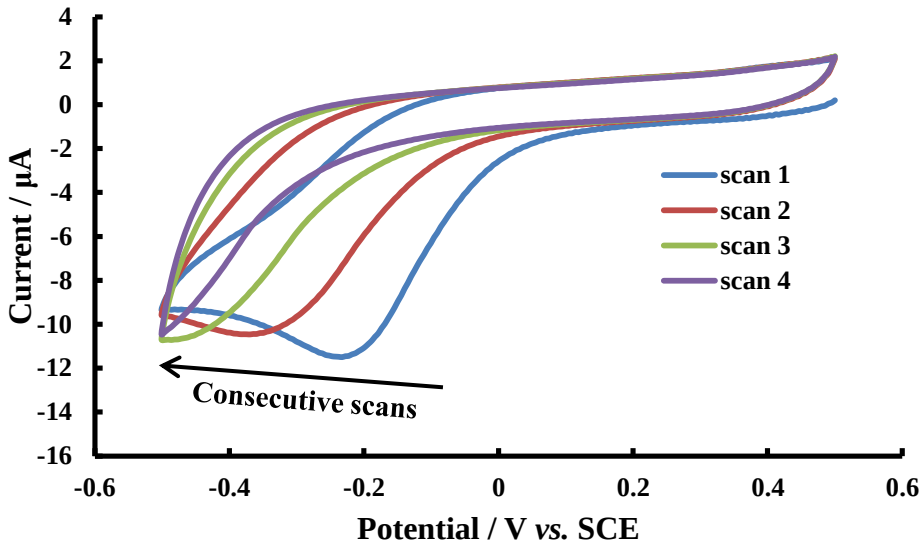

Fig. 3.26. Electrochemical reduction of 1 mM VBB in acetonitrile with 0.1 M TBAP on a 3 mm diameter glassy carbon disc electrode (v = 0.1 V s^{-1}, four consecutive cycles). Saturated calomel reference electrode and a spiral nickel wire counter electrode were applied.

As shown in Fig. 3.26, the reduction peaks shift toward negatively while the number of scans increased. A well-defined reduction peak appears at -0.2 V *vs.* SCE indicates the reduction process of the diazonium salt; and with no reverse oxidation wave agrees with the irreversible process of the release of N_2. Shift of reductive peaks suggests that the electrode surface is covered by the diazonium salt, which leading the reduction process become sluggish and block the entire electrode surface (*i.e.* scan 4). Therefore in the following experiments, one-scan-only functionalization process was performed.

Scheme 3.5 illustrates the reaction mechanism for the functionalisation process. The reduction peak shown in Fig. 3.26 corresponds the one-electron-reduction process of varimine blue B, and the formation of an active radical, which can bond to the electrode surface.

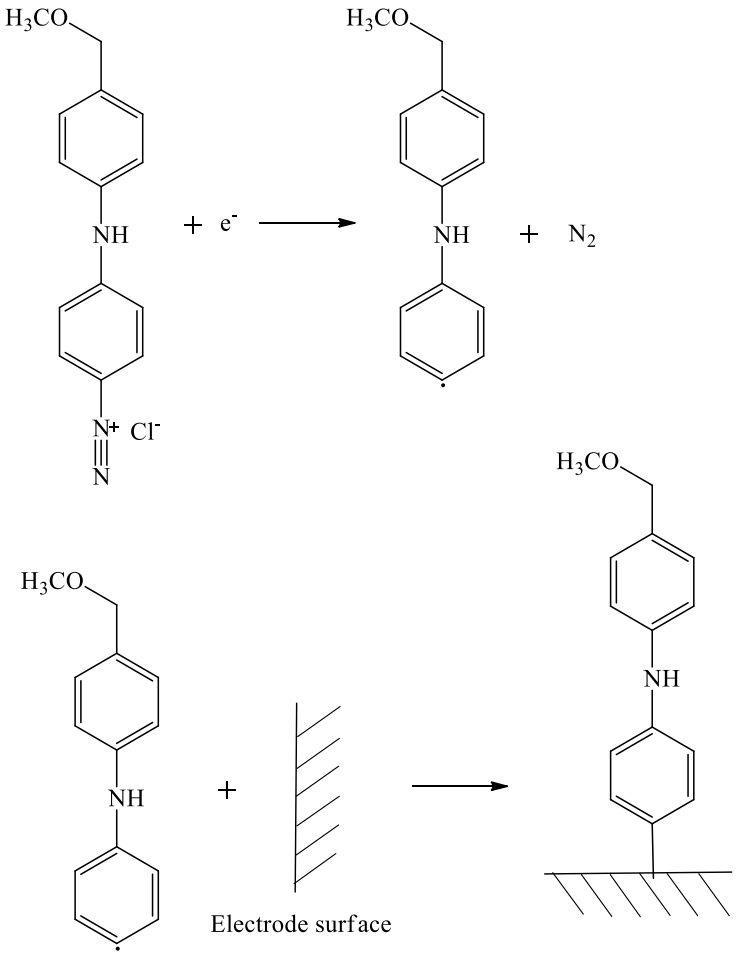

Scheme 3.5. The one-electron-reduction process of varimine blue B and the following functionalization process.

The modified electrode was then dipped into 0.1 M perchloric acid solution and the potential swept from -0.2 to +0.8 to-0.2 V *vs.* SCE for several times. Fig. 3.27 illustrates the voltammogram of the oxidation of the modified electrode. Five consecutive cycles were undertaken, with an oxidation peak appears at +0.7 V *vs.* SCE for the first scan, and a reductive peak shows at +0.45 V *vs.* SCE. The following scans (*i.e.* scans 2~5) show an oxidation peak at +0.5 V *vs.* SCE and again, the corresponding reduction peaks appear at +0.45 V *vs.* SCE. Scans 2~5 overlap each other, suggests that there is no material loss on the electrode surface.

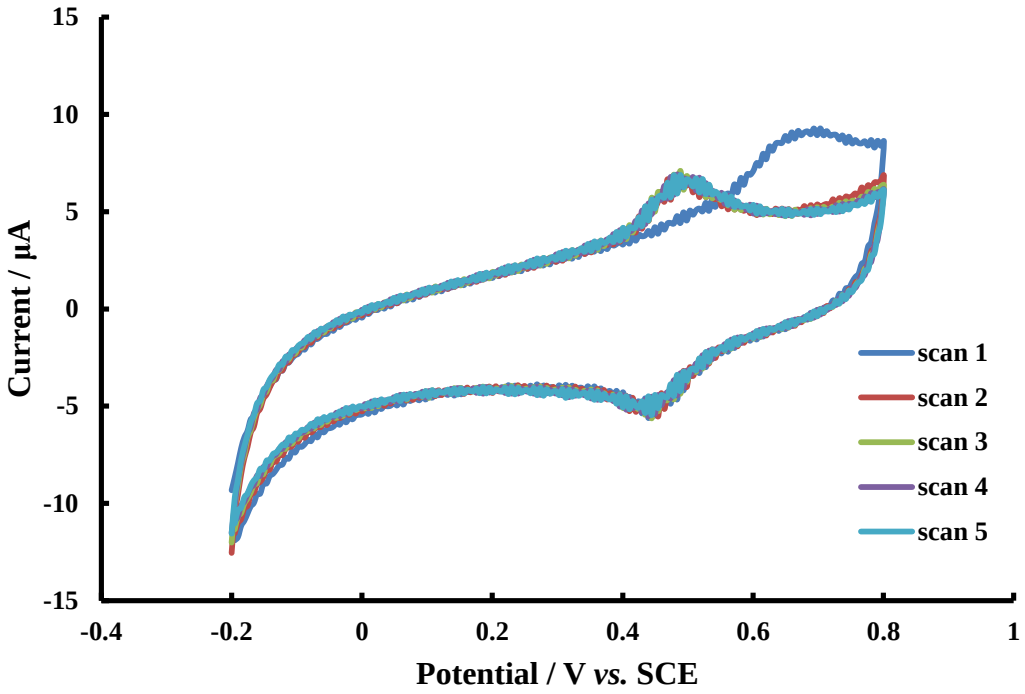

Fig. 3.27. Electrochemical oxidation of varimine blue B modified glassy carbon disc electrode (3 mm diameter) in 1.0 M $HClO_4$ (v = 0.1 V s^{-1}, five consecutive cycles). Saturated calomel reference electrode and a spiral nickel wire counter electrode were applied.

The difference between first scan and its following scans suggests that there is different electron-transfer processes occur. Indeed, the oxidation peak (+0.7 V *vs.* SCE) of the first scan indicates a relatively slow electron transfer process and followed by a relatively quick (fast than the former) oxidation process as shown in Scheme 3.6. The consecutive scans (scans 2~5) indicates the latter one-electron-oxidation process.

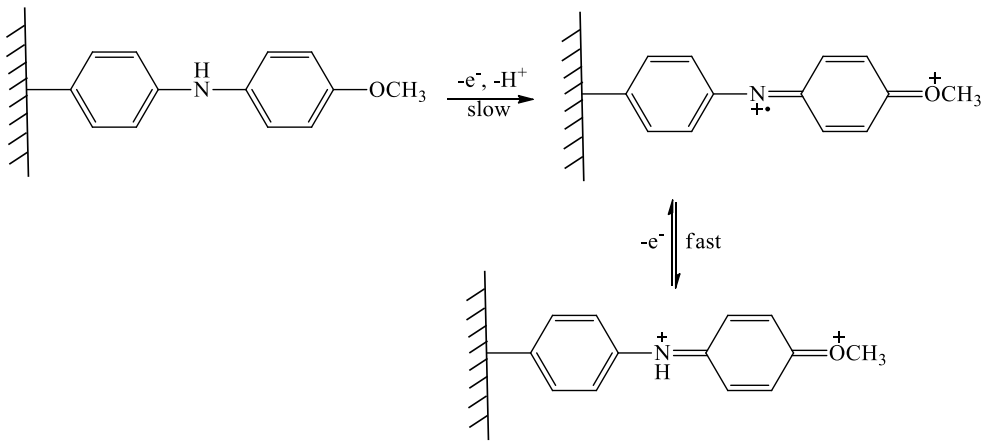

Scheme 3.6. The mechanisms oxidation of variamine blue B modified electrode.

Variable scan rates of the oxidation process were also undertaken. As shown in Fig. 3.28, the peak current for both oxidation peaks and reduction peaks are directly proportional to scan rate, suggesting that the electron-transfer process is not diffusion controlled, but absorbed.

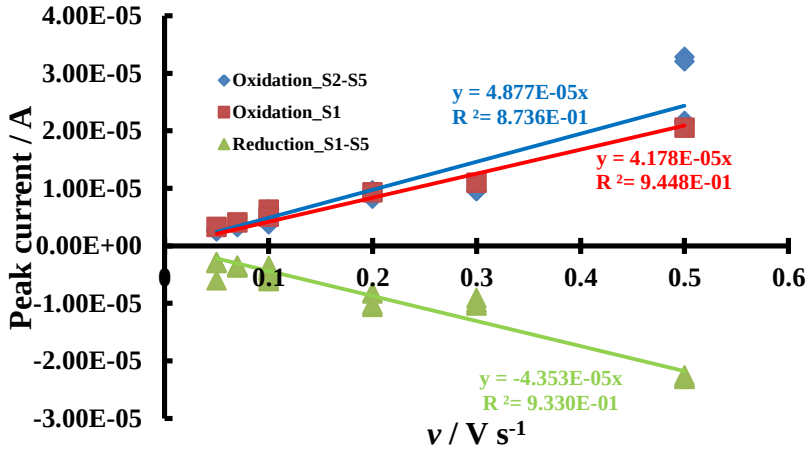

Fig. 3.28. A plot of peak current against scan rate of the oxidation of varimine blue B modified electrode.

The oxidation process was then untaken in different proton concentrations. Mixtures of $HClO_4$ and $NaClO_4$ solutions (with the ionic strength equal to 1.0 M) were used. The plot of peak potential against $HClO_4$ concentration (Fig. 3.29) suggests that there is a large pH dependence on the first scan, whereas there is a small dependence on protons in the consecutive oxidation and reduction process, which in agreement with the mechanisms suggested, as higher acid concentrations leads the first oxidation process difficult as it involves a proton release process.

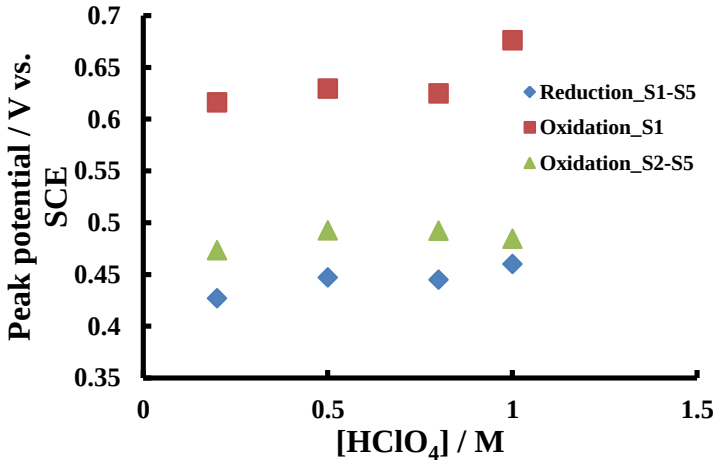

Fig. 3.29. Averaged peak potential in variable scan rates of oxidation of variamine blue B modified electrode against $HClO_4$ concentration.

In order to perform a redox catalytic reaction, a well-known redox reagent, ferrocene derivative, 6-(ferrocenyl)hexanethiol was used to modify the variamine blue B functionalised electrode. The functionalised electrode was dipped in chloroform solution containing 1 mM 6-(ferrocenyl)hxanethiol for overnight. Scheme 3.7 illustrates the nuclearphilic addition of 6-(ferrocenyl)hexanethiol to variamine blue B functionalised electrode.

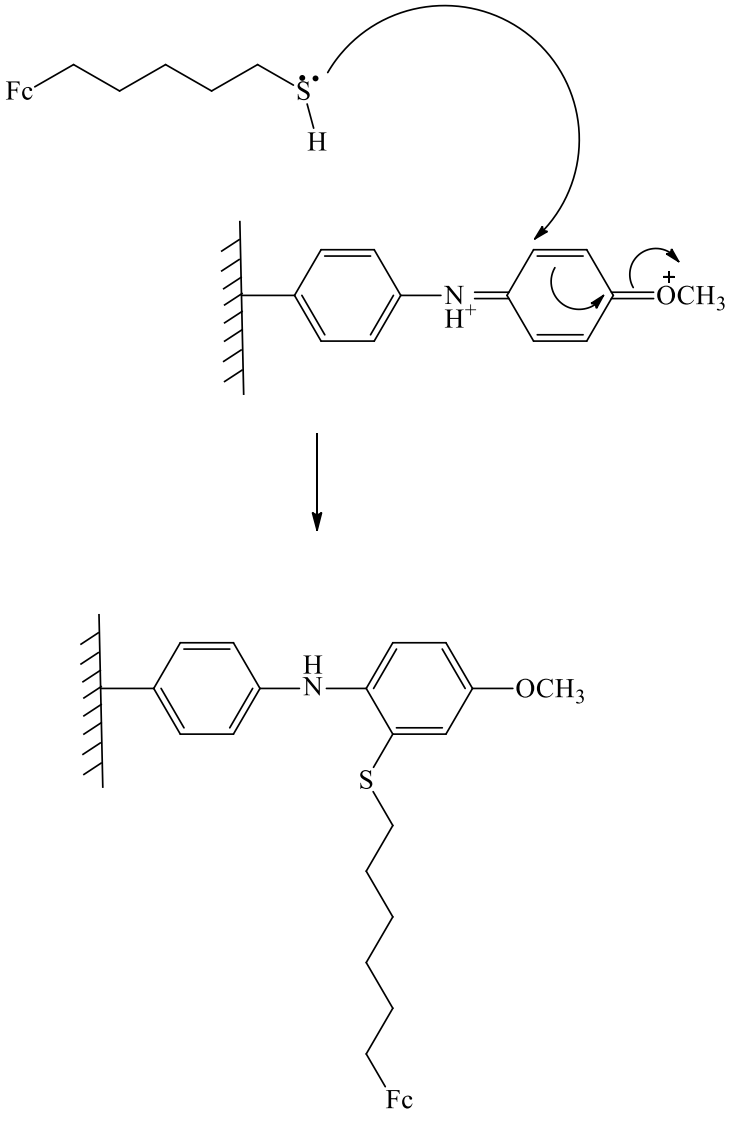

Scheme 3.7.

The final modified electrode was then moved into 0.1 M HClO4 solution and the scan from -0.3 to +0.7 V *vs.* SCE as shown in Fig. 3.30. Clearly, two oxidation and two reduction waves can be observed in Fig. 3.30. The redox process occurs at lower potential is corresponding to the oxidation of ferrocene and the redox process occurs

at higher potential is corresponding to the oxidation of the variamine blue B. The consecutive scans were also been carried out with no loss of signal, suggesting that the modified electrode (sensor) is stable.

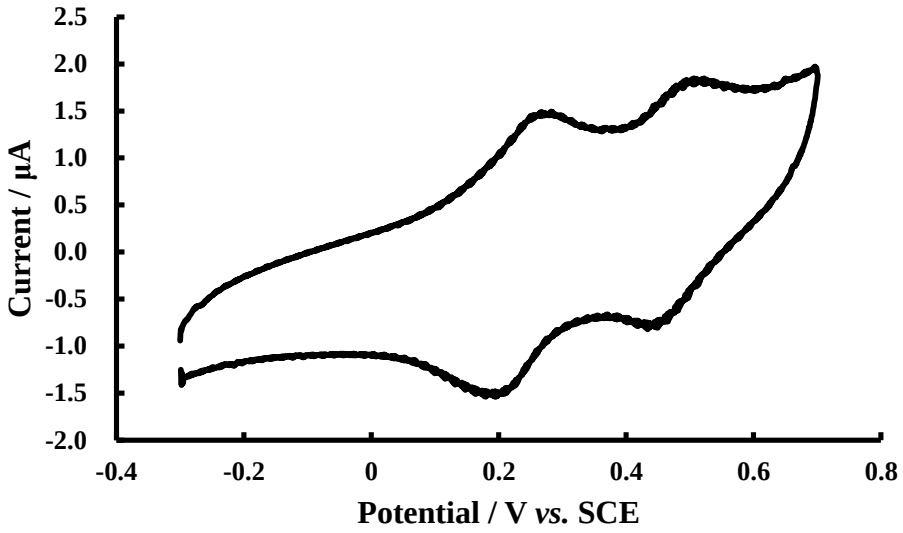

Fig. 3.30. Electrochemical oxidation of ferrocene-variamine blue B modified electrode in 0.1 M $HClO_4$ (v = 0.1 V s^{-1}).

Therefore, in summary, the glassy carbon disc electrode was successfully modified with varimine blue B and 6-(ferrocenyl)hexanethiol. As the redox potential of ferrocene is low, as well as it is a well-known redox catalytic mediator, it can be applied for redox catalytic reactions to act as a potential sensor such as L-cysteine detection.

3.5. Photo electrochemistry of chlorpromazine using channel electrode

In order to understand the photoactivity of chlorpromazine, channel electrode was applied due to its well-defined mass transport and ease of integrate to photo chemistry. The properties and dimensions of channel electrode have been decried in Experiment chapter. However, some modifications were carried out for this experiment.

3.5.1. Design of experiment

The design of the experiment was similar to the setup that mentioned in Experimental chapter. Addition to that is an extra light source. The lamp used has been described in Experimental chapter. 350 nm wavelength was used as chlorpromazine absorb in 350 nm. The light source was placed on top of the platinum electrode over the quartz cover plate with a distance of 5 mm. The light can be observed to cover the entire square-shaped electrode. Grey coloured tape was used to cover rest of the channel and only allow the electrode to be exposed to the light source. Fig. 3.31 illustrates the setups in real case.

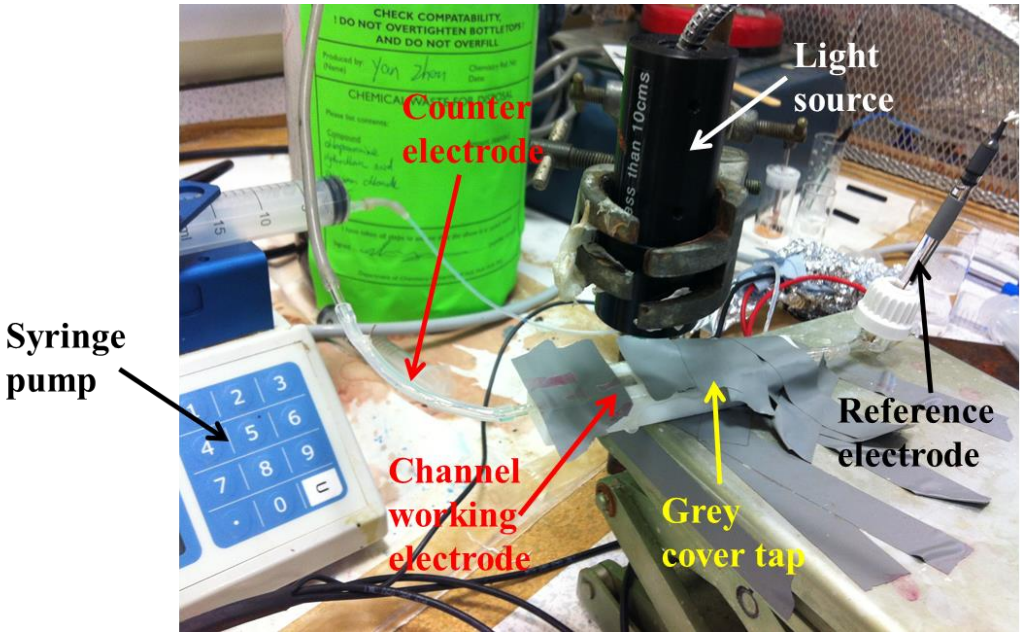

Fig. 3.31. Experimental setup of photo-channel flow electrochemistry system. The reference electrode shown in this picture is Ag/AgCl electrode. PTFE tubing was used upstream of the working electrode and silicone tubing was used downstream of the working electrode, as PTFE is not oxygen permeable.

The intensity of the 350 nm light was measured to be 1440 μW cm^{-2}. The flow rates were used from 0.2 mL min^{-1} to 2 mL min^{-1} in order to get a wide range rate of mass transport.

3.5.2. Calibration of channel electrode

As the diffusion coefficients of different concentrations of chlorpromazine have been measured and calculated using macroelectrode cyclic voltammetry, therefore 1 mM chlorpromazine in 0.1 M KCl was used to calibrate the height of the channel, 2*h*. By plotting the limiting current against cube root of flow rates, the gradient for 1 mM chlorpromazine was found to be 73.03 μA $cm^{-1/3}$ $s^{1/3}$ (Fig. 3.32).

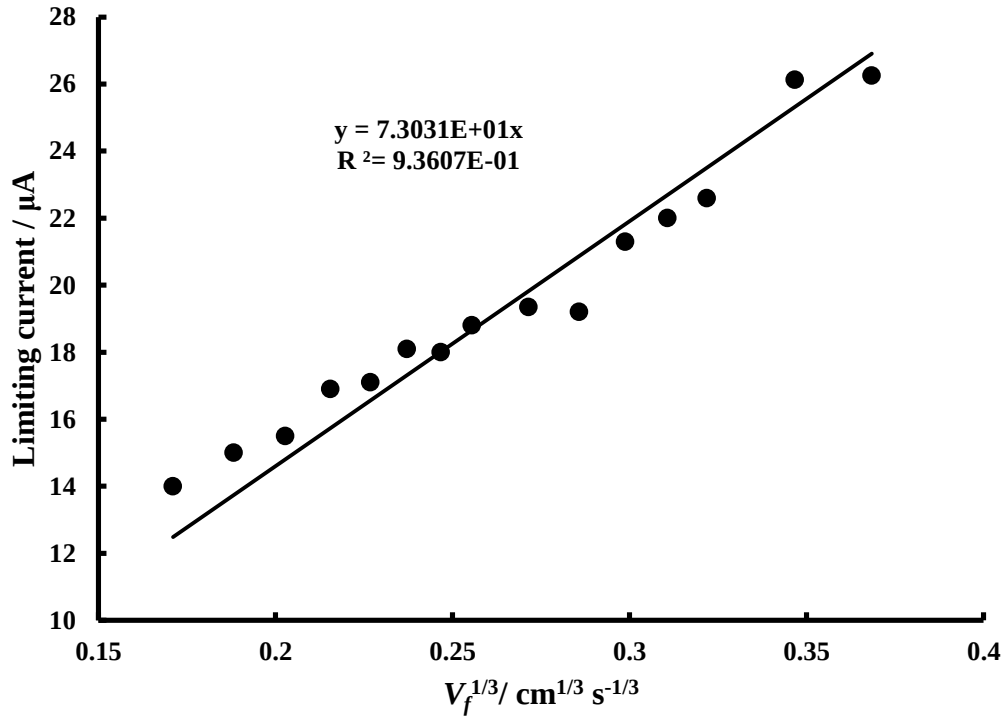

Fig. 3.32. The Levich plot of 1 mM Chlorpromazine in 0.1 M KCl using channel electrode with variable flow rates. A platinum wire was used as the counter electrode and Ag/AgCl electrode was used as reference. A square shaped platinum sheet was used as working electrode with the dimensions: w = 4.5 mm, xe = 5.5 mm, d = 6 mm.

By using the Levich equation, as known the dimensions of the channel electrode, the 2*h* was calculated to be 0.0811 cm.

The experiments were then carried out by using different concentrations of chlorpromazine. By using the 2*h*, which is calculated from 1 mM Chlorpromazine, the

diffusion coefficients for different concentrations of chlorpromazine can be worked out. The data is compared with macroelectrode cyclic voltammetry data and seems reasonable (Fig. 3.33).

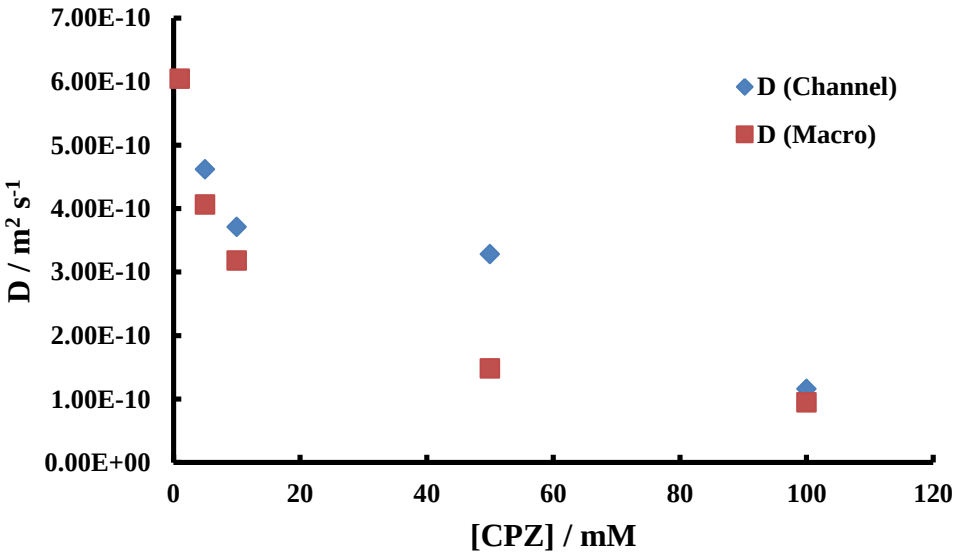

Fig. 3.33. Diffusion coefficients that worked out by using 3 mm diameter glassy carbon disc electrode (blue) and channel electrode (red).

Similar trend can be observed for both channel and macroelectrode data except 50 mM CPZ. This can be due to the measurement of limiting current as syringe pump produces large amount of noises. The overall data indicates the channel electrode was successfully calibrated. The similar trend as macroelectrode data, which the diffusion coefficient decreases with increasing CPZ concentrations, suggests that the CPZ molecules move less fast in high concentrations. Therefore the aggregation of the CPZ is further proved.

3.5.3. Photo-electrochemistry of chlorpromazine using channel electrode

In order to understand the photo-activity of chlorpromazine, as well as the photon effect of the system, photo-electrochemistry experiments using channel electrode was

carried out. As shown in previous section, CPZ itself is photo-active, therefore it suggests that CPZ can be photo excited to CPZ^{*}. It was found that the triplet state is relatively stable than that of the singlet. Therefore $^{3}CPZ^{*}$ is the potential candidate for excited state reactions[91].

The initial investigation was carried out by studying 10 mM CPZ in different ratios of HCl and KCl solution with the ionic strength remains 0.1 M using chronoamperometry combined with channel electrode. The potential was held at +0.3 V, where the potential is not sufficient enough to oxidise the CPZ but enough to reduce the $CPZ^{+\bullet}$ if there is any. The solution was argon saturated in order to prevent any reactions that may be caused by oxygen. 350 nm light was using to excite the CPZ on top of the electrode. An example of chronoamperometry result is shown in Fig. 3.34.

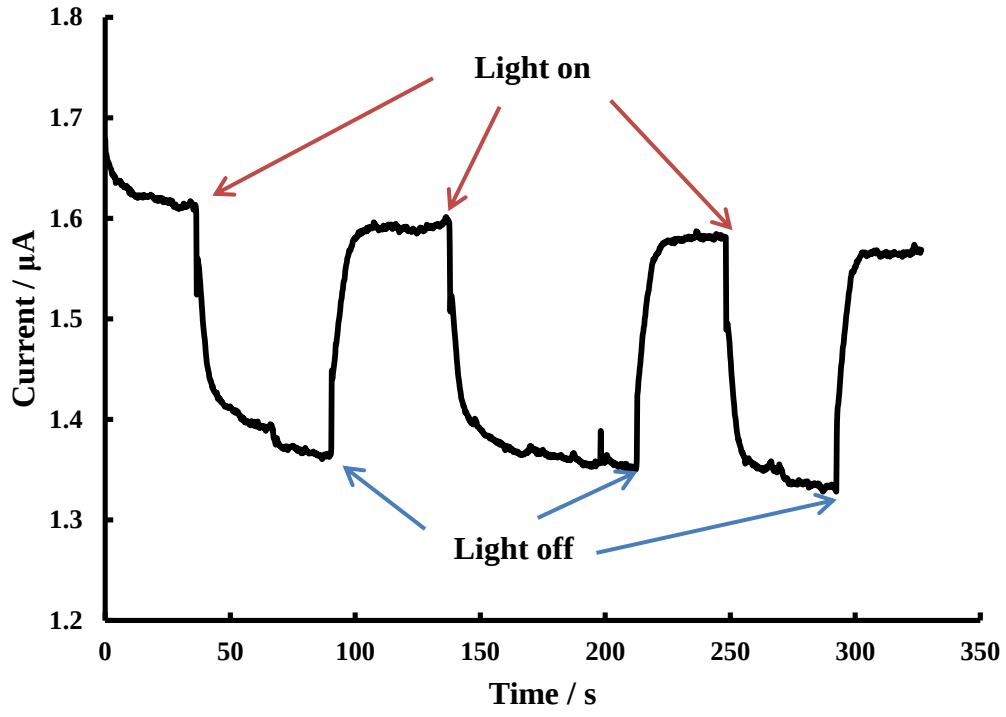

Fig. 3.34. Chronoamperometry of 10 mM CPZ in 0.01 M HCl and 0.09 KCl using channel electrode with 700 µL min-1 flow rate. The potential was held at +0.35 V *vs.* Ag/AgCl. A platinum wire was used as the counter electrode and Ag/AgCl electrode was used as reference. A square shaped platinum sheet was used as working electrode with the dimensions: w = 4.5 mm, x_e = 5.5 mm, d = 6 mm, 2h = 0.811 mm.

As shown in Fig. 3.34, the light causes the current to decrease, suggesting that there is a reductive current observed. In addition, the increase of flow rates causes the photocurrent decrease (Fig. 3.35), suggesting that the faster the flow allows less time for the CPZ to react.

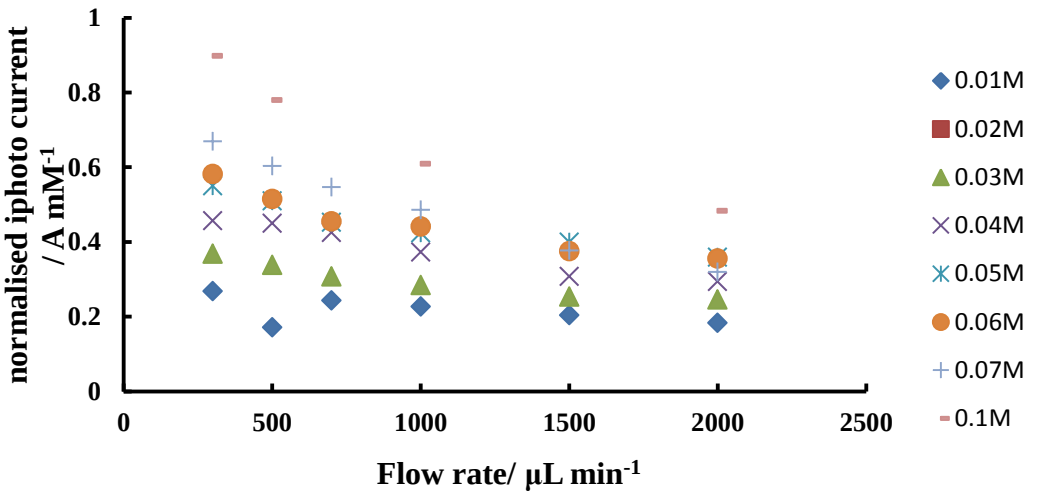

Fig. 3.35. A plot of normalised photo current against flow rates of 10 mM CPZ in variable concentration ratios of HCl and KCl with ionic strength equals to 0.1 M with the potential held at +0.35 V *vs.* Ag/AgCl. 0.01 M to 0.1 M represents the concentrations of HCl. A platinum wire was used as the counter electrode and Ag/AgCl electrode was used as reference. A square shaped platinum sheet was used as working electrode with the dimensions: w = 4.5 mm, x_e = 5.5 mm, d = 6 mm, 2h = 0.811 mm.

Detailed view in Fig. 3.34 shows that there is a spike straight after the light was on. The direction of the spikes is towards positive suggesting there is an oxidation process happening, which are overwhelmed by the reductive signals.

In order to understand the spikes, different concentrations of CPZ was used. 5 mM CPZ was subsequently used with the presence of different ratios of HCl and KCl, with ionic strength equal to 0.1 M, respectively. Surprisingly, oxidative photo-currents were observed with low HCl (c_{HCl} < 0.05 M) concentrations and reductive photo-currents were observed with high HCl ($c_{HCl} \geq 0.05$ M) concentrations. An example which contains both oxidative and reductive photo-current is shown in Fig. 3.36.

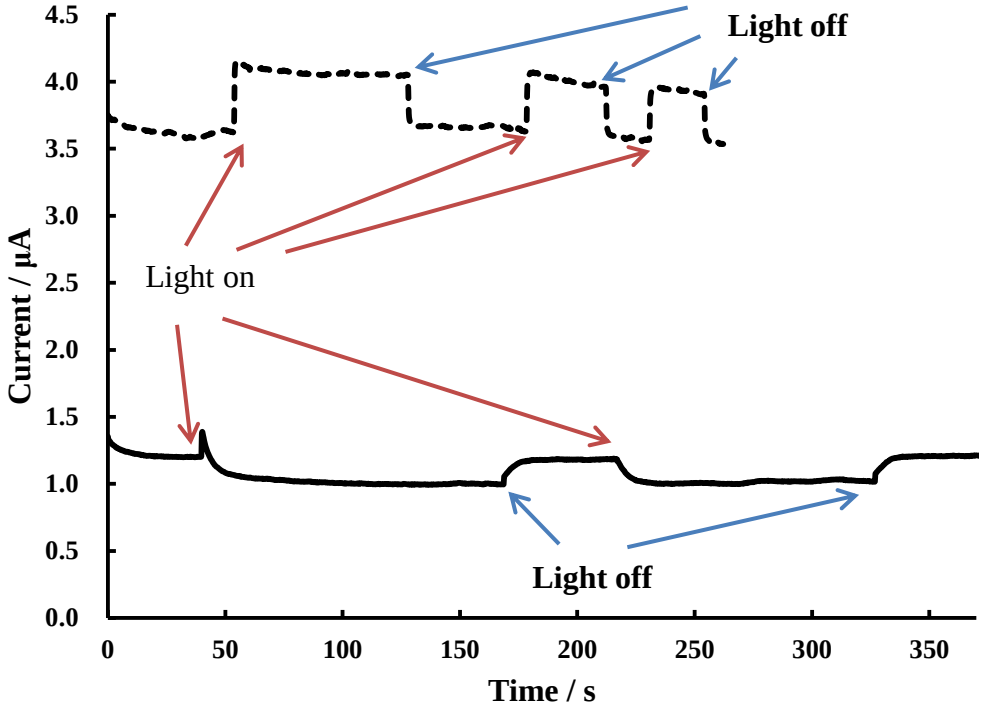

Fig. 3.36. A graph of photo-chronoamperometry of 5 mM CPZ with 0.01 M HCl, 0.09 M KCl (dash) and 0.1 M HCl (solid) using channel electrode with 700 µL min^{-1} flow rate. Potential was held at +0.35 V *vs.* Ag/AgCl. A platinum wire was used as the counter electrode and Ag/AgCl electrode was used as reference. A square shaped platinum sheet was used as working electrode with the dimensions: w = 4.5 mm, x_e = 5.5 mm, d = 6 mm, 2h = 0.811 mm.

As shown in Fig. 3.36, spike can be observed before the reductive photo-current occurs, which in agreement with previous experiments. 2 mM CPZ experiments were also carried out with the same conditions as the 5mM and 10 mM CPZ experiments. Similar observations were found as 5 mM CPZ, but the inversion from oxidative current to reductive current requires higher concentrations of HCl (*i.e.* $c_{HCl} \geq 0.07$ M).

Therefore from all three experiments, it can be concluded that the photo excitation causes both oxidative and reductive process to occur. The oxidation is faster than the reductive process and can be overwhelmed by the reductive photo signal with higher CPZ concentration or higher HCl concentrations. The oxidation process can be due to the photo initiated ionisation, and the reductive process can be due to the reduction of $CPZ^{+\bullet}$. Therefore the reaction scheme can be concluded in Scheme 3.8 – 3.11.

$$CPZ \xrightarrow{hv} CPZ^{*} \quad \text{(Scheme 3.8)}$$

$$CPZ^{*} \rightarrow CPZ^{+\bullet} + e^{-} \quad \text{(Scheme 3.9)}$$

$$CPZ^{*} + H^{+} \rightarrow CPZ^{+\bullet} + \frac{1}{2}H_2 \quad \text{(Scheme 3.10)}$$

$$CPZ^{+\bullet} + e^{-} \rightarrow CPZ \quad \text{(Scheme 3.11)}$$

As shown in Scheme 3.9, ionisation process causes the oxidative current and CPZ cation radical is formed. The CPZ cation radical can be then reduced at +0.3 V to CPZ ground state. In addition, in the presence of HCl, the proton concentration is sufficient to let Scheme 3.3 to occur. Both scheme 3.9 and 3.10 generate CPZ cation radical with the faster homogenous electron transfer (*i.e.* Scheme 3.9), therefore higher proton concentration, the more CPZ cation radical can be generated as well as can be subsequently reduced.

Further experiments were also carried out by hold the potential at both 0 V and -0.25 V using 5 mM CPZ with 0.01 M HCl and 0.09 M KCl. The oxidative spikes are higher at 0 V than -0.25 V, and both conditions provides a reductive decay, suggesting that:

- The reductive current is not caused by the reduction of hydrogen as Ag/AgCl reference electrode was used and potential was held at -0.25 V.
- Higher potentials (*i.e.* 0 V compared to -0.25 V) offers higher oxidative spike, which on the other hand, less Scheme 3.10 is occurring.

An example of 5 mM CPZ with 0.01 M HCl and 0.09 M KCl with holding the potential at both 0 V and -0.25 V is shown in Fig. 3.37. It can be seen that in Fig. 3.37, the reductive current are similar to each other. The oxidative spike at 0 V is higher than that of the -0.25 V but the following spikes becomes similar.

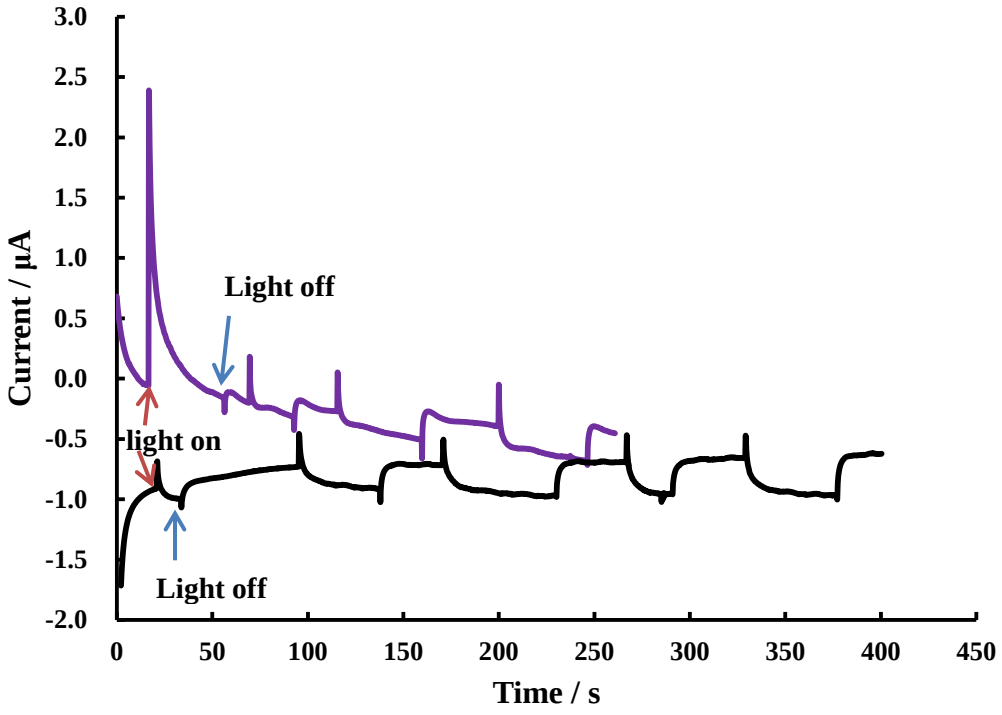

Fig. 3.37. A graph of chronoamperometry of 5 mM CPZ with 0.01 M HCl and 0.09 M KCl using channel electrode with 200 µL min^{-1} flow rate. The potential was held at 0 V (purple) and -0.25 V (black) *vs.* Ag/AgCl. A platinum wire was used as the counter electrode and Ag/AgCl electrode was used as reference. A square shaped platinum sheet was used as working electrode with the dimensions: w = 4.5 mm, x_e = 5.5 mm, d = 6 mm, 2h = 0.811 mm.

3.5.4. Summary

The photo-electrochemistry of chlorpromazine has been studied systemically using channel electrode combine with photo-excitation. The reaction mechanisms are worked out based on the chronoamperometry data.

Lactic acid, on the other hand, could be a potential fuel source to power the sensor itself, therefore, a renewable energy source can be utilised. In chapter 7, simulations of renewable energy storage was discussed in order to provide the efficiency of storage of renewable energies.

3.6. Melamine detection

Besides the detection of the biomarkers, electrochemical sensors in food industry are also crucial. Melamine (Fig. 3.38) is known as industrial synthetic compound used in laminates, coats, adhesive and flame-retardants[92]. However, it became a cattle feed material in 1958 due to its high nitrogen containment (66%), and it was discontinued in 1978 due to incomplete hydrolysation in ruminants[93]. However, because the Kjeldahl method[94] only measures the nitrogen content as a indication for protein levels, therefore melamine was added to food products to increase the protein content. In 2004, it was found that melamine was added to pet food and cased renal failure for dogs and cats in Asia[95]. More seriously, in 2008, more than 54,000 infants and young children were hospitalised due the addition of melamine to dairy products in China and caused at least six deaths[96, 97]. Consequently, the detection of melamine became a crucial task for the government to protect the public health.

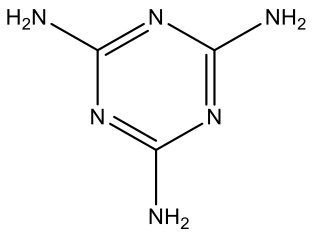

Fig. 3.38. Chemical structure of melamine.

There are many literatures published after the Chinese dairy incident concerning about the detection of melamine. As melamine contains three azine groups, it is highly stable with poor electroactivity[98], and it is rare to see literatures on the direct electrolysis of melamine. There are some detection methods in literatures based on electrochemistry including electrochemiluminescence[99, 100] and voltammetic method using a modified glassy carbon electrode[101], using a modified screen print electrode[98, 102] and using a molecularly imprinted polymer electrode[103]. Overall, the electrode needs to be modified in order to measure the presence of melamine.

As melamine can act as a proton donor because of the three amine groups, the

electrochemical oxidation of 2,4,6-trihydroxybenzoic acid (THBA) was used, and the oxidation process can be favoured by the addition of melamine. The benzoic acid can be hydrolysed in water to form a proton and $R\text{-}COO^-$ group, with addition of melamine, the hydrolysation can be favoured.

3.6.1. Varying scan rates of 2,4,6-trihydroxybenzoic acid (THBA)

Another interesting experiment of catalytic electrochemistry was carried out by using 2,4,6-trihydroxybenzoic acid (THBA) as mediator to determine melamine concentration. However, this approach is not a typical EC′ reaction, as the melamine does not catalyse the THBA. As melamine is known as an organic base[104], therefore it deprotonate an acid molecule, in this case, THBA, which can favour the oxidation of the acid.

A preliminary experiment was carried out by examining the redox process of THBA in 1:1 ratio of water/ethanol in the presence of 0.1 M KCl as supporting electrolyte. As shown in Fig. 3.39a, the increasing number of scans leads decrease in peak current, indicates the electrode surface area changes with number of scans. Therefore electrode polishing is essential between scan rates. Fig. 3.39b shows the oxidation of 1.08 mM of THBA in variable scan rates ($0.02 \leq \nu / V\ s^{-1} \leq 1$), the peak current increase with increasing scan rate, as expected. Notably, at slower scan rates ($0.02 \leq \nu / V\ s^{-1} \leq 0.1$), two peaks can be observed between +0.8 V and +1.1 V, whereas at higher scan rates ($0.2 \leq \nu / Vs^{-1} \leq 1$), the two oxidation peaks merged into one broad peak. The split of two oxidation peaks suggests that the oxidation of THBA is a two-electron transfer process. In addition, the plot of peak current against square root of scan rate (Fig. 3.39c) offers linear dependence for all of the first oxidation peak, second oxidation peak and the merged peak at higher scan rates, and the slope of first oxidation is close to twice of the second oxidation wave, with the merged wave in

between them, suggesting that the effective number of electron transferred at second oxidation potential is twice of the first, and decreased at higher scan rate. The plot of peak potential against logarithm of scan rate (Fig. 3.39d) shows that all of the peak potentials have a dependence on scan rate, suggesting that both electron transfer processes are electrochemically irreversible. Again, half of the slope of second oxidation peak compared to the first one suggests the effective number of electron transferred is doubled, and the merged peak at higher scan rate appeared in between suggests that the effective number of electrons transferred is decreased at higher scan rate.

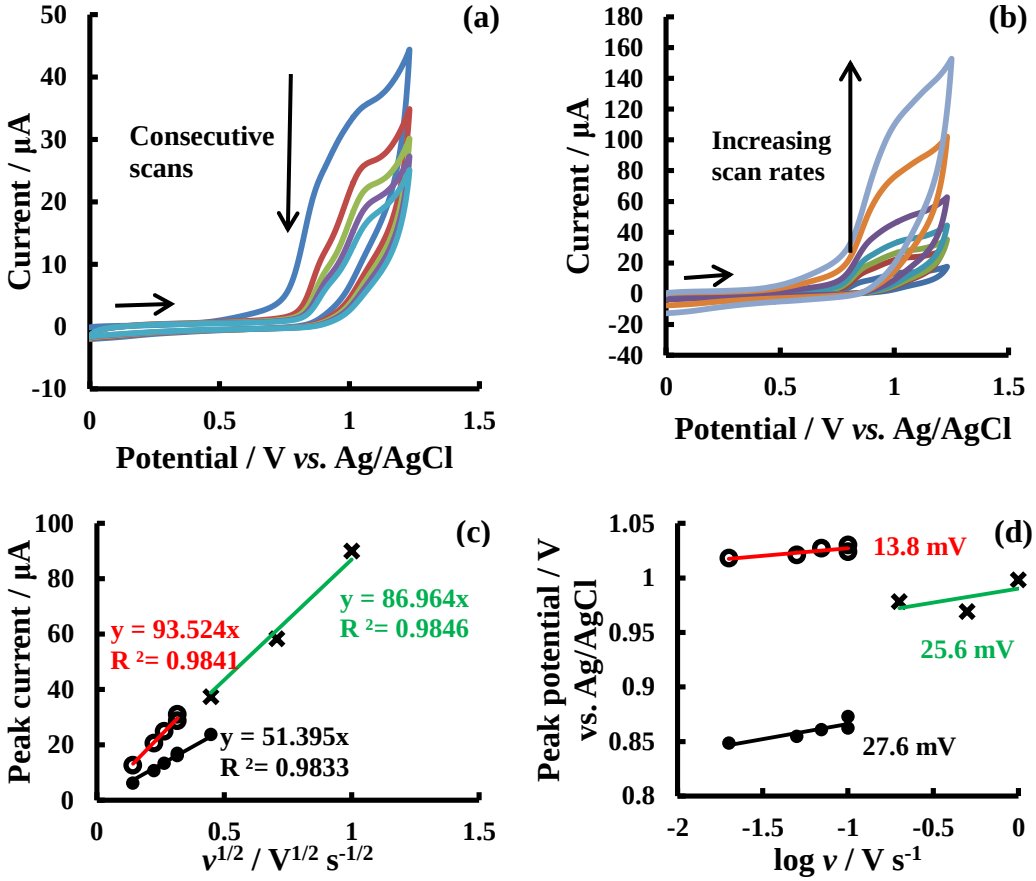

Fig. 3.39. (a) Cyclic voltammetry of 1.08 mM THBA oxidation at 0.1 V s^{-1} scan rate with five scans. (b) Cyclic voltammetry of 1.08 mM THBA oxidation at variable scan rates. (c) A corresponding plot of peak current against square root of scan rates, with solid dots: first oxidation peak; hollow dots: second oxidation peak; cross: merged oxidation peak at higher scan rates. (d) A corresponding plot of peak potential against logarithm of scan rates, with solid dots: first oxidation peak; hollow dots: second oxidation peak; cross: merged oxidation peak at higher scan rates. A 3 mm diameter glassy carbon disc electrode was served as a working electrode, silver/sliver chloride electrode was served as a reference electrode and a spiral platinum wire was used as a counter electrode.

3.6.2. Effects of melamine addition

After the study of THBA on itself, different ratios of TBHA concentrations and melamine concentrations were examined by cyclic voltammetry. Interestingly, after the ratio [Mel]/[THBA] greater than 1, the two oxidation peak merged into one. As shown in Fig. 3.40, the shoulder on the oxidation peak disappeared when the concentration of melamine above 1 mM. Note that the peak currents are slightly different due to the variation of exact concentration of 1 mM THBA.

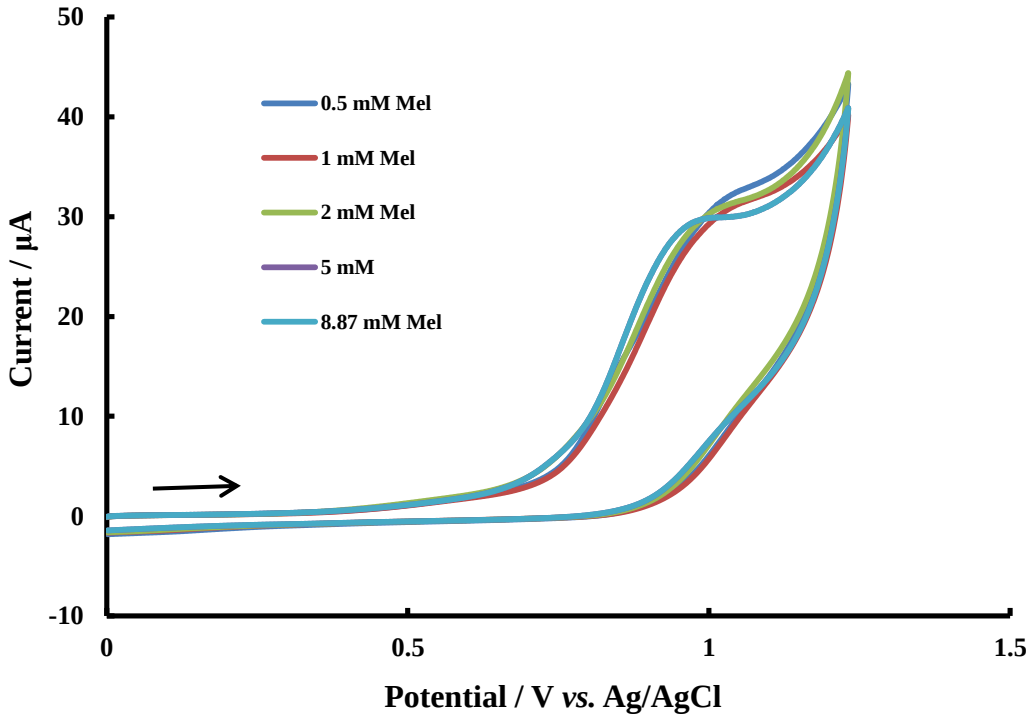

Fig. 3.40. Electrochemical oxidation of 1 mM THBA with variable concentrations of melamine in the mixture of water and ethanol with 1-to-1 ratio. 3 mm diameter glassy carbon disc electrode was served as the working electrode, silver/silver chloride electrode was served as the reference electrode as a spiral platinum wire was used as a counter electrode. Scan rate = 0.1 V s^{-1}.

Therefore the oxidation process can be assumed to be a two-electron oxidation process with a deprotonation process in between (Scheme 3.12). The addition of melamine favours the deprotonation process and leads the oxidation of THBA easier.

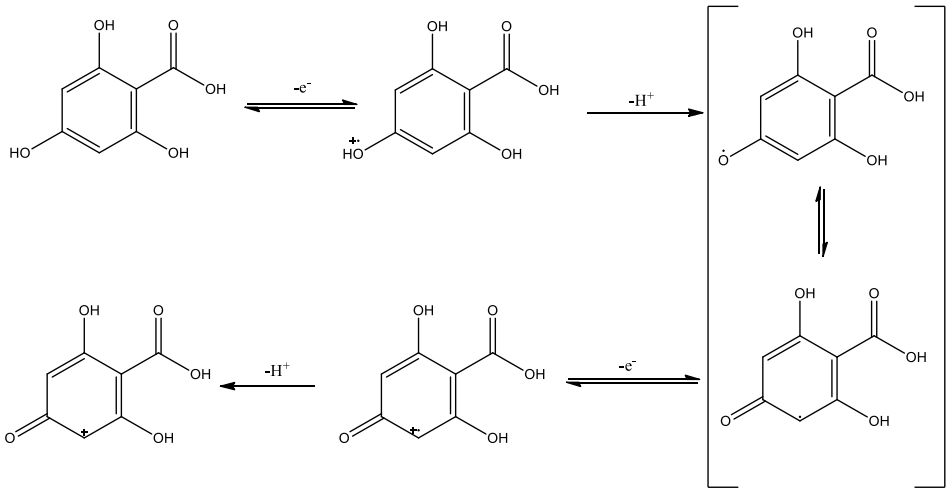

Scheme 3.12. Electrochemical oxidation route of THBA.

As the potential shift on cyclic voltammetry is small, therefore in order to apply this technique in analytical applications, square wave voltammetry (SWV) was used. As the homogenous deprotonation process is a chemical reaction step, the reaction time can be critical. Several measurements were taken for the oxidation of THBA with the presence of melamine (1 mM), as shown in Fig. 3.41, the potential has no change after 5 minutes incubation time of melamine, therefore for the following experiments, 20 minutes incubation time for melamine was used in order to ensure the deprotonation process has been carried out fully.

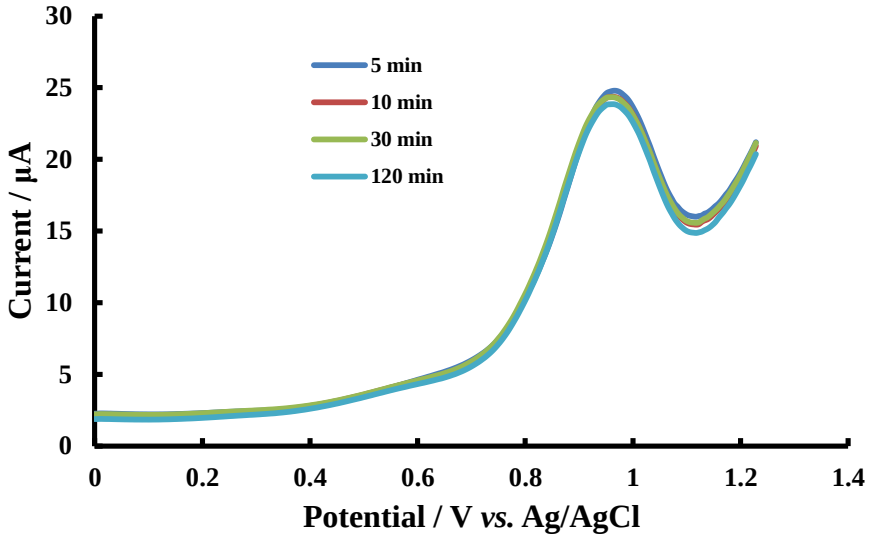

Fig. 3.41. SWV oxidation of 1 mM THBA in ethanol/water solution (in ratio of 1:1) on a 3 mm diameter glassy carbon disc electrode in the presence of 1 mM of melamine. Measurements were taken in different incubation times. Ag/AgCl electrode was served as a reference electrode and a spiral platinum wire was used as a counter electrode.

3.6.3. Analytical approach

In order to apply this technique in an analytical area, variable measurements using SWV were carried out. Three different concentrations of THBA were examined in the presence of variable concentrations of melamine using SWV. As shown in Fig. 3.42, 1 mM of THBA was oxidised using SWV on a 3 mm diameter glassy carbon electrode. Clearly, the peak potential starts shifting with the addition of melamine when the concentration ratio of THBA and melamine reaches to 1-to-1.

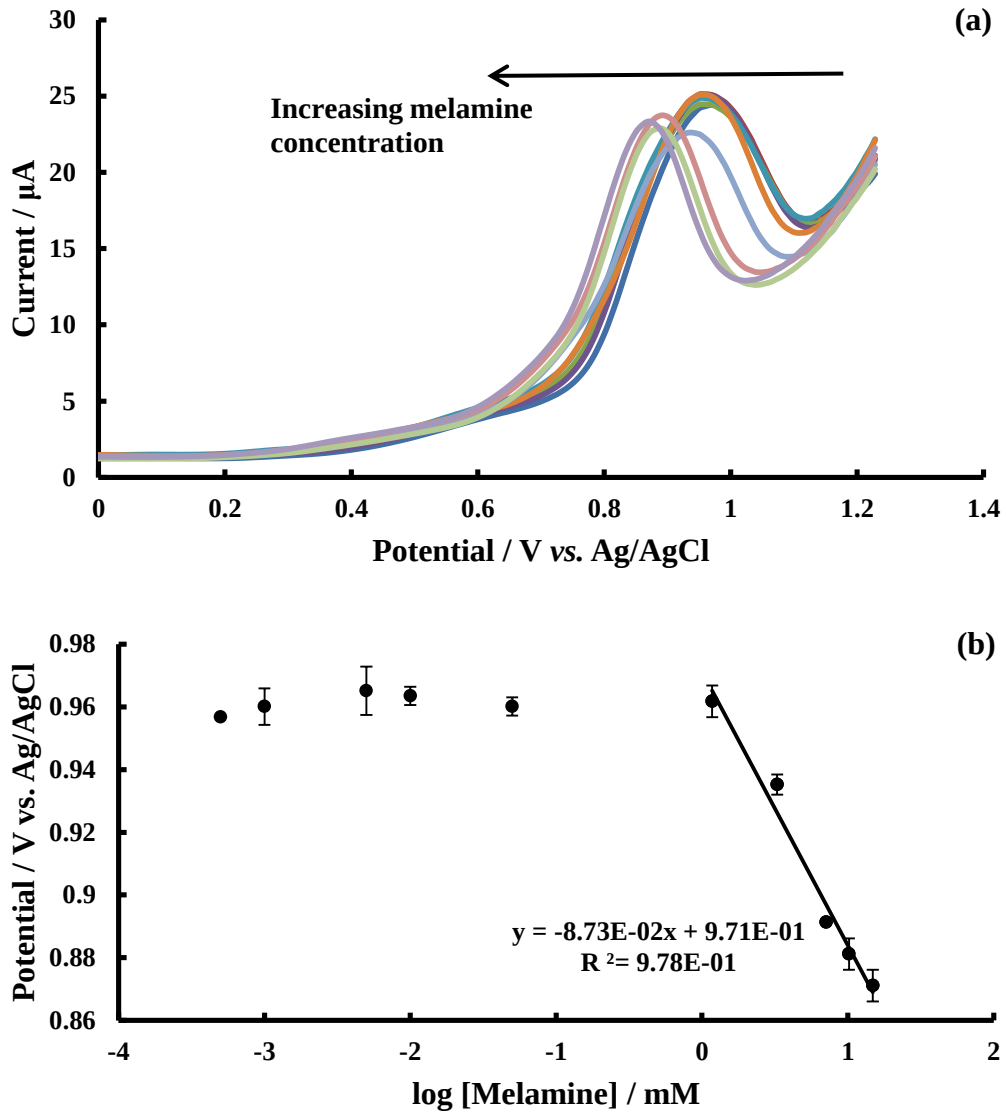

Fig. 3.42. (a) SWV of oxidation of 1 mM THBA in ethanol/water solution (1:1 ratio) on a 3 mm diameter glassy carbon disc electrode with the addition of variable concentrations of melamine. (b) Corresponding plot of potential shift with logarithm of melamine concentration. Ag/AgCl electrode was served as reference electrode and a spiral platinum wire was used as a counter electrode.

Same effects can also be found in different other concentrations of THBA. 0.5 mM and 10 mM of THBA were also examined using SWV as shown in Fig. 3.43. Therefore the detection limit is depending on the concentration of THBA. The lower the THBA concentration, the lower detection limit.

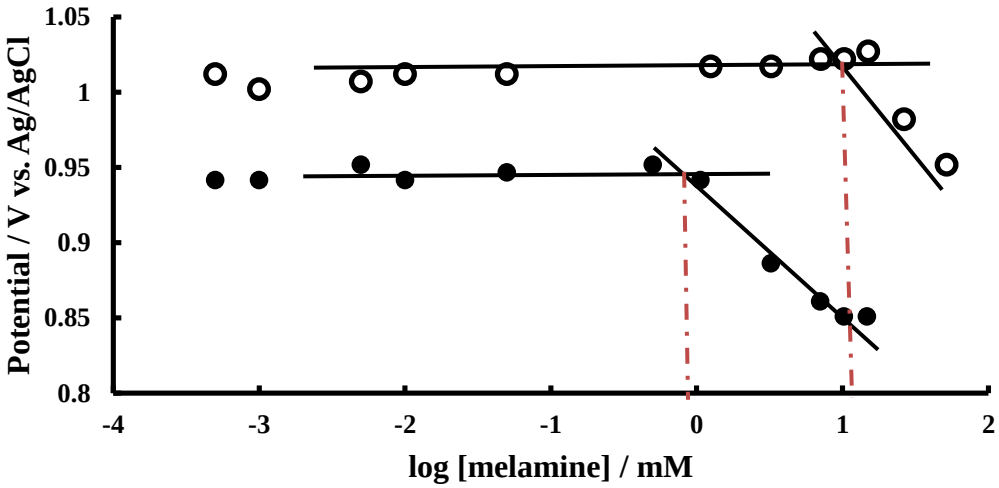

Fig. 3.43. Plots of potential shift with logarithm of melamine concentration with the presence of 0.5 mM THBA (black dots) and 10 mM THBA (white dots). Ag/AgCl electrode was served as reference electrode and a spiral platinum wire was used as a counter electrode.

In conclusion, melamine can be successfully detected by THBA using SWV. It was found that the redox potential of THBA starts to shift towards positive when the concentration ratio of melamine and THBA above 1, indicates of a 1:1 complex being formed.

3.7. Conclusions

In conclusion, several substrates (L-cysteine, glutathione, lactic acid and melamine) were successfully detected using electrochemistry techniques. By using homogeneous catalytical approach, the detection limits for L-cysteine, glutathione were found to be 6.3 ± 0.03 and 4.4 ± 0.07 μM. The detection limits for lactic acid was found to be as low as 5.85 mM, and the LoD was dependent on the chlorpromazine concentration. VBB modified GC electrode was further functionalised by 6-(ferrocenyl)hexanethiol afford a sensor. Finally, melamine was detected by using THBA and the LoD of melamine was dependent on the THBA concentration and the dependence occurred

when concentration ratio of melamine and THBA above 1.

In addition, as mentioned previously, as lactic acid is present in sweat with high concentration, and the redox catalytic reactions suggested that it can be a potential fuel for a battery. This was also verified by our group.

The redox catalysis was studied in this chapter and in the next chapter; electrochemically induced ion proton transfer reactions are examined.

4. PROTONATION AND DEPROTONATION PROCESSES INDUCED BY ELECTROCHEMISTRY

4.1. Introduction

Electron transfer induced reactions have been widely used in organic synthesis[105]. Despite variable types of bonds formation and dissociation, protonation and deprotonation processes can be extremely attractive due to the variable uses of protons[75].

Recent studies on proton-coupled electron transfer reactions suggest that this process can be either stepwised or concerted. The stepwised process has been studied over a few decays whereas the concerted process has only been brought up recently.[106]

A well-known stepwised protonation reaction induced by addition of electrons is Birch reduction[107], the radical anions are generated by the addition solvated electrons and can be subsequently protonated. The reactions of electrochemically induced protonation processes can be initiated by heterogeneous electron transfer (through an ECE or DISP mechanism [108-112], shown in scheme 4.1) or by a homogeneous deprotonation.

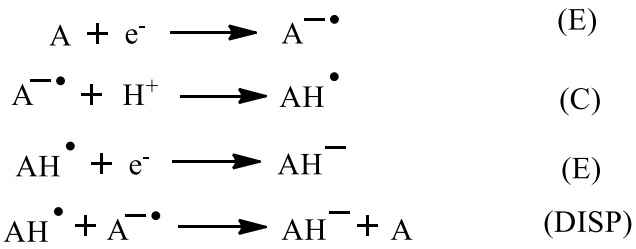

Scheme 4.1.

As shown in Scheme 4.1, both ECE and DISP mechanisms start with an electron transfer process and followed by a homogenous protonation (first order or pseudo-first-order). Then the radical can be either reduced by a heterogeneous electron transfer to form the anion (ECE) or homogenously reduced by the anion radical (DISP).

In addition, the proton-coupled electron transfer can be either initiated by heterogeneous electron transfer or homogeneous proton transfer, the latter may depends on the solvent environment, such as pH.

Another interesting electron transfer induced protonation is the reduction of quinones. Instead of C-H bond formation, O-H bond formation is more attractive in the area of biochemistry[113] as vitamins are quinone derivatives. Therefore vitamin K_1 was studied in order to understand the O-H bond formation, as well as suggested a novel method to support vitamin K_1 on the electrode to obtain better voltammetric signals. General quinone reduction is summarised in Scheme 2.

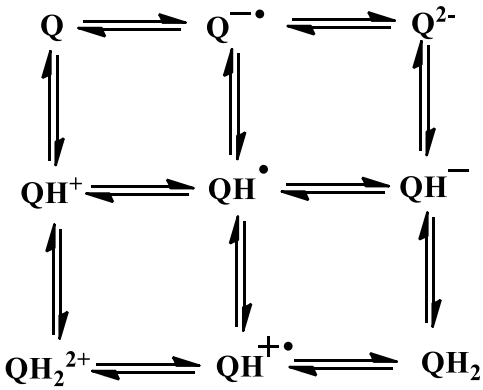

Scheme 4.2. Reaction pathways for quinone reduction.

Due to different reaction conditions such as acidity, different reaction pathways can be observed. As shown in Scheme 4.2, a square-scheme was suggested. The three horizontal pathways are corresponding to the electron transfer process, whereas the vertical pathways are corresponding to the homogenous proton transfer processes.

However, it has been found recently that a quinone derivative, 3,5-di-*tert*-butyl-1,2-benzo-quinone did not fit the square scheme (Scheme 4.2). It was proposed that its second voltammetric cathodic wave was too large[114]. In addition, the large potential shift in hydroquinone oxidation in presence of nearby carboxylate group also does not match the stepwised square scheme[115] (Scheme 4.2). These phenomena were suggested to be a concerted proton-electron transfer process.

Electrochemical oxidation induced proton release can be another proton transfer process to look at. Oxidative proton release of O-H bond in alcohols has been studied by Baciocchi et al.[116-119] and it has been shown that the reactions were strongly pH dependent.

Therefore in this chapter, electrochemically induced protonation and deprotonation process were studied, including the potential usage of organic synthesis, electrode modification and analytical purposes.

4.2. Electrochemical catalysed Birch reduction

This work has been done by myself and in collaboration with A. Andreou and E. Biktagirov. This work has been published in *ELECTROCHEM. COMMUN.*, vol. 12, no. 11, pp. 1493-1497, 2010.

4.2.1. Introduction

2,3-Diphenyl-1,4-diazaspiro[4.5]deca-1,3-diene, **1*** **(**shortened to Spiro-bis-anil in the following text, SBA) is an effective reagent for efficient synthesis of (1R,2S)-1,2-diphenylethane-1,2-diamine, **4**. **4** can be synthesised from **2** in methylene chloride. **2** is a useful ligand and auxiliary[120, 121] for enantioseletive synthesis[122]. The products can then be used for applications such as Diels-Alder and Aldol reactions[122], which are useful for the construction of complex molecules. The synthetic route from **1** to **3** is well-known and published by several authors[122-124]. All synthetic routes suggest that **1** must be converted to **2** under Birch conditions (*i.e.* liquid ammonia, sodium metal in Tetrahydrofuran), resulting in the stable trans-imidazoline, **2,** in high yield. This aminal can be hydrolysed to give, **4**, in the required racemate[122-125]. In addition, because of the delocalisation is present[126], first order thermal rearrangements of the 2*H*-imidazole to the corresponding 1*H*-inmidazole are slow[127], the activation barrier is greater than 200 kJ mol^{-1} at 300 ℃.

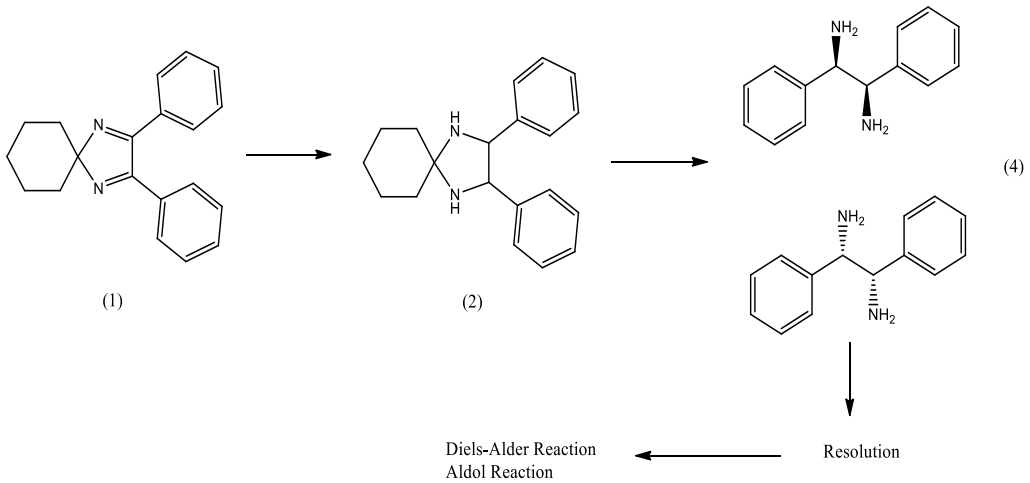

Scheme 4.3. The reaction pathway for 2,3-Diphenyl-1,4-diazaspiro[4.5]deca-1,3-diene (1) to its applicable products.

The reduction of imine functional group was studied previously by several authors. Savéant[128] *et al.* studied several different types of imines such as

* The numbers refers to the molecules in scheme 4.3 and scheme 4.4.

benzophenone-N-methylimine, benzophenone anil, acetophenone anil and benzaldehyde anil. The reduction of these imines was found to be a single two electron wave in both acetonitrile and dimethylformamide. They proposed that the reaction mechanisms discussed were specific to each molecule studied. Benzopheone-N-methylimine and benzophenone anil followed an ECE or DISP1 mechanism in both acetonitrile and DMF, acetophenone followed a DISP2 pathway in DMF whereas benzaldehyde anil gave two waves in DMF and two waves in acetonitrile at higher scan rates which suggested it followed a DISP2 mechanism. It was also found that the protonated intermediate was easier to reduce than the starting material[129]. Moreover, Dessy *et al.*[130] studied benzophenone anil in glyme-dimethoxyethane and observed two waves with one electron in each. The reduction of diimines can leads to up to 4 electron transfer process, and so, to conclude, the reduction of imines is reasonably complicated and dependent on different solvent systems and functional groups.

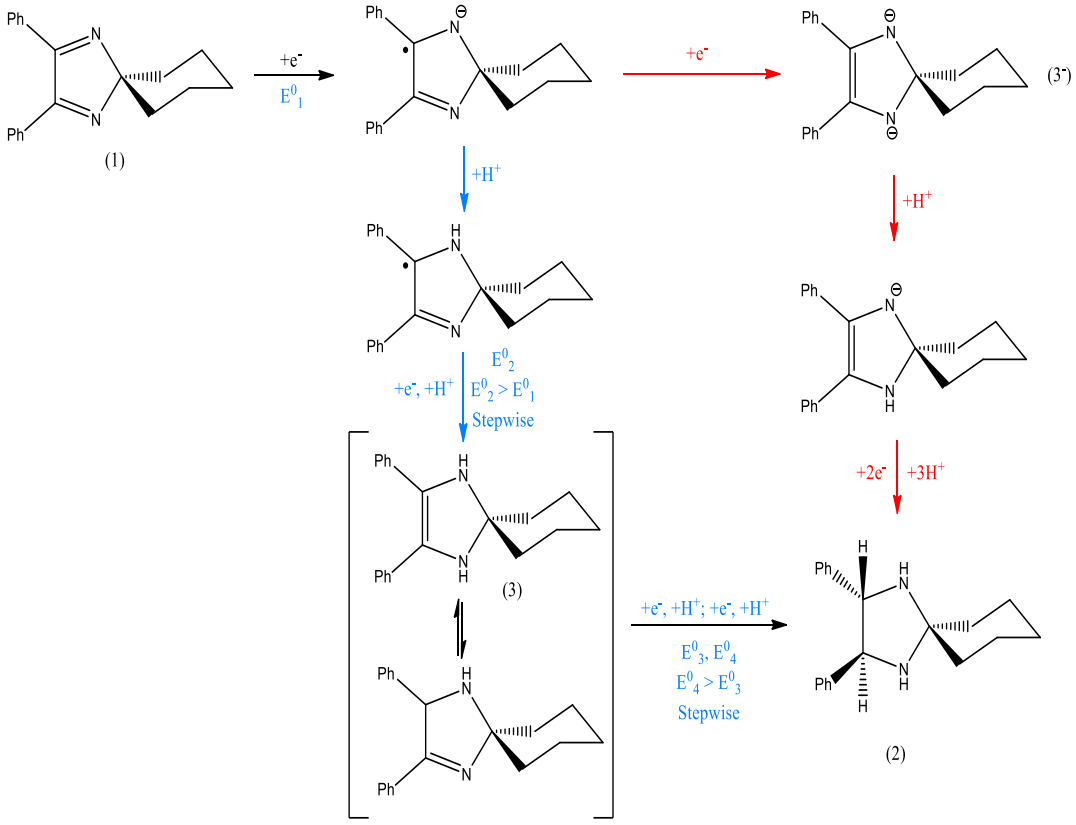

Scheme 4.4. Birch reduction pathway (red) and electrochemical reduction pathway (blue) of **1**.

The reduction mechanisms of imines are complicated, but the reaction of bis-anils can

be even more intricate. It can lead up to four electrons transferred[120-122, 124, 125, 131, 132]. How these electrons are transferred is still open to debate. As no stable intermediate is observed, a stepwise mechanism seems unlikely. Past studies of dimine reductions have all focused on either open chain or six membered ring bis-anils in protic environments[133, 134] and tautomerisation of the diimines can occur within the voltammetric timescale[133], adding even further complication.

In the present work, the reduction of a five-membered ring bis-anil, **1**, was studied. It was found to follow a four electron reduction, similar to other bis-anils previously stated, as predicted. Moreover, a two-electron immediate was observed in the voltammogram, compared to the four-electron Birch reduction pathway (Scheme 4.2).

4.2.2. Electrochemical reduction of 2,3-Diphenyl-1,4-diazaspiro [4.5]- deca-1,3-diene in dry-dimethylformamide

The initial investigation of the reduction of spiro-bis-anil (SBA) was carried out in DMF using a glassy carbon electrode (3 mm diameter). 0.99 mM of SBA was dissolved in dry DMF with 0.1 M Tetrabutylammonium perchlorate (TBAP) as supporting electrolyte. Two reduction waves were observed during the voltammetry experiment (Fig. 4.1a). The first reduction peak appeared between -1.9 V to -2.0 V (also depending on scan rate), whereas the second reduction peak appeared between -2.3 V to -2.4 V (depends on the scan rates). Both the peaks have a shoulder at the half height at slow scan rates, *circa* 20 mV s^{-1}, indicating that the two electron reduction process for each peak contained two discrete steps, with a slow protonation process after the first and third electron transfer process, which is caused by the limited proton source. The reduction waves appeared at relatively negative potentials suggesting that the reduction of the spiro-bis-anil is relatively difficult. The

intermediate could be observed and stable between -2.0 V to -2.5 V. This was expected as the intermediate involves a double bond with electron delocalised in the diimine ring.

Correspondingly, microelectrode voltammetry was carried out using an 11 µm diameter carbon fibre electrode. Two limiting currents can be observed in the voltammogram (Fig. 4.1b), with half wave potential similar to that of the macro-electrode voltammogram, agreeing with the two stepped process.

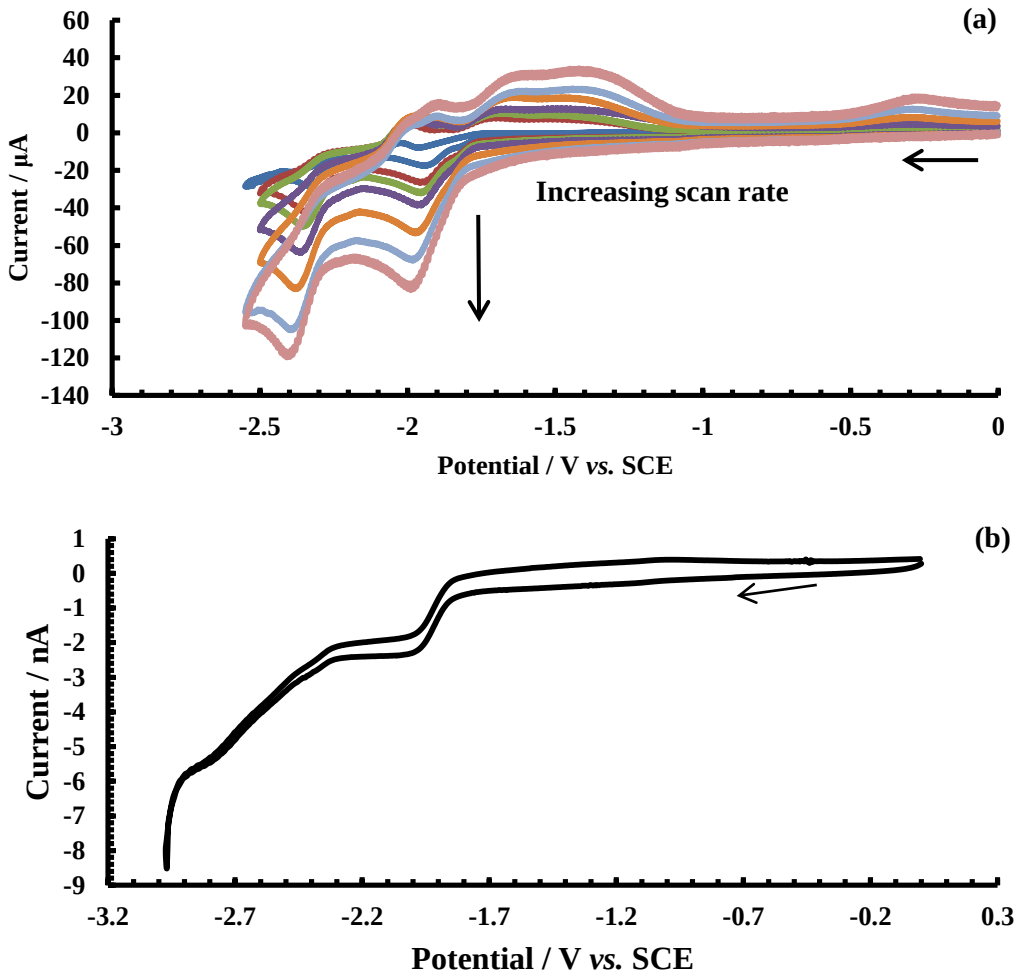

Fig. 4.1. Cyclic voltammogram of electrochemical reduction of 0.99 mM spiro-bis-anil at (a) a glassy carbon macro-electrode (3 mm diameter) or (b) carbon fibre microelectrode (11 µm diameter) in dry DMF with 0.1 M TBAP. A nickel wire was used as a counter electrode, and saturated calomel reference electrode was used. Variable scan rates were carried out in the experiment ($0.02\ V\ s^{-1} \leq \nu \leq 0.5\ V\ s^{-1}$).

As it can be seen from the voltammogram (Fig. 4.1a), the oxidation wave of the

reduction of spiro-bis-anil is complex. Split oxidative peaks can be seen between -2.1 V to -1.2 V *vs.* SCE. This may due to carbon based protonated surface functionalities. The final product can be not fully protonated due to lack of protons available in dry DMF solvent, therefore, some of the anions can be oxidised back relatively easier. Finally, an oxidative wave can be observed at -0.3 V *vs.* SCE. This can be the reverse peak of first reductive wave and leads to a very slow kinetics as the peak to peak separation is significantly large. The size of the oxidation peak at -0.3 V *vs.* SCE is smaller than the oxidation peak between -1.2 V to -2.1 V *vs.* SCE, and this indicates that the two electron reduction product is relatively more stable than that of the four electron product, without the presence of protons.

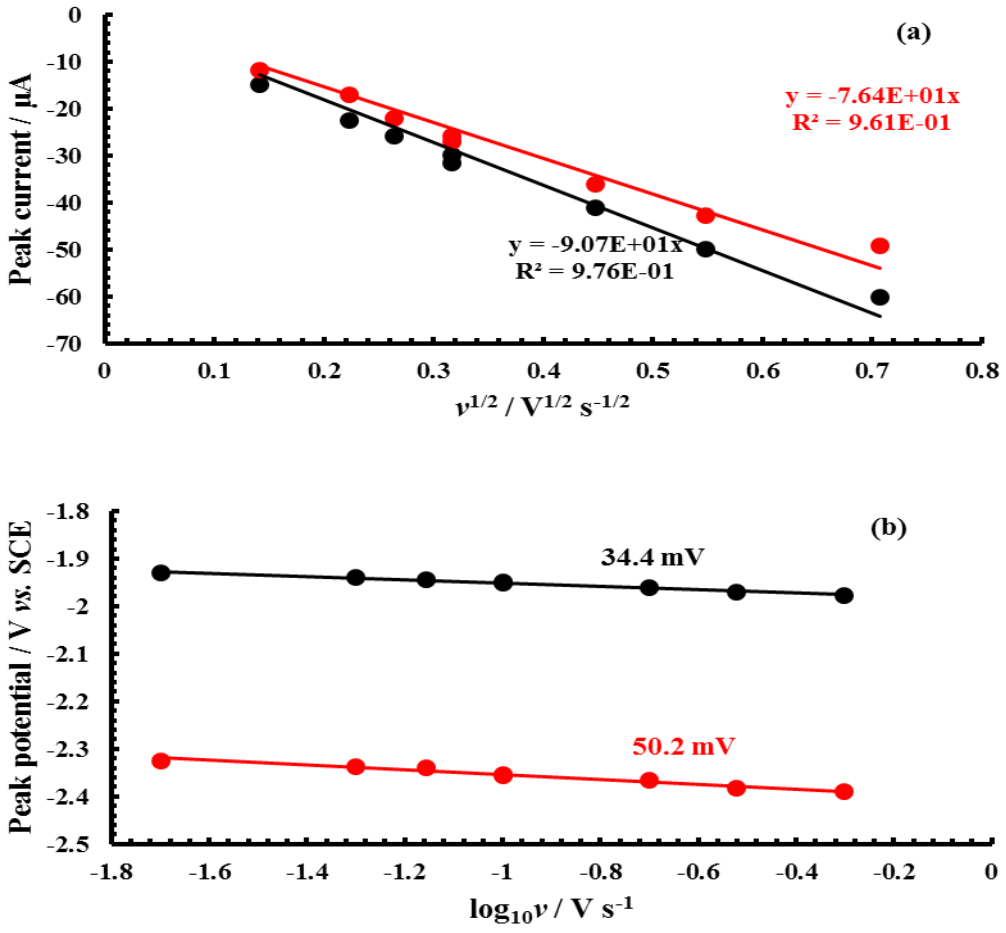

Fig. 4.2. A plot of peak current against square root of scan rate (a) and a plot of peak potential per decade change of scan rate (b) for first reductive peak (black dot) and second reductive peak (red dot) of 0.99 mM spiro-bis-anil, at a glassy carbon macro-electrode (3 mm diameter) in dry DMF with 0.1 M TBAP. A nickel wire was used as counter electrode and a saturated calomel electrode was used as reference electrode. Data obtained from that presented in Fig. 1a.

A plot of peak current against square root of scan rate is shown in Fig. 4.2a. The straight line crossing the origin indicates the electrochemical reduction process is under diffusion control. Due to a complicated and unclear peak in the oxidation wave, observed between -1.2 V to -2.1 V, this analysis was completed. A direct correlation of peak current and square root of san rate can be observed for the oxidation wave at -0.3 V, which indicates the oxidation process is also under diffusion controlled. In order to examine the reversibility of the two reductive peaks, a graph of peak potential against logarithm of scan rate was plotted (Fig. 4.2b). The analysis indicates that both of the first and second reductive peak are electrochemical irreversible. A 34.4 mV slope was observed for the first reductive wave indicates a first order ECE or DISP1 process.

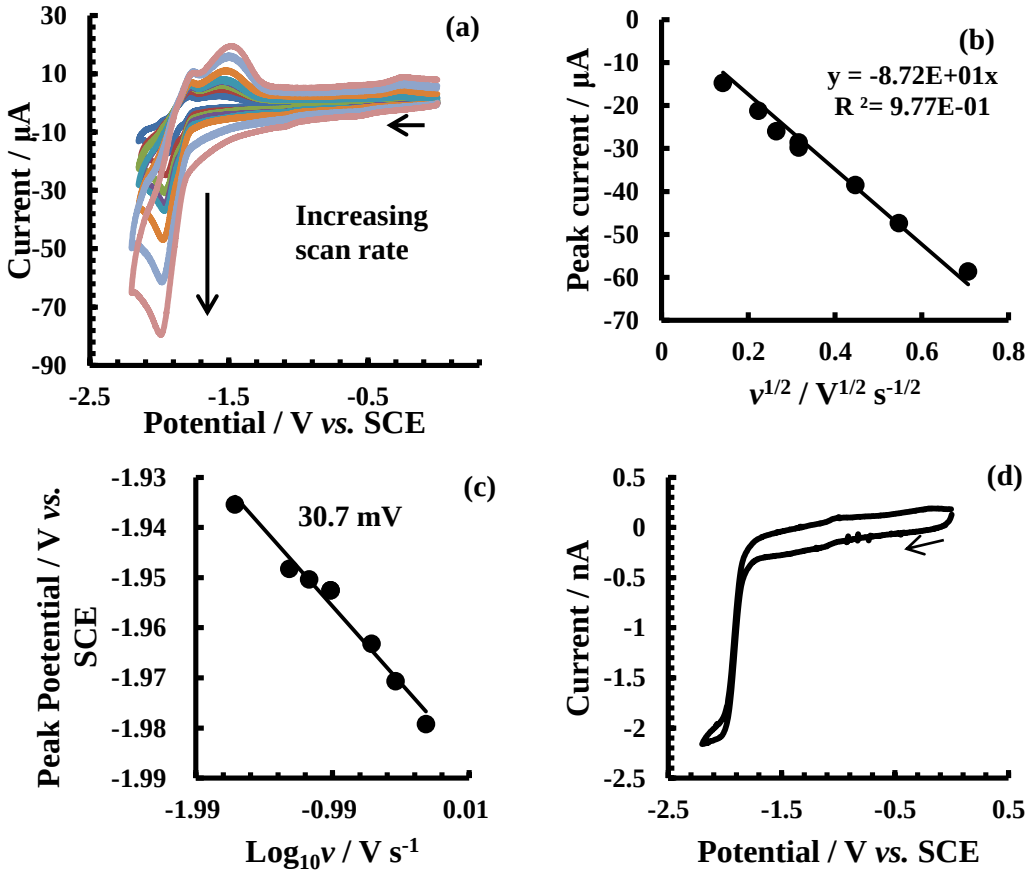

Fig. 4.3. (a) Cyclic voltammogram of electrochemical reduction of 0.99 mM spiro-bis-anil at (a) a glassy carbon macro-electrode (3 mm diameter) or (d) a carbon fibre microelectrode (11 µm diameter) in dry DMF with 0.1 M TBAP. First reductive peak only. Variable scan rates were carried out in the experiment (0.02 V $s^{-1} \leq v \leq$ 0.5 V s^{-1}). (b) a corresponding plot of peak current against square root of scan rates for the first reductive peak. (c) a corresponding plot of peak potential against decade change of scan rates. A nickel wire was used as a counter electrode and a saturated calomel electrode was used as a reference electrode.

As mentioned previously, the reduction of bis-anil can lead to a 4 electron transfer reaction. The reduction peaks shown in Fig. 4.1 are of a similar size, suggesting that the reductions could be two two-electron processes (2 in each wave). In order to understand the first two electron transfer processes, and confirm the two electron process, an experiment was carried out only investigating the first reductive peak only (Fig. 4.3).

It can be seen from Fig. 4.3a, a shoulder was observed in the reductive wave at slower sweep rate, which has the same observation in Fig. 4.1. This can be due to the two electron transfer process. As the electron transfer process is followed by a proton transfer, the proton transfer is difficult in dry-DMF, the second electron transfer can be slowed. In addition, larger time scale allows the molecule to rearrange itself in order to minimise the potential energy, therefore the intermediate, which is formed after the first electron transfer can be relatively more stable after the rearrangement. Similar phenomena can be observed for the second reductive peak. Two oxidative peaks can also be observed in Fig. 4.3a, these peaks could be due to the reverse peak of the two electron transfer reduction. It can be observed that the first oxidative peak (at -1.8 V) is smaller than the second (at -1.5 V), we propose this is due to the two electron reduction product (intermediate in the case of four electron transfer) is relatively more stable than that of the one electron cation radical. Peak current against square root of scan rate and peak potential against logarithm of scan rate is plotted and indicates that the two electron transfer process is controlled by diffusion and electrochemically irreversible. Again, 30.7 mV per decade change of peak potential indicates the first reduction wave follows an ECE or DISP1 reaction pathway.

4.2.3. Electrochemical reduction of 2,3-Diphenyl-1,4-diazaspiro [4.5]- deca-1,3-diene in wet-dimethylformamide

In order to reduce the concern, regarding the role played by carbon-based protonated

surface-functionalities, and enhance voltammetric reproducibility, a mixture of water and DMF was sued as a solvent in the ratio 1:9, respectively. The presence of water provides a large amount of proton source to the system so that the protonation of reduced imine should become more facile. Only the first reductive peak was investigated in DMF/Water mixture initially (Fig. 4.4).

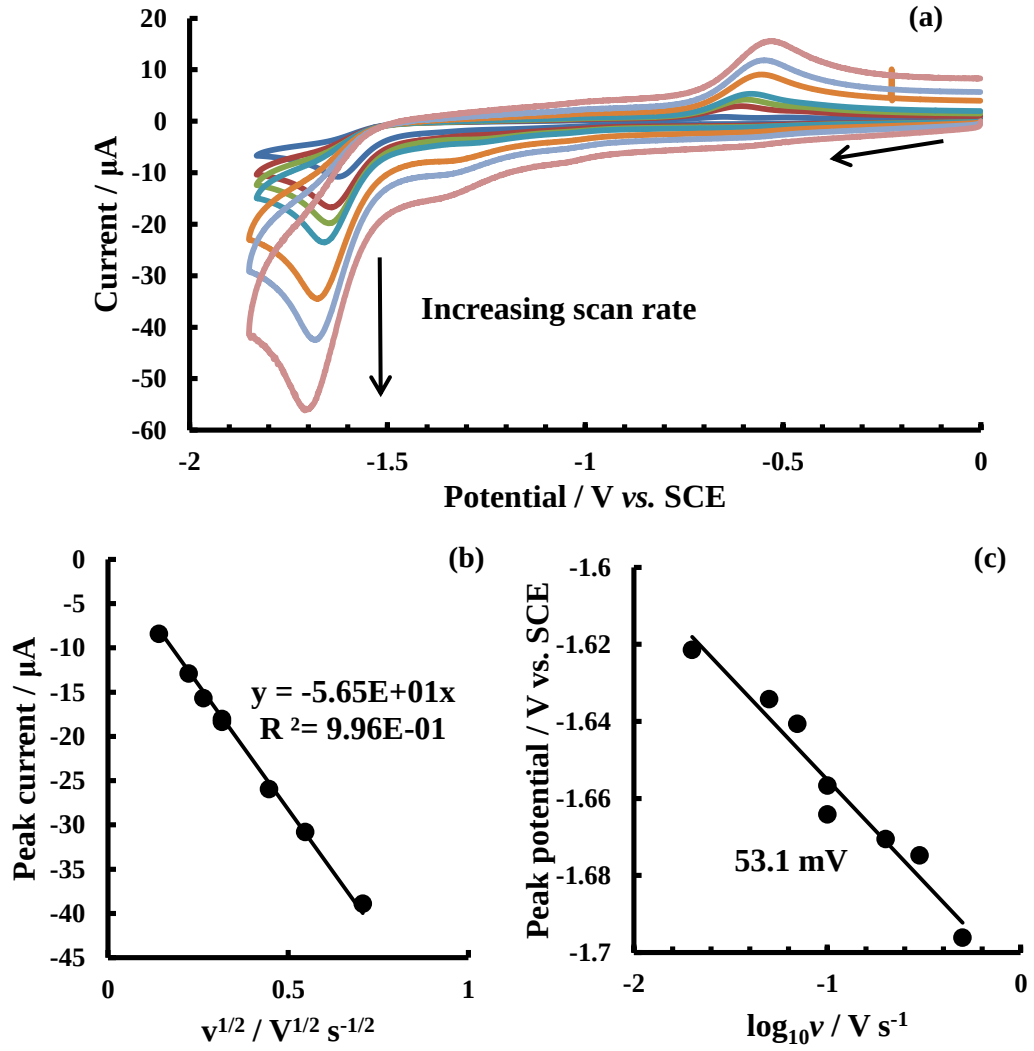

Fig. 4.4. (a) cyclic voltammogram of electrochemical reduction of 0.89 mM spiro-bis-anil at glassy carbon macro-electrode (3 mm diameter) in DMF/Water mixture (ratio of 9:1) with 0.1 M TBAP. First reductive peak only. Variable scan rates were carried out in the experiment (0.02 V $s^{-1} \leq \nu \leq$ 0.5 V s^{-1}). (b) a corresponding plot of peak current against square root of scan rates for the first reductive peak. (c) a corresponding plot of peak potential against decade change of scan rates. A nickel wire was used as a counter electrode and a saturated calomel electrode was used as a reference electrode.

Fig. 4.4a shows the voltammetry of spiro-bis-anil (0.88 mM). Comparing the cyclic voltammetry with those measured in dry DMF, the shoulder of the reductive peaks at

slow scan rate has disappeared in the DMF/Water mixture. This indicates the protonation is favoured by adding water into the system and the second electron transfer can take place rapidly after protonation. It also suggests that the anion radical is relatively more stable than its protonated form. Therefore, this observation suggests that the electron transfer process for the first reductive peak is stepwise and the second electron transfer can only occur after protonation. Additionally, the reverse peaks that are observed at -1.8 V and -1.5 V in dry DMF have also disappeared in Fig. 4.4a and an increased oxidative peak can be detected at approximately -0.5 V. This suggests that the oxidation of cation radical is no longer stable in DMF/Water mixture solvent and can be protonated straight away after been reduced. The oxidation peak at approximately -0.5 V could, therefore, be the oxidation peak of di-imine (chemical **3** in Scheme 4.2). The plot of peak current against square root of scan rate (Fig. 4.4b) indicates the reduction process is controlled by diffusion again, but the slope gives slightly different values due to the change of symmetry factor which caused by the change of the electron transfer kinetics, as the kinetics are complicated in dry DMF solvent. The same reason also causes the slope change of peak potential per decade change of scan rate.

The second reductive peak was subsequently studied. Again, the shoulder on the second reductive peak disappears when performed in the presence of protons, the same as the first peak. This observation can be found in Fig. 4.5a. In addition, the second reductive peak shifts to more negative potential compare to that of in dry-DMF. The elimination of reverse peak (first wave) and shift in potential were also been observed by Andrieux and Savéant[128] for imine electrochemical reduction. Furthermore, both voltammetric waves suffer sluggish heterogeneous kinetics as E_p-$E_{p/2} \neq 55.6/n$, although the data have not been corrected for Ohmic losses, which can be important in high scan rates. This suggests that, if both waves involve a two electron process, where the transfer of the first of these in each case is kinetically slow.

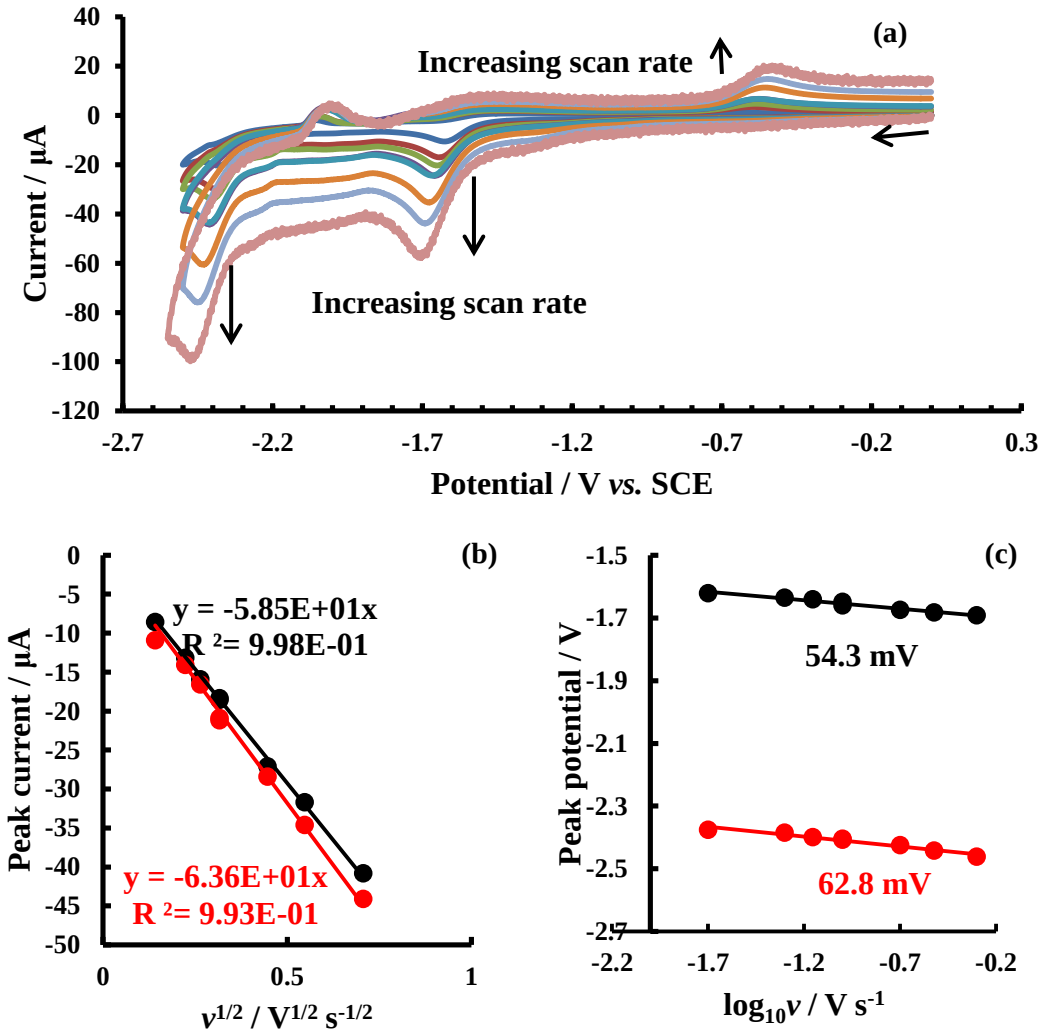

Fig. 4.5. (a) cyclic voltammogram of electrochemical reduction of 0.89 mM spiro-bis-anil at glassy carbon macro-electrode (3 mm diameter) in DMF/Water mixture (ratio of 9:1) with 0.1 M TBAP. Variable scan rates were carried out in the experiment (0.02 V s^{-1} ≤ v ≤ 0.5 V s^{-1}). (b) a corresponding plot of peak current against square root of scan rates for the first reductive peak. (c) a corresponding plot of peak potential against decade change of scan rates. A nickel wire was used as a counter electrode and a saturated calomel electrode was used as a reference electrode.

Furthermore, variable concentrations of SBA were studied in DMF/Water (ratio of 9:1) mixture using both macro- and microelectrodes. With fixed scan rate, *i.e.* 0.1 V s^{-1}, the peak current increase with increasing concentration. The peak current doubled magnitude with doubled concentrations shows that the reaction is first order. Slight shift towards negative potential with higher concentrations on both peaks illustrates the slow kinetics. The macro- and microelectrode behaviour with variable concentrations is illustrated in Fig. 4.6.

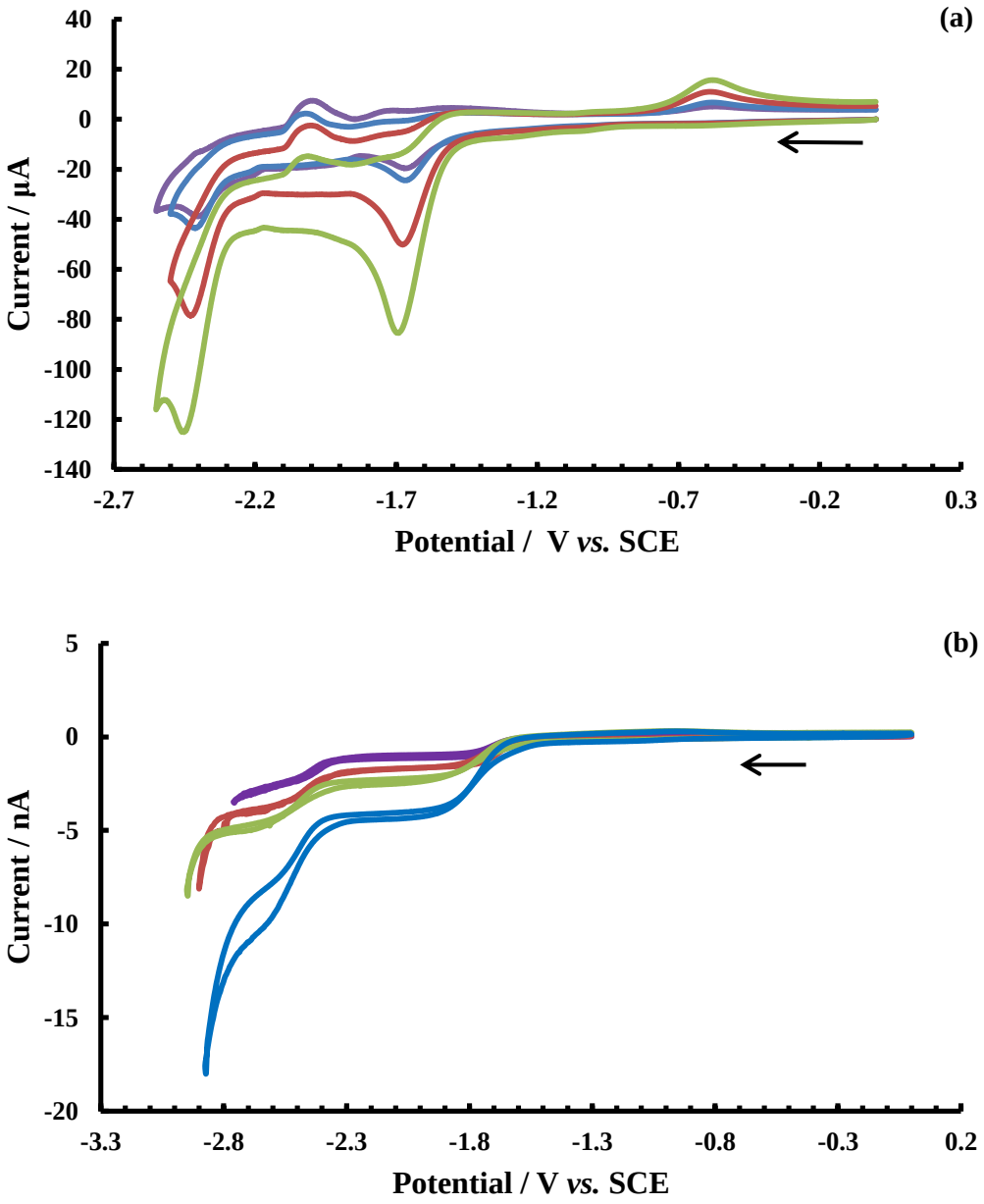

Fig. 4.6. Cyclic voltammetry of 0.58 mM (purple), 0.89 mM (blue), 2.02 mM (red) and 3.75 mM (green) spiro-bis-anil reduction in DMF/Water mixture (9:1) at 3 mm diameter glassy carbon electrode (a) or 11 µm carbon fibre electrode (b) with 0.1 M TBAP. Scan rate = 0.1 V s^{-1}. A nickel wire was used as a counter electrode and a saturated calomel electrode was used as a reference electrode.

In addition, short investigations of spiro-bis-anil reduction were also carried out in acetonitrile, THF as well as DMF/Water mixture with a ratio of 8:2. The second reductive peak was split into two in acetonitrile, which indicates the electron transfer of the fourth electron is relatively difficult than in DMF/Water or pure DMF, this is due to the shortage of proton in pure acetonitrile as DMF adsorbs water slightly more

than acetonitrile. The attempt in THF was also carried out but the result is not ideal (no well-defined waves were observed).

4.2.4. Chronoampermetry analysis of 2,3-Diphenyl-1,4-diazaspiro [4.5]- deca-1,3-diene reduction

Microelectrode chronoampermetry[135] was employed in order to determine the diffusion coefficient of SBA (D) and the number of moles of electrons transferred heterogeneously per mole of SBA (n) for both redox waves, as the Randles-Sevčik equation contains two variables (D and n) in a reversible system and the transfer coefficient can be included in an irreversible system. This method was described in the Introduction, briefly, the dimensionless experimental current, $f(\tau) = \psi_{exp} = \frac{i}{4nFDrc_0}$ and the theoretical dimensionless current, $f(\tau) = \psi_{thy} = 0.7854 + 0.8862\tau^{1/2} + 0.214\exp(-\frac{0.7823}{\sqrt{\tau}})$, with a dimensionless variable, $\tau = \frac{4Dt}{r^2}$, are fitted by varying D and n, and the fitting is shown in Fig. 4.7.

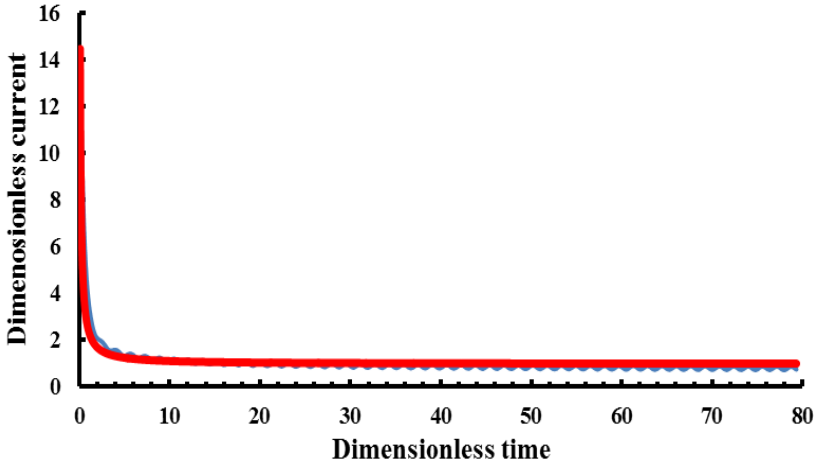

Fig. 4.7. Dimensionless current fitting of 0.89 mM of Spiro-bis-anil in DMF/Water mixture (9:1) with 0.1 M TBAP. Carbon fibre microelectrode was applied (11μm diameter). Blue line: ψ_{exp}; red line: ψ_{thy}.

Accordingly to the fitting process, the first wave was determined as a two electron transfer process with n=2.0 ± 0.02 to form the enamine, and four electron transfer process with the second wave, n = 4.0 ± 0.01. Both diffusion coefficients were determine as D = 4.2 ± 1.4 x 10^{-6} cm^2 s^{-1}.

4.2.5. Overall analysis

According to the cyclic voltammetry and chronoamperometry data, it can be concluded that the reaction is under the control of the electron transfer process with 2 two electron waves observed in all solvent systems at slow sweep rate. The rates determine steps were found to be the first and third electron transfer due to the merged two electron transfer process in each reductive wave. Similar observation has been discovered for carbonyl reduction[136]. Since there is no significant dependence of the voltammetry on the concentration of spiro-bis-anil, the second order processes are unlikely, therefore the both waves could follow ECE-C or DISP1-C reaction pathways. They could not be distinguished as there was neither iR compensation undertaken nor enamine synthesis[137]. Given that the half peak width for both waves is 23.4/α mV, the Bulter-Volmer symmetry factor can be worked out and can be employed in the expression of the peak current equation:

$$i_p = 4.2553 c_0 \sqrt{\alpha} \sqrt{Dv} \qquad \text{(Eqn. 4.1)}$$

Thus the diffusion coefficient can be determined for each solvent system[138]. Table 1 summarised the analysed data.

Consequently, since the physical properties and concentrations of electrolyte can change the viscosity of the system, comment on the data is practically difficult unless they appear to be reasonable.

Table 4.1. Peak potential and current characteristics of the cyclic voltammograms for the electrochemical reduction of the spiro-bis-anil, **1**, at a 3 mm diameter glassy carbon electrode. Notes: I represents the first peak and II refers to the second peak; N/D means values not determined. In the comments, slow refers to electrode kinetic control, first order refers to control by homogeneous kinetics and Ohmic refers to significant presence of iR loss. D^{av} is the arithmetic average diffusion coefficient determined using microdisc chronoamperometry; D^{est} represents the diffusion coefficients determined using estimations of the symemetry factor under the assumption of slow electrode kinetics; D^{WC} indicates the Wilke-Chang estimation of diffusion coefficient[140].

Solvents and concentrations	$-\frac{\partial E_p^I}{\partial lgv}$ / mV decade^{-1}	$E_p^I - E_{p/2}^I$ / mV	$-\frac{10^5}{c_0}\frac{\partial i_p^I}{\partial \sqrt{v}}$ A V$^{-1/2}$ s$^{1/2}$ (mM)$^{-1}$	$-\frac{\partial E_p^{II}}{\partial lgv}$ / mV decade^{-1}	$E_p^{II} - E_{p/2}^{II}$ / mV	$-\frac{10^5}{c_0}\frac{\partial i_p^I}{\partial \sqrt{v}}$ A V$^{-1/2}$ s$^{1/2}$ (mM)$^{-1}$	Comments
Dry DMF *0.1 M TBAP* c_0=0.99 mM	32.5 ±2.6	78.9 ±7.2	8.96 ±0.25	50.2 ±3.2	44.7 ±6.6	7.27 ±0.60	Slow or first order; probably slow; D^{WC}=5.5x10^{-6} cm^2 s^{-1} D^{av}=5.1 ±1.3x10^{-6} cm^2 s^{-1} D^{est}=1.0 ±0.5x10^{-5} cm^2 s^{-1}
DMF *0.1 M TBABF* c_0=1.98 mM	52.4 ±1.4	73.2 ±12.4	6.64 ±0.09	70.2 ±4.0	64.2 ±10.2	5.63 ±0.09	α_I=0.30±0.03; α_{II}=0.52 ±0.09; Slow or first order; probably slow; D^{est}=6.2 ±1.4x10^{-6} cm^2 s^{-1}
DMF/Water (9:1) *0.1 M TBAP* 0.58 mM≤c_0≤3.75 mM	65.0 ±1.8	80.0 ±10.7	6.71 ±0.62	77 ±2.5	63.9 ±9.4	7.04 ±0.69	α_I=0.32±0.05; α_{II}=0.36 ±0.05; Slow; D^{av}=4.2 ±1.4x10^{-6} cm^2 s^{-1} D^{est}=8.0 ± 0.6x10^{-6} cm^2 s^{-1}
DMF/Water (8:2) *0.1 M TBAP* c_0=2.00 mM	99.3 ±5.2	N/D	5.07 ±0.17	130.1 ±4.8	N/D	4.29 ±0.54	α_I=0.29±0.04; α_{II}=0.37 ±0.06; Slow
MeCN *0.1 M TBABF* 0.98 mM≤c_0≤3.90 mM	53.5 ±9.3	67.9 ±10.9	10.22 ±2.73	68.3 ±7.5	60.3 ±6.4	N/D	Slow or first order; probably slow; D^{WC}=1.5x10-5 cm^2 s^{-1} D^{est}=1.7 ±1.0x10^{-5} cm^2 s^{-1}
THF *0.5 M TBAP* c_0=2.01 mM	106.0 ±23.5	102.2 ±21.3	5.21 ±0.48	82.6 ±4.4	N/D	N/D	α_I=0.34±0.04; α_{II}=0.39 ±0.04; Slow and ohmic; D^{WC}=1.1x10^{-5} cm^2 s^{-1} D^{est}=6.5 ±1.3x10^{-6} cm^2 s^{-1}
THF *0.1 M Li+ClO4-* c_0=1.01 mM	197	N/D	N/D	226	N/D	N/D	α_I=0.23 ±0.05; Ohmic
THF *0.1 M Li+ClO4-* *and* *0.1 M NH4+Cl-* c_0=1.00 mM	240	N/D	N/D	98. 7	N/D	N/D	Ohmic

In addition, the half peak width of the second reductive wave is slightly smaller than that of the first, this can be due to the formation of the enamine is slower than its consumption, with the first electron transfer limits the overall rate of reduction, there is the possibility of involving structural reorganisation or intrinsically slow proton-electron transfer[139] as a shoulder is observed in dry-DMF solvent.

4.2.6. Birch reduction pathway

The Birch reduction pathway of SBA was further studied on a bench pathway. Briefly, the addition of four equivalents of sodium to the spiro-bis-anil in THF/liquid ammonia afforded four electron transferred product, **2**, in yield of 84%, after work up. The reason of using THF was to prevent reaction within a two phase system, even with lithium[122, 124]. Given that the pK_a of the first one electron reduced species as *ca.* 25, subsequent reduction leads to species more basic than ammonia, and the protonation can occur *in loco* as proton coupled electron processes. Because these are probably more facile to reduce than **1**[129], the enmine ion $\mathbf{3}^-$ is unstable: $\mathbf{3}^- + \mathbf{3}^- + 2H^+ \rightleftarrows \mathbf{1} + \mathbf{2}$. The assumption was proved by ^{1}H-NMR spectroscopy with only **1** and **2** were determined after the Birch reduction of **1** using two sodium equivalents, and reaffirmed that it is more facile to transfer the third and fourth electrons compared with the first two[141].

4.2.7. Conclusion

In conclusion, the electrochemical reduction of 2,3-Diphenyl-1,4-diazaspiro-[4.5]deca-1,3-diene has been successfully carried out in different solvent systems. It involves a four electron transfer in two reduction processes with a two electron reduction intermediate, with the first and third electron transfer limits the rate of reaction. A diffusion coefficient was found to be $4.2 \pm 1.4 \times 10^{-6}$ cm^2 s^{-1} in wet-DMF using micro-disc chronoamperometry, but can vary from 8.0×10^{-6} to 1.5×10^{-5} cm^2

s^{-1} in different solvent systems. Compared with the typical Birch reduction pathway, the electrochemical reduction offers some major benefits such as room temperature condition, wet solvents and accessible two electron intermediates. Whereas, the conventional Birch reduction needs to be carried out in THF/liquid ammonia, and involves the handling of sodium metal, together with inaccessible two electron intermediates.

Electrochemical reduction of vitamin K_1 is a typical proton transfer reactions as the electrochemical reduction of quinones have been extensively studied as mentioned in Section 4.1. Therefore electrochemical reduction of vitamin K_1 with lipid support was subsequently studied.

4.3. Electrochemical reduction of lipid supported vitamin K_1

4.3.1. Introduction

In order to understand the electro-reduction induced protonation reactions, vitamin K_1 (VK_1) was selected to study, due to its well-known electro-reduction properties and reaction mechanisms. In this section, we used lipid supported vitamin K_1 to offer better electrochemical signal.

Vitamins are essential organic materials for life as they play important and unique roles in biochemistry.[142] Vitamins are so special because they cannot be synthesised by animals and can cause variable disease if lack of them[143]. Vitamins can be either hydrophobic (*e.g.* vitamin A, D, and E) or hydrophilic (*e.g.* vitamin B and C).

Although vitamin K has been discovery for over 50 years, it draws less attention than other hydrophobic vitamins. This is because it was recognised that the only therapeutic use is to help the synthesis of plasma clotting proteins. However, in the

past 20 years, vitamin K has been understood more intensively and varies of roles of vitamin K has been discovered.

Vitamin K has chemical structure based on 2-methyl-1,4-naphthoquinone derivatives with an aliphatic side chain in the 3-position (Fig. 4.8). VK_1 is found to be the only important molecular form in plants, whereas VK_2 has variable derivatives based on the number of prenyl units, and can be synthesised by bacteria. It is involved in cellular respiration and in oxidative phosphorylation as an electron carrier[144]. It is also a known blood clotting cofactor[145]. In addition, it can help the bone mass to increase[146].

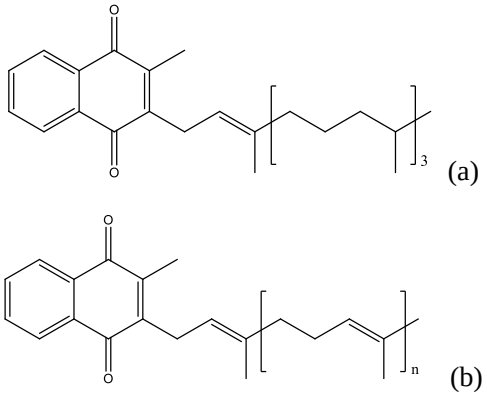

Fig. 4.8. Chemical structures of vitamin K. (a) = vitamin K_1, (b) = vitamin K_2.

Therefore, it is important to understand the electron transfer process of vitamin K in order to understand vitamin K behaviour in biological environments. Studies have been carried out by using polarography[147] and cyclic voltammetry[148, 149] in aqueous and non-aqueous media.

In addition, vitamin K modified electrode can be potentially used as pH sensor[150]. As shown in this research, the change of pH in the local environment can change the redox potential of vitamin K. Unlike the conventional pH meters, VK_1 modified electrode can be no harm for biological systems, especially human organs.

In this project, an electrochemical study of vitamin K_1 was carried out in well buffered condition. Although vitamin K_1 microdroplets has been studied by Wain, *et*

al.[142] supported vitamin K is rarely mentioned in literatures. Previous works done by Halls *et al.*[151] introduced vitamin K dissolved in lyotropic liquid crystals and suggested that vitamin K sits in the organic phase due to its high hydrophobicity. Most recent work by R. Bilewicz *et al.*[10] suggested that VK_1 can be supported by a lipidic cubic mesophase. Therefore in this thesis, the vitamin K_1 was supported by lipids in order to obtain a better understanding of the electron transport process, in an environment that resembled that of a biological system.

4.3.2. Results and discussion

The number of electrons transferred in the redox process per molecule involved can be calculated quantitively by putting a certain amount of reactant onto the BPGE. As BPGE has much larger electroactive surface area than GCE, therefore the accumulation can be ensured that all the reactants accumulated on the electroactive surface on BPGE, not the electro-inactive protection part of the electrode.

Fig. 4.9 shows the voltammogram of VK_1 reduction with 30 μL accumulation of VK_1 solution on BPGE. The modified electrode was then dipped into 1.0 M HCl.

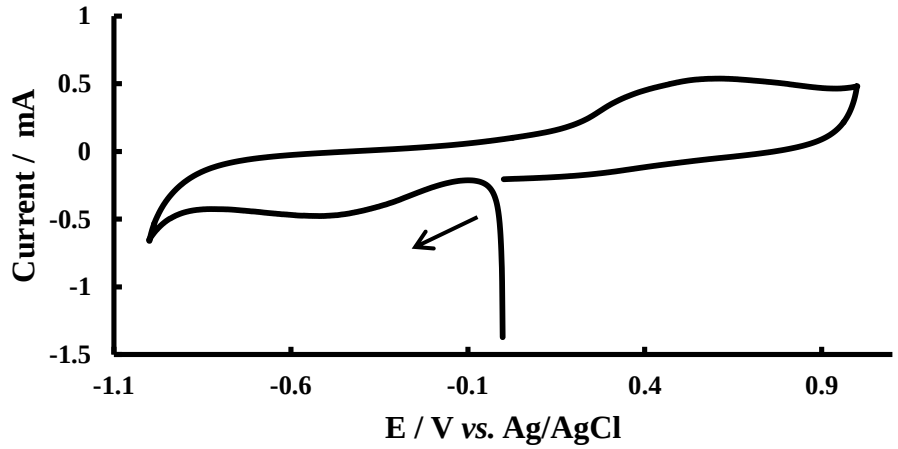

Fig. 4.9. The voltammogram of reduction of VK_1 without lipid in 1.0 M HCl. 30 μL VK_1 was accumulated on BPGE. Scan rate = 0.1 V s^{-1}.

In the voltammogram, the reduction of VK_1 is occurred at approximately -0.5 V and the corresponding oxidative peak appear at approximately +0.5 V. The area

underneath the peak (either oxidation or reduction) in the voltammogram shows the total amount of charge required to perform the overall electrode reaction. The relationship between charge and n is shown in Eqn. 4.2.

$$Q = nNF \qquad \text{(Eqn. 4.2)}$$

Where Q is charge in C, n is the number of electrons transferred, N is the number of moles of reactant and F is the Faraday's Constant (96484.6 C mol^{-1}). The integration of the reductive peak shows the charge is 5.610 X 10^{-3} C. Therefore n can be worked out as 1.88, which is close to 2 electrons.

After the number of electrons was worked out, the experiment was then moved on to GCE rather than BPGE. The solution, which performing the electrochemistry was changed to Britton-Robinson Buffer (BRB) solution in order to obtain data in variable pH. And the vitamin K_1 was supported by LC lipid.

10 µL of vitamin K_1 with lipid solution was accumulated on the surface of GCE electrode. The modified electrode was then dipped into BRB solution with variable pH values. Fig. 4.10 shows the voltammogram of reduction of VK_1 with lipid in pH 2 BRB solution.

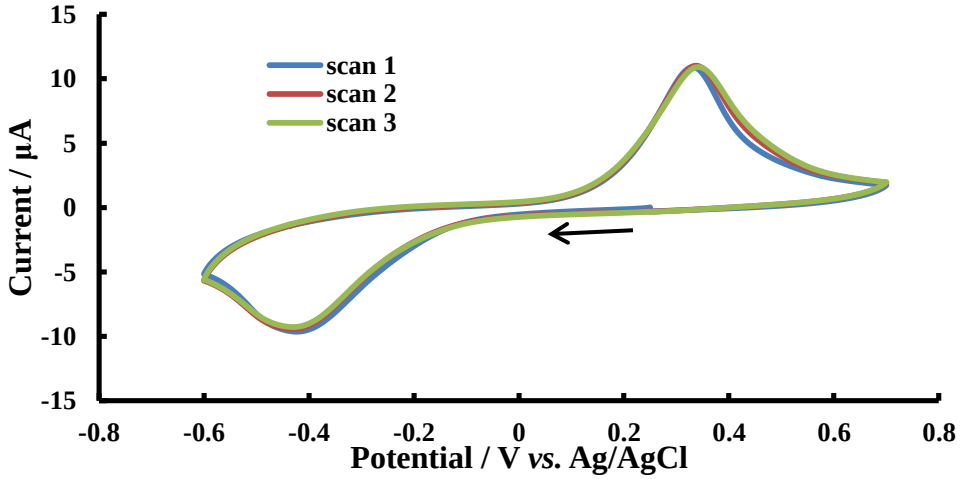

Fig. 4.10 Voltammogram of reduction of VK_1 with lipid in BRB solution in pH 2. VK_1/lipid was accumulated on GCE. Scan rate = 0.1 V s^{-1}.

Repetitive cycling as shown in Fig. 4.10, showed no change in response. The peak potential and peak current stays same as scan 1, suggesting there is no material lost on the electrode during the experiment.

A plot of logarithm of peak current against the logarithm of scan rate is shown in Fig. 4.11 for reduction of VK_1/lipid on GCE in BRB solution at pH 2.

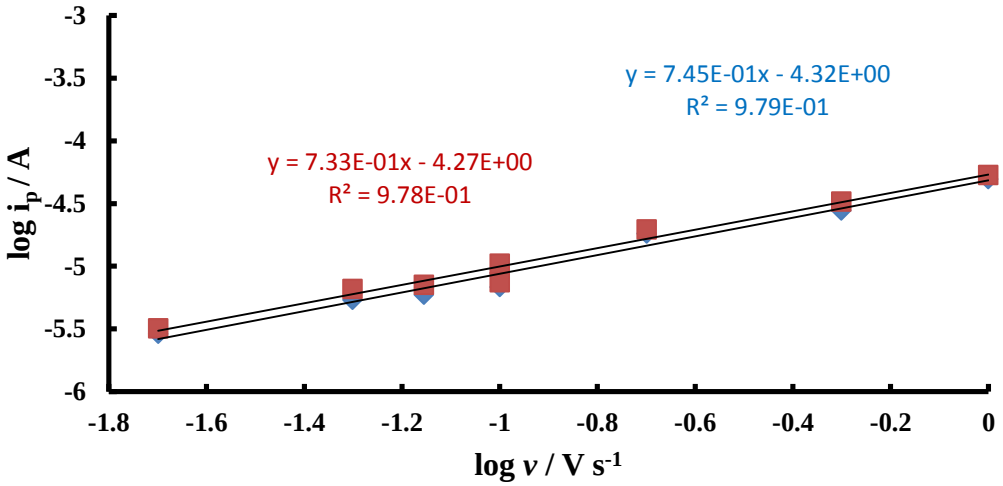

Fig. 4.11. A plot of logarithm of peak current against logarithm of scan rates. Blue: Reduction, Red: Oxidation.

The linearity of the plot in Fig. 4.11 represents the redox process on the electrode is not under diffusion controlled, which indicates the reduction of VK_1/lipid is adsorbed on the electrode surface. And both reduction and oxidation gives almost identical gradient suggesting that there is no material lost in the reverse scan.

A plot of E_p against logarithm of scan rate for the above condition is shown in Fig. 4.12. As shown in the graph, there is a slope for both reduction and oxidation peaks suggests that the process is electrochemically irreversible. The dependence becomes more obvious at scan rates above 0.1 V s^{-1}. As the scan rates getting slower, the process becomes more likely electrochemically reversible.

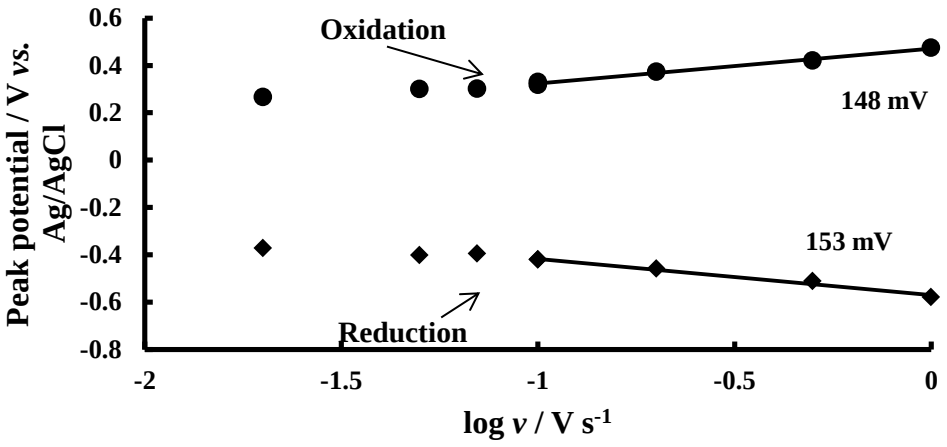

Fig. 4.12. A plot of peak potential against logarithm of scan rates. pH 2.

The reduction of VK_1/lipid was then carried out in different pH values; the voltammogram for this is shown in Fig. 4.13.

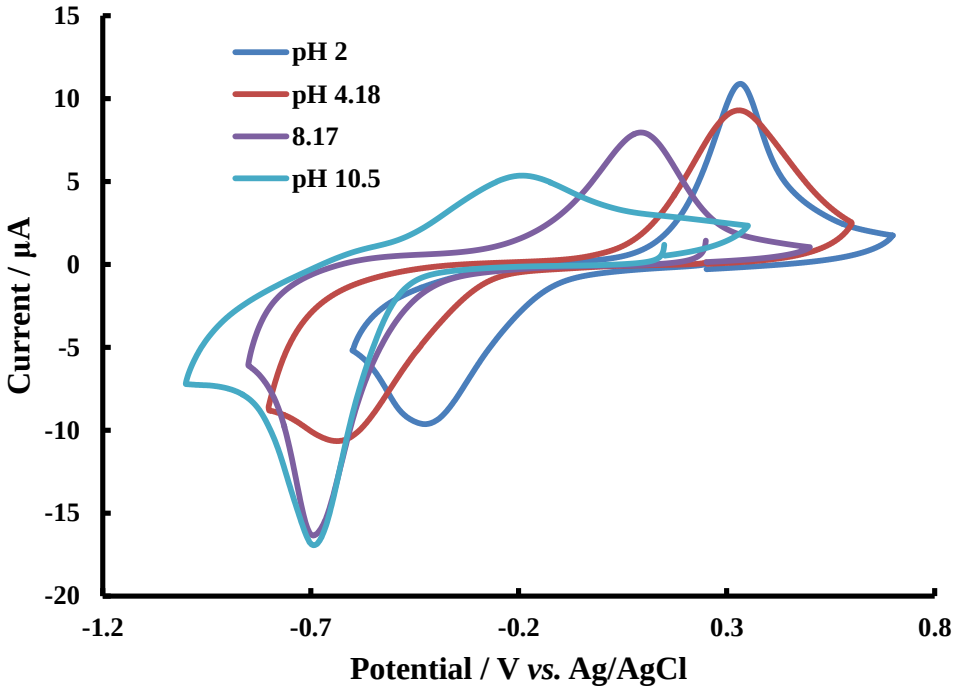

Fig. 4.13. The voltammogram of reduction of VK1/lipid on GCE in BRB solution in different pH values.

Clearly, as the pH increase, the reductive peak moves towards more negatively, similar phenomena shows in the corresponding oxidative peak. This indicating the reduction of VK_1 becomes harder to be reduced as increase the pH. Notably, when pH

increases from 2 to 4.8, the reductive peak shifts towards negative dramatically whereas the corresponding oxidative peak almost stays in the same potential; and from pH 8.17 to pH 10.5, the reductive peak stays unchanged but the corresponding oxidative wave shifts towards negative dramatically. This phenomenon is illustrated by plotting E_p against pH, shown in Fig. 4.14.

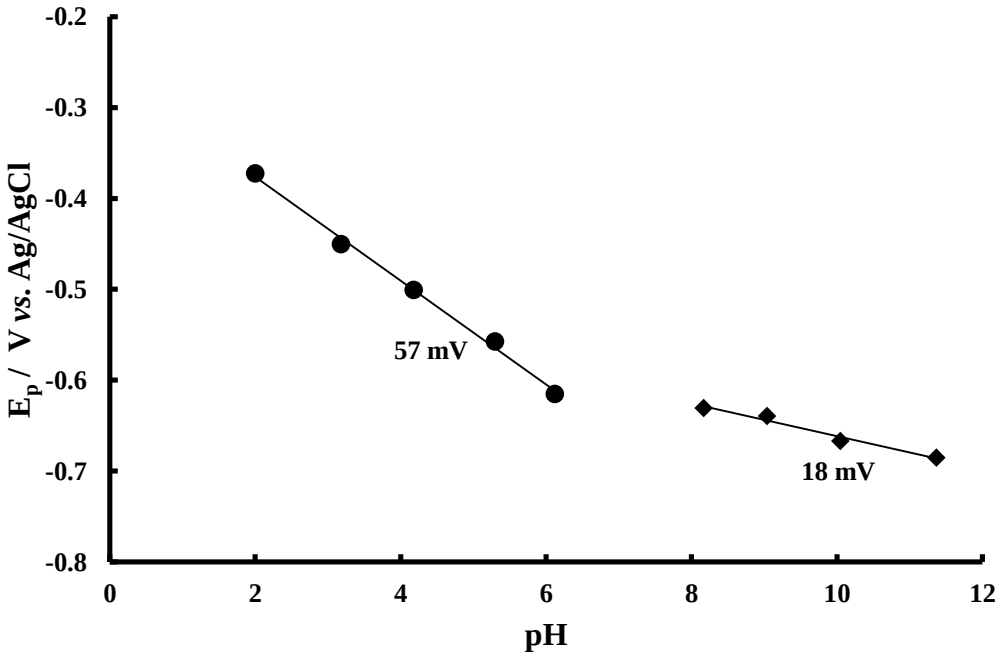

Fig. 4.14. A plot of E_p against pH. E_p was obtained from 0.02 V s^{-1}.

The peak potentials used in Fig. 4.14 are all the reductive peak potentials at scan rate 0.02 V s^{-1} which is the most close scan rate for a reversible process as shown in Fig. 5.5. According to the Nernst equation for reversible cases[152, 153], as shown in Fig. 4.12, below pH 6.12, $\partial E_p/\partial pH$ = -57 mV, suggests the formation of H_2VK_1 by reduction of VK_1 via two proton (2 H^+) two electron (2 e^-)process. And when pH values above 8, the $\partial E_p/\partial pH$ gives 18 mV suggests the process becomes one proton, two electron transfer process. The mechanism can be described with these data (Scheme 4.5).

Therefore in acidic environment (pH below 6.12), as there is an excessive protons in the solution, the reduced VK_1 is easily protonated, whereas in basic environment,

there is lack of protons in the solution leads the reduced VK_1 harder to be protonated. Similar effects were also observed by Wain *et al.*[142]

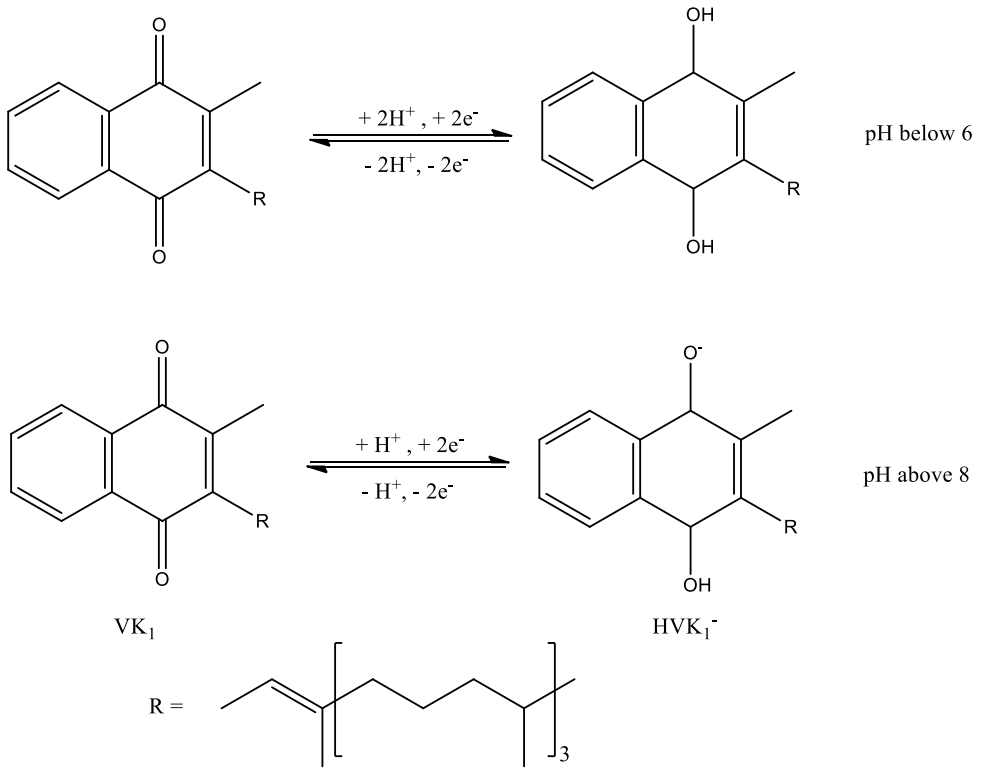

Scheme 4.5. Reaction pathway of vitamin K_1.

4.3.3. Conclusion

In conclusion, the LC supported VK_1 was accumulated on both BPGE and GCE successfully. The continuous scan shows there is no material loses on the surface of the electrodes. The reduction of VK_1 with supported by lipid is understood in buffered solution. The reduction undergoes a two proton, two electron transfer process in acidic conditions (pH below 6.12) and a one proton, two electron transfer process in basic conditions (pH above 8).

Electrochemically induced deprotonation is other point of interest. The oxidation of sudan dyes causes the depronation to take place, therefore electrochemical oxidation of Sudan III was characterised.

4.4. Electrochemical study of Sudan III

4.4.1. Introduction

Sudan dyes are widely used in chemical industries, household commodities, textile, leather, waxes, plastics, and wood industries for colouring materials[154, 155]. Sudan dyes mainly involve sudan I, sudan II, sudan III and sudan IV. Fig. 4.15 shows the structures for these sudan dyes. Most of the literatures focused on the determination of sudan dyes[154-158] because they are currently added into food like chilli powder for colouring. However, very little has been published to describe the mechanism for the oxidation of Sudan dyes.

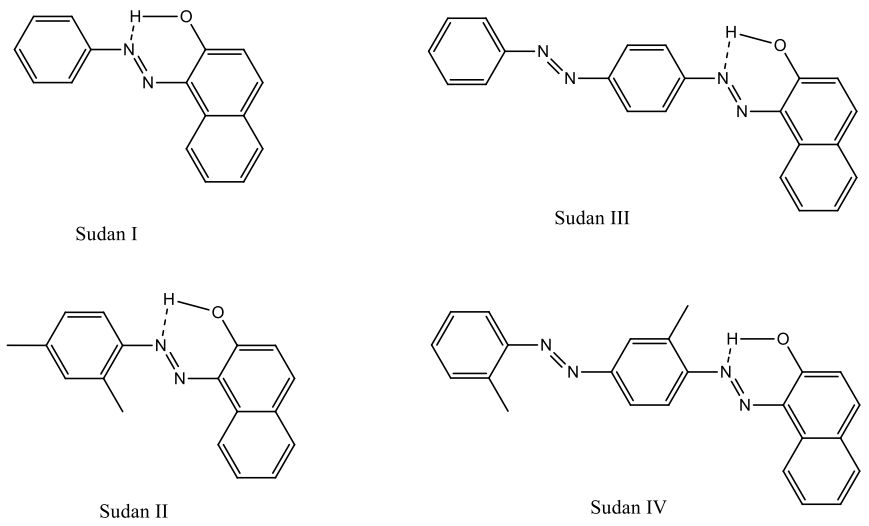

Fig. 4.15. Chemical structures of Sudan dyes.

Sudan dyes have a common 2-naphthol group. According to the literature[159], the oxidation of 2-naphthol leads to a proton release. Therefore the other aim of this project is to prove there is a proton release during the oxidation process. Sudan III was used in this project.

In addition, there is hydrogen bonding between the –OH group and the nitrogen (as shown in dashed line in Fig. 4.15). Therefore tautomerisation process can occur.

4.4.2. Results and discussion

5 µL of 10 mM sudan III solution was accumulated on the GCE, the cyclic voltammetry was first applied for the oxidation of Sudan III in pH 7. Fig. 4.16 shows a voltammogram of sudan III oxidation.

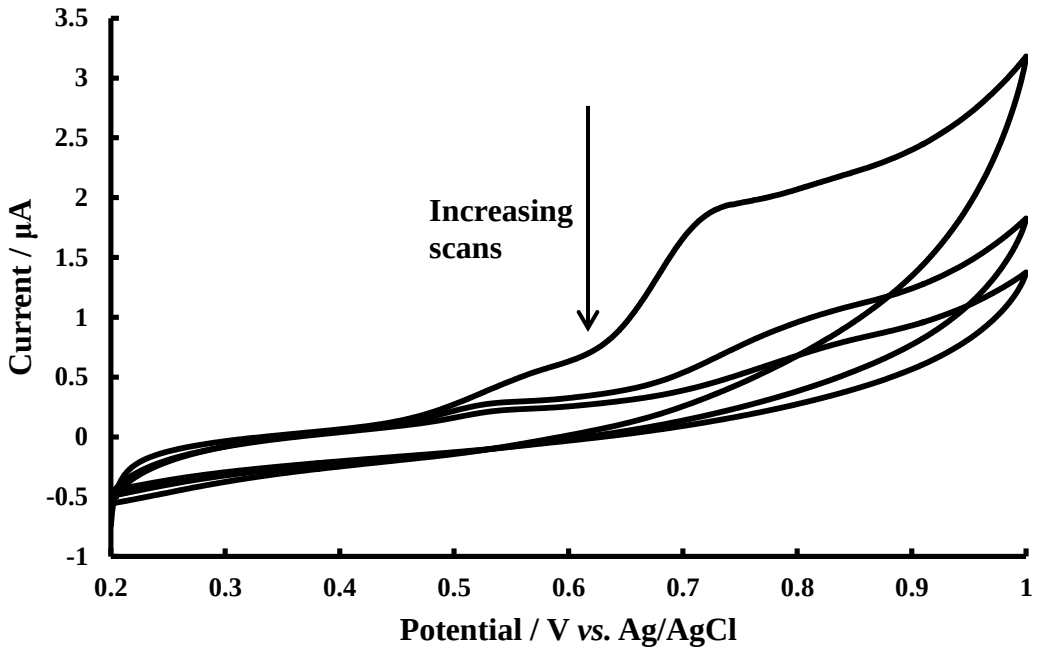

Fig. 4.16. Cyclic voltammogram of oxidation of Sudan III in PBES at pH 7. Scan rate = 0.1 V s^{-1}. Glassy carbon electrode used as working electrode.

As the number of scans increase, the oxidative current decreases. This indicates that there is a loss of material during the experiment. Based on to Panizza *et al.* work on oxidation of 2-naphthol[159], this can be due to the release of proton. On the other hand, the electrochemical oxidation of Sudan III introduces charge on the molecule, which consequently causes dissolution.

Then the cyclic voltammogram of oxidation of sudan III in phosphate buffer solution in variable pH was carried out, as shown in Fig. 4.17.

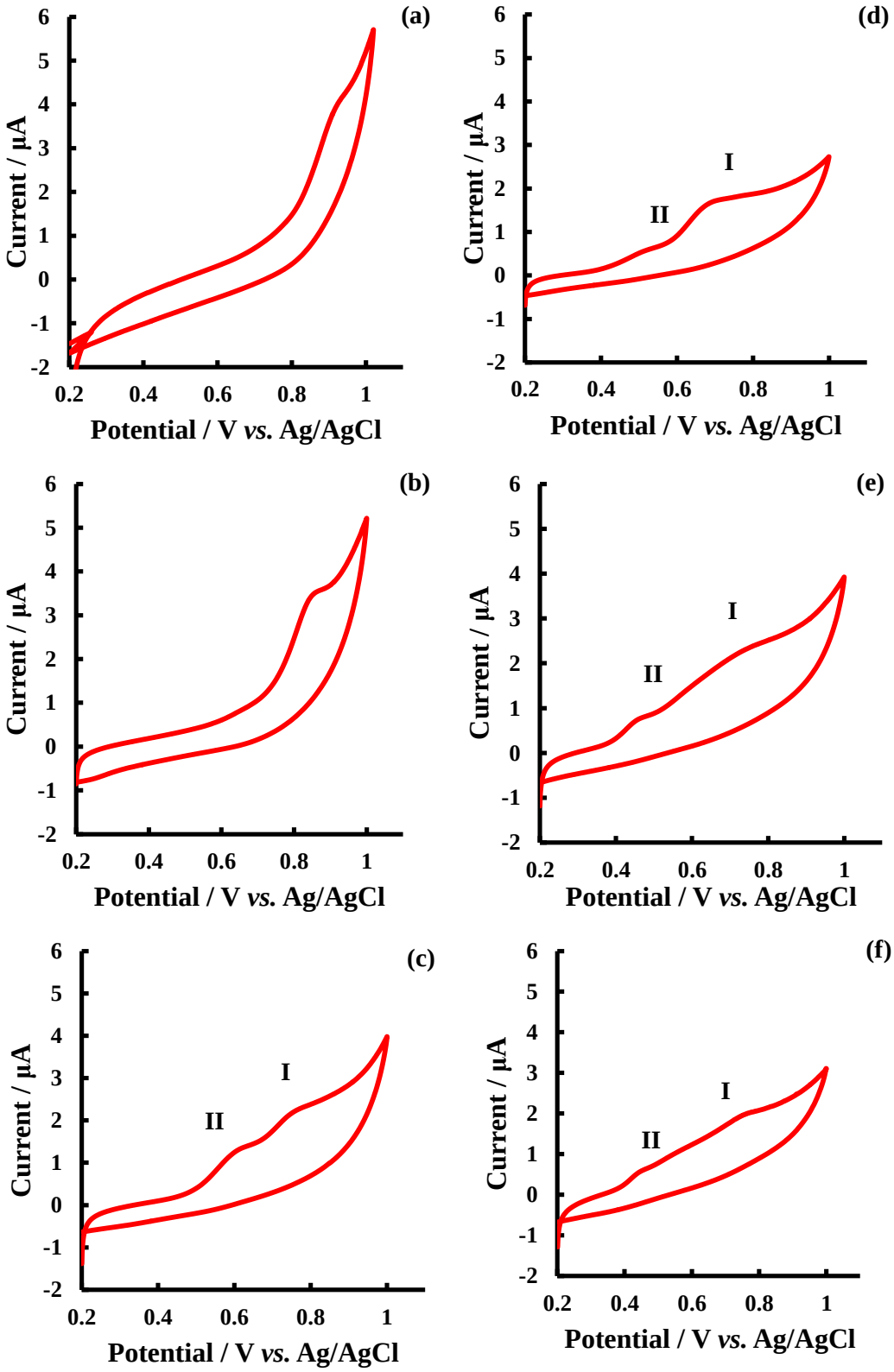

Fig. 4.17. Cyclic voltammetry of oxidation of Sudan III with pH 2.08 (a), pH 4.44 (b), pH 6.67 (c), pH 8.03 (d), pH 9.23 (e), pH 10.07 (f). Scan rate taken at 100 mV s^{-1}. A spiral nickel wire served as a counter electrode and saturated calomel electrode was served as the reference electrode.

According to the voltammogram, at lower pH (pH 2.08 to pH 6.67), there is only one

oxidative peak at approximately +0.9 V and shift more negatively as increase the pH. At higher pH (pH 6.67 or above), the oxidative peak split into two oxidative peaks with continuing shifting toward negative. This suggests that there is a two electron oxidation, which can be separated at high pH values. This will be discussed in further detail later on.

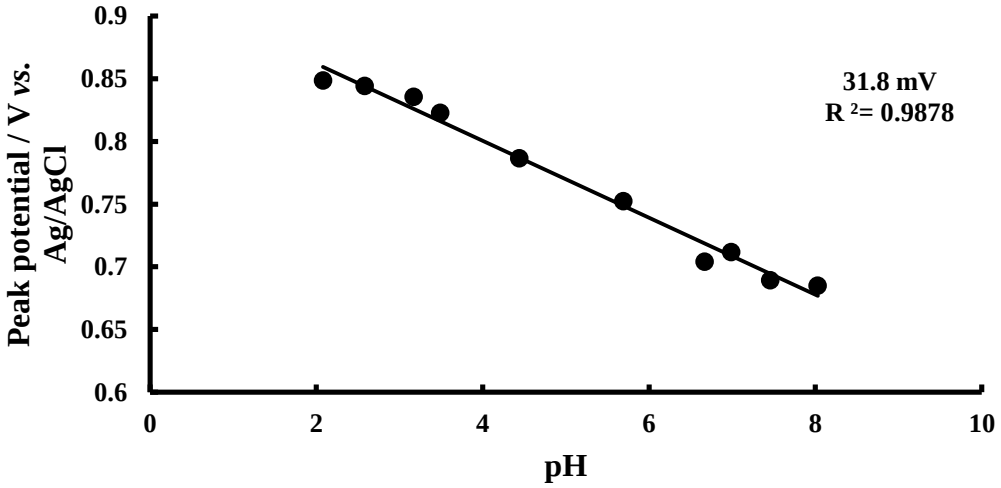

Fig. 4.17. A plot of Ep *vs.* pH of oxidation peak I at 10 mV s^{-1} scan rate.

The plot of E_p *vs.* pH at pH below 8 gives linear dependence with a slope of 31.5 mV (Fig. 4.17). A manipulation of the Nernst Equation gives that the observed redox potential change of m/n(59 mV) per pH, for an m H^+ and n e^- redox process. Therefore in this case, the redox process can be one proton two electron transfer process.

At pH above 9.23, the peak potential is nearly has no dependence on pH, suggesting that there is no proton transfer process during the electrochemical reduction. This can be due to the deprotonation process that happens before the electron transfer process as in basic condition.

Therefore the reaction can be suggested as:

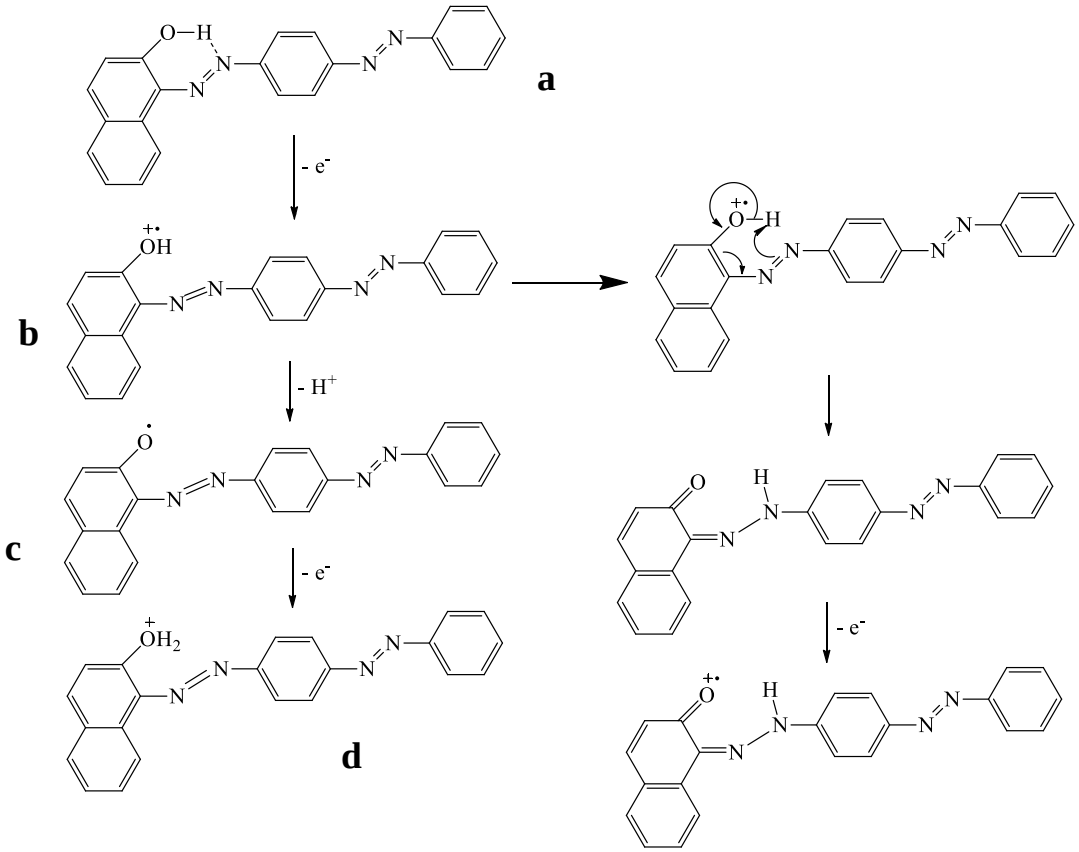

Scheme 4.6. Reaction pathway of Sudan III.

As shown in the voltammogram (Fig. 4.17), when pH below 8.3, the strong acidic environment makes **a**/**b** redox stabilises **a** with the excess of proton source. The deprotonation process happens after the first electron transfer process, **a**/**b**. When pH above 9.23, the strong basic environment readily deprotonates a before the first electron transfer process, therefore there is no dependence observed between peak potential and pH. As the plot of peak potential versus pH at slow scan rate (in the reversible regime) gives a slope of 31.8 mV, suggests that the process is two-electron-one-proton transfer reaction, therefore **c**/**d** redox couple is suggested.

On the other hand, an intramolecular tautomerisation can also occur (righ-hand-side route in Scheme 4.6). Without loss of hydrogen, the hydrogen atom on the –OH group can be transferred to nitrogen (*viz.* N-H bond is stronger than O-H bond). The intramolecular proton transfer may show some dependence between peak potential and pH change. Therefore both routes are possible, with the left-hand-side route more

likely.

There is no reverse peak seen from the voltammogram suggesting that the product **d** either further hydrolysed, or forms couple with –OH group in higher pH; or, tautomerisation occurs (right-hand-side route) with a relatively more stable N-H bond.

4.4.3. Conclusion

In conclusion, the oxidation of sudan III leads to either a deprotonation process or an intramolecular tautomerisation process. The former process involves 2 electrons and 1 proton transfer. The experiment suggested the reaction mechanism and suggesting the deprotonation step (**b** to **c** in Scheme 4.6) is relatively slower than the electron-transfer process. Hydrogen ions are released by the oxidation of sudan III. And the latter process involves two-electron transfer and an intramolecular proton transfer. Therefore further works can be carried out in order to discriminate these two processes.

Proton, as a positive ion transfer, has been studied in this chapter, in the next chapter, negative ion release through bond cleavage was studied.

5. ELECTROCHEMICALLY INDUCED ION RELEASE

Electrochemically induced ion release has been studied over a few decades[160]. It has been shown varies of advantages such as efficient and well defined qualities. Variable ions release has been studied in this project. Cyanide ion release was studied predominantly whereas halogen ions, such as iodide release have also been investigated.

Besides, the ions which formed after electrochemical reductions may form an ion-pair with the electrolyte molecules. It was found that large alkali salts, such as tetraalkylammonium perchlorates, tetrafluoroborates, hexafluoro phosphates, *etc.* in conventional dipolar aprotic solvents, such as acetonitrile, *N*,*N*-dimethylformamide, dimethylsulfoxide, *etc.*, are usually moderate in ion pairing.[161] Savéant found that the increasing extent of ion pairing (*i.e.* increasing the binding constant and/or the concentration of associating ion), causing a positive shift on the reversible half-wave (or peak) potential by 59.6 mV (at 298 K) per decade change of the associating ion concentration. The ion release process can be stepwised or concerted, depending on the bond dissociation free energies.

Accordingly, electrochemical methods offers great advantages on the mechanistic studies on ion release processes, with association of ion pairing. Based on Marus-Hush theory, the relationships between reorganisation energy (*i.e.* rate of electron transfer) and association constant was established by Savéant,[161] with the limiting current proportional to the association constant in the reduction case.

5.1. Electrochemical reduction of nitroprusside in acetonitrile

5.1.1. Introduction

Nitroprusside ion (Fig. 5.1), $[Fe(CN)_5NO]^{2-}$, has been the subject of extensive investigation by chemists after its medical applications were noted.[162] It was firstly discovery by Playfair in 1849[163]. Since then, Boedeker[164] first introduced its pharmaceutical usage and follow by the first clinical trial in 1928 by Johnson[165]. It was found that nitroprusside ion is an effective peripheral vasodilator, which acan be applied to the patients who are suffering a hypertensive emergencies[166] (*i.e.* high blood pressure). Therefore the studies on its reduction mechanisms as well as its chemical and physical properties have been intensively carried out.

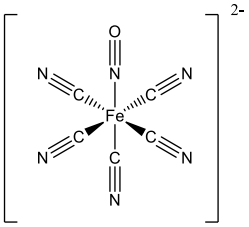

Fig. 5.1. Chemical structure of nitrprusside ion.

The nitroprusside ion involves five CN^- ligands and one NO^+ ligand bonded on the iron metal centre. According to the valence theory, each CN^- group donates one negative charge and the NO^+ group donates one positive charge, the iron is 2+ charged and therefore the overall charge on the ion is 2-. The crystal structure of the nitroprusside ion was determined by X-ray crystallography[167]. The bond distance of F-C was found 1.90 Å and C-N is 1.16 Å. Compared to the F-C bond, F-N bond gives shorter distance of 1.63 Å with N-O bond length of 1.13 Å. Interestingly, the N-F-$C_{equatorial}$ bond angle 96^o, which is slightly larger than the expected 90^o. The electronic structure of nitroprusside ion was systematically studied by Manoharan and Gray[168] (see Fig. 5.2). They suggested that the molecular orbital energy levels of the nitroprusside ion with the two highest filled molecular orbitals in the ground state of

the ion, which are represented by the term symbols of 6e and $2b_2$ (Fig. 5.2), with 6e level involves mainly d_{xz} and d_{yz} and 24.8% π*NO and small fractions of πCN, π*CN and σCN, whereas the $2b_2$ level contains 84.5% d_{xy}, 13.9% πCN and 1.6% π*CN. The lowest unoccupied molecular orbital is the 7e level, which contains 75.5% π*NO and small percentages of d_{xy}, d_{yz}, d_{xz}, σCN, πCN and π*CN orbitals. Furthermore, the final charge distribution is given to be $Fe^{+0.3166}(CN)_4{}^{-2.2000}(CN)^{-0.5809}(NO)^{+0.4643}$.

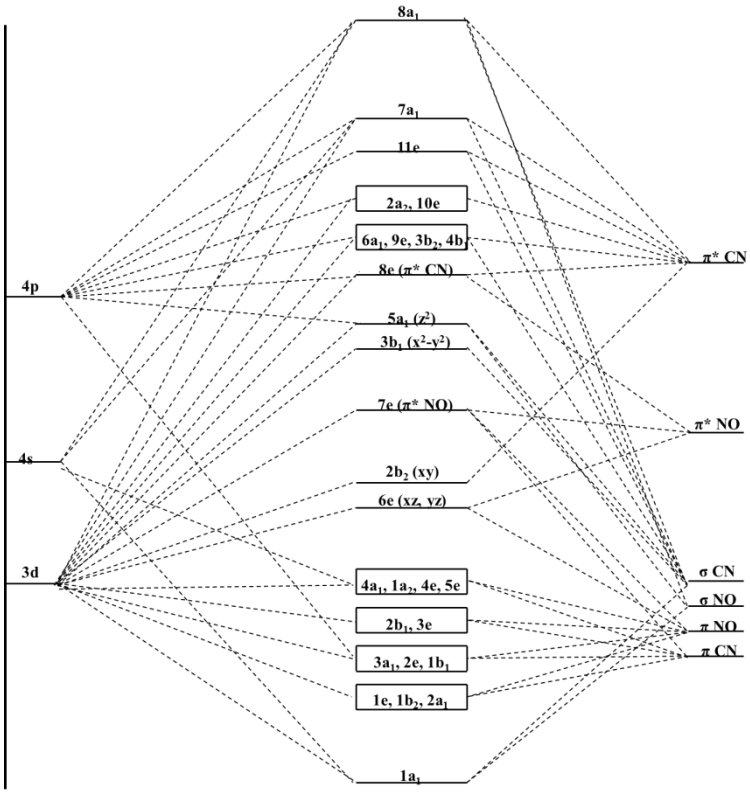

Fig. 5.2. Molecular orbital energy levels of the nitroprusside ion. Redrawn from Manoharan, P.T; Gray, H. B., *J. Am. Chem. Soc.*, **1965**, 87, 3340.

Infrared studies were also carried out for the nitroprusside ion, Tosi and Danon determined that the stretching frequency of CN is higher than those of other $Fe^{II}(CN)_5X$ (X = NH_3, H_2O, NO^{2-} and $SO_3{}^{2-}$), which suggested the less π-bonding in the Fe-C bond for the nitroprusside ion. The C-N stretch band is also split, which is consistent with the C_{4v} symmetry[169] of the ion.

In order to understand the reduction mechanism of the nitroprusside ion, as well as the NO release process, electrochemical studies of the nitroprusside ion were also

performed in the past several decades. The electrochemical reduction of $Fe^{II}(CN)_5NO^{2-}$ were intensively studied and different pathways were suggested (Fig. 5.3). In the presence of water, the reduced nitroprusside can be protonated in either its one electron or two electron reduced form. In addition, Carapuça *et al.*[170] suggested that there is comproportionation after the first one electron reduction in acidic solutions with relatively high concentration of nitroprusside.

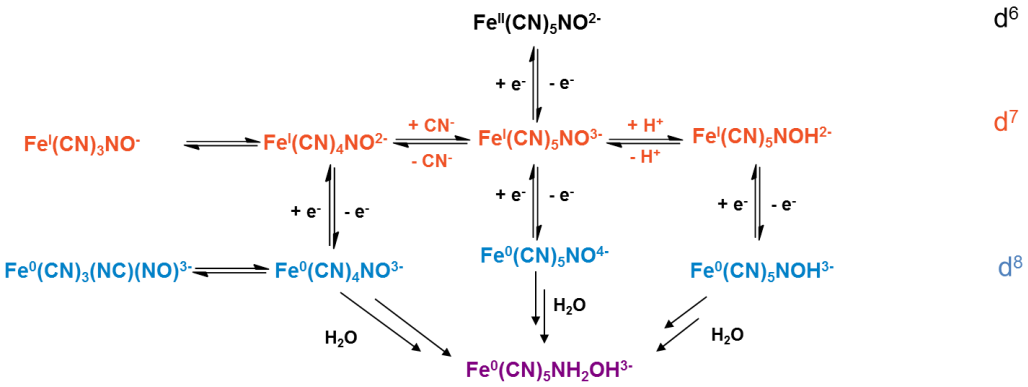

Fig. 5.3. Electrochemical reduction route of the nitroprusside ion in aqueous solution.

Additionally, the electrochemical reduction of nitroprusside ion was also studied in non-aqueous solvents and first published by Bowden *et al.*[39] They performed the electrochemical reduction of tetra-*n*-butylammonium nitroprusside in acetonitrile and dichloromethane and the reaction pathway was found as shown in Fig. 5.4. However, studies of electrochemical reduction of nitroprusside in organic solvent have been carried out by very few people, whereas understanding the reduction mechanism of nitroprusside in non-aqueous solvent is essential, especially for pharmaceutical purposes.

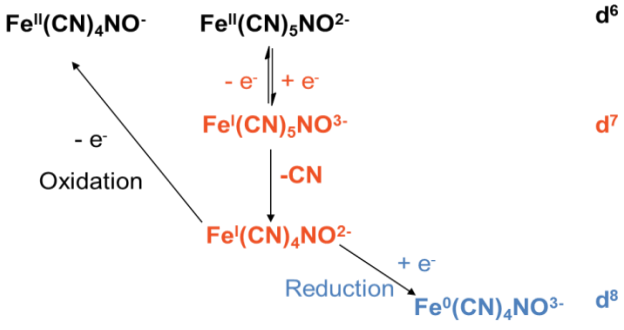

Fig. 5.4. Electrochemical reduction rout of the nitroprusside ion in non-aqueous solution.

The question may rise: whether the reaction pathway of $Fe^{II}(CN)_5NO^{2-}$ to $Fe^{I}(CN)_4NO^{2-}$ is concerted or stepwise (*i.e.* whether the electron transfer and ion release process are separate or within the same step)? The assumption, kinetic salt effect, can be suggested if the reaction follows:

1. stepwised process
2. ion pair formed between CN^- and $Fe(CN)_4NO^{2-}$

5.1.1.1. Kinetic salt effect

If the ion release process is stepwised and $CN|Fe(CN)_4NO^{2-}$ ion pairs are formed, then there are two ways to illustrate the first reductive process:

$$Fe^{II}(CN)_5NO^{2-} \underset{-\,e^-}{\overset{+\,e^-}{\rightleftharpoons}} Fe^{I}(CN)_5NO^{3-} \underset{k_b}{\overset{k_f}{\rightleftharpoons}} Fe^{I}(CN)_4NO^{2-} + CN^-$$

$$Fe^{I}(CN)_4NHO^{2-} + CN^- \overset{K}{\rightleftharpoons} \{\, Fe^{I}(CN)_4NHO^{2-} \;\; CN^- \,\} \xrightarrow{k'_b} Fe^{I}(CN)_5NO^{3-}$$

(Scheme 5.1)

Therefore there are two ways to illustrate the rate of formation of the intermediate:

$$\frac{d[Fe^{I}(CN)_5NO^{3-}]}{dt} = k_b[Fe^{I}(CN)_4NO^{2-}][CN^-] \qquad \text{(Eqn. 5.1)}$$

$$\frac{d[Fe^{I}(CN)_5NO^{3-}]}{dt} = k'_b[\{Fe^{I}(CN)_4NO^{2-} \cdot CN^-\}] \qquad \text{(Eqn. 5.2)}$$

Where k_b and k_b' are the rate of backward reaction.

The K, equilibrium constant, is given by:

$$K = \frac{a_{\{Fe^I(CN)_4NO^{2-}\cdot CN^-\}}}{a_{Fe^I(CN)_4NO^{2-}} a_{CN^-}} = \frac{\gamma_{\{Fe^I(CN)_4NO^{2-}\cdot CN^-\}}}{\gamma_{Fe^I(CN)_4NO^{2-}}\gamma_{CN^-}} \times \frac{[\{Fe^I(CN)_4NO^{2-}\cdot CN^-\}]}{[Fe^I(CN)_4NO^{2-}][CN^-]} \quad \text{(Eqn. 5.3)}$$

Where,

$$K_\gamma = \frac{\gamma_{\{Fe^I(CN)_4NO^{2-}\cdot CN^-\}}}{\gamma_{Fe^I(CN)_4NO^{2-}}\gamma_{CN^-}} \quad \text{(Eqn. 5.4)}$$

Therefore by substitution,

$$\frac{d[Fe^I(CN)_5NO^{3-}]}{dt} = k_b'[\{Fe^I(CN)_4NO^{2-}\cdot CN^-\}] = \frac{k_b' K}{K_\gamma}[Fe^I(CN)_4NO^{2-}][CN^-] \quad \text{(Eqn. 5.5)}$$

Because,

$$\frac{d[Fe^I(CN)_5NO^{3-}]}{dt} = k_b[Fe^I(CN)_4NO^{2-}][CN^-] \quad \text{(Eqn. 5.6)}$$

Therefore,

$$\frac{k_b' K}{K_\gamma} = k_b \quad \text{(Eqn. 5.7)}$$

At infinite dilution,

$$K_\gamma^0 = 1 \quad \text{(Eqn. 5.8)}$$

Therefore,

$$k_b = \frac{k_b^0}{K_\gamma} \quad \text{(Eqn. 5.9)}$$

Take logarithms,

$$\log k_b = \log k_b^0 - \log K_\gamma$$

$$= \log k_b^0 - \log \gamma_{\{Fe^I(CN)_4NO^{2-}\cdot CN^-\}} + \log \gamma_{Fe^I(CN)_4NO^{2-}} + \log \gamma_{CN^-} \quad \text{(Eqn. 5.10)}$$

By using Robinson-Stokes equation:

$$\log \gamma = -\frac{AZ_i^2\sqrt{I}}{1+Ba\sqrt{I}} + cI \quad \text{(Eqn. 5.11)}$$

Where I is the ionic strength, γ is activity coefficient A, B and a are constants, c is the concentration of charged species, Z_i is the charge of species i.

Therefore,

$$\log k_b = f(I) \qquad \text{(Eqn. 5.12)}$$

where,

$$\mathrm{I} = \frac{1}{2}\sum c_i Z_i^{\,2} \qquad \text{(Eqn. 5.13)}$$

where c_i is the concentration of charged species i.

Therefore the release on cyanide ion can be reflected on the kinetic salt effect as the favours the formation of a single, highly charged ionic complex[171]. Therefore, in this case, a kinetic salt effect is expected by the addition of electrolyte.

In summary, it is expected that there is a decrease in peak (or plateau) current with increasing concentration of electrolyte, with, the current decrease caused by viscosity effect is not as dramatic as the kinetic salt effect. In this thesis, an attempt of varying electrolyte concentration to examine the mechanism of cyanide ion release was undertaken. It was found that there is no kinetic salt effect, or the effect is not as large as expected.

5.1.2. Electrochemical reduction of NP in acetonitrile

The initial investigation was undertaken through the electrochemical reduction of nitroprusside ion. 1.23 mM of tetrabutylammonium nitroprusside in acetonitrile with 0.1 M TBAP was studied using both a glassy carbon macro-electrode (3 mm diameter) and an 11 μm diameter carbon fibre microelectrode as shown in Fig. 5.5a and Fig. 5.5d. The experiment was carried out by using cyclic voltammetry, scan from 0 V to -1.8 V in variable scan rates. The corresponding analysis of data (*i.e.* plot of peak current against square root of scan rates and plot of peak potential against logarithm of scan rates) are also shown in Fig. 5.5.

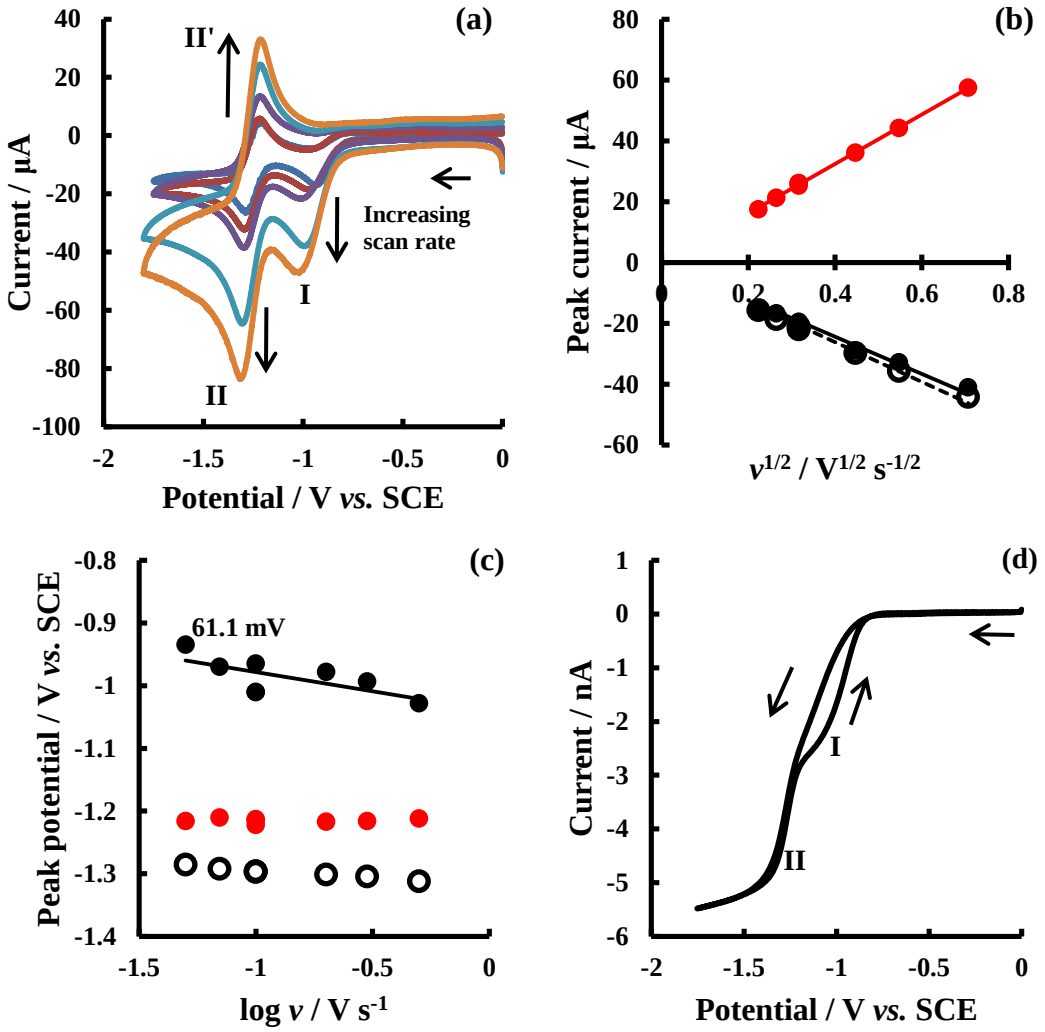

Fig. 5.5. (a) Cyclic voltammogram of 1.23 mM nitroprusside reduction in acetonitrile with 0.1 M TBAP with variable scan rates ($0.05 \leq v$ / V $s^{-1} \leq 0.5$) on a glassy carbon electrode (3 mm diameter) and (d) on a carbon fibre microelectrode (11 µm diameter). Sliver/Silver chloride electrode was used as reference electrode; a nickel spiral wire was served as counter electrode. (b) a corresponding plot of peak current against square root of scan rates for the reductive peak I (black dot), reductive peak II (black circle) and oxidative peak II' (red dot). (c) a corresponding plot of peak potential against decade change of scan rates for the reductive peak I (black dot), reductive peak II (black circle) and oxidative peak II' (red dot).

It can be seen that from Fig. 5.5a, two reduction peaks and one oxidation peak are observed. The first irreversible wave appears at -0.8 V and second reversible wave appears -1.26 V, with its corresponding oxidative wave at -1.23 V, suggesting that a multi-electron transfer process with the formal potential for peak I is much smaller than peak II. The loss of reverse peak of the first electron transfer process suggests that the product formed after the first electron transfer is stable and cannot be oxidised

back to the starting material. The plot of peak current over square root of scan rates (Fig. 5.5b) affords a straight line across the origin, suggests that the electron transfer process is a diffusion controlled process; the reasonable overlap between the first and second reduction peak suggests same number of electrons have been transferred in each process. The plot of peak potential against logarithm of scan rates (Fig. 5.5c) affords 61.1 mV shifts for the first reduction peak and relatively negligible shift at slow scan rates (*i.e.* $v \leq 0.1$ V s^{-1}) and a slight shift at higher scan rates (*i.e.* $v \geq 0.1$ V s^{-1}) for peak II, suggesting that the first reduction process is electrochemically irreversible and the second electron transfer is electrochemically quasi-reversible.

Fig. 5.5d shows the reduction of nitroprusside ion at an 11 μm diameter carbon fibre microelectrode and steady state current were obtained. The trace cross over at the sweeping point suggests that the process is ECE, with a consistence to the scheme 4. The shoulder on the reverse scan suggests that there are two electron transfer processes, with the first electron transfer process harder to be oxidised compare to the second electron transfer.

In order to examine the mechanism systematically, variable concentrations of nitroprusside was undertaken. Therefore, 2.11 mM nitroprusside was examined subsequently. Again, as shown in Fig. 5.6a, three peaks were observed as the same as previously. The corresponding data analysis is shown in Fig. 5.6b and 5.6c and the microelectrode cyclic voltammetry diagram is shown in Fig. 5.7d.

Again, the diffusion-controlled electron transfer process is suggested by the linear dependence of peak current over square root of scan rates for both reduction and oxidation processes. 61.3 mV change of peak potential per decade change of scan rates of the first electron transfer suggests, again, electrochemically irreversible; the shift at higher scan rates ($v \geq 0.1$ V s^{-1}) for the second electron transfer becomes more obverse than that of 1.23 mM nitroprusside. Most interestingly, the

microelectrode CV, affords an increased half-wave difference between the reduction and oxidation process, suggesting that the increased nitroprusside concentrations slow down both electron transfer processes, with the first electron transfer more obviously.

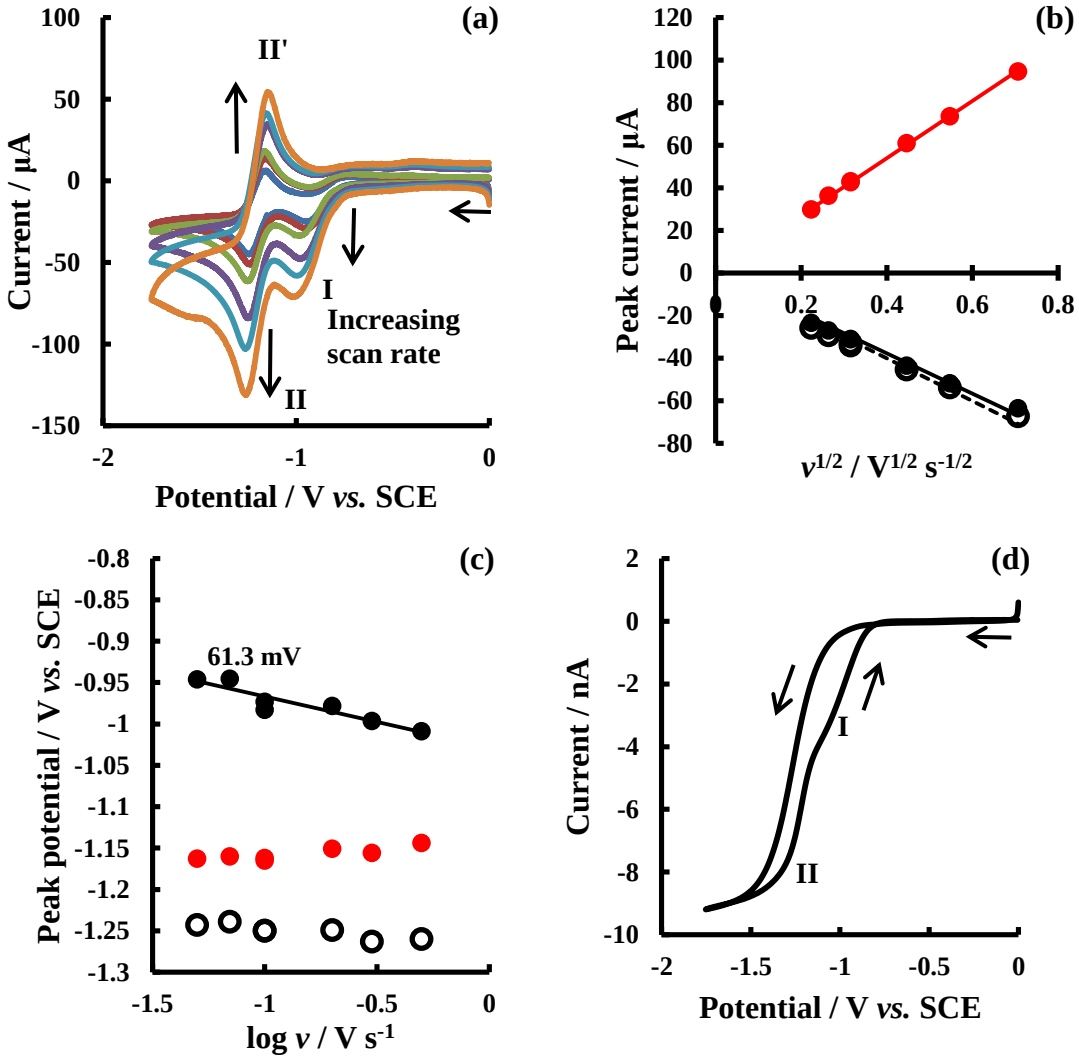

Fig. 5.6. (a) Cyclic voltammogram of 2.11 mM nitroprusside reduction in acetonitrile with 0.1 M TBAP with variable scan rates ($0.05 \leq \nu$ / V $s^{-1} \leq 0.5$) on a glassy carbon electrode (3 mm diameter) and (d) on a carbon fibre microelectrode (11 µm diameter). Sliver/Silver chloride electrode was used as reference electrode; a nickel spiral wire was served as counter electrode. (b) a corresponding plot of peak current against square root of scan rates for the reductive peak I (black dot), reductive peak II (black circle) and oxidative peak II' (red dot). (c) a corresponding plot of peak potential against decade change of scan rates for the reductive peak I (black dot), reductive peak II (black circle) and oxidative peak II' (red dot).

Due to the change in the cyclic responses in changing nitroprusside concentrations, especially the change in microelectrode signal, it is necessary to repeat the experiment in another nitroprusside concentration. Consequently, 5.01 mM nitroprusside was then

undertaken. As shown in Fig. 5.7a, the CV diagram on glassy carbon macroelectrode affords similar trends to that of 1.23 mM and 2.11 mM nitroprusside data. Both first and second electron transfer processes were under diffusion-controlled through, again, the linear dependence between peak current and square root of scan rates (Fig. 5.7b). However, the shift in peak potential becomes more dramatic, with 103.5 mV shift per decade change of scan rate for the first electron transfer process and the quasi-reversible behaviour becomes more obvious for the second electron transfer process (as shown in Fig. 5.7c).

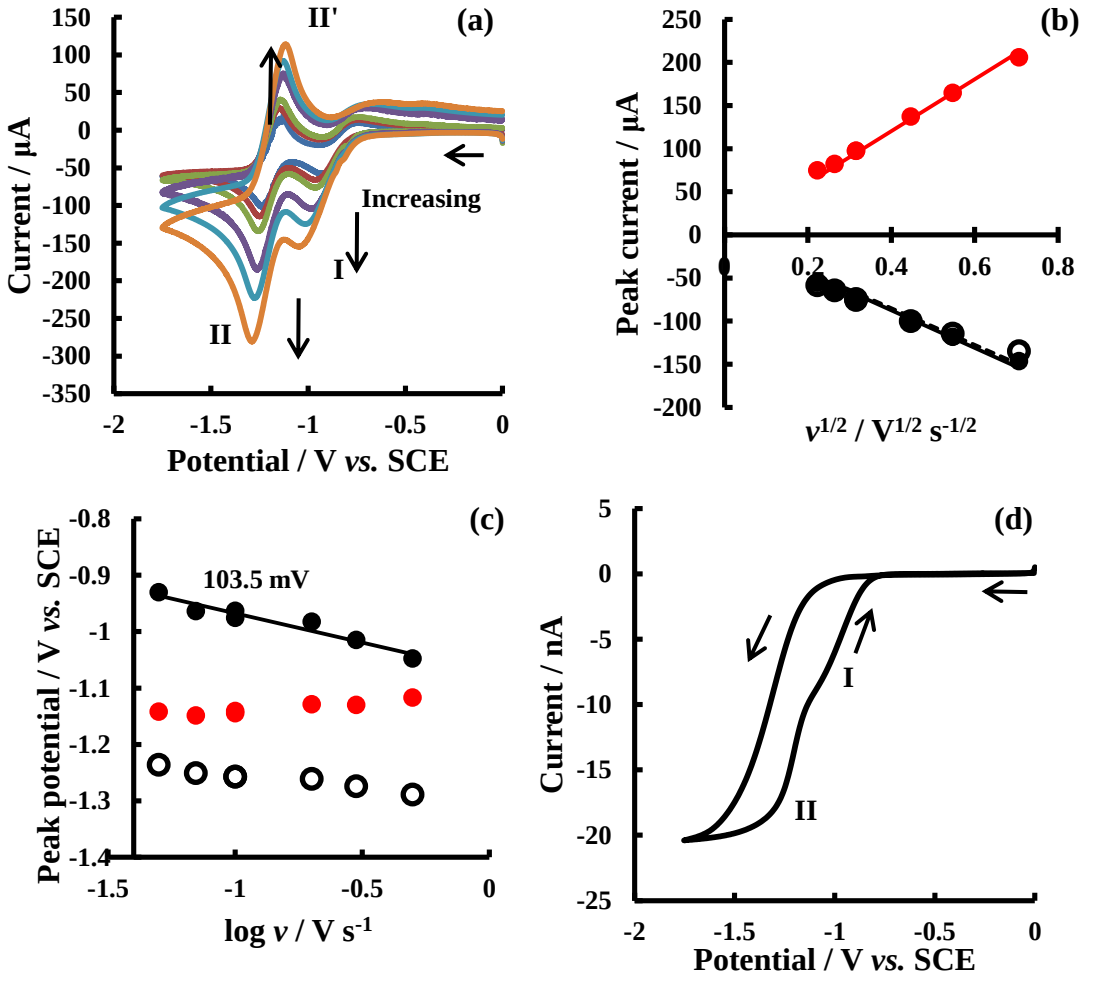

Fig. 5.7. (a) Cyclic voltammogram of 5.01 mM nitroprusside reduction in acetonitrile with 0.1 M TBAP with variable scan rates ($0.05 \leq v$ / V $s^{-1} \leq 0.5$) on a glassy carbon electrode (3 mm diameter) and (d) on a carbon fibre microelectrode (11 µm diameter). Sliver/Silver chloride electrode was used as reference electrode; a nickel spiral wire was served as counter electrode. (b) a corresponding plot of peak current against square root of scan rates for the reductive peak I (black dot), reductive peak II (black circle) and oxidative peak II' (red dot). (c) a corresponding plot of peak potential against decade change of scan rates for the reductive peak I (black dot), reductive peak II (black circle) and oxidative peak II' (red dot).

It is worth note that the microelectrode signal, again, the separation between forward and backward scan increased with increasing concentration of nitroprusside concentration, suggests that the increase of nitroprusside concentration affords sluggish electron transfer process.

Moreover, the CV diagrams for all the concentrations show similar trend, which are strongly consistent with other authors' work[39]. As the process has been studied previously and was suggested that it involves two-electrons, the diffusion coefficient can be worked out from limiting current, with $D = 1.81 \pm 0.05 \times 10^{-9}$ m^2 s^{-1}.

Table 5.1 shows the slope of all three peak currents against square root of scan rates for three nitroprusside concentrations. By applying reversible Randle-Sevick equation the diffusion coefficient can be worked out, with $D = 1.14 \pm 0.05 \times 10^{-9}$ m^2 s^{-1}, similar the value calculated from steady-state voltammetry.

Table 5.1. Slope of peak currents against square root of scan rates for three different concentrations of nitroprusside.

	Peak I	Peak II	Peak II'
[NP] (mM)	$\frac{\partial \mid ip \mid}{\partial\sqrt{v}\ (\mu A\ V^{-1/2}\ s^{1/2})}$	$\frac{\partial \mid ip \mid}{\partial\sqrt{v}\ (\mu A\ V^{-1/2}\ s^{1/2})}$	$\frac{\partial \mid ip \mid}{\partial\sqrt{v}\ (\mu A\ V^{-1/2}\ s^{1/2})}$
1.23	65.41	61.11	81.04
2.11	100	94.6	134.6
5.01	212.6	218.6	300.9

In order to demonstrate the cyanide release during the reduction of nitroprusside ion, variable concentrations of cyanide ions were added into the solvent. Tetrabutylammonium cyanide was used to provide cyanide ions, with tetrabutylammonium perchlorate addition to maintain the ionic strength to be 0.1 M. As it is suggested in Scheme 5.2, the increase of cyanide ion concentration should shift the equilibrium of reaction (Scheme 5.2b) towards left, which unfavours the cyanide release process. Therefore a back oxidation wave of Scheme 1a can be

observed.

$$[Fe(CN)_5NOH]^{2-} + e^- \rightleftharpoons [Fe(CN)_5NO]^{3-} \quad (a)$$

$$[Fe(CN)_5NO]^{3-} \longrightarrow [Fe(CN)_4NOH]^{2-} + CN^- \quad (b)$$

$$[Fe(CN)_4NOH]^{2-} + e^- \rightleftharpoons [Fe(CN)_4NOH]^{3-} \quad (c)$$

Scheme 5.2. Electrochemical reduction route of nitroprusside ion.

Indeed, as shown in Fig. 5.8, the addition of cyanide ion in the solution leads the appearance and increase of oxidative peak I', suggesting that the addition of cyanide ion favours the backward reaction of b in Scheme 5.2, which favours the formation of $[Fe(CN)_5NO^{3-}]$, and peak I' indicates the oxidation wave of $[Fe(CN)_5NO^{3-}]$ to $[Fe(CN)_5NO^{2-}]$. The plot of ipI'/ipI against TBACN concentration is shown in Fig. 8b, the oxidation peak increase dramatically from when TBACN concentration increased from 0 M to 0.02 M and tends to 1, indicates that the increase of TBACN concentration makes the size of oxidation wave similar to the reduction wave, and this suggests that the similar amount of $Fe(CN)_5NO^{3-}$ formed from reduction of $Fe(CN)_5NO^{2-}$ were oxidised back to $Fe(CN)_5NO^{3-}$ while the increase of TBACN concentration.

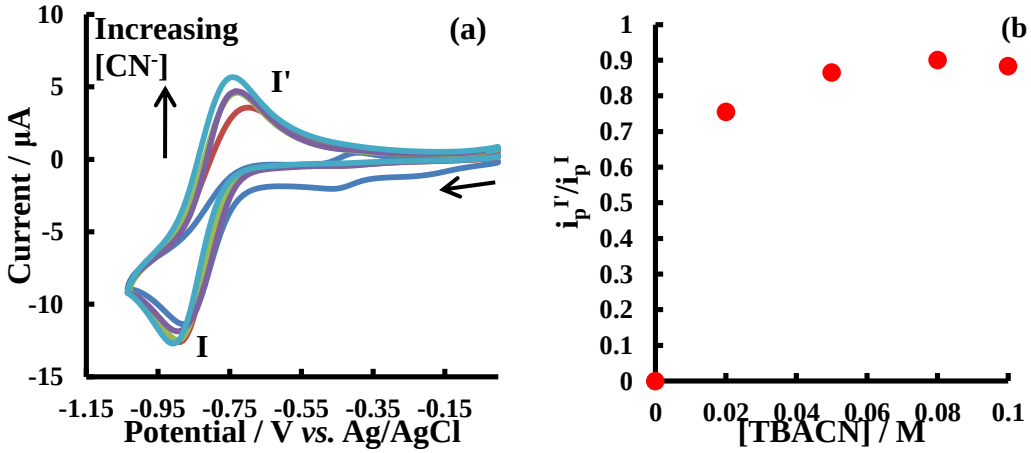

Fig. 5.8. (a) Electrochemical reduction of 1.00 mM nitroprusside ion in acetonitrile on a 3 mm diameter glassy carbon macroelectrode from 0 V to -1.035 V with different concentration ratios of TBAP and TBACN, with fixed ionic strength = 0.1 M. Scan rate = 0.05 V s^{-1}. Blue: 0.00 M TBACN, 0.1 M TBAP; Red: 0.02 M TBACN, 0.08 M TBAP; Green: 0.05 M TBACN, 0.05 M TBAP; Purple: 0.08 M TBACN, 0.02 M TBAP; Cyan: 0.10 M TBACN, 0.00 M TBAP. Ag/AgCl was applied as a reference electrode and a platium spiral wire was served as a counter electrode. (b) a plot of oxidation peak current over reduction peak current against TBACN concentration.

Fig. 5.9 shows an example reduction of nitroprusside using a 3 mm diameter glassy carbon disc electrode in variable san rates with the presence of cyanide ion (0.05 M TBAP and 0.05 M TBACN). As shown in Fig. 9a, the increase of scan rate increases the reductive peak current and the reductive peak potential shifts towards more negative as expect, on the other hand, the increase of scan rate leads the oxidation wave to be flattened and broaden, suggests that although the presence of cyanide in the solution favours the backward reaction of b in Scheme 5.2, the chemical reaction is reasonably fast than the experiment time scale, therefore the increase scan rate leads less formation of $Fe(CN)_5NO^{3-}$ from $Fe(CN)_4NO^{2-}$ and CN^-. Moreover, the second reduction wave is unaffected and shows the similar trend as that of reduction in 0.1 M TBAP.

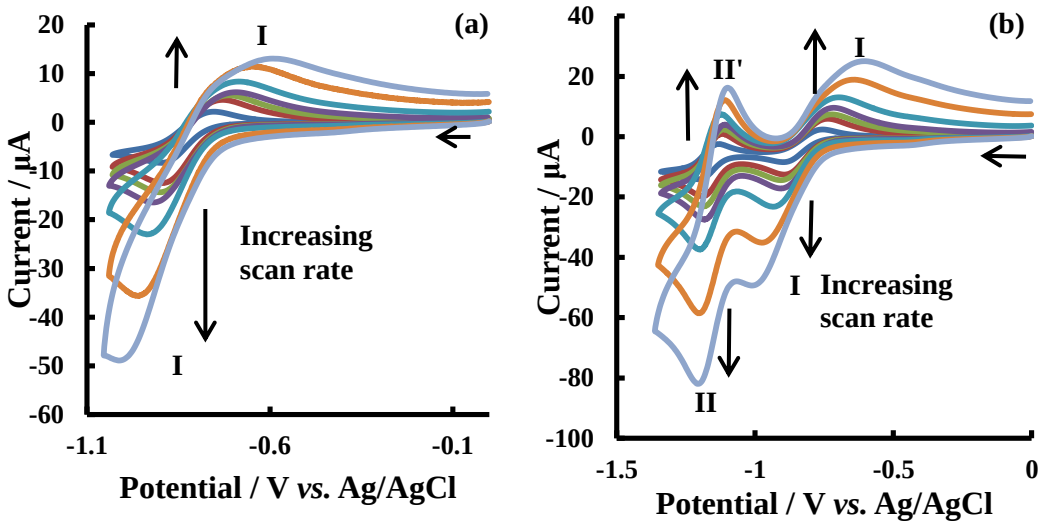

Fig. 5.9. Electrochemical reduction of 1.00 mM nitroprusside ion in acetonitrile on a 3 mm diameter glassy carbon macroelectrode scan from 0 to -1.035 V (a) and scan from 0 to -1.35 V (b) in variable scan rate ($0.02 \leq v$ / V $s^{-1} \leq 1$), with 0.05 M TBAP and 0.05 M TBACN (ionic strength = 0.1 M). A Ag/AgCl electrode was applied as a reference electrode and a platium spiral wire was served as a counter electrode.

Fig. 5.10 illustrates both reduction waves of nitroprusside with changing cyanid ion centrations using both 3 mm diamter glassy carbon macroelectrode (Fig. 5.10a) and 11 µm diamter carbon fiber microelectrode electrode (Fig. 5.10b). Although the change of cyanide ion centrations in the system causes the increase of oxidation peak I', other redox processes were unaffected. As shown in Fugure 5.10b, the increase of

cyanide ion concentrations unaffect the limiting current.

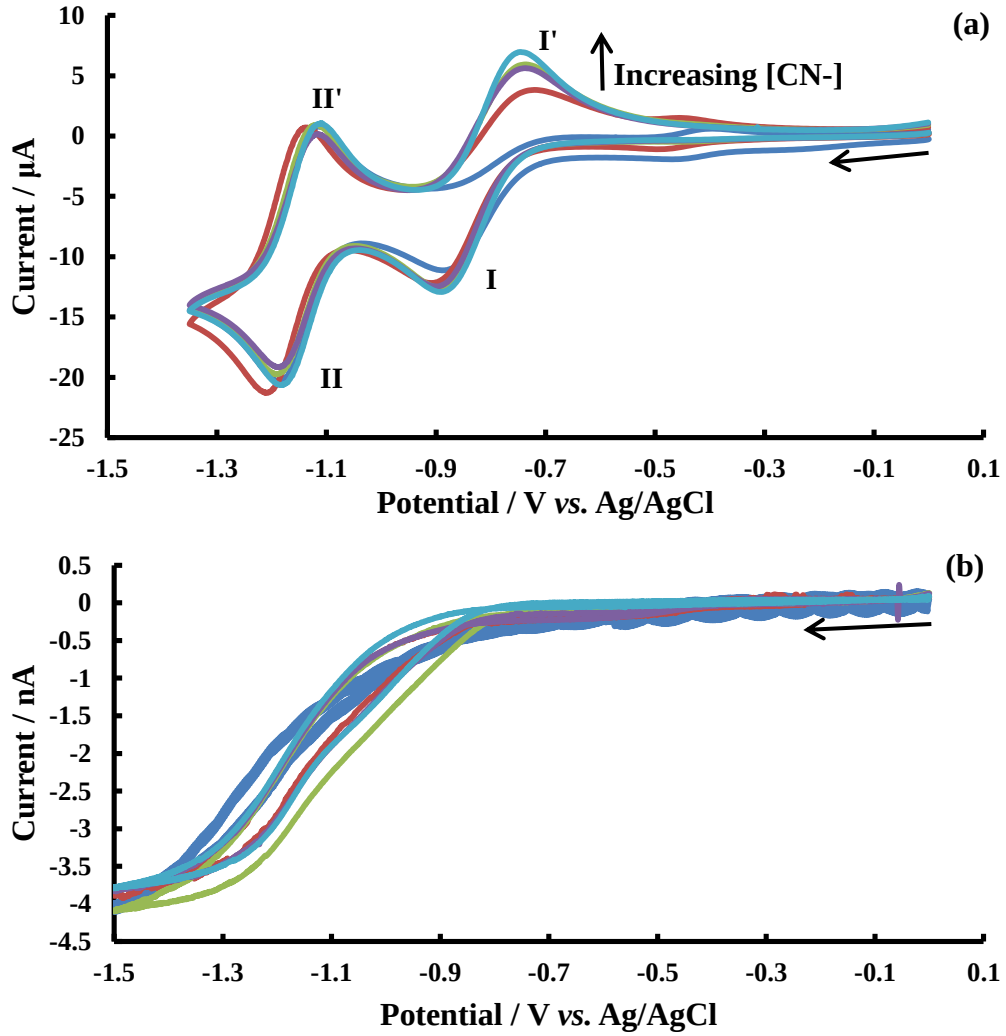

Fig.5.10. Electrochemical reduction of 1.00 mM nitroprusside ion in acetonitrile on a 3 mm diameter glassy carbon macroelectrode (a) scan from 0 to -1.35 V and a 11 µm diameter carbon fiber microelectrode (b) scan from 0 to -1.5 V with different concentration ratios of TBAP and TBACN, with fixed ionic strength = 0.1 M. Scan rate = 0.05 V s^{-1}. Blue: 0.00 M TBACN, 0.1 M TBAP; Red: 0.02 M TBACN, 0.08 M TBAP; Green: 0.05 M TBACN, 0.05 M TBAP; Purple: 0.08 M TBACN, 0.02 M TBAP; Cyan: 0.10 M TBACN, 0.00 M TBAP. Ag/AgCl was applied as a reference electrode and a platium spiral wire was served as a counter electrode.

5.1.3. The effects on changing electrolyte concentration

In order to verify whether the cyanide release process is concerted or stepwise, kinetic salt effect can be applied. The theory is given in previously section (Section 5.1.1.1). Briefly, according to the kinetic salt effect theory, the increased concentrations of

electrolyte favours the rate of backward reaction in Scheme 5.2b, therefore higher ionic strength stabilises $[Fe(CN)_5NO]^{3-}$ ion.

The experiment was then carried out by adding electrolyte (TBAP) into the solution in order to increase the ionic strength in the solution. Fig. 5.11 shows the cyclic voltammograms of variable concentrations of nitroprusside reduction with variable concentrations of TBAP. As shown in Fig. 5.11, the increase of TBAP concentration causes the shift of E_p^I towards more positive, suggests that the formation of $[Fe(CN)_5NO]^{3-}$ is favoured. As the second electron transfer process is dependent on the former one, there is also a positive shift on E_p^{II}. Additionally, the addition of TBAP also causes the decrease in peak current. These phenomena were then further investigated.

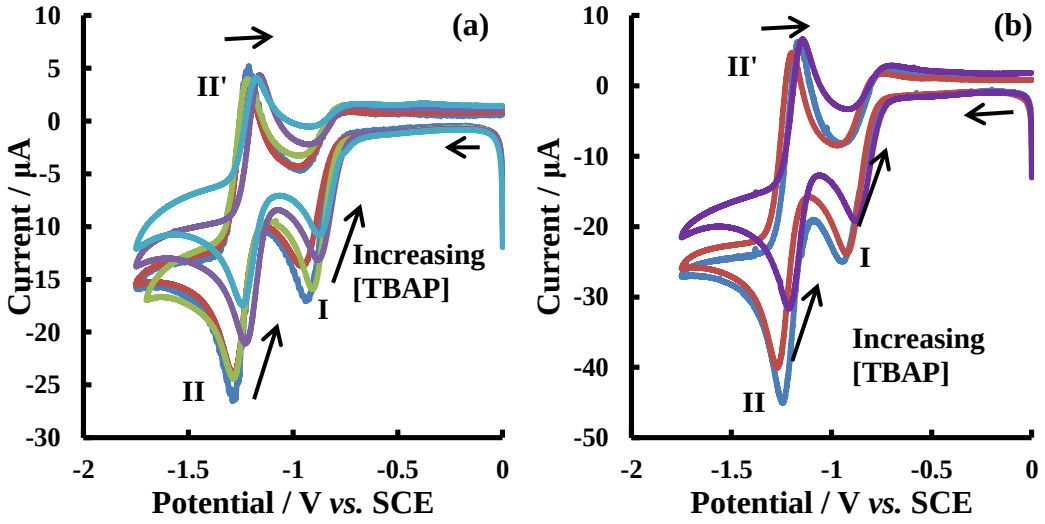

Fig. 5.11. Cyclic voltammograms of 1.23 mM (a) and 2.11 mM (b) of nitroprusside ion reduction on a glassy carbon macroelectrode (3 mm diameter) in acetonitrile at 0.05 V s^{-1} scan rate with variable concentrations of TBAP: 0.1 M (blue), 0.2 M (red), 0.29 M (green), 0.5 M (purple) and 0.95 M (light blue). A silver/silver chloride electrode was used as the reference electrode and a nickel spiral wire was used as counter electrode.

In order to verify the observation of peak current decrease, which caused by the addition of electrolyte, a steady-state limiting experiment was carried out using an 11 µm diameter carbon fibre electrode. It can be seen from Fig. 5.12 that the increasing concentration of TBAP decreases the limiting current from both electron transfer

process. Noting that at low TBAP concentrations, only one sigmoidal shaped wave can be observed. In addition, a shift of half-wave potential, $E_{1/2}$, can be observed for both electron transfer process, which has similar trend with the macroelectrode data. However, it is important to realise, that the shift on the half-wave potential of the microelectrode data, is not as big as the macroelectrode. This will be discussed in more details in the following text.

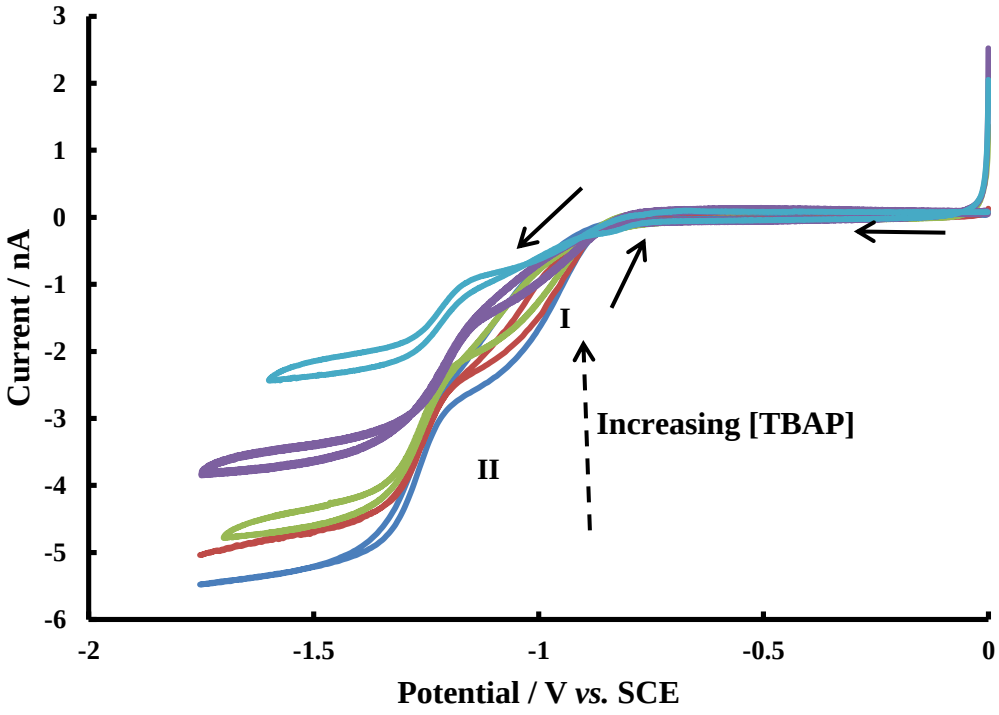

Fig. 5.12. Steady-state cyclic voltammogram of 1.23 mM of nitroprusside ion reduction on a carbon fibre microelectrode (11 μm diameter) in acetonitrile with variable concentrations of TBAP: 0.1 M (blue), 0.2 M (red), 0.29 M (green), 0.5 M (purple) and 0.95 M (light blue). A silver/silver chloride electrode was used as the reference electrode and a nickel spiral wire was used as counter electrode.

So far, all the observations are suggesting that the addition of electrolyte causes the decrease in current and this observation is agreed with the kinetic salt effect as it favours the formation of $Fe(CN)_5NO^{3-}$. However, the addition of electrolytes can also cause the change of viscosity and the change of viscosity can change the diffusion coefficient that leads the current to decrease. Therefore a measurement of viscosity of acetonitrile with different concentrations of TBAP was carried out.

5 different concentrations of TBAP were dissolved in acetonitrile in order to perform the viscosity measurements as shown in Table 5.2. By plotting the TBAP concentration against viscosity, a linear dependence was obtained (Fig. 5.13), suggesting that the viscosity measurements were reasonable.

Table 5.2. Viscosity of acetonitrile solution with the presence of variable concentrations of TBAP

[TBAP] / M	Viscosity* / cP
0.102	0.4559
0.2	0.4756
0.29	0.5294
0.4999	0.5960
0.9506	0.7480

* Viscosities were measurement at 20 ℃.

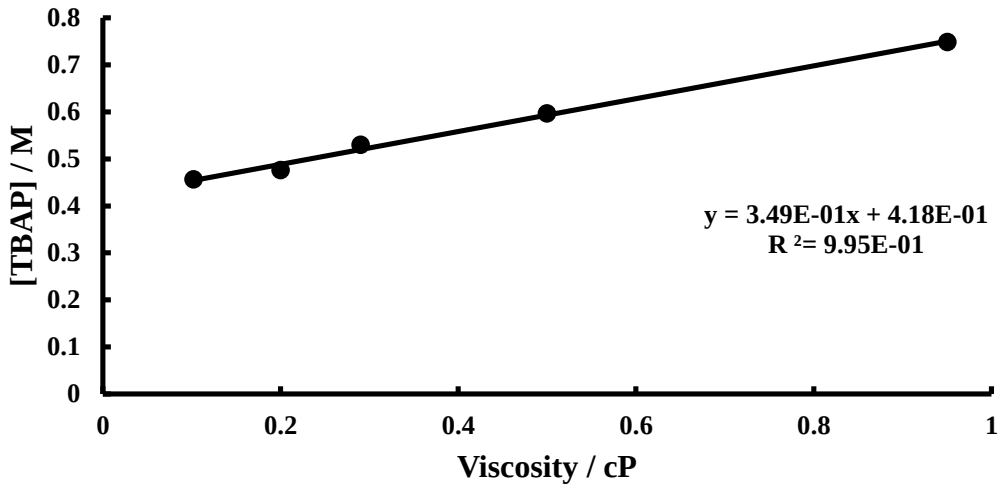

Fig. 5.13. Viscosity of acetonitrile solution change with changing concentrations of TBAP.

Consequently, cyclic voltammetries were carried out by using both 3 mm diameter glassy carbon disc electrode and 11 μm diameter carbon fibre disc electrode. By applying Randles-Sevick equation and steady-state equation, the diffusion coefficient for nitroprusside in acetonitrile with variable TBAP concentrations can be worked out. The diffusion coefficient can be then normalised by viscosity as shown in Fig. 5.14. By plotting diffusion coefficient over viscosity against viscosity, suggesting that the increased concentration of TBAP affect the viscosity so much that causing the

diffusion coefficient changes dramatically. Therefore by examining the viscosity, the current drop for both Macro and Micro-electrodes are caused by viscosity change rather than the kinetic salt effects.

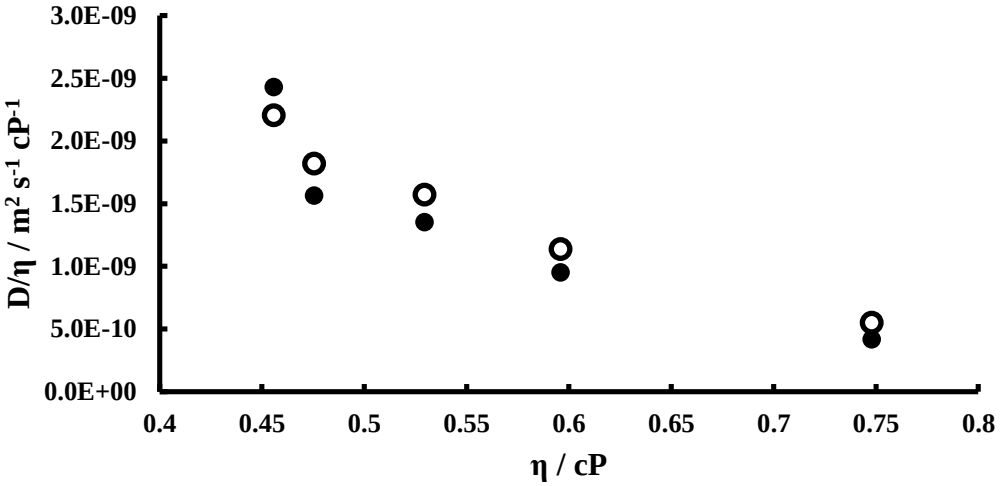

Fig. 5.14. A plot of normalised diffusion coefficient by viscosity against viscosity. Diffusion coefficients were obtained from both macro (black dots) and micro (white dots) electrodes.

Therefore, although the preliminary results suggest the signs of kinetic salt effect, by taking viscosity account, the phenomena that been seen previously are actually caused by viscosity effect. Therefore, back to the different shift magnitude on macroelectrode and microelectrode question addressed previously, the shift in potential on microelectrodes and macroelectrode can be due to the slower mass transport and probably, poor reference.

5.1.4. Kinetic analysis

Although it has been proved that there is no kinetic salt effect based on the peak current or limiting current change, the kinetic data of nitroprusside reduction can be worked out. Barnes *et al.*[172] suggested the analysis route of finding kinetic data for an EC process at microdisk electrode with both reversible and irreversible homogenous process. If assuming $Fe^{II}(CN)_5NO^{2-}$ is A, $Fe^{I}(CN)_5NO^{3-}$ is B and $Fe^{I}(CN)_4NO^{2-}$ is C, then the reactions cane be written as:

$$A + e^- \underset{}{\overset{k_0}{\rightleftharpoons}} B$$

$$B \underset{k_b}{\overset{k_f}{\rightleftharpoons}} C$$

Scheme 5.3

And the dimensionless parameters are illustrated in Table 5.3.

Table 5.3. Dimensionless parameters.

Parameter	Expression
Concentration	$c = c/c_{bulk}$
Time	$T = D_A t/r^2$
Potential	$\theta = (F/RT)(E-E_f)$
Heterogeneous rate constant	$K_0 = k_0 r/D_A$
Homogeneous rate constant	$K_f = k_f r^2/D_A$
Equilibrium constant	$K_{eq} = k_f/k_b$

As Barnes at co-workers[172] found that the half-wave potential shifts by 2.303/2θ units per decade increase of K_f, the relationship between $\theta_{1/2}$ and K_f can be given by Eqn. 5.14 if assuming the microdisk is a hemispherical electrode with radius (2/π)r.

$$\theta_{1/2} = \ln(1 + \frac{2}{\pi}\sqrt{K_f}) \qquad \text{(Eqn. 5.14)}$$

Therefore, according to Eqn. 5.14, assuming the formal potential is -0.8 V, the rate of forward homogenous reaction can be worked out and given in Table 5.4. In addition, given that:

$$\theta_{1/2} = -2.3 \log K_{eq} \qquad \text{(Eqn. 5.15)}$$

The equilibrium constant can be worked out, and consequently, as described in Table 5.3, the rate of backward homogenous reaction can be worked out.

Table 5.4. 1 mM nitroprusside

[TBAP]/M	k_f	k_b
0.10	8.87E+01	1.23E-03
0.20	6.53E+01	1.34E-02
0.29	6.55E+01	2.59E-03
0.50	2.94E+01	4.98E+00
0.95	3.25E+01	1.10E-02

According to Table 5.4, the forward rate constant is more than 3 orders to magnitude larger than that of the backward reaction. This explains the irreversible behaviour of cyanide ion release. Note that the 0.4999 M concentration of TBAP affords k_b outside the range, this may be due to some experimental errors. Overall, the increasing concentration of TBAP favours the rate of backward reaction and unfavours the forward homogenous reaction, and this is in agreement of the microelectrode data that the shifts of half-wave potential. In addition, the cyanide addition experiments suggests that the cyanide ion release process can be reversible if the cyanide ion concentration is sufficient, therefore lack of back peak of the first reduction wave in the TBAP change experiment suggests that the addition of TBAP causes the viscosity change in the solution and subsequently causes a sluggish electron transfer.

Although the limiting current change is due to the viscosity effect, the rate of forward and backward reaction change can be due to either viscosity effect or a slight kinetic salt effect.

5.1.5. Conclusion

In conclusion, the reduction of nitropursside ion in acetonitrile was studied. The release of cyanide ion has been observed. The addition of TBAP was carried out to examine whether there is a kinetic salt effect. However the increase of TBAP concentration causes the increase of viscosity of the solution. By taking account of viscosity, the decrease in peak current and limiting current is mainly due to the viscosity change. In addition, by calculating the rate constants for the homogeneous

reaction, k_b increased with the addition of TBAP suggesting that the increased viscosity slows down the reaction kinetics. No evidence was found that there is a kinetic salt effect.

Next, 1-iodo-4-nitrobenzen was examined as halogen ion release is a field of interest. In addition, the reduction of halogen nitrobenzene has been widely studied and it was suggested to be a stepwised ion release process. Therefore by undertaking electrochemical reduction of halogen nitrobenzene, it can be helpful to understand the cyanide release process.

5.2. Electrochemical reduction of 1-iodo-4-nitrobenzene

In addition to the studies of ion release process, halogen ions, such as iodide has also been studied. Bond cleavage of C-X (carbon-halogen) reaction has been studied for decades[173-178]. The cleavage of halogen ion can be populated in the local environment, and can be further used for other applications such as halogen lighting. The electrochemical reduction of iodo-nitrobenzene in organic solvents has been studied and known to give I^- release, via an ECE process[179, 180]. Such mechanism involves one electron transfer process followed by a chemical reaction, and followed by another electron transfer process. The mechanism is given by:

$$m - I - \phi - NO_2 + e^- \rightarrow [m - I - \phi - NO_2]^{\bullet -} \quad \text{(a)}$$

$$[m - I - \phi - NO_2]^{\bullet -} \rightarrow I^- + \bullet C_6H_4NO_2 \quad \text{(b)}$$

$$\bullet C_6H_4NO_2 + HS \rightarrow \phi - NO_2 \quad \text{(c)}$$

$$\phi - NO_2 + e^- \rightarrow [\phi - NO_2]^{\bullet -} \quad \text{(d)}$$

Scheme 5.4.

Where ϕ is a benzene group and HS dontes the solvent-supporting electrolyte system.

As the study is focused on the ion release process, which is the EC process, the reactions c and d in Scheme 5.4 were not been examined.

Similar experiments were carried out for electrochemical reduction of iodo-nitrobenzene as the reduction of nitroprusside ions. Preliminary investigation was carried out by looking at the shape of voltammogram and variable scan rate effects.

5.2.1. Varying scan rates

The preliminary experiments for iodo-nitrobezene reduction are to look into the shape of voltammogram as well as scan rate effects. As shown in Fig. 5.15, the consecutive cyclic voltammetric sweeps for the reduction of 5.0 mM 1-iodo-4-nitrobenzene in acetonitrile with 0.1 M TBABF at a 3 mm diameter glassy carbon electrode at 0.1 V s^{-1} scan rate shows A single reductive wave is observed at -1.1 V and the corresponding oxidative wave appears at -1.0 V *vs.* SCE. Repetitive scanning shows there is no change to either peak current or peak potential, suggesting that there is no adsorption of 1-iodo-4-nitrobenzene on the electrode surface. The appearance of the reverse wave (oxidative wave) suggests that this reduction process is chemically reversible.

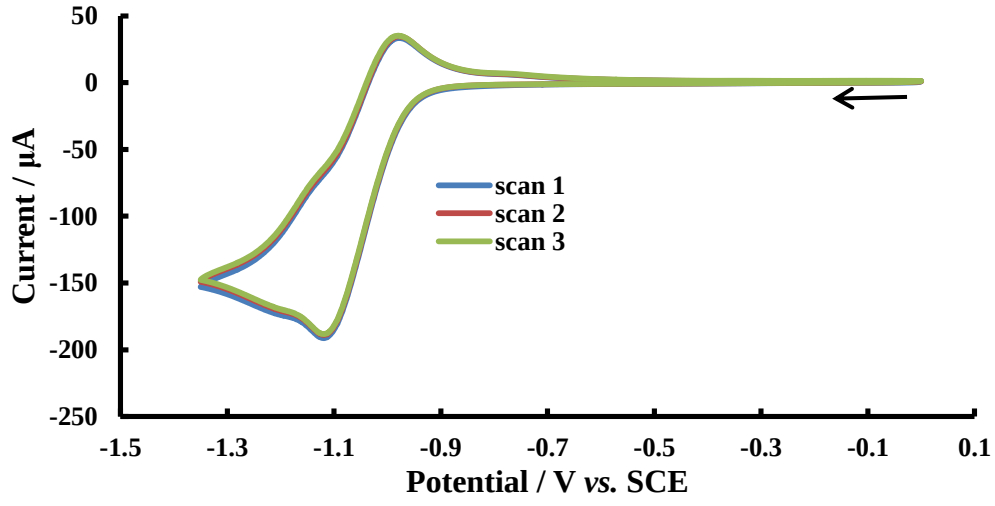

Fig. 5.15. Cyclic voltammogram of reduction of 5.0 mM 1-iodo-4-nitrobenzene on a GCE in MeCN with 0.1 M TBABF4. Repetitive scans is shown at 0.1 V s^{-1} scan rate.

Variable scan rate voltammetry (Fig. 5.16) and subsequent data analysis (Fig. 5.17) for the reduction of iodo-nitrobenzene were then carried out. It is clear that both reductive and oxidative peak current increases with increasing scan rates and peak potentials shifts with increasing scan rates.

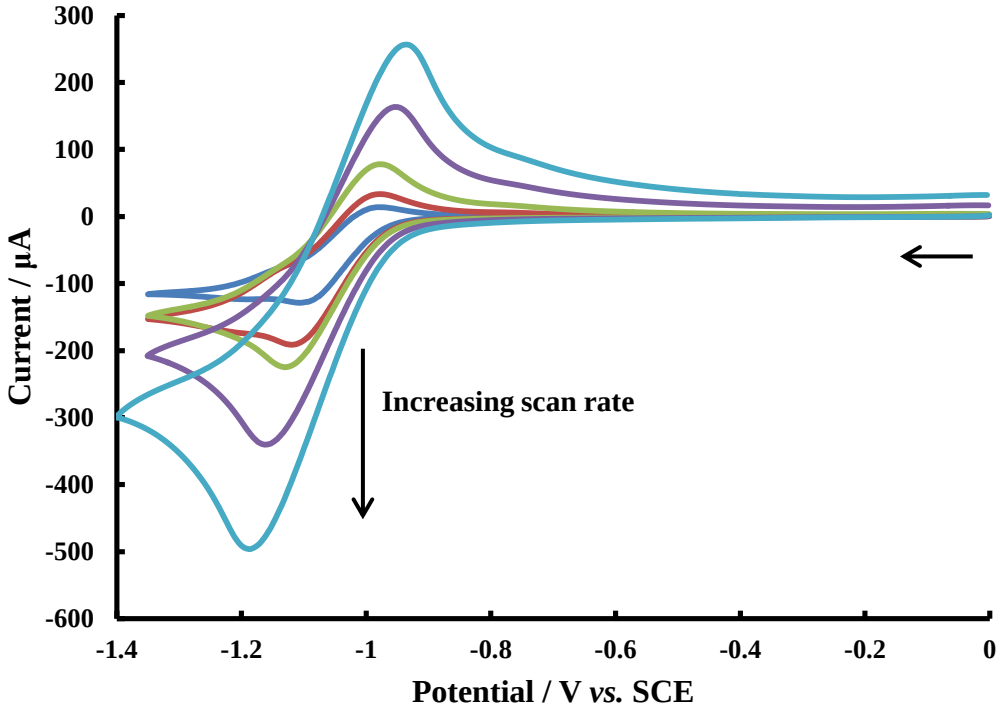

Fig. 5.16. Cyclic voltammogram of reduction of 5.0 mM 1-iodo-4-nitrobenzene on a GCE in MeCN with 0.1 M TBABF4 at different scan rates.

From the data analysis of peak current against square root of scan rates (Fig. 5.17a), clearly that there is a linear dependence between peak current and square root of time scale, suggesting that this process is under diffusion controlled. The slopes of reductive and oxidative peak are similar to each other with reductive peak slightly larger than that of oxidative peak, suggests that the effective number of electrons transferred in reductive process are similar to the oxidative process, with a slight loss of material in the oxidation.

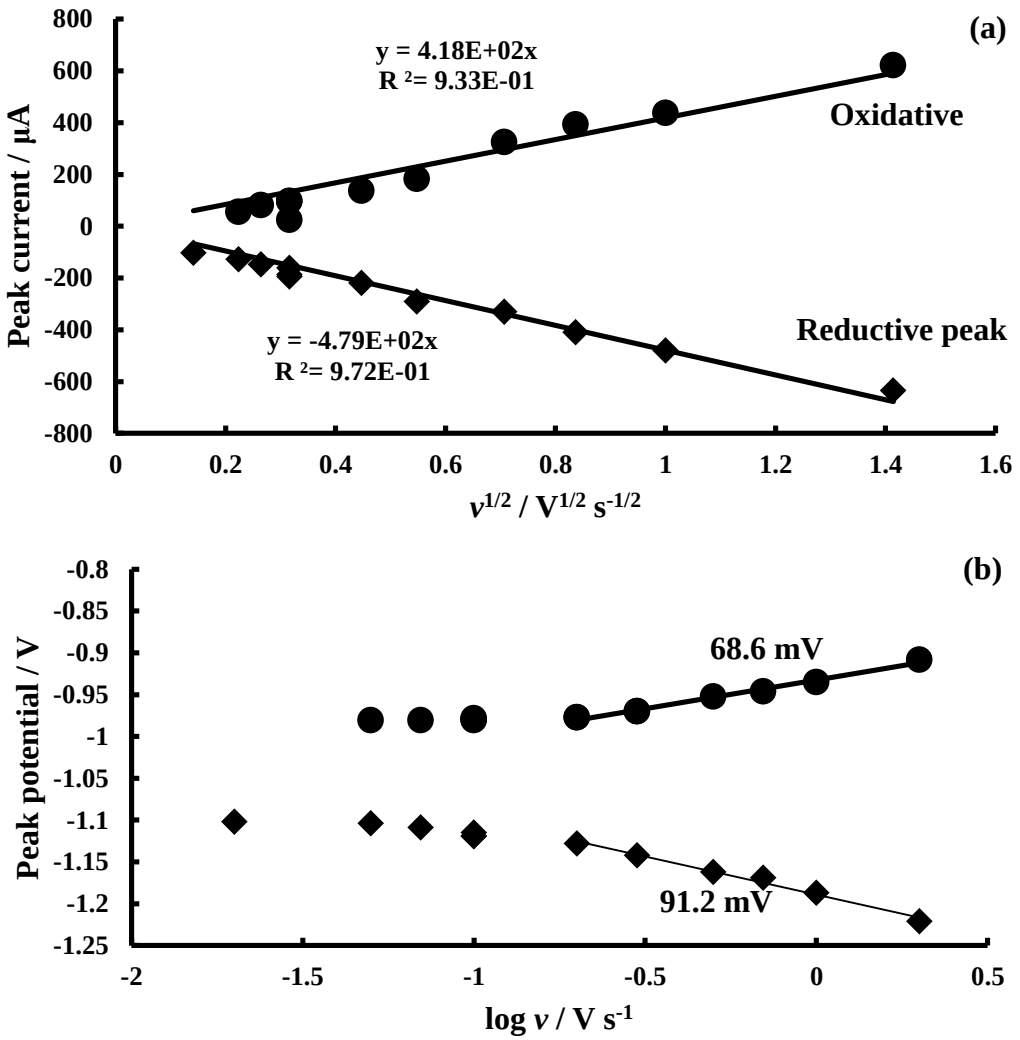

Fig.5.17. (a) a plot of peak current against square root of scan rate. (b) a plot of peak potential against logarithm of scan rate of the reduction of 5.0 mM 1-iodo-4-nitrobenzene at GCE.

The curvature on the graph of peak potential over logarithm of scan rates (Fig. 5.17b) suggests that both reductive and oxidative processes are quasi-reversible.

5.2.2. Effect of iodide ion addition

Iodide ion release was observed by the addition of iodide ion concentration in the solution. By fixing the ionic strength, the change of voltammograms of iodo-nitrobenzene reduction on a 3 mm GCE is shown in Fig. 5.18.

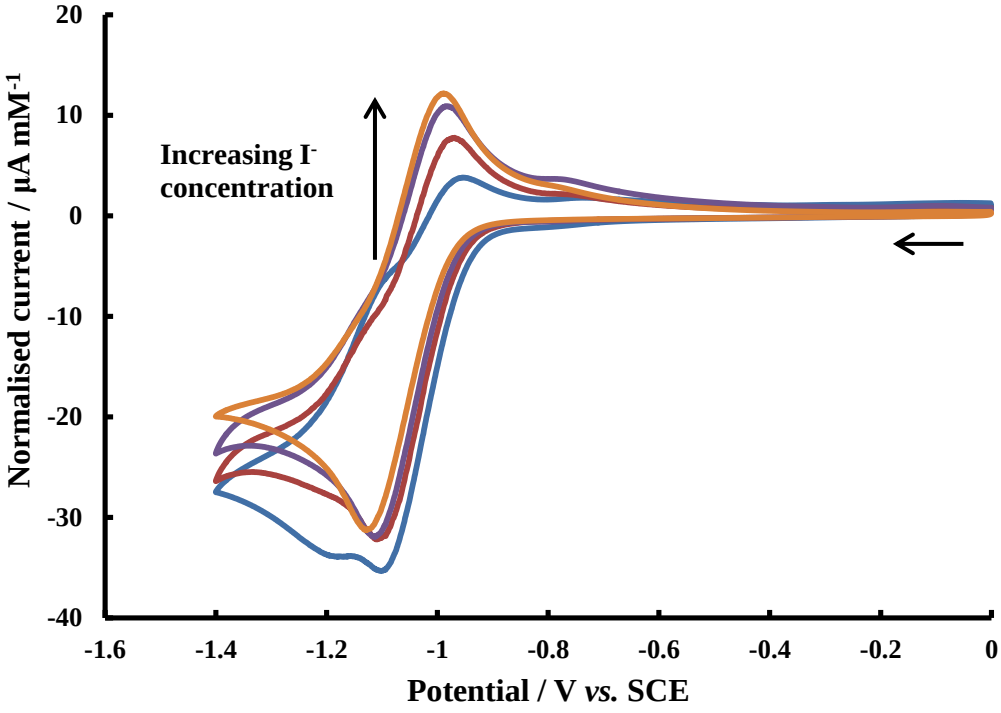

Fig.5.18. Cyclic voltammogram of reduction of 5.0 mM 1-iodo-4-nitrobenzene on a GCE in MeCN with different concentrations of I- whereas the ionic strength is fixed to be 0.1 M.

In addition, although less obvious, the reductive peak current decreased with the increasing concentration of I^-. Considering the step of I^- release (Scheme 5.5), increasing concentration of I^- fasten the back reaction, k_b. Therefore it inhibits the following reduction.

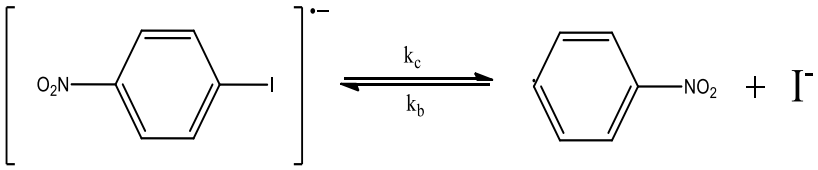

Scheme 5.5.

Same phenomenon has been observed on gold macroelectrode (Fig. 5.19).

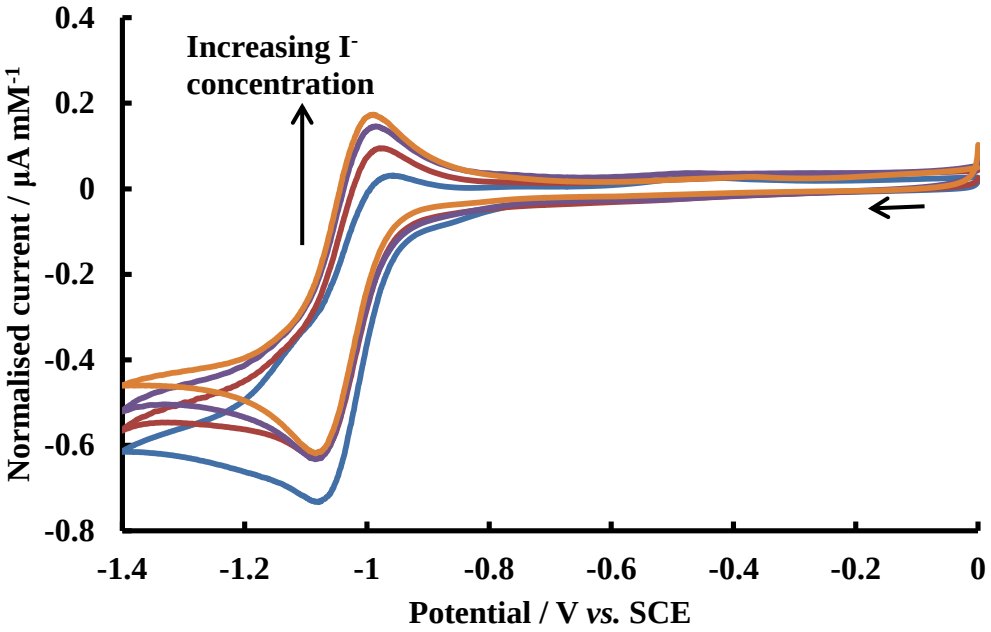

Fig. 5.19. Cyclic voltammogram of reduction of 5.0 mM 1-iodo-4-nitrobenzene on a gold macroelectrode in MeCN with different concentrations of I^- whereas the ionic strength is fixed to be 0.1 M.

Furthermore, the cyclic voltammetry was also carried out using microelectrodes of different sizes (*i.e.* diameters). Fig. 5.20 illustrates the cyclic voltammogram of the reduction of 1.0 mM 1-iodo-4-nitrobenzene at microelectrodes in MeCN/0.1 M TBABF solution.

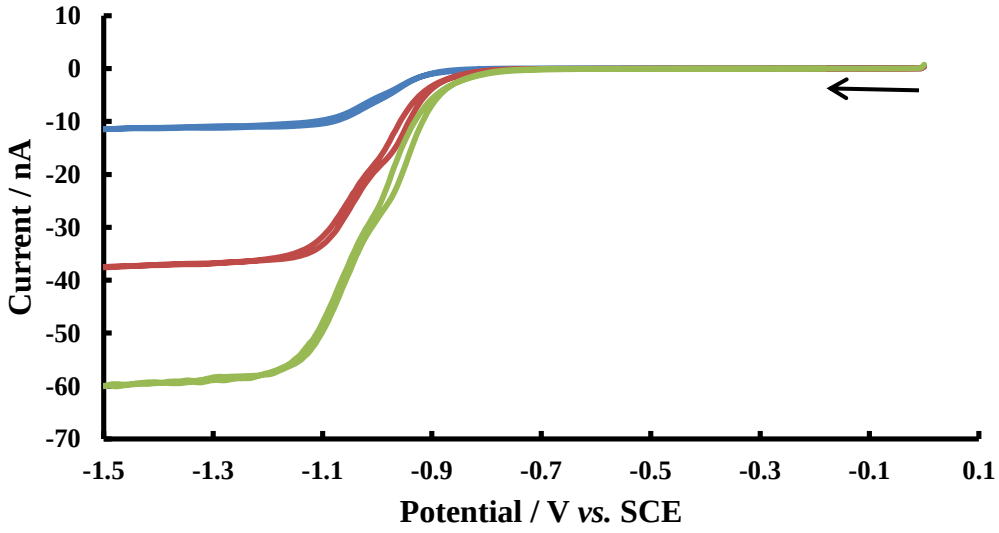

Fig. 5.20. Cyclic voltammogram of the reduction of 1.0 mM 1-iodo-4-nitrobenzene at microelectrodes in MeCN with 0.1 M $TBABF_4$. Blue line: voltammogram at 11 µm carbon fibre electrode; Red line: voltammogram at 33 µm gold electrode; Green line: voltammogram at 50 µm electrode.

As shown in Fig. 5.20, the half wave potential is found to be approximately -1.0 V, which gives a similar value compared to E_p at macroelectrode. The reason for the small shift can be due to the larger resistance on the macroelectrode leads the peak potential shifts more negative.

The effective number of electrons transferred in the process is found to be 2 by applying Eqn. 5.16. This has the agreement with the macroelectrodes data.

$$i = 4nFDr \qquad \text{(Eqn. 5.16)}$$

where all the terms were explained in Chapter 1.

5.2.3. Conclusion

In conclusion, the reduction of 1-iodo-4-nitrobenzene has been studied electrochemically. Reduction process is an ECE process where is I^- released during first the reduction. The release of I^- ion was proved by changing the concentration of I^- present in the solution. With a constant ionic strength, a decrease of reductive peak and an increase of oxidative peak were observed, suggests that the equilibrium was changed by changing the concentration of I^- ion.

5.3. Electrode modification – controlled bromide ion release

The ion release processes studied in previous sections were occurred homogenously in solution phase. However, in really cases, the local environment does not allow the presence of starting materials, a controlled release process from the electrode surface

is then essential. The modification of electrode surface can be then applied in order to release ions without contaminate the local environment by the starting materials.

In electrochemistry, aryl diazonium salts can be grafted onto the electrode surface[181] to afford ion release process. In this thesis, 4-bromobenzenediazonium salt was used to modify the glassy carbon electrode surface. The grafting process is shown in Fig. 5.31.

The aim of this section is to provide a brief understanding of bromide ion release through a chemically modified electrode. If it is successful, then various of ions can be released using the same way to provide an in-vivo ion drug release system.

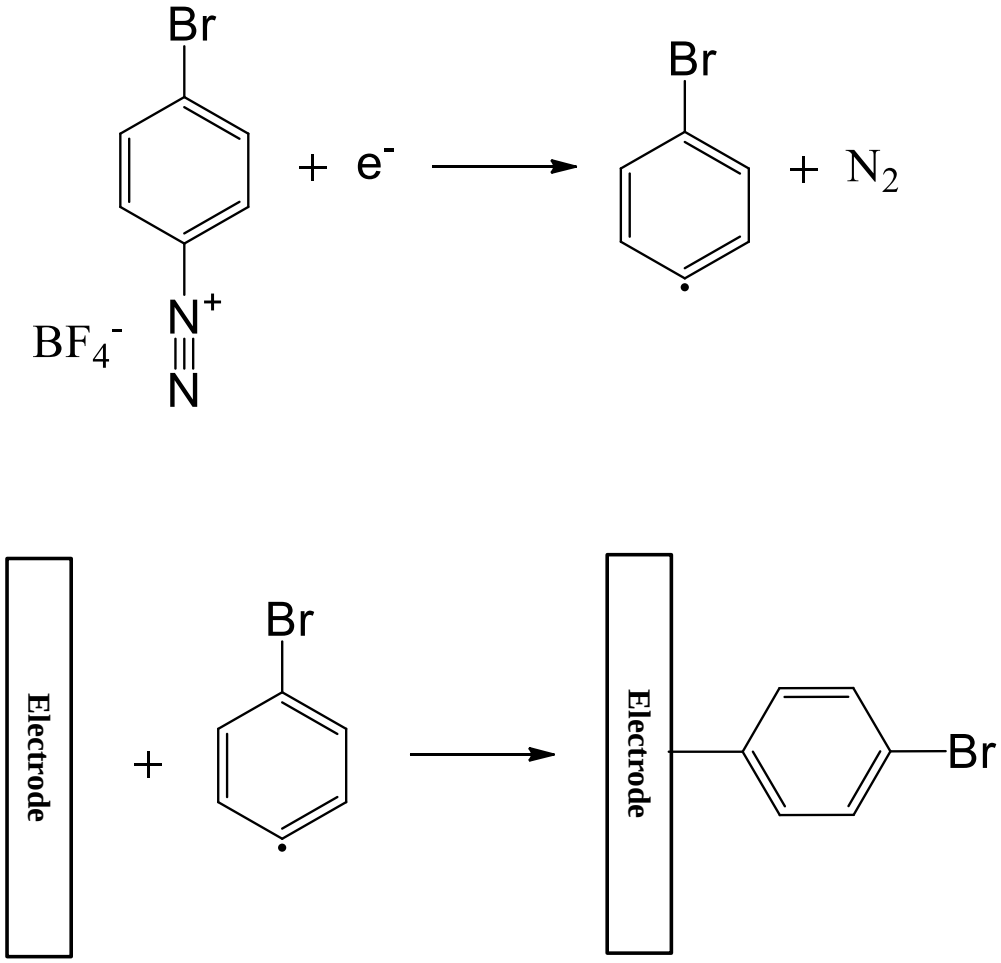

Fig. 5.31. A schematic diagram of the grafting process of 4-bromobenzenediazonium salt onto electrode surface.

5.3.1. Electrode modification *via* reduction of 4-bromobenzenediazonium salt

The initial experiments were carried out in order to reduce the 4-bromobenzenediazonium salt and graft the chemical onto the electrode surface. 2 mM 4-bromobenzenediazonium tetrafluoroborate (BDTB) was dissolved in acetonitrile containing 0.1 M TBAP. Then the BDTB was reduced on a glassy carbon electrode (3 mm diameter, BAS). Fig. 5.32 shows the voltammogram of BDTB scanning potential from +0.8 V to -0.7 V *vs.* SCE.

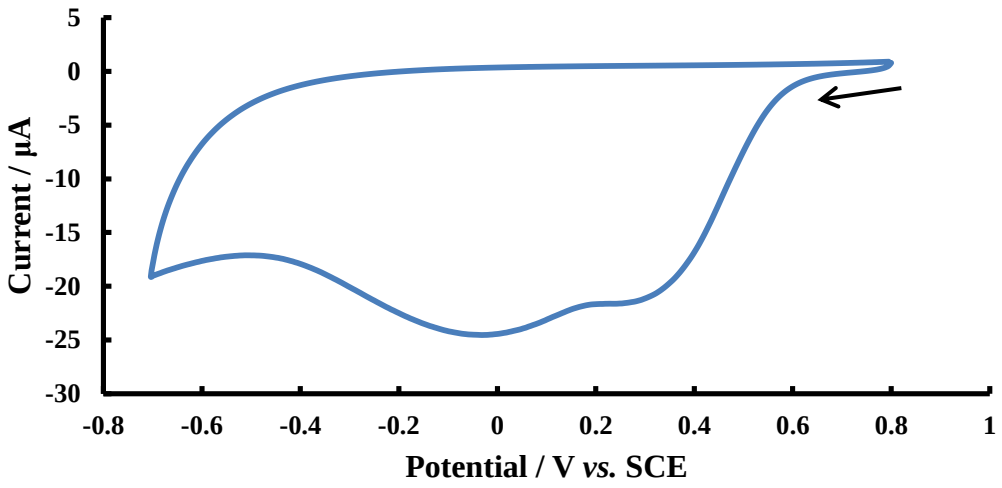

Fig. 5.32. Cyclic voltammetry of the reduction of 2 mM 4-bromobenzenediazonium tetrafluoroborate in acetonitrile with 0.1 M TBAP on a glassy carbon disc electrode (3 mm diameter, iBAS). Scan rate = 0.1 V s^{-1}. A spiral platinum wire served as the counter electrode and a saturated calomel electrode was used as reference electrode.

As shown in Fig. 5.32, a broad reduction wave can be observed at 0 V *vs.* SCE with a pre-absorption wave at +0.3 V *vs.* SCE. The potential is consistent to the reduction of 4-nitrobenzene diazonium tetrafluoroborate[181], suggests that the reduction is due to the reduction of nitrogen as shown in Fig. 5.31.

5.3.2. Electrochemical trigger bromide ion

The modified electrode was then placed in to degased acetonitrile solution which contains 0.1 M TBAP electrolyte. It was then scanned form 0 V to -1.5 V *vs.* SCE three times. The reduction voltammogram is shown in Fig. 5.33.

As shown in Fig. 5.33, there is a reductive peak shows at -1.0 V *vs.* SCE, interestingly, the reverse scan shows that there is a cross over between reduction and oxidation wave at approximately -0.8 V *vs.* SCE. The corresponding oxidation peak appears at +0.4 V *vs.* SCE. Subsequently, after the first scan, the reduction peak for scan 2 and scan 3 shift towards more positively, appears at -0.7 V *vs.* SCE, suggests that the electron transfer process became easier after first reduction scan. In addition, the cross over became tends to less obvious and disappeared while the scan rates increased.

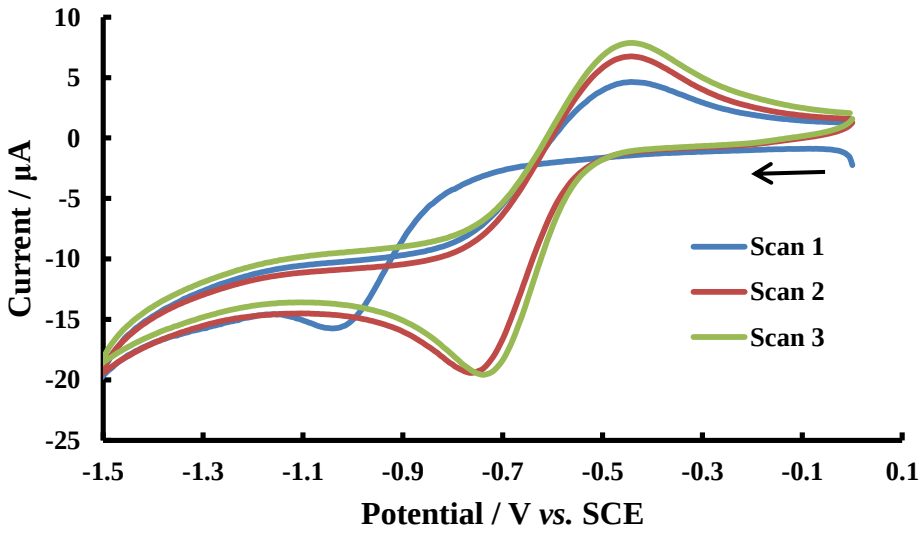

Fig. 5.33. Electrochemical reduction of the 4-bromobenzene modified glassy carbon disc electrode in acetonitrile with 0.1 M TBAP. Scan rate = 0.1 V s^{-1}. Scan 1, 2, 3 indicate the number of scans, respectively. A spiral platinum wire served as the counter electrode and a saturated calomel electrode was used as reference electrode.

Accordingly, the reduction peak of scan 1 can be due to the triggering process of bromide ion into the solution as this process is chemically irreversible. The cross over suggests that less chemicals was re-oxidised than that of reduced, this indicates that the triggering process was occurred successfully, leading:

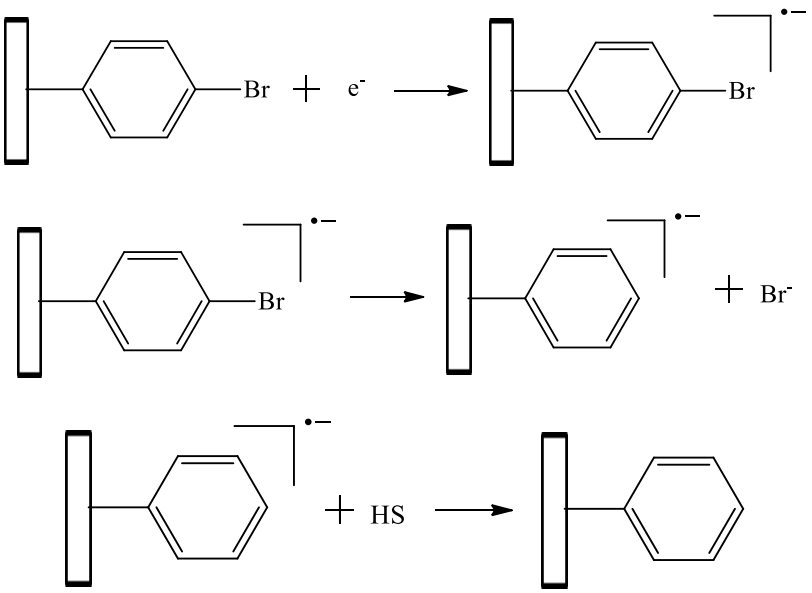

Scheme 5.6

And then follow,

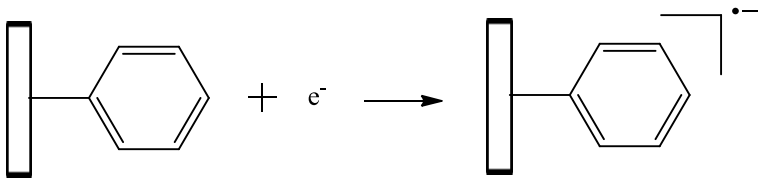

Scheme 5.7

The benzene can be oxidised to form cation radical, which correlates on the graph (Fig. 5.33), is the oxidation wave of first scan, the meachansim is shown in Scheme 5.8.

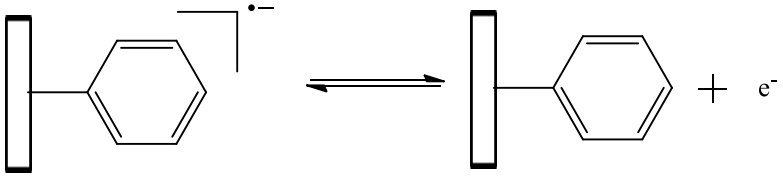

Scheme 5.8

Therefore the 4-bromobenzene was successfully grafted onto the GC electrode surface and bromide ions were triggered from the modified electrode successfully.

5.3.3. Variable scan rates on the modified electrode

In addition, variable scan rates were carried out on the modified electrode surface. Fig. 5.34 shows the plot of peak potential of the reduction peak and the corresponding

oxidation peak of first scan against logarithm of scan rates.

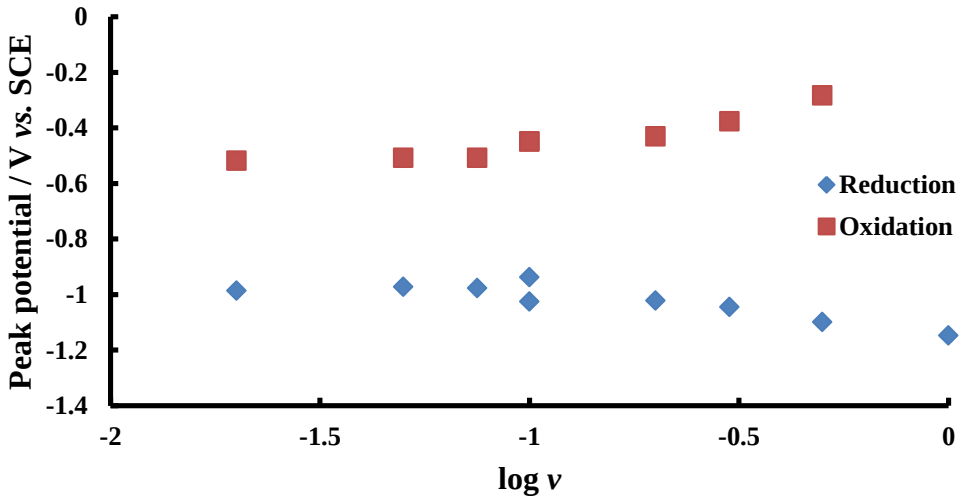

Fig. 5.34. A plot of peak potential of both reductive and oxidative peak of scan 1 corresponding to Fig. 5.33.

Clearly, it can be seen from Fig. 3.32, the both reductive and oxidative peak potential is dependent on scan rates, suggesting that both of the triggering process and the oxidation of surface-attached-benzene are slow.

5.4. Conclusions and future works

In summary, the ion release process was studied for cyanide ion, iodide ion and bromide release. It was found in the cyanide ion release experiments that the addition of electrolyte causes the increase of solution viscosity. The slowed mass transport leads a sluggish kinetics. For the iodo-nitrobenzene experiment, the addition of idodie ion in the solution favours the backward reaction, which has similar effect which is observed in nitroprusside experiment. By comparison, the cyanide ion release is a stepwised process. Moreover, the electrode surface modification by halogen-diazonium salt was carried out successfully, with the success release of bromide ion, leading the ion experiment towards more application side and the halo-benzene modified electrode can undergo Suzuki reaction to form a rather more complex molecular wire[182].

So far, all the electrochemistry experiments were undertaken in liquid, however, liquid crystals have been wide studied recently, therefore, mass transport was then studied in the next chapter.

6. Electrochemistry of Organometallic Lyotropic Chromonic Liquid Crystals

6.1. Chapter overview

The development of lightweight, self-assembling, self-"healing" and flexible molecular wires, over which long-range electron transport my occur, is currently of interest[183] since these empower, *inter alia*, fast and efficient communications[184], "hi-tech" redox-based security systems[185], and, ambitiously, towards redox-controlled logic for molecular computers[186] – systems that can be moulded into the geometries/volumes needed for the pragmatic and ergonomic technologies currently revolutionising modern lifestyles.

Chromonic lyotropic liquid crystals are mesophases which can be formed through the aggregation of dye molecules in water. Two phases maybe formed under different concentrations: of dye at lower concentrations nematic array of columns, known as N phase, can be formed (Fig. 6.1a), with a two-dimensional packed columns, known as M phase, formed at higher concentrations (Fig. 6.1b). Transition metal phthalocyanines[187-191] (Fig. 6.1c) are of interest for since chronomic systems represent an interesting class of metal-organic liquid nanomaterials, which may provide a framework for long-range electron transport for technological exploitation. These systems have no Krafft point or critical micelle concentration and the aggregation monomers are thought to engage in isodesmic π-π stacking to yield the

H-aggregates depicted in Fig. 6.1. These optically and diffusively anisotropic systems have, hitherto, not been characterised electrochemically. The aim of this chapter is to formulate and characterise these systems.

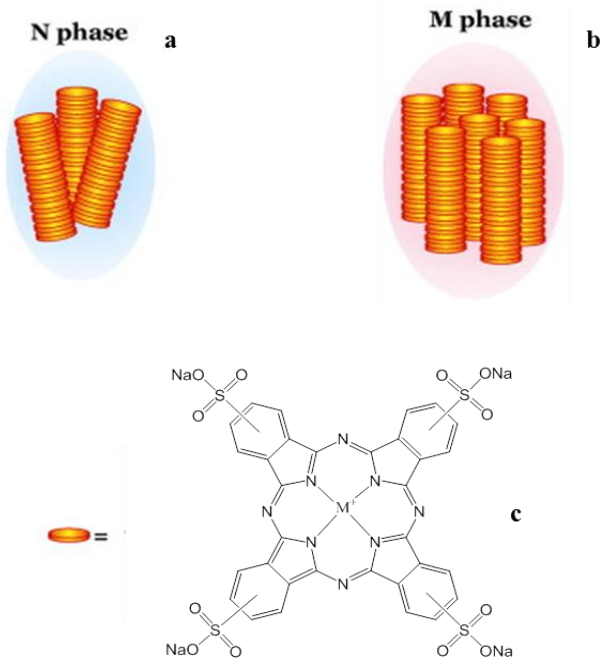

Fig. 6.1. Schematic diagram of N (a) and M (b) phases of chromonic lyotropic liquid crystals based on tetrasulfonated phthalocyanines (c).

This work has been published in *Electrochem. Commun.*; the candidate acknowledges the help of J. E. Halls, R. W. Bourne, K. J. Wright, L. I. Partington, M. G. Tamba, T. Ramakrishnappa, G. H. Mehl, S. and M. Kelly in assisting this work.

6.2. Results and discussion

The M and N chronomic phases formed using either copper(II) or nickel(II) phthalocyanine tetrasulfonic acid tetrasodium salt are studied in this chapter.

6.2.1. Structural studies

Two different phases were characterised in this project. N-phase of nickel(II) complex was observed only at 20 wt.% (0.26 M) in aqueous containing sodium hydroxide at pH 8 as shown in Fig. 6.2a. As shown in the graph, Schlieren textures can be observed

under crossed polariser. The N-phase of copper(II) complex can be observed with concentration greater than 27 wt.% (0.38 M) and the M-phase occurring at 46 wt.% (0.88 M), as shown in Fig. 6.2b.

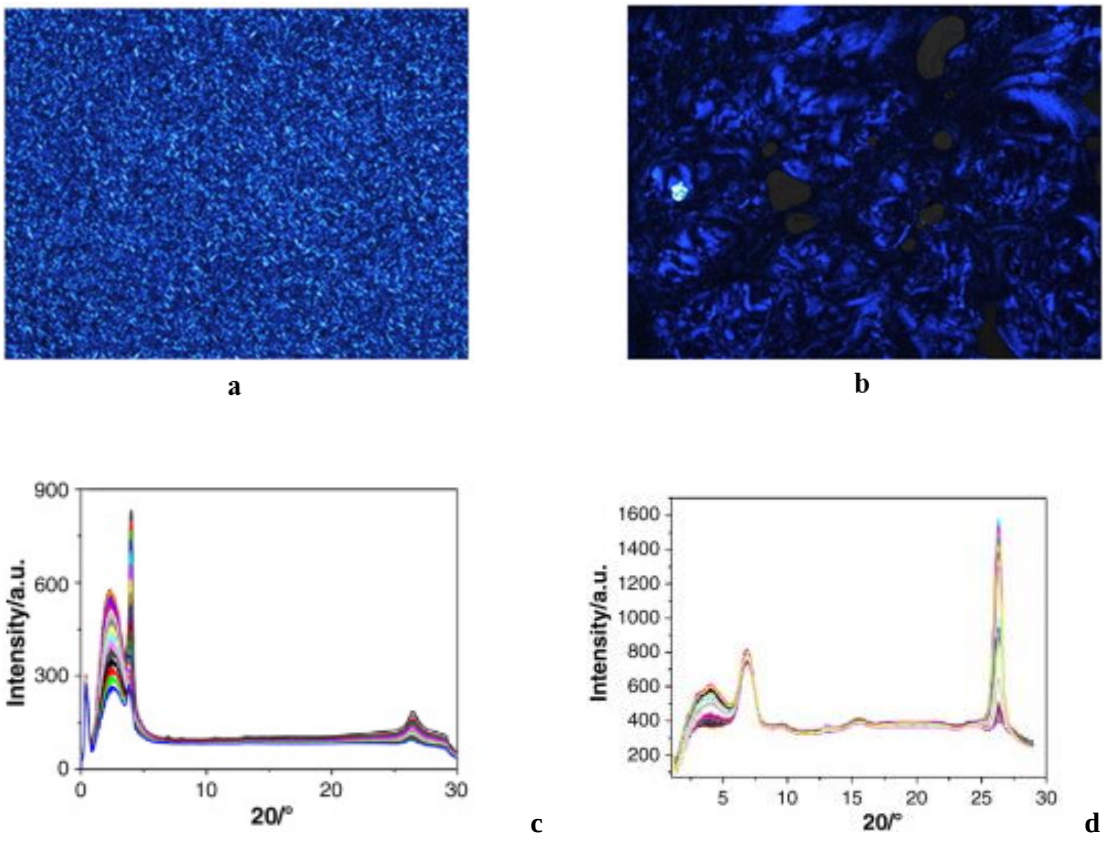

Fig. 6.2. Textures of (a) Nickel(II) complex of N-phase and (b) copper(II) complex of M-phase optical polarising microscope and X-ray scattering patterns for Nickel (II) complex (c) and copper(II) complex (d).

UV-Vis and X-ray scattering measurements were also carried out. The extinction coefficient for Ni(II) complex was found to be 46970 M^{-1} cm^{-1} (λ_{max} = 623 nm) and 25236 M^{-1} cm^{-1} (λ_{max} = 613 nm) for Cu(II) complex, as shown in Fig. 6.2. All the physical characteristics of N and M chromonic liquid crystals are shown in Table 6.1. It was also found that the intramolecular marcrocyle separation is 3.4 Å using X-ray scattering. The aggregation length was found to be 43.5 Å for Ni(II) complex and 30.7 Å for Cu(II) complex, suggesting that there are 13 molecules per aggregate for Ni(II) complex and 9 molecules per aggregate for Cu(II) complex.

Table 6.1. Physical characteristics of the N and M lyotropic chromonic liquid crystals prepared.

	N phase Nickel (II) phthalocyanine tetrasulfonic acid tetrasodium salt (0.26 M) in water with pH 8			M phase copper (II) phthalocyanine tetrasulfonic acid tetrasodium salt (0.88 M) in water									Isotropic solution 0.1 M aqueous KCl
ρ^a/Ω cm	12.70			9.17									11.29
R^b/Ω	5773			4585									
$C_d{}^c$ / mF cm^{-2}	12.3			2.1									
X-ray 2θ/°	2.03	3.99	26.5	2.88	4.07	6.81	10.5	13.0	15.6	21.2	24.4	26.3	
scatter d^d/Å	43.5	22.1	3.36	30.7	21.7	13.0	8.45	6.78	5.68	4.18	3.64	3.39	
ing q^e/Å^{-1}						0.485	0.744	0.926	1.11	1.50	1.73		
data $^fq/q_0$						1.00	1.53	1.91	2.28	3.10	3.56		
Assignment	length	width	spacing	Length	Width	q_0	$q_0\sqrt{3}$	$2q_0$	$q_0\sqrt{7}$	$3q_0$	$2q_0\sqrt{3}$	spacing	

[a] Resistivity measured at 293 ± 1 K.

[b] Resistance determined using $R = \rho/(4r_0)$ with r0 = 5.5 μm (N-phase) or 5.0 μm (M-phase).

[c] Specific double-layer capacitance inferred from cyclic voltammetry.

[d] Fundamental crystal spacing determined using $d/A = 1.54/(2\sin\theta)$.

[e] Scattering vector estimated through $q = 2\pi/d$.

[f] q0 is the fundamental repeat distance in the hexagonal system (*viz.* the centre-to-centre separation between [cylindrical] aggregates).

6.2.2. Electrochemical characterisation

The oxidation of 0.26 M of Nick(II) phethalocyanine tetrasulfonic acid tetrasodium in water salt at pH 8 and 0.88 M Copper(II) phethalocyanine tetrasulfonic acid tetrasodium salt in water on a 3 mm diameter glassy carbon disc electrode is shown in Fig. 6.3 and Fig. 6.4. For the Ni(II) system (Fig. 6.3a), two one-electron waves are observed, at +0.7 and +0.9 V *vs.* Ag/AgCl, as in dilute solutions[192, 193], and which are attributed to phthalocyanine ligand-based oxidations. Variable scan rates were carried out with direct proportionation between the peak current and the square-root of scan rate (Fig. 6.3b), indicates a diffusion-controlled nature and consistent with quasi-reversible electrode kinetics (Fig. 6.3c).

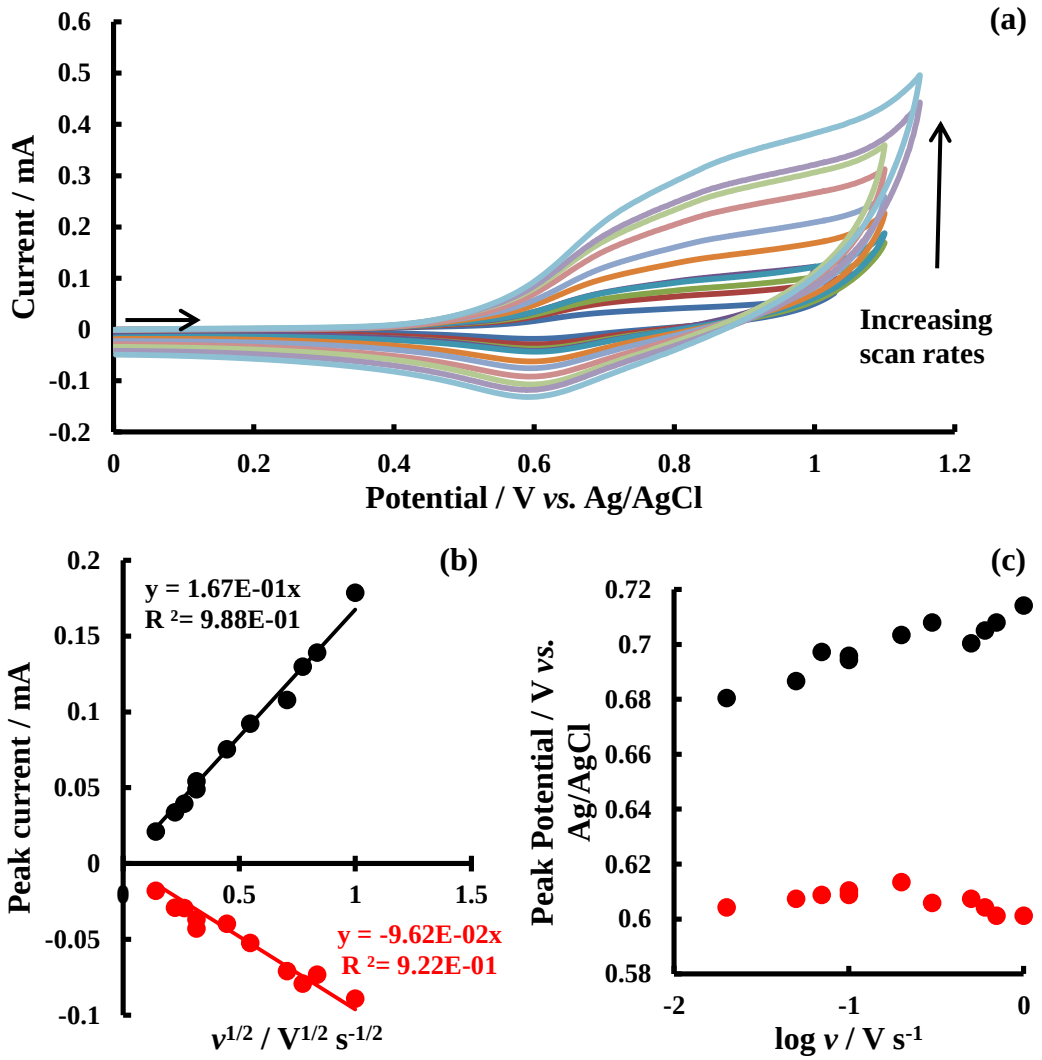

Fig. 6.3. Electrochemical oxidation of Nickel(II) phthalocyanine tetrasulfonic acid tetrasodium salt chronomic lyotropic liquid crystal (20 wt.%) using cyclic voltammetry in variable scan rates, (0.02 V s^{-1} ≤ v ≤ 1 V s^{-1}) (a), at a 3 mm diameter glassy carbon electrode, a spiral nickel wire served as counter electrode and silver/silver chloride reference electrode was applied. (b) a corresponding plot of peak current against square root of scan rates for both oxidation peak (black) and reduction peak (red). (c) a corresponding plot of peak potential against decade change of scan rates for the oxidation peak (black) and reduction peak (red).

In contrast, the Cu(II) system exhibits a single oxidation wave as shown in Fig. 6.4a with oxidation peak appears at between +1.4 V and +1.9 V *vs.* Ag/AgCl depending on the scan rates. This phenomenon was also observed in dilute aqueous solution[192, 194], also thought to orginate from ligand oxidation in a complex, multi-electron transfer process. Variable scan rates experiments afford, again, direct proportionation between the peak current and the square-root of scan rate (Fig. 6.4b), which suggests a diffusion-controlled nature and consistent with quasi-reversible electrode kinetics (Fig.

6.4c).

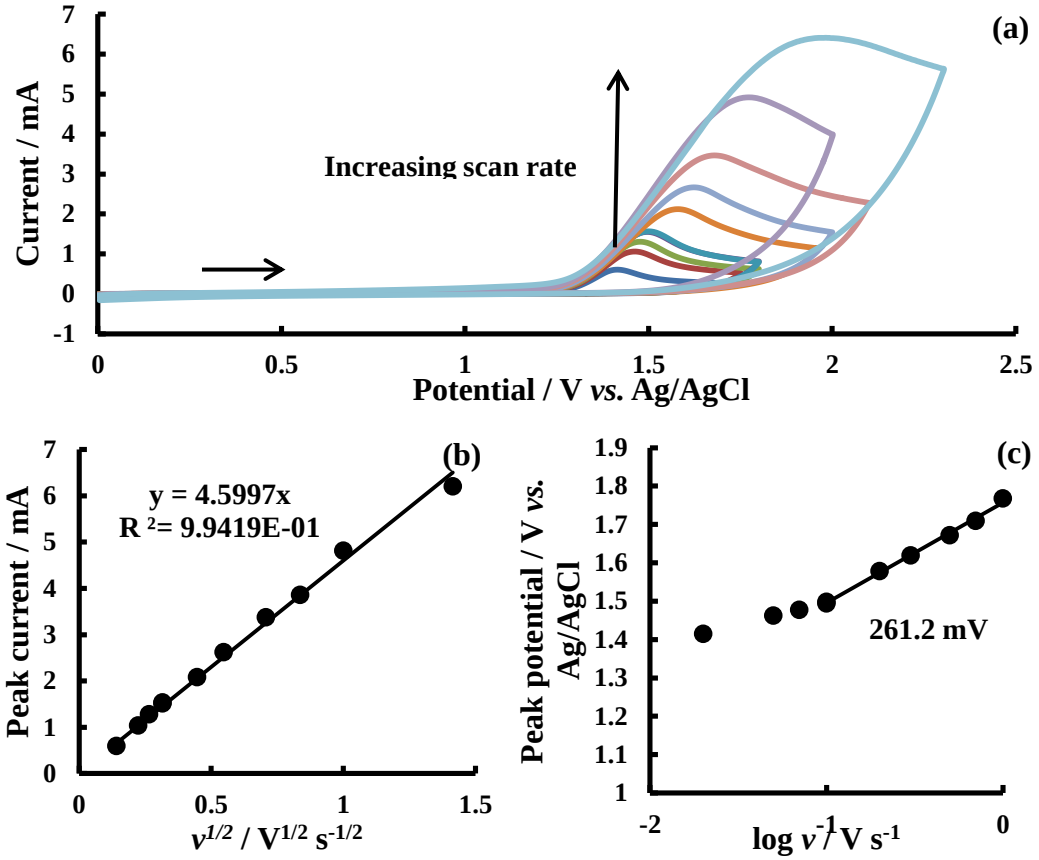

Fig. 6.4. Electrochemical oxidation of copper(II) phthalocyanine tetrasulfonic acid tetrasodium salt chronomic lyotropic liquid crystal (27 wt.%) using cyclic voltammetry in variable scan rates, (0.02 V s^{-1} ≤ v ≤ 2 V s^{-1}) (a), at a 3 mm diameter glassy carbon electrode, a spiral nickel wire served as counter electrode and silver/silver chloride reference electrode was applied. (b) a corresponding plot of peak current against square root of scan rates for the oxidative peak. (c) a corresponding plot of peak potential against decade change of scan rates.

Both of the Ni(II) system and Cu(II) system data are entirely consistent with aggregate diffusion or charge transport between aggregate stacks, given that Cu(II) phthalocyanine itself is considered to be a prototypical organic semiconductor,[194] therefore intra-aggregate charge transport should be very fast.

The reduction of the M phase 0.88 M copper(II) phthalocyanine tetrasulfonic acid tetrasodium salt in water at a Pt microelectrode was also carried out as microelectrodes offer better insight of the 2-D anisotropic structure.[195] It can be seen in Fig. 6.5 that the reduction on microelectrode affords waves instead of sigmoidal shape, which are not at steady-state, but are consistent with a two-electron process

with following slow, irreversible chemical reaction[192], with $\sqrt{D_r D_z}$ ~ 10^{-13} m^2 s^{-1}.[196]

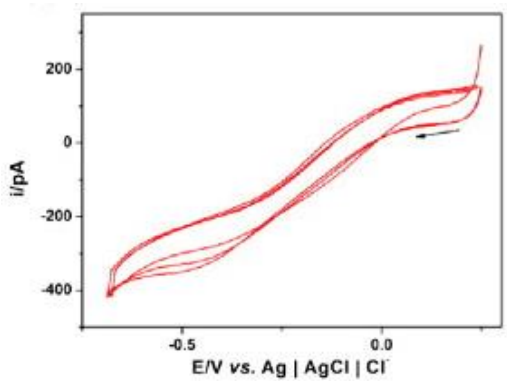

Fig. 6.5. Cyclic voltammetry of the Cu(II) system reduction on a 10 μm diameter platinum microdisc electrode. a spiral nickel wire served as counter electrode and silver/silver chloride reference electrode was applied.

In order to assess the occurrence of anisotropic diffusion within these ordered, ionic aggregates, micro-disc potential-step chronoamperometry experiment was carried out for both systems, potentiostating the electrode after the two-electron oxidation waves. This methodology has been used in previous work[196]. Likewise the method mentioned in the introduction chapter, the dimensionless current-time for both experimental data and theoretical data need to fit each other. Unlike the normal solution environment, the diffusion coefficient in the normal direction, *i.e.* perpendicular (D_z) is different from that of the tangential (D_r) to the electrode surface. Therefore the equation is modified to fit these two parameters:

$$\psi = \frac{i}{4nF\sqrt{D_z D_r}ac_{bluk}} = 0.7854 + 0.8862\tau^{-0.5} + 0.2146\exp(-0.7823\tau^{-0.5})$$

(Eqn. 6.1)

where n = 2, F is the Faraday constant *viz.* 96484.6 C mol^{-1}, a is the microelectrode radius, cbulk is the effective homogeneous concentration of the redox system. τ is the dimensionless time variable as described in introduction chapter. The fitting is employed by varying D_z and D_r within in a reasonable range ($-17 \leq \log D_i / m^2 s^{-1} \leq -8$,

with *ca.* 10% uncertainty). The difference minimisation parameter, $\wp$, which is also illustrated in introduction chapter, is applied to find the best fit over the whole normalised temporal domain. As shown in Fig. 6.6, both of copper(II) and nickel(II) systems fit reasonably well over the most temporal domain. It is found that Dr for the nickel(II) N phase system is $3.8 \pm 0.4 \times 10^{-8}$ cm^2 s^{-1} and D_z is $2.2 \pm 1.5 \times 10^{-9}$ cm^2 s^{-1}, whereas, for the copper(II) M phase system, D_r is found to be $1.2 \pm 0.9 \times 10^{-8}$ cm^2 s^{-1} and D_z is found to be 4.4 $\pm$ 1.7 x 10-11 cm^2 s^{-1}. Note that the chronoamperometric experiment for Ni(II) system was oxidation, whereas for Cu(II) system was reduction, as those two processes are well-known and widely available from literatures, unlike the complex ligand oxidation process for Cu(II) complex or oxygen affected Ni(II) complex reduction.

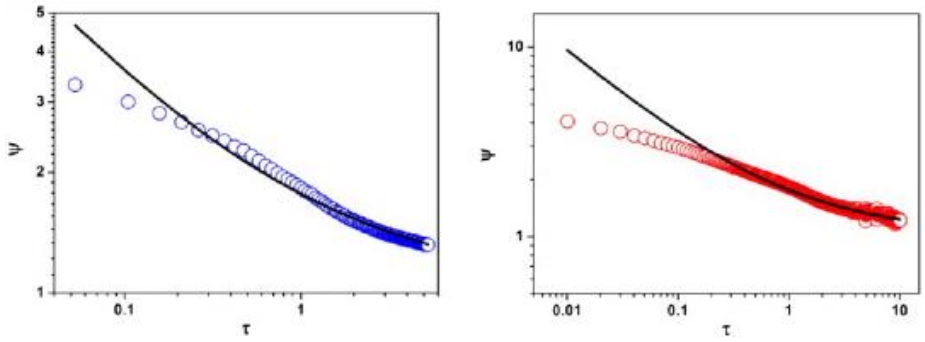

Fig. 6.6. Reduced space chronoamperometric transients corresponding to the two-electron oxidation of the Ni(II) system (blue) with a 11 μm diameter carbon fibre microelectrode, potential was held at 1.06 V *vs.* Ag/AgCl; and two-electron reduction of the Cu(II) system (red) with a 10 μm diameter platinum microelectrode, potential was held at -0.7 V *vs.* Ag/AgCl. Both the open circles represent the experimental data and solid lines represent the theoretical fit. A spiral nickel wire was used as counter electrode.

According to the D_r and D_z for both Cu(II) and Ni(II) systems, the diffusion is faster in the direction radial to the electrode surface compared with that in the perpendicular direction. The anisotropic ratios of D_r/D_z is found to be ~20 for Ni(II) system and ~300 for Cu(II) system, respectively. It can be due to the presence of the electric field at the electrode surface, which can orientate the stacks, so that the peripherial functionalities are located close to the electrode surface as shown in Fig. 6.7. The stacks adopt a homogenous alignment in the electrochemical around the electrode surface, so that in both Ni(II) and Cu(II) systems, D_r represents the transport of

electrons along the stacks and limited by the thermal basculation (*i.e.* the size of aggregate), and D_z represents the electron transport between columnar aggregates, and therefore D_z is smaller in M-phase compared to that of in N-phase as M-phase affords worse lateral aggregate electronic couplings, as expected. Note that aggregate distances are at least on the order of q_0, a Dahms-Ruff view suggests bimolecular electron hopping kinetics between aggregates in the direction perpendicular to the stack ordering of 1 x 10^6 M^{-1} s^{-1} for Ni(II) system or 6 x 10^3 M^{-1} s^{-1} for Cu(II) system, allowing for the inference of Einstein mobilities in this direction of 2 x10^{-7} cm^2 s^{-1} V^{-1} for Ni(II) system or 3 x 10^{-9} cm^2 s^{-1} V^{-1} for Cu(II) system.

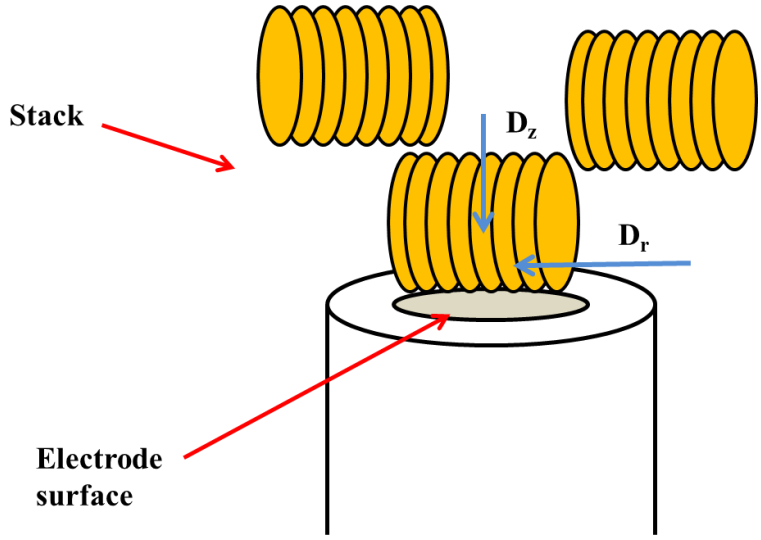

Fig. 6.7. A schematic diagram of electron transfer directions in both of the Ni(II) and Cu(II) systems.

The diffusion coefficient values are lower than that of in dilute aqueous solution consistent with the greater viscosities of the highly concentrated redox liquid crystals. As shown in Fig. 6.7, the theoretical data only fits the experimental data after $\tau \sim 0.2$ for Ni(II) and 0.5 for Cu(II), suggesting that the diffusion model overestimates the current at a short time period, which can be due to adsorption or electro-induced orientation effect. The orientation effect may stem from the degree of counterion condensation onto the stacks, with the Cu(II) system being less ionised than that of the Ni(II) system due to the lower double layer capacitance on Cu(II) system. This effect was recently modelled theoretically by Chami *et al.*[197] on sunset yellow

chromonic liquid crystal.

6.3. Conclusion

Self-assembling chromonic liquid crystals within the nematic phase allow routes for diffusion (physical transport or through carrier hopping) to occur in at least two dimensions. Mobilities are likely affected by the size of the gaps between aggegates, mesogens stacks and stack defects. It is not clear whether the nature of the metal centre is significant compared with the order of the structured liquid nanosystem; the archetypal molecular semiconductor, copper(II) phthalocyanine is known to have a complex electronic structure caused by overlap of the metal 3 d levels with the ligand 2p orbitals, leading to both localised and delocalised states at the Fermi level, which can be distorted by the presence of dioxygen. The exact role played by peripheral group dissociation has not been unravelled; the extent of this may be controlled by the applied electric field, encouraging phase alignment and migrative structuring of the phase, in a manner similar to that proposed for room temperature ionic liquids, or through local changes in proton concentration.

Hetherto, this thesis has been concerned with the development of molecular electrochemical systems for applications in sensing systems and protocols. The next chapter moves to examine the effect of the specific electrochemical waveform perturbation on the response of and electrochemical device.

7. Computing Simulation of Energy Storage via Battery Systems

The work presented in this chapter was undertaken with assistance from J. E. Halls, A. Hawthornthwaite, R. J. Hepworth, N. A. Roberts, K. J. Wright, S. J. Haswell, S. K. Haywood and S. M. Kelly.

7.1. Introduction

The increased electrification of energy consumed by the end users necessitates the deployment of efficient and strategic routes for the energy which it can be both generated and stored[198, 199]. In order to employing automated information and communications intelligence on both supplier and consumer to improve the distribution efficiency, sustainability and economics (through the promotion of competition), the "smart grid"[200], which are storage systems allow for a fluidity in energy provision through load levelling peak shaving or energy arbitrage through differential pricing approaches, *viz.* in storing surplus energy generated during off-peak times, with grid support during times of high demand. Large scale redox flow batteries[201-203] (which are typically used for applications requiring kW power scales, but can be deployed for MW-GW scale), unlike other forms of energy storage (compressed air or pumped hydropower) are highly attractive and cost-effective for these applications, and especially for uninterrupted/backup supplies, as they are not limited to particular geographical locations, whilst being able to maintain the advantages of the rapidity of energy provision afforded by alternatives (~1-10 min), through deep discharge under conditions of *ambient temperature and pressure* (whatever those may be); Stirling engines (for compressed air energy storage) rely on

temperature differences so require some form or heating/cooling, superconducting magnetic energy storage requires very low temperatures, whilst efficient storage in flywheels is limited by the maintenance of vacuum conditions. Furthermore, redox batteries are *closed loop* systems are not limited by the availability of any fuel source, and require no external input (except electricity), making them suitable for underground installation, or even for use in electrical vehicles.[204, 205]

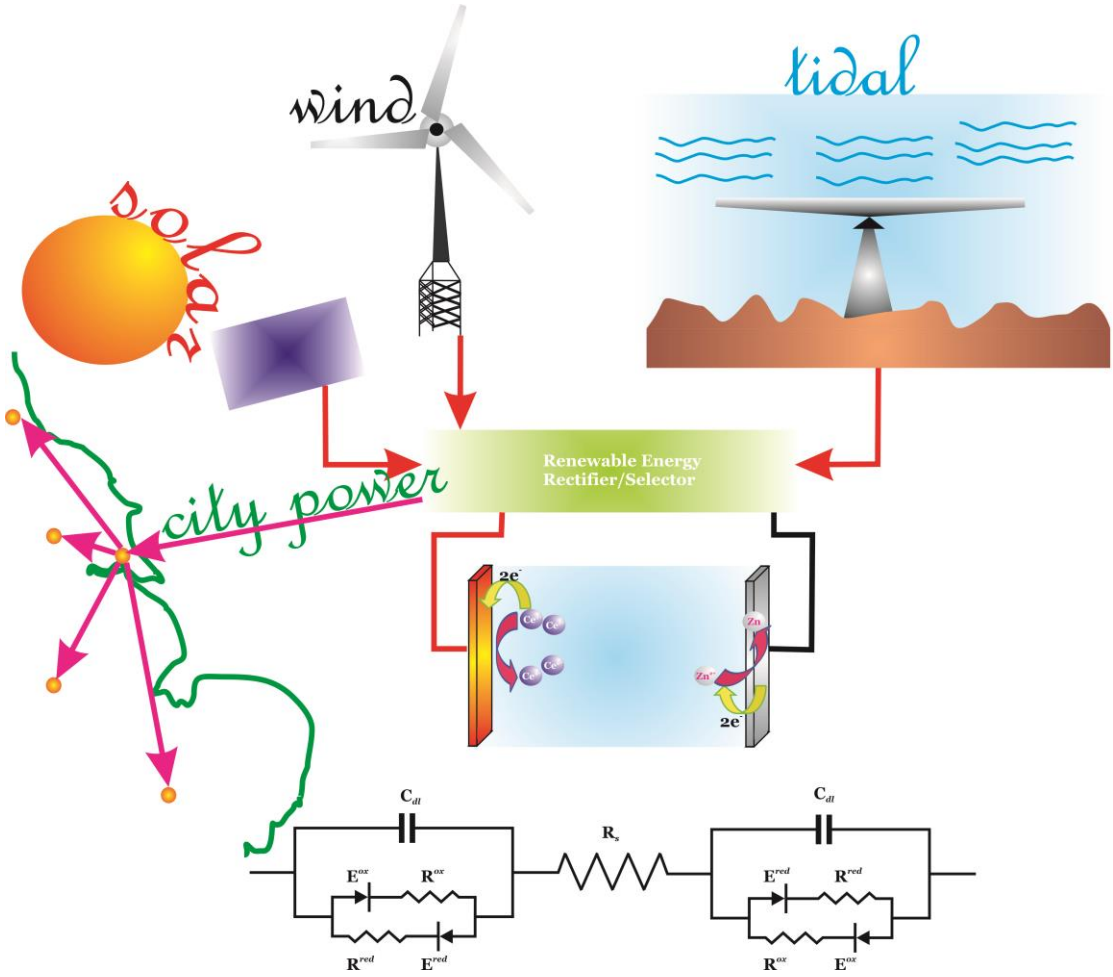

Fig. 7.1. Cartoon illustrating the approach taken in this work: solar, wind or tidal power is generated and used to charge-up a cerium-zinc redox battery, with the latter used to power cities. The rectifier/selector system also contains invertors to reconvert the battery DC output into AC. Note that for the tidal power case, we have chosen to depict the oscillating hydrofoils pioneered by Pulse Tidal (http://www.pulsetidal.com; accessed on 1 August, 2012) which sweep up and down, as demonstrated within the River Humber, Hull. Also illustrated is the electrical circuit equivalent to the battery system.

Although these flow battery systems have been quoted[203] to have energy efficiencies (ratio of energy generated during discharge to energy utilised for charging) of 70-90%,

the pumping of the electrolyte consumes ~10-15%, so that practical energy efficiencies are closer to *ca.* 60%. Nevertheless, several installations utilising redox flow batteries already exist, such as the ZBB Energy Corp zinc bromine system utilised at military bases, or for elevator back-up at NIDON Clean Energy, Hawaii, USA[206], and Cellenium's vanadium redox battery system operational since December, 2008 in Thailand[207]. The integration of battery-stored renewable energies into electricity grids then requires infrastructure capable of managing the direct currents (DC) generated by batteries. These days, this is not such a major issue as it first appears, given the requirements of modern technology devices (such as computers, mobile accessories, *etc.*) which utilise DC and the development of DC microgrids,[208] coupled with advances in invertors, high power semiconductor thyristors and insulated gate bipolar transistors; although transmission through high voltage, low alternating current (AC) won the so-called "Current Wars", high voltage DC (HVDC) is considered to be more economical for transmission over long distances (especially underwater), whilst suffering lower electrical losses, even though it requires a single point of origin and termination.[199] Such long distances typically occur between areas of renewable energy availability (for electricity generation) and regions of human civilisation (for electricity consumption).[199] This is exemplified through the Xianjiaba Dam to Shanghai, China line commissioned in 2010 (which operates at 800 kV – approximately the upper DC limit due to corona discharge, delivering 6.4 GW over 1980 km),[209] the Rio Madeira link soon to be commissioned between Porto Velho (Amazonas) and Araraquara (São Paulo State), Brazil (to operate at 600 kV so as to deliver 3.15 GW power over in excess of 2500 km) – the World's longest HVDC line,[209] and the East West Interconnector from Country Dublin to close to Liverpool, connecting the Irish grid with the UK grid (200 kV at 500 MW, with 75 km underground and 186 km submarine cabling), allowing excess wind power generated in Ireland to be exported to the UK.[209]

It then follows that the efficient storage of renewable energies requires sufficient *capability* to adapt to the uncertainties in the weather characteristics (which may last

from seconds to days), and which may affect up to 70% of daytime solar (on cloudy days), and 100% wind (on calm days),[199] thereby causing the maximum power load factor (ratio of average available power to rated power) of the renewable energy transducer to be significantly smaller than unity, since the output is related to the power input. Existing installations of redox batteries coupled to solar and/or wind include the all-vanadium system installed by Prudent Energy[210] or Sumitomo Electric Industries, Ltd.[211] (who commissioned the world's largest redox flow battery in July, 2012), or the zinc-bromine system developed by RedFlow, Ltd.[212]

But this is not all – energy abundance during windy, clear sky (with air mass, AM 1.5) days at, say, tidal barrages, is naturally affected by the *temporal variation* in the renewable energy form (the sun rises and sets, and winds blow and cessate, with tides that rise and ebb periodically based on Moon-Earth-Sun gravitational interactions), and which translates into time-dependent electricity generation; storage efficiency of this electrical energy through charging galvanic cells would thus appear to be commanded by the *type* of renewable energy, and its amount. This governance relationship is often overlooked in comparing renewable energies, and we seek to unravel its significance within this work.

An understanding of the DC current generation characteristics of biofuel burning/wind, tidal and solar power (see the cartoon in Fig. 7.1) were first developed, and of the use of these to control the single cycle charging of cerium-zinc redox battery system pioneered by the now defunct Plurion, Ltd.,[213-217] since this cell chemistry has recently been shown to exhibit promising operational characteristics within a membrane-free (undivided) cell,[214] and, hitherto, no mathematical model has been offered to simulate its chemistry.[201-203, 218-223] Such cells, though not employed in any large scale system as yet, are highly attractive, given the extent of power loss (i^2R) through the costly separating membrane (of typical electrical resistances between 1 – 10 Ω cm^{-2}) that is generally employed, and preclude the otherwise necessary consideration of junction potentials; in any cases, we are

interested in the *efficiency of charging* the battery, rather than battery optimisation.

7.2. Diffusion Model for Battery Charge and Discharge

7.2.1. Classification of renewable energy current generation characteristics

Whilst battery systems require DC for charging, owing to the occurrence of Faradaic electrolysis, of the renewable energies considered here, only solar photovoltaic or the less popular photogalvanic systems immediately and exclusively provide a DC output; the other rely on the induction of current through conductor motion within a magnetic field – turbine generation, which affords AC in the armature, or DC (if subsequently rectified, or through the use of split-ring commutators). Bearing this in mind, we may classify individual renewable energies through their characteristics profiles for power generation, as has very recently been undertaken by Aziz.[224] However, these are directly related to the temporal variations of their impact on a turbine: in an approximately twelve hour day period, biofuel burning can be made to achieve a constant current output, or, if so desired, an output that could change with time; wind, if present due to a land-sea breeze, is variable about a constant level; tidal current output varies in a sinusoidal manner on a diurnal (24 h) or semidiurnal timescale. Even solar power generation is time dependent owing to its dependence on light intensity; clear sky (AM 1.5) days at the Equator afford a semi-elliptical power generation rate, peaking at 12H00, followed by a resting state. It follows that, if the idealised renewable energy power generator operates on a windy, clear day at a tidal barrage near the Equator, the battery charging current is of a form characteristic of the energy exploited.

The formulation of equations for these current outputs for our purposes, however,

causes a quandary in consideration of whether it is the total power of the generated current, or the state-of-charge (SOC) of the battery system that should be constant, for the comparison of these waveforms. The root mean square charging current, *viz.* $i_{rms} = \sqrt{\int_0^{2t_s} \frac{i^2}{2t_s} dt}$, is chosen; and it is identical for each type of current waveshape; by definition, this ensures that the heat dissipated through Ohmic loss within the system (Joule heating[225]) is then constant for all considered waveforms, and allows for simplicity in that it is only the total energy that needs to be considered; the thermal energy loss in discharge as well as charge in this work was ignored.

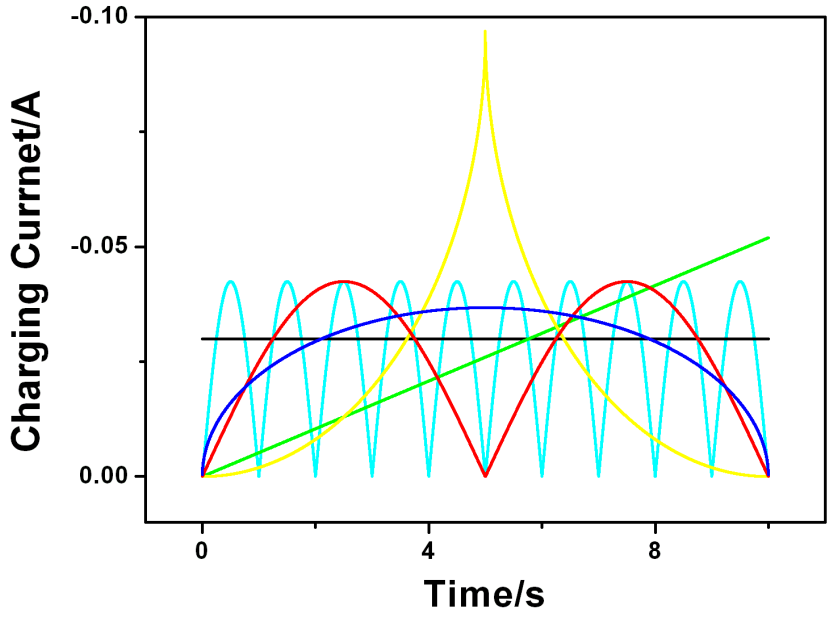

Fig. 7.2. Battery charging waveshapes: pure, constant DC (black), DC ramp (green), DC accelerator-decelerator (yellow), fully rectified AC at 0.5 Hz with constant DC offset (cyan), rectified tidal (red), solar (blue). Note that the rectified AC signal is illustrated here at an exaggerated frequency (0.5 Hz) than that used in simulations (50 Hz), so that the nature of its waveshape is seen.

Thus, for daytime generation, we may consider the six types of battery charging waveform, noting that more complex waveforms (to account for rectified AC variation) may be constructed from these, through linear superimposition. Note that the operation timescale was reduced – on real time day (24 h) maps to 20 s in this work (*vide infra*).

Pure, constant DC:

$$i = i_0 + A \quad \Rightarrow \quad \int_0^{2t_s} i dt = 2At_s \qquad \text{(Eqn. 7.1)}$$

DC ramp:

$$i = i_0 + \frac{A\sqrt{3}}{2t_s}t \quad \Rightarrow \quad \int_0^{2t_s} i dt = \sqrt{3}At_s \qquad \text{(Eqn. 7.2)}$$

DC accelerator-decelerator:

$$t \leq t_s \quad i = i_0 + \frac{A}{\sqrt{\frac{5}{3}-\frac{\pi}{2}}}\left(1 - \frac{1}{t_s}\sqrt{|{t_s}^2 - t^2|}\right) \quad \Rightarrow \quad \int_0^{2t_s} i dt = \frac{\left(2-\frac{\pi}{2}\right)}{\sqrt{\frac{5}{3}-\frac{\pi}{2}}}At_s \qquad \text{(Eqn. 7.3)}$$

$$t > t_s \quad i = i_0 + \frac{A}{\sqrt{\frac{5}{3}-\frac{\pi}{2}}}\left\{1 - \frac{1}{t_s}\sqrt{|{t_s}^2 - (t-2t_s)^2|}\right\} \qquad \text{(Eqn. 7.4)}$$

Fully rectified AC at 50 Hz with constant DC offset:

$$i = i_0 + \left|A\sqrt{2}\sin(100\pi t)\right| \quad \Rightarrow \quad \int_0^{2t_s} i dt = \frac{4\sqrt{2}}{\pi}At_s \qquad \text{(Eqn. 7.5)}$$

Rectified tidal, no AC:

$$t \leq t_s \quad i = i_0 + A\sqrt{2}sin\left(\frac{\pi}{t_s}t\right) \quad \Rightarrow \quad \int_0^{2t_s} i dt = \frac{4\sqrt{2}}{\pi}At_s \qquad \text{(Eqn. 7.6)}$$

$$t > t_s \quad i = i_0 - A\sqrt{2}sin\left(\frac{\pi}{t_s}t\right) \qquad \text{(Eqn. 7.7)}$$

Solar:

$$i = i_0 + \frac{A}{t_s}\sqrt{\frac{3}{2}}\sqrt{t(2t_s - t)} \quad \Rightarrow \quad \int_0^{2t_s} i dt = \frac{1}{2}\sqrt{\frac{3}{2}}\pi At_s \qquad \text{(Eqn. 7.8)}$$

In the above, *i* is the current, i_0 is a background level (taken to be zero in this work), A is then the maximum current carried through a pure, constant DC supply (taken to be -30 mA in this work, where charging currents are negative), t is the time variation, and t_s is the half-time period (kept at 5.0 s in this work, so that diffusive mass transport in the battery may only be considered; the occurrence of natural convection is precluded through the imposition of this limitation[226, 227]). Also given above is the charge

passed during the charging cycle when $i_0 = 0$: $Q_0 = \int_0^{2t_s} idt$, where it is clear that the SOC of the battery decreases with the waveforms in the order constant DC > solar > tidal = rectified AC > DC ramp > DC accelerator-decelerator. The function waveshapes used to charge-up the battery system are illustrated in Fig. 7.2.; the discharge was modelled as occurring immediately after charging, primarily so that there is no additional contribution from electrode corrosion (vide infra), and occurring under a constant DC load (current, with no reactive power), as we are interested in the performance of the system under light and heavy drain.

7.2.2. Evaluation of the Battery Performance with the Renewable Energy Waveforms

The determination of which of the renewable energy waveforms when used for charging the galvanic cell described in Fig. 7.1 yields efficient energy storage, high power characteristics of the battery under discharge, and a reasonable characteristic time (order of magnitude of the energy: power ratio) are interested. For the first of these figures of merit, for conditions of constant current in discharge, we consider the energy loss ratio (ELR) defined as the ratio between the energy generated under cell discharge versus the energy used for cell charging:

$$\mathrm{ELR} = \left\{1 - \frac{i_{discharge} \int_{2t_s}^{t_{discharge}} V dt}{\int_0^{2t_s} i_{charge} V dt}\right\} \times 100 \qquad \text{(Eqn. 7.9)}$$

The other two depend on the position of the system under discharge within the energy-power plane (Ragone plot). However, it is important to encompass effects due to the variable SOC with change in charging waveform; The SOC is defined as the ratio of the charge passed during cell charging to the total possible charge that could be passed during charging, *viz.* $\mathrm{SOC} = \frac{Q_0}{Fc^0{}_{Ce^{3+}Sl}}$ for the system considered in this work (*vide infra*). Thus, in order to understand how to normalise the Ragone plot, the

electrical principles of an ideal battery, viz. one which exhibits no frequency-dependent response and no non-linear responses due to Faradaic or pseudocapacitative contributions are recapitulated. Thus, for an ideal cell, charged to an arbitrary SOC, to afford a terminal potential difference at open circuit of V_{oc}, the *maximum energy deliverable* is $V_{oc}Q_o$. The constant current discharge of this battery, of internal resistance R_s, over an external resistance, R_i, affords, by Kirchhoff's laws, a terminal potential difference, V, of:

$$V = iR_i = V_{oc} - iR_s \qquad \text{(Eqn. 7.10)}$$

Clearly, under open circuit conditions, when $i \to 0$, $V \to V_{oc}$. At short circuit, $V = 0$, allowing a maximum current, i_{sc}, to flow:

$$i_{sc} = \frac{V_{oc}}{R_s} \qquad \text{(Eqn. 7.11)}$$

Now, the electrical power delivered across the load is:

$$p = iV = i(V_{oc} - iR_s) = iV_{oc} - i^2 \frac{V_{oc}}{i_{sc}} \qquad \text{(Eqn. 7.12)}$$

so that the current flowing in terms of the power delivered is:

$$i = \frac{i_{sc}}{2} \pm \sqrt{\frac{{i_{sc}}^2}{4} - p\frac{i_{sc}}{V_{oc}}} \qquad \text{(Eqn. 7.13)}$$

Thus, as $p \to 0$, $i \to 0$ (open circuit condition, corresponding to $R_i \to \infty$) or $i \to i_{sc}$ (short circuit conditions, corresponding to $R_i \to 0$) – in these two limits, no electrical power is produced. The maximum power that can be delivered by the ideal

battery can be determined from,

$$\frac{\partial p}{\partial V} = i_{sc} - 2i_{sc}\frac{V}{V_{oc}} = 0 \qquad \text{(Eqn. 7.14)}$$

Furnishing a current at the power point of $i_{mp} = \frac{1}{2}i_{sc}$ at an associated voltage $V_{mp} = \frac{1}{2}V_{oc}$, indicating that the maximum power that can be drawn from the ideal battery is $p_{max} = \frac{1}{4}i_{sc}V_{oc}$, as indicated in Fig. 7.3. Also indicated in this figure are the electrolytic ($i < 0$) and supergalvanic ($i_{sc} > 0$) regimes, where electrical power has to be supplied to the galvanic cell for charging ($_p < 0$, $i < 0$, $V > V_{oc}$), or for Joule heating ($p < 0$, $i > i_{sc}$, $V < 0$).

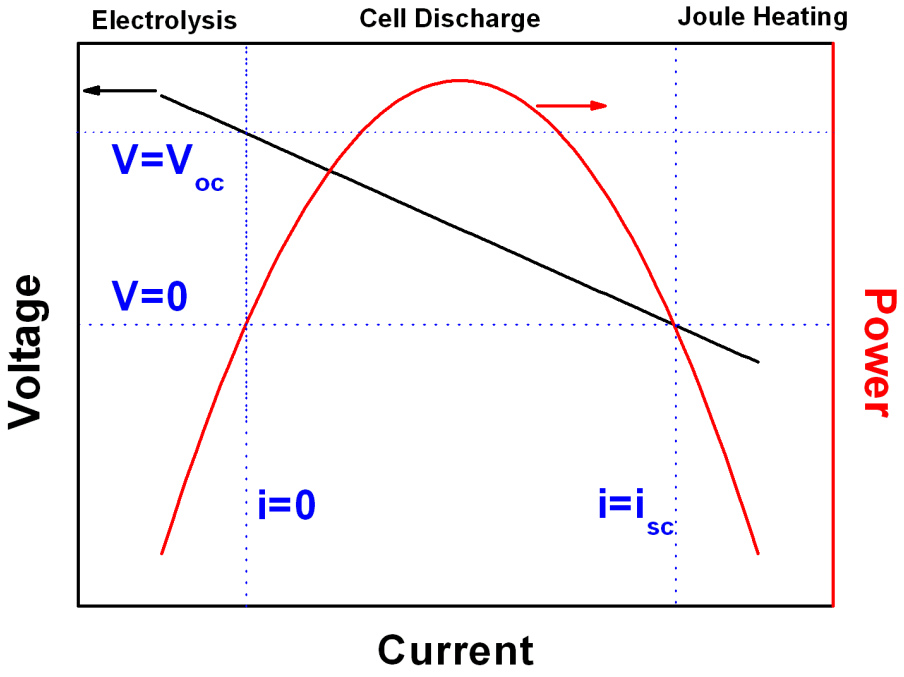

Fig. 7.3. Characteristics of an ideal battery, identifying the electrolytic, galvanic and supergalvanic regions from left-to-right.

As the renewable energy waveforms depend on the time passed, as indicated above, experimental data need to be analysed within the temporal domain; for constant current discharge,

$$\text{energy generated} = i_{discharge} \int_{2t_s}^{t_{discharge}} V dt \qquad \text{(Eqn. 7.15)}$$

$$\text{power delivered} = \frac{i_{discharge}}{t_{discharge}} \int_{2t_s}^{t_{discharge}} V dt \qquad \text{(Eqn. 7.16)}$$

Hence, for performance evaluation purposes, an adimensional Ragone plot may be constructed with $\frac{i_{discharge}}{Q_0 V_{oc}} \int_{2t_s}^{t_{discharge}} V dt$ on the ordinate and $\frac{4 i_{discharge}}{t_{discharge} i_{sc} V_{oc}} \int_{2t_s}^{t_{discharge}} V dt$ on the abscissa, or *vice versa*.

These parameters may be determined through knowledge of the battery chemistry is described next.

7.2.3. Model for an Undivided Galvanic cell

For a storage system, a zinc-cerium hybrid redox battery have been chosen based operated under diffusion-only conditions, for simplicity – there is then no need to consider intrinsic energy loses due to pumping the electrolyte through the cell, nor to worry about the changing thickness of the diffusion layer thickness between the upstream and downstream edges of the electrode surface, which itself is a function of the volume flow rate. Flow batteries of this system have been demonstrated to operate under mild, ambient temperature conditions (295 K) in a fully electrochemically supported undivided cell (see Fig. 7.1). The cell electrolyte is assumed to be oxygen-free (to prevent any electrode passivation through zinc oxide precipitation) and supposed that it contains additives so that the hydrogen evolution (due to proton reduction) and oxygen evolution (through water oxidation) reactions do not proceed within the cell even under the most extreme potentials generated at the electrodes. Further assumptions are made that the electrodes are perfectly flat (fractal dimension of exactly 2.0), allowing heterogeneous electron transfer reactions to proceed uniformly on the electrode surface, and so that there is no dendrite formation on the electrode surfaces. These assumptions allow the surface area of the electrodes in

contact with the electrolyte to be constant throughout the electrolysis. Note that other models for hydrogen or oxygen evolution within redox batteries command a similar assumption, *viz.* the Laplace pressure is sufficiently small to prevent bubble formation. The galvanic cell can thus be written through the following cell diagram.

$$Zn\left|Zn^{2+}\ (aq, {c^0}_{Zn^{2+}} = 1.5\ M), Ce^{4+}(aq, {c^0}_{Ce^{4+}} = 10^{-3}\ M), Ce^{3+}(aq, {c^0}_{Ce^{3+}} = 0.5\ M)\right|C$$

Note that the above concentrations are experimentally realistic for flow batteries, with an initial concentration of Ce^{4+} ions set at three orders of magnitude higher than that typically used for "ion-free" conditions, to ensure full stability of the numerical simulations employed herein (*vide infra*). Furthermore, for the charging reactions, the vast excess of Zn^{2+} compared with Ce^{3+} ensures that is the limiting reagent.

The planar electrode, parallel–plate battery system illustrated in Fig. 7.1 using single spatial co-ordinate (x) se was defined so that the carbon surface facing the solution is at x=0, with the electrolyte-exposed zinc surface at $x=l$. the electrolyte used in realised experimental systems consists mainly of aqueous methansulfonic acid of high concentration (typically between 4-6 M) to suppress electrical migration of the redox species, and reduce the electrical resistance (R_s) between the electrode plates. This additionally sets up electrical double layers, of capacitance (C_{dl1} and C_{dl2}) at each electrode which need to be charged and discharged with change in the voltage in time (*vide infra*) in parallel with the redox reaction at each electrode (see Fig. 7.1). No parasitic reactions (other than those considered below) causing leakage or shunt currents to occur in parallel to the load resistances was assumed.

7.2.3.1. Cell Chemistry

Thus, at open-circuit (no current flowing, no power delivered), the following potential-determining equilibria may be written.

Right-hand-side electrode:

$$Ce^{4+}(aq) + e^{-} \rightleftharpoons Ce^{3+}(aq)$$

$$E^{0\prime}{}_{Ce^{3+}|Ce^{4+}} = +1.44\,V\ vs.SHE;\ k_s = 6.8 \times 10^{-4}\,cm\,s^{-1};\ \alpha = \frac{2}{5}$$

Left-hand-side electrode:

$$\frac{1}{2}Zn^{2+}(aq) + e^{-} \rightleftharpoons \frac{1}{2}Zn(s)$$

$$E^{0\prime}{}_{Zn|Zn^{2+}} = -0.76\,V\ vs.SHE;\ k_{s_2} = 4.0 \times 10^{-4}\,cm\,s^{-1};\ \alpha = \frac{2}{5}$$

Note that these half-cell reactions are idealistic; all activity coefficients are assumed to be unity, so that the formal potentials quoted correspond to standard electrode potentials against the standard hydrogen scale (SHE). It is well-known, in acidic aqueous solutions, the thermodynamic and kinetic oxidising ability of cerium (IV) depends on the nature of the acid counter ion: in H_2SO_4, the following complexation reactions are thought to occur.[228]

$$Ce^{4+} + \mathrm{HSO_4}^{-} \rightleftharpoons Ce(SO_4)^{2+} + H^{+}$$

$$Ce(SO_4)^{2+} + \mathrm{HSO_4}^{-} \rightleftharpoons Ce(SO_4)_2 + H^{+}$$

$$Ce(SO_4)_2 + \mathrm{HSO_4}^{-} \rightleftharpoons HCe(SO_4)_3{}^{-}$$

Scheme 7.1

with the last anionic cerium(IV) form predominating at high H_2SO_4 concentrations, thereby suppressing hydrolysis of Ce^{4+}. Accordingly, the formal electrode potential was supposed for the cerium(III)/cerium(IV) half-cell within methanesulfonic acid is the same as sulphuric acid. Although the value of the standard heterogeneous rate constant (k_s) for the reduction of Ce^{4+} varies in the literature from 5.3×10^{-5}~ 1.3×10^{-3} cm s^{-1}, the electrode reaction is sluggish on most electrodes, and occurs with a transfer coefficient (α) in the range 0.1~0.5; Randle and Kuhn[229] have used such data to provide evidence to suggest the electrode reaction involves the sulfato-complexes forms in sulphuric acid. Nevertheless, only the basic electron transfer reaction is considered, using literature-averaged values for k_s and α.

Likewise, the reduction of zinc is considered to occur as a single two-electron process, even though it is known[230] that zinc reduction (at least on mercury) occurs in a CE type process, involving the adsorption of zinc ions. Nevertheless, the single step process is also kinetically slow (the standard rate constant and symmetry factor given above are also averages taken from the literature[216, 230, 231]), with nucleation (at least on carbon) thought to processed through an instantaneous (rather than progressive) mechanism,[217] *viz.* the number density of nucleation centres equals the number of active sites – a time-independent constant. Voltage ripple (AC variation superimposed on DC) is assumed that it has no effect on zinc plating uniformity[232], and likewise, as mentioned earlier, suppose that the electrolyte contains additives to suppress dendrite formation during zinc plating. Moreover, it is assumed that the plating of zinc onto the electrode during charge does not alter the cell thickness, as this would otherwise require a dynamic, not static, spatial grid to be deployed. This is a reasonable assumption since approximately $\frac{|A|t_s}{F}$ mol zinc are deposited, corresponding to ~4000 monolayers, resulting in uniform deposits that are ~520 nm thick (assuming an atomic radius of zinc of 133.2 pm), which is *ca.* 1% of the thinnest cell depth considered in this work, *vide infra*).

The less-than-unity value of the transfer coefficient for zinc ion reduction (taken to be 0.4 in this work) is consistent with a near-symmetric barrier of a single step two-electron process ($2\alpha = 0.8 \approx 1$), rather than the adsorbed single charge species mechanism that is thought to occur in neutral and non-complexing solutions:

$$Zn^{2+}(aq) \rightleftharpoons Zn^{2+}(ads)$$

$$\mathrm{Zn}^{2+}(ads) + e^- \xrightarrow{slow} Zn^{+}(ads)$$

$$\mathrm{Zn}^{+}(ads) + e^- \rightleftharpoons Zn(s)$$

Scheme 7.2

The assumption that the electrolyte contains corrosion inhibitors to suppress the hydrogen evolution reaction (*vide supra*) is reasonable: the standard exchange current

density for hydrogen oxidation on zinc at 298 K is reported as being 10^{-11} A cm^{-2}.

Although the energy storage efficiency of the particular charging waveform is interesting, it is noted that most experimental systems involve the plating of zinc onto carbon during charge, and are thus limited by zinc dissolution under discharge. Thus, rather than assuming that the zinc electrode is physically thick, *viz.* with a surface coverage, Γ_{Zn}, inflated by some large factor over its monolayer value, the surface coverage is sited to take the typical monolayer value of 10^{-10} mol cm^{-2}, and employ a bulk stripping boundary condition (*vide infra*).

Thus, the cell reaction occurring under short circuit is $Ce^{4+}(\text{aq}) + \frac{1}{2}\text{Zn(s)} \rightarrow Ce^{3+}(aq) + \frac{1}{2}Zn^{2+}(aq)$, *viz.* the right-hand electrode becomes positive relative to that at the left-hand side, in a thermodynamically spontaneous process; the observed open circuit voltage under non-standard conditions is:

$$V_{oc} = E_{cell} = E_{LHS} - E_{RHS} = E^{0'}_{cell} + \frac{RT}{F} ln \left\{ \frac{c^0_{Ce^{4+}} c_s^{1/2}}{c^0_{Ce^{3+}} c^{1/2}_{Zn^{2+}}} \right\} \qquad \text{(Eqn. 7.17)}$$

where the potential of the right-hand side electrode of the cell diagram,

$$E_{RHS} = E_{Ce^{3+}|Ce^{4+}} = E^{0'}_{Ce^{3+}|Ce^{4+}} + \frac{RT}{F} ln \left\{ \frac{c^0_{Ce^{4+}}}{c^0_{Ce^{3+}}} \right\} \qquad \text{(Eqn. 7.18)}$$

and the potential of the left-hand side electrode,

$$E_{LHS} = E_{Zn|Zn^{2+}} = E^{0'}_{Zn|Zn^{2+}} + \frac{RT}{F} ln \left\{ \frac{c^{1/2}_{Zn^{2+}}}{c_s^{1/2}} \right\} \qquad \text{(Eqn. 7.19)}$$

are Nernstian expressions, c_s is the standard concentration (1.0 M), R is the molar gas constant, T is the absolute temperature (taken to be 298 K in this work), F is Faraday's

constant and

$$E_{cell}^{0'} = E_{Ce^{3+}|Ce^{4+}}^{0'} - E_{Zn|Zn^{2+}}^{0'}. \qquad \text{(Eqn. 7.20)}$$

7.2.3.2. Open Circuit Corrosion of the Znic Electrode

Since the corrosion rate for zinc in acidic solutions of pH < 3 is low, typically ~40 mm yr^{-1}, as a result of kinetic limitations (*vide supra*), it is supposed that zinc dissolution with hydrogen evolution to be negligible. However, it is well known that, at least in brine, Ce^{3+} suppresses corrosion of zinc, whilst Ce^{4+} present initially (else cell potentials would tend to -∞, a value that is impossible to use in numerical simulations), the open circuit voltage will not be given by the Nernst expression owing to the occurrence of generation and depletion conditions at the zinc electrode, due to the spontaneous heterogeneous reaction:

$$Ce^{4+}(aq) + {}^{1}/_{2}\, Zn(s) \rightarrow Ce^{3+}(aq) + {}^{1}/_{2}\, Zn^{2+}(aq) \qquad \text{(Scheme 7.3)}$$

The effect of this is to alter the concentration profiles of Ce^{3+}, Ce^{4+} and Zn^{2+} within the cell, and thus impact on the charge-discharge characteristics of the cell.

To account for this mixed-potential corrosion at open-circuit when no current flows between the two electrodes, the net corrosion current has to be zero; provide corrosion occurs *uniformly* over the zinc electrode, the total reduction rate must match the total rate of oxidation, at every point on the surface, *viz.*,

$$i^{corr}{}_{Ce^{4+}\rightarrow Ce^{3+}} = 2i^{corr}{}_{Zn\rightarrow Zn^{2+}} \qquad \text{(Eqn. 7.21)}$$

in which the factor of two for the zinc dissolution current merely reflects the reaction stoichiometry. Hence, under a Bulter-Volmer formalism,

$$k_{s_3}(c_{Ce^{4+}})_{x=l}\exp\left(\frac{\alpha_3 FE^{0\prime}_{cell}}{RT}\right)\exp(-\alpha_3\xi_2) + 2k_{s_2}(c_{Zn^{2+}})_{x=l}\exp(-2\alpha_2\xi_2) =$$

$$k_{s_3}(c_{Ce^{3+}})_{x=l}\exp\left[\frac{(\alpha_3-1)FE^{0\prime}_{cell}}{RT}\right]\exp[(1-\alpha_3)\xi_2] + 2k_{s_2}c_s\exp[2(1-\alpha_2)\xi_2]$$

(Eqn. 7.22)

where k_{s_3} is the standard heterogeneous rate constant for Ce^{4+} reduction on zinc, with α_3 the associated symmetry factor and denote the reduced potential $\xi_2 = \frac{F}{RT}\left(E_{LHS} - E^{0\prime}{}_{Zn|Zn^{2+}}\right)$. For the case when $\alpha_3 = 2\alpha_2 = 1$, the above can be solved to afford the following value of the corrosion potential.

$$E_{LHS}$$

$$= E^{0\prime}{}_{Zn|Zn^{2+}}$$

$$+\frac{RT}{F}ln\left\{\frac{-k_{s_3}(c_{Ce^{3+}})_{x=l} + \sqrt{{k_{s_3}}^2(c_{Ce^{3+}})^2_{x=l} + 8k_{s_2}c_s\left[2k_{s_2}(c_{Zn^{2+}})_{x=l} + k_{s_3}(c_{Ce^{4+}})_{x=l}e^{\frac{F}{RT}E^{0\prime}_{cell}}\right]}}{4k_{s_2}c_s}\right\}$$

(Eqn. 7.23)

Satisfyingly, the above reduces to the Nernst expression in the absence of cerium-induced zinc corrosion, *viz.* when $k_{s_3} = 0$. Thus, for the general case of $\alpha_3 \neq 2\alpha_2 \neq 1$, the above was used as a first approximation in a Newton-Raphson iterative solution (dummy variable ς), with subsequent estimates of the corrosion potential determined through the relation,

$$\chi_\varsigma$$

$$= \chi_{\varsigma-1}$$

$$-\frac{k_{s_3}(c_{Ce^{4+}})_{x=l}e^{\frac{\alpha_3 FE^{0\prime}_{cell}}{RT}} - k_{s_3}(c_{Ce^{3+}})_{x=l}e^{\frac{(\alpha_3-1)FE^{0\prime}_{cell}}{RT}}\chi_{\varsigma-1} - 2k_{s_2}c_s\chi_{\varsigma-1}^{[\alpha_3+2(1-\alpha_2)]} + 2k_{s_2}(c_{Zn^{2+}})_{x=l}\chi_{\varsigma-1}^{(\alpha_3-2\alpha_2)}}{-k_{s_3}(c_{Ce^{3+}})_{x=l}e^{\frac{(\alpha_3-1)FE^{0\prime}_{cell}}{RT}} - 2k_{s_2}c_s[a_3+2(1-\alpha_2)]\chi_{\varsigma-1}^{(\alpha_3+1-2\alpha_2)} + 2k_{s_2}(c_{Zn^{2+}})_{x=l}(\alpha_3-2\alpha_2)\chi_{\varsigma-1}^{(\alpha_3-1-2\alpha_2)}}$$

(Eqn. 7.24)

where $\chi = e^{\xi_2}$. Typically, 29 iterations were required for non-zero values of k_{s_3} to achieve convergence to within the required threshold (10-10 in χ).

There are two limiting cases that interested in: (i) $k_{s_3} = 0\ cm\ s^{-1}$, corresponding to no corrosion of the zinc electrode, so that its potential is as given in section 7.2.3.1, and (ii) $k_{s_3} = k_s$ and $\alpha_3 = \alpha$ – the kinetics of cerium(IV) reduction on zinc are commensurate with those at the carbon electrode. For the experimental conditions given, these cases correspond to *instantaneous initial* open circuit voltages of (i) +2.04 V and (ii) +1.60 V, respectively; the occurrence of corrosion reduces the open circuit voltage (V_{oc}), as anticipated.

7.2.3.3. Cell Geometry

In the laboratory-scale experimental system developed by Walsh[214], the galvanic cell has symmetric, parallel plate, porous electrodes of dimensions $4.5 \times 2.0 \times 0.5$ cm, separated by 1.85 cm, with electrolyte that is flowed from, and collected by, a single reaction reservoir, at a linear flow velocity of 3.9 cm s^{-1}. Similar values for cell dimensions and flow rate have been employed by Roberts[233, 234] in an undivided redox flow battery for solar energy storage, or for an all-chromium system. However, for the diffusion-only galvanic cell considered in this work, such values do not allow for the occurrence of effects of transport-limited electrolysis during the charge step, nor allow for corrosive generation conditions at the zinc electrode to impact on the carbon electrode under the timescale limitation imposed. Accordingly, it is chosen to realise a system in which the parallel-plate electrodes are assumed to be of identical area, *S*, separated by the fixed distance *l* (cell thickness), and to compute the cell depth in terms of multiples of the diffusion layer thickness of Ce^{3+} ions at the right-hand electrode, *viz.*,

$$l = \iota\sqrt{2\pi D_{Ce^{3+}} t_s} \qquad \text{(Eqn. 7.25)}$$

where D_i is the diffusion coefficient of species i, $1 \leq \iota \leq 10$, and to keep the electrode surface area as a factor, φ, larger than that required for complete charging of the thinnest cell considered within the allocated time, using a pure, constant DC input:

$$S = \frac{\sqrt{2}}{\sqrt{\pi}} \frac{\varphi |A| \sqrt{t_s}}{F c^0_{Ce^{3+}} \sqrt{D_{Ce^{3+}}}} \qquad \text{(Eqn. 7.26)}$$

The above formulation was determined to be optimised, since complete electrolysis during charge would otherwise cause faster depletion of redox species at the electrode compared with mass transport, leading to cell voltages that could not be determined through numerical methods. For typical experimental values considered in this work, $40 \leq l/\mu m \leq 400$, with square electrodes of side 2.0 cm, corresponding to $\varphi \simeq 2.5$.

7.2.3.4. Transport and Faradaic Currents

The performance of this galvanic system under load is interested, and thus it needs to seek a solution to the following transport equations, which describe the mass transfer resistance R^{ox} and R^{Red} in the equivalent circuit illustrated in Fig. 7.1,

$$\frac{\partial C_{Ce^{3+}}}{\partial t} = D_{Ce^{3+}} \frac{\partial^2 c_{Ce^{3+}}}{\partial x^2} \qquad \text{(Eqn. 7.27)}$$

$$\frac{\partial C_{Ce^{4+}}}{\partial t} = D_{Ce^{4+}} \frac{\partial^2 c_{Ce^{4+}}}{\partial x^2} \qquad \text{(Eqn. 7.28)}$$

$$\frac{\partial C_{Zn^{2+}}}{\partial t} = D_{Zn^{2+}} \frac{\partial^2 c_{Zn^{2+}}}{\partial x^2} \qquad \text{(Eqn. 7.29)}$$

under the following boundary conditions, where they can be assumed that Butler-Volmer kinetics are sufficient to describe the current dependence on the potential at each electrode (these are represented being electrically equivalent to a junction diode within the circuit diagram in Fig. 7.1; it can be recognised that were

the electrode kinetics to account for the density of electronic states within the electrode through modelling *via* non-adiabatic Marcus-Hush theory, the electrical circuit equivalent is merely a thermionic diode). Note that, although as alluded to earlier (*q.v.* Section 2.1), it has been no explicitly allowed for the inclusion of natural convection as a transport means; this is possible simply by allowing the individual diffusion coefficients, D, to be apparent diffusion coefficients, D_{app}, which are fourth-order functions of the distance normal to the electrode surface,

$$D_{app} = D\left\{1 + 1.522\left(\frac{x}{\delta_{conv}}\right)^4\right\} \qquad \text{(Eqn. 7.30)}$$

in which δ_{conv} is the thickness of the convection-free layer.

$$\text{t} \leq 0 \qquad c_{Ce^{3+}} = c^0_{Ce^{3+}};\;\; c_{Ce^{4+}} = c^0_{Ce^{4+}};\;\; c_{Zn^{2+}} = c^0_{Zn^{2+}};\;\; \Gamma_{Zn} = \Gamma_T$$

$$\forall x \qquad \text{(Eqn. 7.31)}$$

$$\text{t} > 0 \qquad \frac{i_f}{FS} = -D_{Ce^{3+}}\left(\frac{\partial c_{Ce^{3+}}}{\partial x}\right)_{x=0} = 2D_{Zn^{2+}}\left(\frac{\partial c_{Zn^{2+}}}{\partial x}\right)_{x=l} + D_{Ce^{4+}}\left(\frac{\partial c_{Ce^{4+}}}{\partial x}\right)_{x=l}$$

$$x = 0 \qquad \left(\frac{\partial c_{Ce^{3+}}}{\partial x}\right)_{x=0} + \frac{D_{Ce^{4+}}}{D_{Ce^{3+}}}\left(\frac{\partial c_{Ce^{4+}}}{\partial x}\right)_{x=0} = 0$$

$$\left(\frac{\partial c_{Zn^{2+}}}{\partial x}\right)_{x=0} = 0$$

$$\left(\frac{\partial c_{Ce^{3+}}}{\partial x}\right)_{x=0} = \frac{k_s}{D_{Ce^{3+}}}\left\{(c_{Ce^{3+}})_{x=0}e^{(1-\alpha)\xi} - (c_{Ce^{4+}})_{x=0}e^{-\alpha\xi}\right\}$$

(Eqn. 7.32)

$$x = l \qquad \left(\frac{\partial c_{Ce^{3+}}}{\partial x}\right)_{x=l} + \frac{D_{Ce^{4+}}}{D_{Ce^{3+}}}\left(\frac{\partial c_{Ce^{4+}}}{\partial x}\right)_{x=l} = 0$$

$$\frac{\partial \Gamma_{Zn}}{\partial t} = -D_{Zn^{2+}}\left(\frac{\partial c_{Zn^{2+}}}{\partial x}\right)_{x=l}$$

$$\frac{\partial \Gamma_{Zn}}{\partial t} = k_{s_2}\left\{c_s e^{2(1-\alpha_2)\xi_2} - (c_{Zn^{2+}})_{x=l}e^{-2\alpha_2\xi_2}\right\}$$

$$\left(\frac{\partial c_{Ce^{4+}}}{\partial x}\right)_{x=l} = \frac{k_{s_3}}{D_{Ce^{4+}}}\left\{(c_{Ce^{4+}})_{x=l}e^{-\alpha_3\xi_3} - (c_{Ce^{3+}})_{x=l}e^{(1-\alpha_3)\xi_3}\right\}$$

(Eqn. 7.33)

In the above, they are identified explicitly that the Faradaic current as i_f, employ the reduced potentials $\xi = \frac{F}{RT}\left(E_{RHS} - E^{0\prime}_{Ce^{3+}|Ce^{4+}}\right)$ and $\xi_3 = \frac{F}{RT}\left(E_{LHS} - E^{0\prime}_{Ce^{3+}|Ce^{4+}}\right)$, and keep to the convection that discharge currents are positive. The unusual formulation of the stripping condition is to account for the fact that this is the condition for the *upper* boundary of the simulation (q.v. Fig. 7.1). Note that the surface condition for the sacrificial zinc anode corresponds to bulk stripping; as such, $\lim_{t\to\infty} \Gamma_{Zn} \geq 0$, so that $k_{s_2} c_s e^{2(1-\alpha_2)\xi_2}$ is set to zero when $\Gamma_{Zn} = 0$.

The occurrence of corrosion of zinc (at open circuit), coupled with the deactivation of cerium(IV) at the zinc electrode (under closed circuit conditions) within the undivided cell thus casuses the three species Ce^{3+}, Ce^{4+} and Zn^{2+} to be intimately coupled through the Neumann conditions at the zinc electrode. Accordingly, the partial differential equations are soluble using the Backward Implicit finite difference approach, solving first for the concentrations of species Ce^{3+} and Ce^{4+} simultaneously, using a *pentadiagonal* matrix algorithm (see Appendix 10.2), *followed* by solution for the concentration of Zn^{2+} through the use of the Thomas algorithm, using experimentally realistic values of the diffusion coefficients, *viz.*, $D_{Ce^{3+}} = D_{Ce^{4+}} = 5 \times 10^{-7}\, cm^2 s^{-1}$ and $D_{Zn^{2+}} = 6.9 \times 10^{-6}\, cm^2 s^{-1}$, where the smaller value for the cerium(III)/cerium(IV) species implicitly accounts for complex formation that is thought to occur within the aqueous methansulfonic electrolyte.

Thus, under current-controlled (galvanostatic) discharege, the surface concentrations of all species may be ascertained through the following finite difference relationships of the Neumann boundary conditions at the electrode surfaces, where square brackets are used to denote concentrations normalised by the speciation-independent total concentration of cerium ions, with surface concentrations reduced through normalisation with the maximum possible surface coverage (Γ_T).

$$[Ce^{3+}]_0^t = [Ce^{3+}]_1^t + \frac{i_f \Delta x}{FSD_{Ce^{3+}}\left(c^0_{Ce^{3+}} + c^0_{Ce^{4+}}\right)} \quad \text{(Eqn. 7.34)}$$

$$[Ce^{4+}]_0^t = [Ce^{4+}]_1^t - \frac{i_f \Delta x}{FSD_{Ce^{4+}}\left(c^0_{Ce^{3+}} + c^0_{Ce^{4+}}\right)} \quad \text{(Eqn. 7.35)}$$

$$[Zn^{2+}]_0^t = [Zn^{2+}]_1^t \quad \text{(Eqn. 7.36)}$$

$$[Zn^{2+}]_l^t = [Zn^{2+}]_{l-1}^t + \frac{i_f \Delta x}{2FSD_{Zn^{2+}}\left(c^0_{Ce^{3+}} + c^0_{Ce^{4+}}\right)} - \frac{D_{Ce^{4+}}}{2D_{Zn^{2+}}}\{[Ce^{4+}]_l^t - [Ce^{4+}]_{l-1}^t\} \quad \text{(Eqn. 7.37)}$$

$$[\Gamma_{Zn}]^t = [\Gamma_{Zn}]^{t-1} - \frac{D_{Zn^{2+}} \Delta t (c^0_{Ce^{3+}} + c^0_{Ce^{4+}})}{\Delta x \Gamma_T}\{[Zn^{2+}]_l^t - [Zn^{2+}]_{l-1}^t\} \quad \text{(Eqn. 7.38)}$$

$$[Ce^{4+}]_l^t = \left\{\frac{\frac{D_{Ce^{4+}}}{\Delta x} - k_{s_3} e^{(1-\alpha_3)\xi_3} \frac{D_{Ce^{4+}}}{D_{Ce^{3+}}}}{\frac{D_{Ce^{4+}}}{\Delta x} - k_{s_3} e^{-\alpha_3 \xi_3} - k_{s_3} e^{(1-\alpha_3)\xi_3} \frac{D_{Ce^{4+}}}{D_{Ce^{3+}}}}\right\}[Ce^{4+}]_{l-1}^t - \left\{\frac{k_{s_3} e^{(1-\alpha_3)\xi_3}}{\frac{D_{Ce^{4+}}}{\Delta x} - k_{s_3} e^{-\alpha_3 \xi_3} - k_{s_3} e^{(1-\alpha_3)\xi_3} \frac{D_{Ce^{4+}}}{D_{Ce^{3+}}}}\right\}[Ce^{3+}]_{l-1}^t$$

(Eqn. 7.39)

$$[Ce^{3+}]_l^t = \left\{1 + \frac{k_{s_3} e^{(1-\alpha_3)\xi_3} \frac{D_{Ce^{4+}}}{D_{Ce^{3+}}}}{\frac{D_{Ce^{4+}}}{\Delta x} - k_{s_3} e^{-\alpha_3 \xi_3} - k_{s_3} e^{(1-\alpha_3)\xi_3} \frac{D_{Ce^{4+}}}{D_{Ce^{3+}}}}\right\}[Ce^{3+}]_{l-1}^t - \frac{D_{Ce^{4+}}}{D_{Ce^{3+}}}\left\{1 - \frac{\frac{D_{Ce^{4+}}}{\Delta x} - k_{s_3} e^{(1-\alpha_3)\xi_3} \frac{D_{Ce^{4+}}}{D_{Ce^{3+}}}}{\frac{D_{Ce^{4+}}}{\Delta x} - k_{s_3} e^{-\alpha_3 \xi_3} - k_{s_3} e^{(1-\alpha_3)\xi_3} \frac{D_{Ce^{4+}}}{D_{Ce^{3+}}}}\right\}[Ce^{4+}]_{l-1}^t$$

(Eqn. 7.40)

These calculated values can then be employed to determine the potentials at each electrode. For the case of the right-hand side electrode, this was undertaken through Newton-Raphson iteration (dummy index q).

$$\vartheta_q = \vartheta_{q-1} - \frac{\left[\frac{i_f}{k_S FS(c^0_A + c^0_B)}\right]\vartheta_{q-1}^{\alpha} + [Ce^{3+}]_0^t \vartheta_{q-1} - [Ce^{4+}]_0^t}{\alpha\left[\frac{i_f}{k_S FS(c^0_A + c^0_B)}\right]\vartheta_{q-1}^{\alpha-1} + [Ce^{3+}]_0^t} \quad \text{(Eqn. 7.41)}$$

where $\vartheta = exp(\xi)$, and to a threshold of 10^{-10} in ϑ, employing, as a first approximation, the potential obtained when $\alpha = \frac{1}{2}$, *viz.*,

$$E_{Ce^{3+}|Ce^{4+}} = E^{0\prime}_{Ce^{3+}|Ce^{4+}} + \frac{2RT}{F} \ln\left[\frac{1}{2[Ce^{3+}]_0^t}\left(\frac{-i_f}{k_S FS\left(c^0_{Ce^{3+}} + c^0_{Ce^{4+}}\right)} + \sqrt{\left[\frac{i_f}{k_S FS\left(c^0_{Ce^{3+}} + c^0_{Ce^{4+}}\right)}\right]^2 + 4[Ce^{3+}]_0^t [Ce^{4+}]_0^t}\right)\right]$$

(Eqn. 7.42)

Typically three iterations were required for convergence of the electrode potential. The mixed-flux boundary condition for the left-hand side electrode causes a slightly more intricate calculation to take place, again through Newton-Raphson iteration (dummy variable ς),

$$\chi_{\varsigma} = \chi_{\varsigma-1} - \frac{\left[\frac{i_f}{FS\left(c^0_{Ce^{3+}}+c^0_{Ce^{4+}}\right)}\right]\chi_{\varsigma-1}^{\alpha_3} - 2k_{s_2}[Zn^{2+}]_l^t\chi_{\varsigma-1}^{(\alpha_3-2\alpha_2)} + 2k_{s_2}\left[\frac{c_s}{\left(c^0_{Ce^{3+}}+c^0_{Ce^{4+}}\right)}\right]\chi_{\varsigma-1}^{[\alpha_3+2(1-\alpha_2)]} + k_{s_3}[Ce^{3+}]_l^t e^{(\alpha_3-1)\frac{F}{RT}E^{0'}_{cell}}\chi_{\varsigma-1} - k_{s_3}[Ce^{4+}]_l^t e^{\alpha_3\frac{F}{RT}E^{0'}_{cell}}}{\left[\frac{i_f}{FS\left(c^0_{Ce^{3+}}+c^0_{Ce^{4+}}\right)}\right]\alpha_3\chi_{\varsigma-1}^{(\alpha_3-1)} - 2k_{s_2}[Zn^{2+}]_l^t(\alpha_3-2\alpha_2)\chi_{\varsigma-1}^{(\alpha_3-2\alpha_2-1)} + 2k_{s_2}\left[\frac{c_s}{\left(c^0_{Ce^{3+}}+c^0_{Ce^{4+}}\right)}\right](2-2\alpha_2+\alpha_3)\chi_{\varsigma-1}^{(1-2\alpha_2+\alpha_3)} + k_{s_3}[Ce^{3+}]_l^t e^{(\alpha_3-1)\frac{F}{RT}E^{0'}_{cell}}}$$

(Eqn. 7.43)

employing, for the first approximation, the solution obtained for the case of $\alpha_3 = 2\alpha_2 = 1$, *viz.*

$$\chi = \frac{\left(c^0_{Ce^{3+}}+c^0_{Ce^{4+}}\right)}{4k_{s_2}c_s} - \left\{k_{s_3}[Ce^{3+}]_l^t + \frac{i_f}{FS\left(c^0_{Ce^{3+}}+c^0_{Ce^{4+}}\right)}\right\} + \sqrt{\left\{k_{s_3}[Ce^{3+}]_l^t + \frac{i_f}{FS\left(c^0_{Ce^{3+}}+c^0_{Ce^{4+}}\right)}\right\}^2 + 8k_{s_2}c_s\left\{k_{s_3}[Ce^{4+}]_l^t e^{\frac{F}{RT}E^{0'}_{cell}} + 2k_{s_2}[Zn^{2+}]_l^t\right\}}$$

(Eqn. 7.44)

A maximum of 28 iterations were required for the potentials to be converged to within the required threshold (10^{-10} in χ). Note that in the case when zinc corrosion/depletion is such that $\Gamma_{Zn} = 0$, all terms involving c_s are set to zero, so that a first approximation to the electrode potential is:

$$\xi_2 = ln\left\{\frac{2k_{s_2}+k_{s_3}[Ce^{4+}]_l^t e^{\frac{F}{RT}E^{0'}_{cell}}}{k_{s_3}[Ce^{3+}]_l^t + \frac{i_f}{FS\left(c^0_{Ce^{3+}}+c^0_{Ce^{4+}}\right)}}\right\} \qquad \text{(Eqn. 7.45)}$$

Thus, in the absence of effects due to double layer charging or Ohmic drop, the cell voltage is:

$$\mathrm{E}_{cell} = E_{Ce^{3+}|Ce^{4+}} - E_{Zn|Zn^{2+}} \qquad \text{(Eqn. 7.46)}$$

7.2.3.5. Capacitative Currents and Ohmic Loss

The large majority of battery models for operation under galvanostatic conditions do not account for contributions due to charging or discharging of the electrical double layer present at each electrode. In order to incorporate capacitative contributions, the double layers at each of the two electrodes were treated as symmetrical series capacitors, each of capacitance[235] 40 μF cm^{-2}, so that the effective equivalent capacitance for the cell is $C_{dl} = \frac{C_{dl1}C_{dl2}}{C_{dl1}+C_{dl2}} = 20\ \mu F\ cm^{-2}$, giving rise to,

$$C_{dl} = \frac{\sqrt{2}}{5\sqrt{\pi}} \frac{\varphi|A|\sqrt{t_s}}{Fc^0_{Ce^{3+}}\sqrt{D_{Ce^{3+}}}} \qquad \text{(Eqn. 7.47)}$$

which, for the electrode area employed in this work corresponds to 80 μF.

The total current passing through the cell (*q.v.* Fig. 7.1) is the comprised of Faradaic (i_f) and capacitative (i_{cap}) contributions, by kirchhoff's laws:

$$i = i_f + i_{cap} \qquad \text{(Eqn. 7.48)}$$

However, both contributions are coupled through the Ohmic loss within the cell, where it is the solution resistance (R_s) that acts as the major cause of this voltage drop. This parameter is related to both the cell geometry and the nature of the supporting electrolyte,

$$R_s = \frac{\rho_s l}{S} = \frac{2\pi\iota\rho_s D_{Ce^{3+}} Fc^0_{Ce^{3+}}}{\varphi|A|} \qquad \text{(Eqn. 7.49)}$$

where ρ_s is the solution resistivity. Given the average value of the supporting electrolyte concentration (~5 M), the solution resistance is dominated by the

resistivity of the mehanesulfonic acid solution; at 298 K, literature data on molar conductance of this aqueous electrolyte[236] affords the following relation for methanesulfonic acid concentrations, c_0, in the range of $0.01 \leq c_0/\mathrm{M} \leq 2.0$,

$$\log(\rho_s/\Omega\, m) = -0.91351 \log(c_0/M) - 1.4575 \qquad \text{(Eqn. 7.50)}$$

with a Pearson's product-moment correlation coefficient of 0.9986. Extrapolation to 5.0 M concentrations affords ρ_s = 0.080 mΩ, leading to $0.8 \leq R_s/\mathrm{m}\Omega \leq 8.0$ as estimates for the undivided cell geometries considered here, where we are not concerned with the development of membrane junction potentials. This leads to experimental cell time constants of $64 \leq R_s C_{dl}/\mathrm{ns} \leq 640$. It was noted that since the electrolyte is aqueous (and of assumed specific heat capacity at constant pressure, C_p = 4.18 J g^{-1} K^{-1}), Joule heating of the cell $\left(\frac{2{i_{rms}}^2 R_s t_s}{4.18Sl}\right)$ affords merely a *ca.* 0.1 mK temperature rise, a change which has negligible impact on the cell potential $\left(\Delta V \sim \frac{R\Delta T}{F} \approx 10\ nV\right)$, as anticipated (*vide supra*).

The following iterative strategy was adopted to compute the non-Faradaic competent. Initially, the capacitative current was assumed to be zero, so that the cell voltage could be determined as above, albeit with Ohmic losses accounted through: $V = E_{cell} - iR_s$. Note that this causes the cell voltage to be increased compared with the case of no Ohmic drop (charging currents are negative), and decreased under discharge. This allows for the first approximation to the capacitative contribution, using,

$$\left|i_{cap}\right| = \left|\frac{d}{dt}\left(SQ_{cap}\right)\right| = S\left|\frac{dQ_{cap}}{dt}\right| + Q_{cap}\left|\frac{dS}{dt}\right| = C_{dl}S\left|\frac{dE_{cell}}{dt}\right| = \frac{1}{5}\left|\frac{dE_{cell}}{dt}\right| \qquad \text{(Eqn. 7.51)}$$

assuming that the electrode contact area with the electrolyte is constant (*viz.* no gas produced / phase change / dendrite formation), and in which Q_{cap} is the charge density of the electrode | electrolyte interface. Note that the capacitative current is

dependent on the rate at which the voltage across the *Warburg impedance* varies, and so does not include the Ohmic correction, as is evident from the equivalent circuit illustrated in Fig. 7.1. The *charging* of the capacitor *diminishes* the Faradaic current, reducing the extent of electrolysis,

$$i_f^{charge} = i^{charge} + \left|i_{cap}\right| \qquad \text{(Eqn. 7.52)}$$

where i^{charge} is negative. Under discharge, since the temporal change in the cell voltage *generates* a capacitative current to flow, capacitative discharege also *decreases* the Faradaic current that is allowed to flow:

$$i_f^{discharge} = i^{discharge} - \left|i_{cap}\right| \qquad \text{(Eqn. 7.53)}$$

These first estimates were then employed to recalculate both i_f and V iteratively, to an absolute error of < 1.0 μA in $\left|i_{cap}\right|$. A maximum of three iterations were found to be necessary.

Although not examined, it was noted that this approach, unlike others, holds the advantage of allowing for potential-dependence of the capacitance to be incorporated within the simulation.

7.2.3.6. Short Circuit Current

At short circuit, the potentials of the two electrodes are equal: V = 0; $E_{RHS} = E_{LHS} = E_{sc}$ – there is negligible resistance in the external circuit connecting the two electrodes, allowing the maxmum current, $i_{sc} = i_f^{sc} + i_{cap}^{sc}$, to flow under any SOC, whilst delivering no workable power (*q.v.* Section 7.2.2). The instantaneous Faradaic contribution can be determined from the concentration profiles corresponding to a particular SOC of the system, and is instantaneously supplemented by the full

capacitative current: $i_{cap}^{sc} = C_{dl} S \frac{V_{oc}}{\Delta t}$, where V_{oc} is the open circuit voltage across the terminals of the cell immediately prior to discharge.

However, the time dependence of the short circuit current is not a point of interest, nor the potential of the individual electrodes. Accordingly, the short circuit current from the solution resistance and the open circuit voltage can be calculated:

$$i_{sc} = \frac{V_{oc}}{R_s} \qquad \text{(Eqn. 7.54)}$$

where V_{oc} is given by the concentration profiles immediately after cell charging through either the Nernst expression or the corrosion-corrected value, as detailed in Sections 7.2.3.1 and 7.2.3.2, respectively.

7.2.4. Computing

Dense spatio-temporal grids were found to be required (typically 50000 nodes in time and 20000 nodes in space) to ensure sufficient numerical convergence of the resulting concentration profiles; the use of $\Delta t \gg R_s C_{dl}$ assisted in damping oscillatory instabilities under short times due to the small cell time constants. Furthermore, to avoid the cell cutting out to open circuit due to complete electrolysis, except for the case of the week-long solar charging simulation, all data reported herein were obtained under the condition that the concentrations of all species (including the surface concentration of zinc) were greater than zero (a necessary constraint for finite difference simulations of galvanic cells) with $\frac{\partial V}{\partial t} \leq 0$ under discharge; this constraint is tantamount to the "cut-off" voltage used in experimental battery testing. Simulations were undertaken through program encoding in GNU FORTRAN with double precision variables using the freely available g77 compiler, and were excuted on an Intel Pentium processor (2.4 GHz; 1.98 GB RAM). single charge-discharge experiments typically were found to cost a maximum of *ca.* 250 s in CPU time. A

summary of experimental parameters used for the simulations is given in Table 7.1.

Table 7.1. Typical values employed for the simulations reported herein.

Parameter	***Value***
Ambient conditions	
T	298 K
P	1.0 bar
Initial concentrations	
Ce^{3+}	500 mM
Ce^{4+}	1 mM
Zn^{2+}	1500 mM
Zn coverage	10^{-6} mol m^{-2}
Cell geometry & temporal resolution	
l (thin)	39.6 μm
l (thick)	396 μm
S	4×10^{-4} m^2
t_s	5.0 s
Δx (thin)	1.98 nm
Δx (thick)	19.8 nm
Δt	400 μs
Diffusion coefficients	
Ce^{3+}	5.0×10^{-11} m^2 s^{-1}
Ce^{4+}	5.0×10^{-11} m^2 s^{-1}
Zn^{2+}	6.9×10^{-10} m^2 s^{-1}
Electrical properties	
C_{dl}	80 μF
R_s(thin)	0.8 mΩ
R_s(thick)	8.0 mΩ
Cell kinetics	
k_s	6.8×10^{-6} m s^{-1}
k_{s2}	4.0×10^{-6} m s^{-1}
k_{s3} (no corrosion)	0.0 m s^{-1}
k_{s3} (with corrosion)	6.8×10^{-6} m s^{-1}
α	0.4
α_2	0.4
α_3	0.4
Current control	
i_0	0.00 A
A	-30.0 mA
Discharge current minimum	15.0 mA
Discharge current maximum	50.0 mA

7.3. Results and Discussion

The results obtained in charging and discharging the cell of thin and thick depth, with and without corrosion occurring at the zinc electrode is first considered, followed by evaluate the data through the performance characteristics of the discharged cell.

7.3.1. Cell charging

The six waveforms illustrated in Fig. 7.2 and described in Section 7.2.1 afford cell charging waveforms as given in Fig. 7.4 for thin and thick cell geometries (panels a, b and c, d, respectively), where deactivation of Ce^{4+}/zinc corrosion is both present (panels b, d) and absent (panels a, c), and affords cells of the characteristics reported

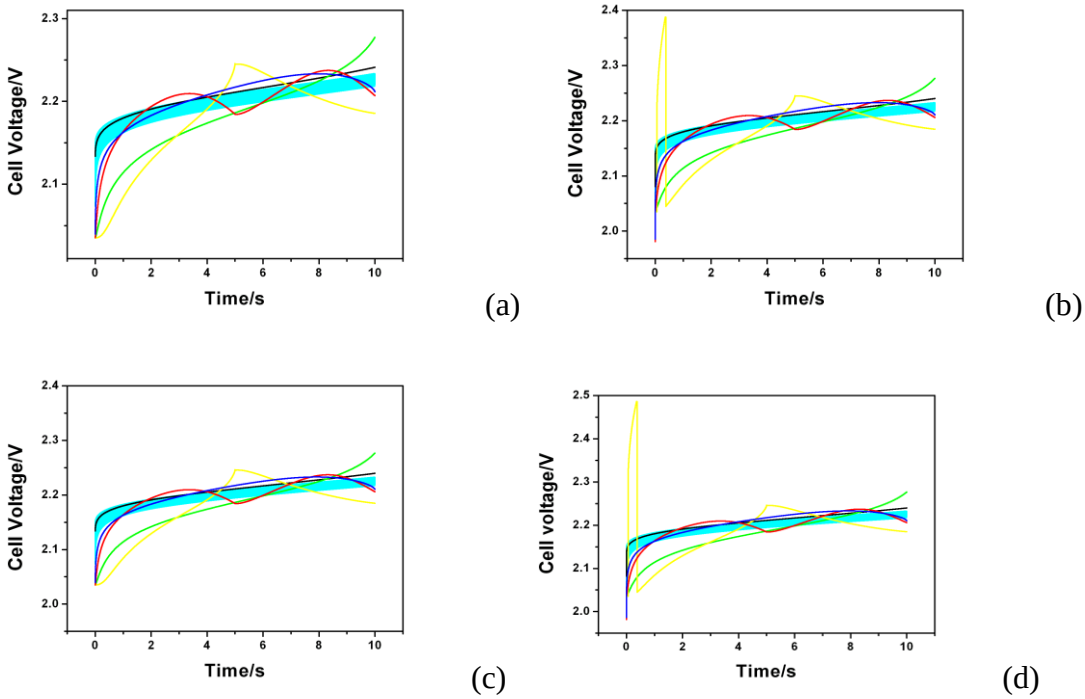

Fig. 7.4. Variation of the cell voltage during charge: pure, constant DC (black), DC ramp (green), DC accelerator-decelerator (yellow), fully rectified AC at 50 Hz with constant DC offset (cyan), rectified tidal (red), solar (blue); the cell geometry was thin (panels (a),(b)) or thick (panels (c),(d)), with no corrosion/deactivation at the zinc electrode (panels (a),(c)) or with corrosion (panels (b), (d)).

in Table 7.2. Note that the quality $k_{s_3} = k_s$ for the presence of corrosion was

assumed given the paucity of literature data. the value of A chosen for the simulations (-30 mA) was taken since this value does not cause the cell potentials to tend to infinity due to transport-limited electrolysis for any cell/waveform combination (due to electrolytic consumption being faster than mass-transport refreshment of Ce^{3+} and Zn^{2+}). However, in the cases of the DC ramp and the DC accelerator-decelerator systems, the slow/concave variation of the current with time at short times causes any corrosive/deactivation behaviour to dominate at the zinc electrode, resulting in $\Gamma_{Zn} \rightarrow 0$. For the case of the DC accelerator-decelerator waveform, the calculation could only complete if the first approximation to the electrode potential discussed in Section 7.2.3.4 was employed, causing the cell voltage to spike until the charging current became sufficiently large for deposition conditions to be established at the zinc electrode (*q.v.* Fig. 7.4b and d). In general, the charing current causes a net increase in the cell voltage compared with the initial state of the system, as expected, and is particularly influenced by the charging current gradient: the maximum in the cell voltage lags any current maximum, with the time delay being influenced by the steepness by which the current rises and falls; the cell voltage always follows the cell current, and decreases for the case of solar, tidal and DC accelerator-decelerator systems in accordance with the associated electrode boundary conditions. This effect is more highly pronounced for this latter waveform. In the case of the fully rectified AC signal, the constant charge and discharge of the electrical double layers is manifested by a greater noise in the cell voltage under charge and a loss in voltage compared with the pure, constant DC signal, even though the same trend in the voltage rise during charge is observed. The cell voltage observed for the DC ramp exhibits the most extreme behaviour, where activation, Ohmic and concentration polarisations are readily discernible. Such effects are pronounced in the time variation of the capacitative currents flowing (Fig. 7.5), which exhibit discontinuities at maxima and minima in the cell voltage.

Table. 7.2. Characteristics of the cells charged with the renewable energy waveforms. See Table 1 for definitions of "thick" and "thin" cells, and likewise for "with corrosion" and "without corrosion". Note that $2t_s$ = 9.9996 s in the computations.

(a)

Charging Regime			**Thin Cells, No corrosion**			**Thin Cells, With corrosion**		
	Q_0 / C	**%SOC**	**V_{oc} / V**	**i_{sc} / A**	**$\int_0^{2t_s} iVdt$ / J**	**V_{oc} / V**	**i_{sc} / A**	**$\int_0^{2t_s} iVdt$ / J**
Pure, constant DC	0.300	39.3	2.23	2790	0.663	2.23	2790	0.662
DC ramp	0.260	34.0	2.25	2820	0.574	2.25	2820	0.574
DC accelerator-decelerator	0.208	27.2	2.19	2730	0.460	2.18	2730	0.460
Fully rectified AC at 50 Hz with constant offset	0.270	35.3	2.19	2770	0.594	2.22	2770	0.594
Rectified tidal	0.270	35.3	2.21	2760	0.596	2.21	2760	0.596
Solar	0.289	37.8	2.21	2760	0.638	2.21	2760	0.638

(b)

Charging Regime			**Thick Cells, No corrosion**			**Thick Cells, With corrosion**		
	Q_0 / C	**%SOC**	**V_{oc} / V**	**i_{sc} / A**	**$\int_0^{2t_s} iVdt$ / J**	**V_{oc} / V**	**i_{sc} / A**	**$\int_0^{2t_s} iVdt$ / J**
Pure, constant DC	0.300	3.93	2.23	280	0.663	2.23	280	0.663
DC ramp	0.260	3.40	2.25	280	0.574	2.25	280	0.574
DC accelerator-decelerator	0.208	2.7	2.18	270	0.460	2.18	270	0.460
Fully rectified AC at 50 Hz with constant offset	0.270	3.53	2.22	280	0.594	2.22	280	0.594
Rectified tidal	0.270	3.53	2.21	280	0.596	2.20	280	0.596
Solar	0.289	3.78	2.21	280	0.638	2.21	280	0.638

The open circuit voltage, current under short circuit and state-of –charge of all simulated systems are presented in Table 7.2. It is clear that in all cases, the SOC is less than 50% (as designed), and decreases in the order constant

DC>solar>AC=tidal>DC ramp>DC accelerator-decelerator as noted in Section 7.2.1. However, the open circuit voltage of the charged system decreases in the order DC ramp>constant DC>solar=tidal=AC>DC accelerator-decelerator. Accordingly, the amount of electrical work done in charging the cell (note the power dissipated by heat over the full charging period, and thus the energy wasted as heat, is independent of the charging current waveform) decreases in the order constant DC>solar>tidal=AC>DC ramp>DC accelerator-decelerator, *viz.* commensurate with the electrical charge passed. These trends are important since they detail the amount of energy available for discharge, and are essentially independent of the cell type/conditions: the occurrence of corrosion at the zinc electrode does not manifest significantly on the cell characteristics after charge. In considering the difference between thick and thin cells, the SOC is observed that it is smaller in the former case, as expected. This also impacts on the short circuit current that flows, as this is proportional to the cell conductance, which is inversely proportional to the cell thickness.

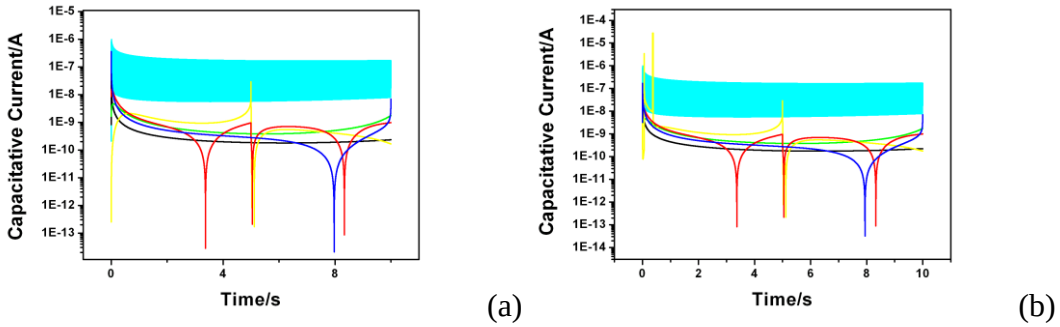

Fig. 7.5. Variation of the modulus of the capactative current during cell charge: pure, constant DC (black), DC ramp (green), DC accelerator-decelerator (yellow), fully rectified AC at 50 Hz with constant DC offset (cyan), rectified tidal (red), solar (blue); the cell geometry was thin with (b) or without (a) corrosion/deactivation at the zinc electrode.

For all cell geometries and electrode boundary conditions considered, the ramp, AC, constant DC, solar and tidal charging scenarios hold cell voltages which cross-over close to the maximum in the solar and tidal scenarios (typically *ca.* 8 s). This is quite significant, since it may suggest that, although the SOC will be lower if the charge cut-off time is reduced from 10 s to 8 s, the higher open circuit voltage that results may allow for a more efficient discharge of the cell. This is not considered within this

work, since the energy lost to heat would then be different for each waveform.

7.3.2. Cell Discharge

Cells were discharged under constant DC currents in the range $15 \leq i/mA \leq 50$, with the constraint in cell voltage gradient as a "cut-off" imposed (*q.v.* Section 7.2.4); Fig. 7.6 provides a selection for both thick and thin cells. In each case, the three

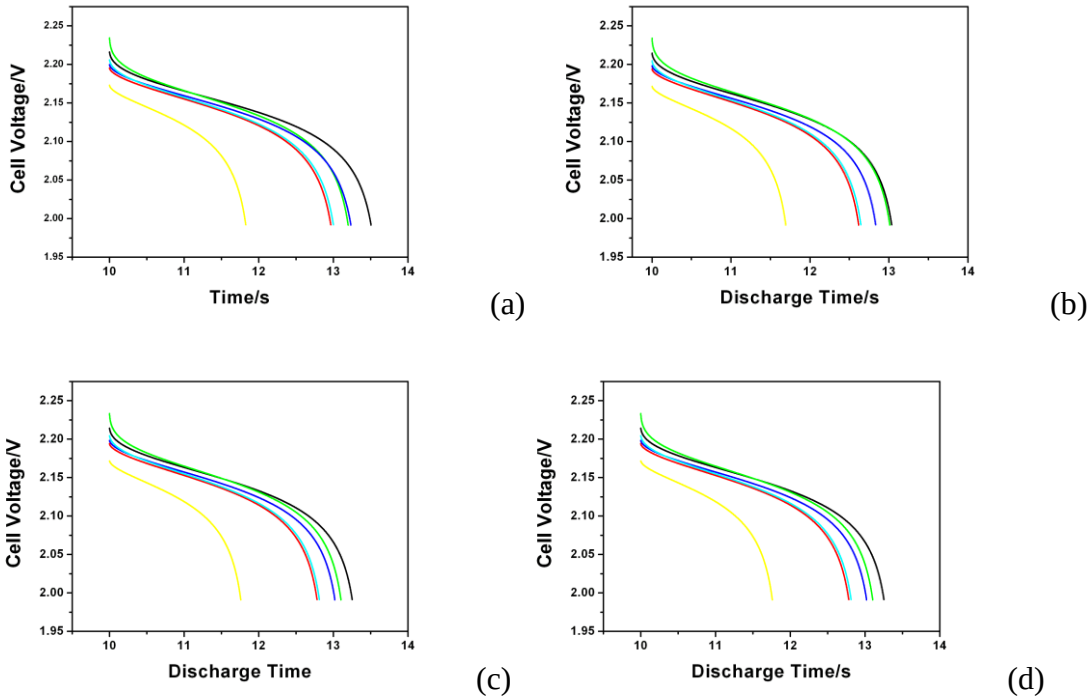

Fig. 7.6. Variation of the cell voltage during constant current (30 mA) discharge, immediately after charge: pure, constant DC (black), DC ramp (green), DC accelerator-decelerator (yellow), fully rectified AC at 50 Hz with constant DC offset (cyan), rectified tidal (red), solar (blue); the cell geometry was thin (panels (a),(b)) or thick (panels (c),(d)), with no corrosion/deactivation at the zinc electrode (panels (a),(c)) or with corrosion (panels (b), (d)). Note that the cell was charged for the first 10 s and allowed to discharge over the next 10 s.

characteristic regions of activation, Ohmic and concentration polarisations are observable. These classical waveshapes cause a "U"-shape in the modulus of the capacitative current that is generated (Fig. 7.7). In all cases the cells charged with the DC accelerator-decelerator waveform are discharged most rapidly, since this reflects the SOC. However, the discharge characteristics for the other waveforms are a

convolution between SOC and the open circuit voltage, for both thick and thin cells. Furthermore, it is apparent that the presence or absence of corrosion is more significant for the discharge of the thin cells rather than the thick cells: in the former, discharge is faster in the presence of corrosive deactivation; in the latter, there is no apparent difference in the discharge rates. This is as expected, since reactant cross-over can occur in the timescales considered for the thin cells only.

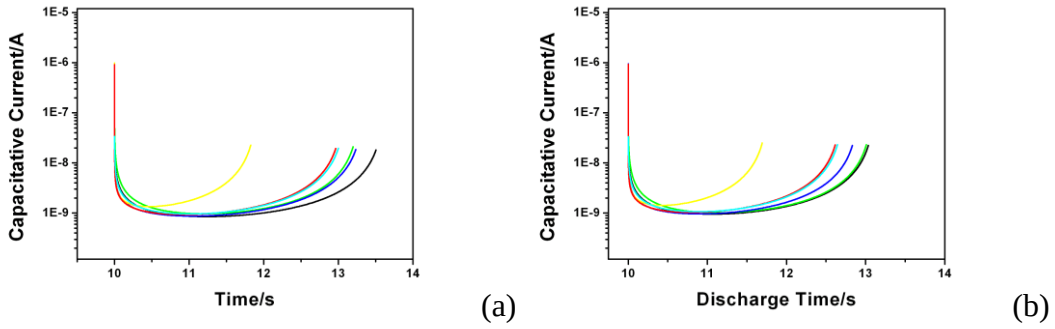

Fig. 7.7. Variation of the modulus of the capactiative current during cell discharge (from 10 s) after charging for the first 10 s: pure, constant DC (black), DC ramp (green), DC accelerator-decelerator (yellow), fully rectified AC at 50 Hz with constant DC offset (cyan), rectified tidal (red), solar (blue); the cell geometry was thin with (b) or without (a) corrosion/deactivation at the zinc electrode.

The performance characteristics of the cell in the light of the figure-of-merit introduced in Section 7.2.2 is considered next.

7.3.3. Performance Characteristics

7.3.3.1. Energy Loss Ratio (ELR)

Fig. 7.8 illustrates the variation of the ELR with discharge current for both thin (panel a) and thick (panel b) cells. In general, energy conversion efficiencies decrease with increasing drain, as expected, with the most inefficient cell (affording at most 30% efficiency in energy conversion) is the cells charged by the DC accelerator-decelerator function; the most efficient cell is a thin cell with no corrosion/deactivation at the zinc electrode, charged either through a constant DC current, or through a clear sky solar

waveform, and discharged under a low drain (~48% efficient). However, in general, the most efficient charging waveform is the DC ramp, since this protocol charges to a high open circuit voltage, whilst expending the second lowest amount of energy. This scenario is well known.

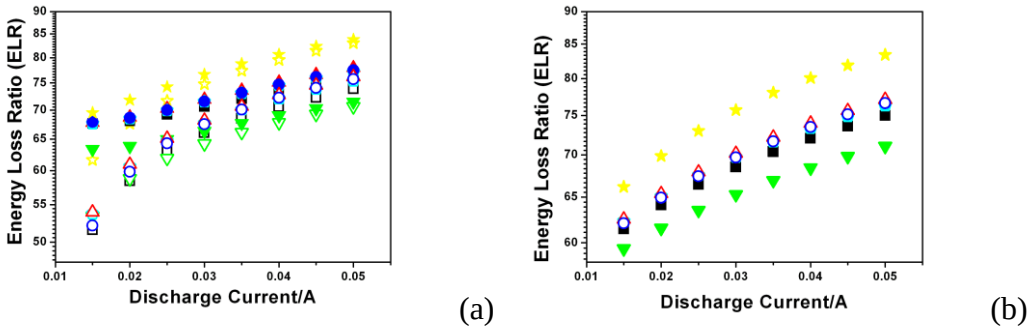

Fig. 7.8. Variation of the energy loss ratio with drain current for thin (a) or thick (b) cells; closed and open symbols refer to cells with or without corrosion/deactivation at the zinc electrode, respectively. Key: pure, constant DC (black squares), DC ramp (green inverted triangles), DC accelerator-decelerator (yellow stars), fully rectified AC at 50 Hz with constant DC offset (cyan pentagons), rectified tidal (red triangles), solar (blue circles).

As anticipated from Section 7.3.2, there is little, if any difference between the performance of cells in the presence and absence of corrosion/deactivation at the zinc electrode for thick cells (Fig. 7.8b). For this case, the solar, tidal and AC waveforms are approximately as efficient as each other, and deviate from the constant DC system with increasing drain. In contrast, thin cells are more efficient in energy conversion than thick cells when corrosion/deactivation is not rapid at the sacrificial electrode. Here, solar charged cells are amongst the most efficient for energy conversion at low drain, but become almost as inefficient as thin, corroding cells at high drain. Indeed, in this limit, the most efficient cell is that charged by a DC ramp, with comparative efficiency for thin and thick cells.

7.3.3.2. Energy-Power Plane (Ragone Plot) Characteristics

Integration of the discharge curves as outlined in Section 7.2.2 empowers the energy (ε) and power (p) delivered under discharge; the characteristic time for all cells

simulated was determined to be between 1-10 s, essentially varying with the SOC. Ragone plots normalised as indicated in Section 7.2.2 and with respect to the cell volume are illustrated in Fig. 7.9 for both thin (panel a) and thick (panel b) cells. The superimposition of symbols for the case of with and without corrosion in the case of Fig. 7.9b is expected, as are the trends in Fig. 7.9a, where it is clear corrosion-free solar-charged cells outperform most other cells under lower power drain, with, in all cases the DC ramp charged cell performing best under high drain.

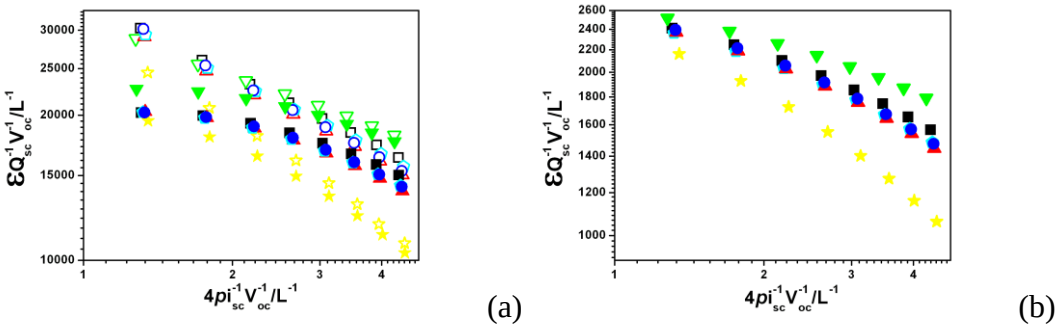

Fig. 7.9. Ragone plots for thin (a) or thick (b) cells; closed and open symbols refer to cells with or without corrosion/deactivation at the zinc electrode, respectively. Key: pure, constant DC (black squares), DC ramp (green inverted triangles), DC accelerator-decelerator (yellow stars), fully rectified AC at 50 Hz with constant DC offset (cyan pentagons), rectified tidal (red triangles), solar (blue circels).

The normalisation of the dimensionless energy and power with cell volume highlights the nature of these "supercabatteries":[237] at a constant dimensional power, the amount of dimensional energy delivered is larger for thin cells with large electrodes, emphasising that scale-out of these systems is more important than scale-up.

In order to examine the performance of the systems over repeated charge-discharge cycles, the solar-charged cell over a period of one week is next examined (corresponding to 140 s in the mapped time).

7.3.3.3. Solar Charging over One Week

Cells were charged and discharged over a period of seven days as indicated in Fig.

7.10a, assuming daytime for the first six days consisted of clear skies, with a full day solar eclipse on the seventh day, and with a variable discharge for the first five nights, with open circuit occurring for the last two nights. This particular regime was chosen to illustrate the effects of diffusion layer thickness at the electrode surface, and differences in corrosion between the two extreme limits in cell geometry and electrode kinetics.

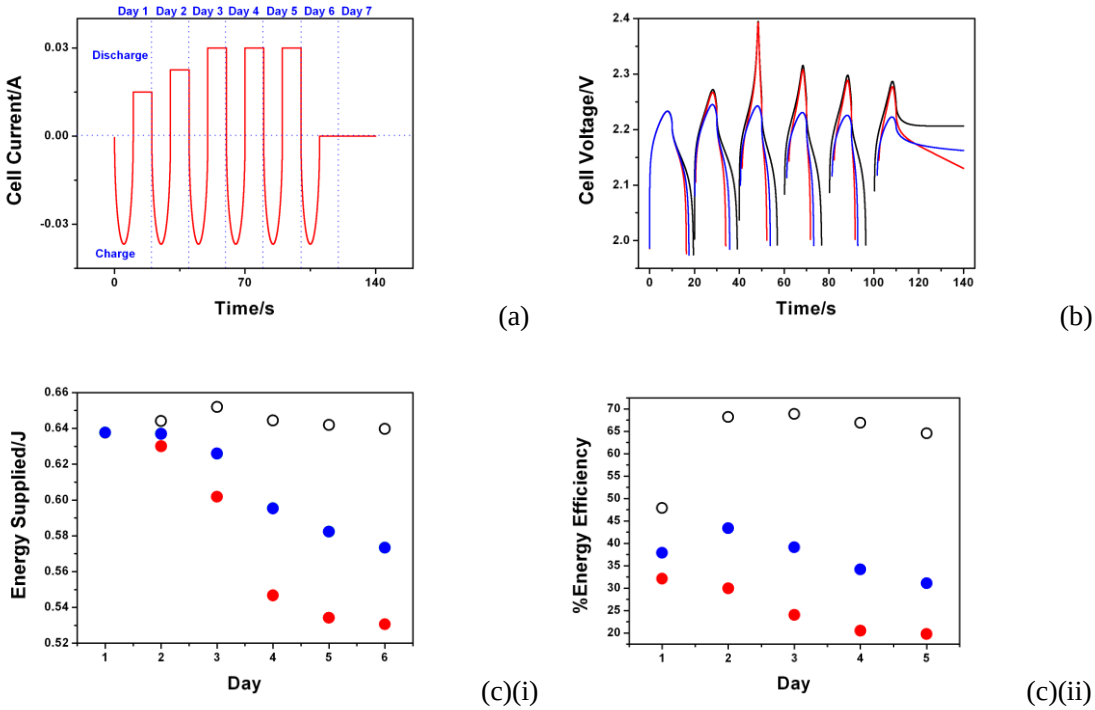

Fig. 7.10. Performance characteristics of the galvanic cell under one-week of solar illumination, with no work undertaken during the evening of Day 6 and Day 7, with the morning of Day 7 having no Sun.

(a) current-charge and discharge characteristics

(b) Cell performance characteristics for thin (black and red) and thick (green and blue) cells in the presence (red and blue) or absence (black and green) of corrosion/deactivation at the zinc electrode.

(c) Variation of (i) the energy used to charge-up the cell and (ii) the energy efficiency of the cell over the studied time period; key: open symbols refer to the absence of corrosion with closed symbols indicating corrosion of the zinc electrode, at thin (black and red) or thick (green and blue) cells.

Note that the absence of appearance of green trace in (b) and (c) is due to them lying immediately beneath the blue traces.

Fig. 7.10b illustrates the charge-discharge curves. Note that all cut-off limits were removed for the collection of these data; the discontinuities between night discharge

and day charge reflect the cases when the electrode surface concentrations tend to zero, giving rise to smaller diffusion layer thicknesses with as the discharge current increases. The decrease in the open circuit voltage for thick, non-corrosive cells is understood through the diffusive mixing of material from bulk to surface.

Whilst the thick cells (which again do not discriminate between corrosive and non-corrosive conditions) maintain approximately a uniform characteristic over the week, with a maximum change of *ca*. 10% in energy required for charge (Fig. 7.10b) and a reasonably constant energy efficiency (Fig. 7.10c), thin cells only afford high energy efficiency, and stability of the open circuit voltage under non-corrosive conditions. It is important to realise that both discharge conditions and cell history contribute to the energy efficiency.

7.4. Conclusions

In this work, the performance of various charging waveforms have been examined, some of which directly mimic a renewable energy output profile, on a redox battery operated under diffusion-only conditions. It has been seen that both cell geometry and electrode kinetics play important roles which are not always immediately predictable – thick cells do not discriminate between corrosive and non-corrosive boundary conditions; the energy efficiency of a cell (thin or thick) in the absence of corrosion is optimised if the cell is more concentrated in the diffusion layer than in the bulk. Moreover, for single charge-discharge experiments, it has been seen that renewable energy waveforms charge cells that exhibit good performance under low drain. This is entirely in the line with expectation, in the light of our earlier work on solar-rechargeable galvanic cells.[238]

In returning to the question posed in the title, it has been suggested that storage efficiency of a particular renewable energy in redox batteries is as much a function of

the cell type (geometry and electrode kinetics) as the cell discharge drain and battery charge-discharge cycle history, at least for the system we have considered. Thus, provided corrosion-free, low drainage conditions can be enforced, the use of solar energy charging of redox batteries can be made to be attractive; the smart grid would need to process information on weather characteristics, individual cell geometry and kinetics, cell cycle history, and power demand, since the cell discharge must match the cell type for optimised performance. This is potentially pragmatically achievable with modern computing facilities.

Last, it is noted that, *irrespective of charging waveform*, banks of redox cells are required for any large scale system, with thinner cells providing greater volumetric energies than thick ones. In translating our simulations concerning diffusion-only conditions to the convective-diffusion transport of redox flow batteries, it can be suggested that microfluidic redox flow batteries wired in parallel would then allow for high energy and power characteristics – allowing for the desired top right hand corner of the energy – power playing field to be populated.

8. CONCLUSIONS

In summary, the main focus of this thesis is to investigate in the depth for molecular electrochemistry in several ways including sensing, mechanistic study of bond formation/cleavage, mass transport profile in liquid crystals and digital simulations.

It was found that electrochemistry is a great analytical tool for analysis substrates such as sensing. Redox catalytic reactions were applied in order to monitoring certain substrates such as L-cysteine and glutathione, and the analytical performance have been shown successful. Lactic acid was found that it can be detected by combining photo- and redox catalytic methods. Furthermore, lactic acid was also found to be a potential fuel for a renewable battery. Accordingly digital simulations were successfully carried out in both different cells (thick and thin) and different waveforms.

Bond formation/cleavage was also studied in variety ways. Protonation and deprotonation process was studied by using a spiro-bis-anil, vitamin K_1 and Sudan III. Especially for the spiro-bis-anil, a comparison between conventional Birch reduction and electrochemical reduction was made and suggested that electrochemistry offers advantages over conventional Birch reduction including mild conditions and observable intermediate. Both vitamin K_1 and sudan III were examined in different pH, and reaction mechanisms were suggested including two different reduction routes for vitamin K_1 depending on the pH and tautomerisation process may occur in the oxidation of Sudan III. Ion release was then studied using nitroprusside, 1-iodo-nitrobenzene and bromobenzene diazonium salt. With a step-by-step attempt, the ions can be controlled to release without a contamination to the solvent, and it was found that there is no kinetic salt effect when ions were released to the solution with different electrolyte concentrations.

Mass transports in liquid has been studied extensively since electrochemistry has been suggested, rear to see the mechanistic studies of mass transport in lyotropic liquid crystals. By using both N and M phase chromic liquid crystals; it was found that two-dimensional diffusion was occurring on a macroelectrode, with a possibility of electron hopping.

Digital simulations that in the topic of which type of renewable energy form is suitable for a cerium-zinc redox flow battery were carried out. The diffusion only condition was considered. It was found that the storage efficiency of a particular renewable energy in redox batteries counts on both cell type (geometry and electrode materials – kinetics) and cell charge-discharge cycle history. In the future, a cerium-zinc redox flow battery will be examined and microfluidic technologies will be applied.

9. REFERENCES

1. Zhou, Y.; Andreou, A.; Biktagirov, E.; Eames, J.; Wadhawan, J., *Electrochem. Commun.* **2010,** *12*, 1493-1497.
2. Compton, R. G.; Banks, C. E.; Editors, *Understanding Voltammetry*. World Scientific: London, 2007; p 384 pp.
3. Frankenthal, R. P., *Proc. - Electrochem. Soc.* **2002,** *2002-13*, 1-10.
4. Pourbaix, M., *Corros. Sci.* **1974,** *14*, 25-82.
5. Uslu, B.; Ozkan, S., *Anal. Lett.* **2011,** *44*, 2644-2702.
6. Grieshaber, D.; MacKenzie, R.; Voros, J.; Reimhult, E., *Sensors* **2008,** *8*, 1400-1458.
7. Weaver, M. J.; Anson, F. C., *J. Electroanal. Chem.* **1975,** *65*, 737-758.
8. Attard, P., Electrolytes and the Electric Double Layer. In *Advances in Chemical Physics*, John Wiley & Sons, Inc.: 2007; pp 1-159.
9. Fisher, A. C., *Electrode Dynamics*. Oxford University Press: Oxford, 1998.
10. Stern, O. Z., *Electrochem.* **1924,** *30*, 508.
11. Grahame, D. C., *Chem. Rev.* **1947,** *41*, 441-501.
12. Bockris, J. O. M.; Devanathan, M. A. V.; Muller, K., *Proc. R. Soc. London, Seri. A* **1963,** *274*, 55-79.
13. Meijer, E. W., *Angew. Chem., Int. Ed.* **2001,** *40*, 3783-3789.
14. Van Houten, J., *J. Chem. Educ.* **2002,** *79*, 21.
15. Marcus, R. A., *J. Chem. Phys.* **1956,** *24*, 966-978.
16. Fletcher, S.; Varley, T. S., *Phys. Chem. Chem. Phys.* **2011,** *13*, 5359-5364.
17. Tender, L.; Carter, M. T.; Murray, R. W., *Anal. Chem.* **1994,** *66*, 3173-3181.
18. Kissinger, P. T.; Heineman, W. R., *J. Chem. Educ.* **1983,** *60*, 702-706.
19. Scholz, F.; Meyer, B., *Electroanal. Chem.* **1998,** *20*, 1-86.
20. Hughes, M.; Shaffer, M. S. P.; Renouf, A. C.; Singh, C.; Chen, G. Z.; Fray, D.

J.; Windle, A. H., *Adv. Mater.* **2002,** *14*, 382-385.

21. Lu, X. Q.; Zhang, L.; Sun, P.; Yao, D., *Eur. J. Chem.* **2011,** *2*, 120-124.
22. Hynek, D.; Prasek, J.; Koudelka, P.; Chomoucka, J.; Trnkova, L.; Adam, V.; Hubalek, J.; Kizek, R., *Curr. Phys. Chem.* **2011,** *1*, 299-324.
23. Armstrong, F. A., *Bioelectrochem.: Princ. Pract.* **1997,** *5*, 205-255.
24. Matsuda, H.; Ayabe, Y., *Z. Elecktrochem* **1955,** *59*, 494.
25. Randles, J. E. A., *Trans. Faraday Soc.* **1948,** *44*, 322-327.
26. Randles, J. E. A., *Trans. Faraday Soc.* **1948,** *44*, 327-338.
27. Savéant, J.-M., *Chem. Rev.* **2008,** *108*, 2348-2378.
28. Nekrassova, O.; Kershaw, J.; Wadhawan, J. D.; Lawrence, N. S.; Compton, R. G., *Phys. Chem. Chem. Phys.* **2004,** *6*, 1316-1320.
29. Compton, R. G.; Dryfe, R. A. W.; Fisher, A. C., *J. Chem. Soc., Perkin Trans. 2* **1994**, 1581-1587.
30. Nadjo, L.; *Savéant*, J. M., *J. Electroanal. Chem.* **1971,** *33*, 419-451.
31. Compton, R. G.; Wellington, R. G.; Dobson, P. J.; Leigh, P. A., *J. Electroanal. Chem.* **1994,** *370*, 129-133.
32. Unwin, P. R., *J. Electroanal. Chem.* **1991,** *297*, 103-124.
33. Compton, R. G.; Banks, C. E., *Understanding Voltammetry*. 1st ed.; World Scientific Publishing: 2007; p 265.
34. Nelsen, S. F.; Echegoyen, L.; Evans, D. H., *J. Am. Chem. Soc.* **1975,** *97*, 3530-3532.
35. Ramaley, L.; Krause, M. S., *Anal. Chem.* **1969,** *41*, 1362-1365.
36. Economou, A.; Fielden, P. R., *Anal. Chim. Acta* **1993,** *273*, 27-34.
37. Shoup, D.; Szabo, A., *J. Electroanal. Chem.* **1982,** *140*, 237-45.
38. Bard, A. J.; Faulkner, L. R., *Electrochemical Methods Fundamentals and Applications*. 2nd ed.; JOHN WILEY & SONS: 2003.
39. Bowden, W. L.; Bonnar, P.; Brown, D. B.; Geiger, W. E., *Inorg. Chem.* **1977,** *16*, 41-43.
40. Byrne, H. A.; Tieszen, K. L.; Hollis, S.; Dornan, T. L.; New, J. P., *Diabetes Care* **2000,** *23*, 500-503.

41. Ho, W. O.; Krause, S.; McNeil, C. J.; Pritchard, J. A.; Armstrong, R. D.; Athey, D.; Rawson, K., *Anal. Chem.* **1999,** *71*, 1940-1946.

42. Liao, J. C.; Mastali, M.; Gau, V.; Suchard, M. A.; Møller, A. K.; Bruckner, D. A.; Babbitt, J. T.; Li, Y.; Gornbein, J.; Landaw, E. M.; McCabe, E. R. B.; Churchill, B. M.; Haake, D. A., *J. Clin. Microbiol.* **2006,** *44*, 561-570.

43. Weetall, H. H.; Hotaling, T., *Biosensors* **1987,** *3*, 57-63.

44. Albery, W. J.; Bartlett, P. N.; Cass, A. E. G.; Craston, D. H.; Haggett, B. G. D., *J. Chem. Soc., Faraday Trans. 1 F* **1986,** *82*, 1033-1050.

45. Mazzei, F.; Botrè, F.; Montilla, S.; Pilloton, R.; Podestà, E.; Botrè, C., *J. Electroanal. Chem.* **2004,** *574*, 95-100.

46. Leonard, P.; Hearty, S.; Brennan, J.; Dunne, L.; Quinn, J.; Chakraborty, T.; O'Kennedy, R., *Enzyme. Microb. Technol.* **2003,** *32*, 3-13.

47. Rawson, D. M.; Willmer, A. J.; Turner, A. P. P., *Biosensors* **1989,** *4*, 299-311.

48. Dou, Y.-H.; Haswell, S. J.; Greenman, J.; Wadhawan, J., *Electroanalysis* **2012,** *24*, 264-272.

49. White, P. C.; Lawrence, N. S.; Davis, J.; Compton, R. G., *Anal. Chim. Acta* **2001,** *447*, 1-10.

50. White, P. C.; Lawrence, N. S.; Davis, J.; Compton, R. G., *Electroanalysis* **2002,** *14*, 89-98.

51. Goodman, M. T.; McDuffie, K.; Hernandez, B.; Wilkens, L. R.; Selhub, J., *Cancer* **2000,** *89*, 376-382.

52. Lang, C. A.; Mills, B. J.; Mastropaolo, W.; Liu, M. C., *J. Lab. Clin. Med.* **2000,** *135*, 402-405.

53. Kleinman, W. A.; Richie Jr, J. P., *Biochem. Pharmacol.* **2000,** *60*, 19-29.

54. Mathews, C. K.; van Holde, K. E.; Ahern, K. G., *Biochemistry*. Addison-Wesley Pulishing Company: San Francisco, 2000.

55. Lawrence, N. S.; Davis, J.; Compton, R. G., *Talanta* **2001,** *53*, 1089-1094.

56. Lawrence, N. S.; Davis, J.; Jiang, L.; Jones, T. G. J.; Davis, S. N.; Compton, R. G., *Analyst* **2000,** *125*, 661-663.

57. Wring, S. A.; Hart, J. P.; Birch, B. J., *Analyst* **1991,** *116*, 123-129.

58. Hua, C.; Smyth, M. R.; O'Fagain, C., *Analyst* **1991,** *116*, 929-931.
59. Le Gall, A.-C.; van den Berg, C. M. G., *Analyst* **1993,** *118*, 1411-1415.
60. von Wandruszka, R.; Yuan, X.; Morra, M. J., *Talanta* **1993,** *40*, 37-42.
61. Banica, F. G.; Fogg, A. G.; Moreira, J. C., *Analyst* **1994,** *119*, 2343-2349.
62. Bănică, F. G.; Fogg, A. G.; Moreira, J. C., *Talanta* **1995,** *42*, 227-234.
63. Banica, F. G.; Moreira, J. C.; Fogg, A. G., *Analyst* **1994,** *119*, 309-318.
64. Hignett, G.; Threlfell, S.; Wain, A. J.; Lawrence, N. S.; Wilkins, S. J.; Davis, J.; Compton, R. G.; Cardosi, M. F., *Analyst* **2001,** *126*, 353-357.
65. Rabenstein, D. L.; Yamashita, G. T., *Anal. Biochem.* **1989,** *180*, 259-263.
66. Cox, J. A.; Dabek-Zlotorzynska, E., *J. Chromatogr. A* **1991,** *543*, 226-232.
67. Luo, P.; Zhang, F.; Baldwin, R. P., *Anal. Chem.* **1991,** *63*, 1702-1707.
68. O'Shea, T. J.; Lunte, S. M., *Anal. Chem.* **1993,** *65*, 247-250.
69. O'Shea, T. J.; Lunte, S. M., *Anal. Chem.* **1994,** *66*, 307-311.
70. Zhong, M.; Lunte, S. M., *Anal. Chem.* **1998,** *71*, 251-255.
71. Sudeep, P. K.; Joseph, S. T. S.; Thomas, K. G., *J. Am. Chem. Soc.* **2005,** *127*, 6516-6517.
72. Mao, L.; Yamamoto, K., *Electroanalysis* **2000,** *12*, 577-582.
73. Cataldi, T. R. I.; De Benedetto, G. E.; Bianchini, A., *Electroanalysis* **1998,** *10*, 1163-1167.
74. Zhao, S.; Lennox, R. B., *J. Electroanal. Chem.* **1993,** *346*, 161-173.
75. Lund, H.; Hammerich, O., *Organic Electrochemistry*. 4th ed.; Marcel Dekker: New York, 2001.
76. Perez-Villar, V.; Vazquez-Iglesias, M. E.; de Geyer, A., *J. Phys. Chem.* **1993,** *97*, 5149-5154.
77. Horn, J. J.; Watson, A.; Lewis, M.; McCreedy, T.; Wadhawan, J. D., *Electrochem. Commun.* **2008,** *10*, 1384-1387.
78. Adsul, M. G.; Varma, A. J.; Gokhale, D. V., *Green Chem.* **2007,** *9*, 58-62.
79. Robinson, S.; Robinson, A. H., *Physiol. Rev.* **1954,** *34*, 202-20.
80. Cai, X.; Yan, J.; Chu, H.; Wu, M.; Tu, Y., *Sens. Actuators, B* **2010,** *143*, 655-659.

81. Parra, A.; Casero, E.; Vázquez, L.; Pariente, F.; Lorenzo, E., *Anal. Chim. Acta* **2006,** *555*, 308-315.

82. Mickelsen, O.; Keys, A., *J. Biol. Chem.* **1943,** *149*, 479-490.

83. Dill, D. B.; Hall, F. G.; Edwards, H. T., *Am. J. Physiol.* **1938,** *123*, 412-19.

84. Van, H. R.; Weiner, J. S., *J. Physiol.* **1952,** *116*, 395-403.

85. Thurmon, F. M.; Ottenstein, B., *J. Invest. Dermatol.* **1952,** *18*, 333-9.

86. Ottenstein, B., *Arch. Dermatol. Syph.* **1950,** *191*, 116-22.

87. Marquette, C. A.; Degiuli, A.; Blum, L.; amp; x; c, J., *Biosens. Bioelectron.* **2003,** *19*, 433-439.

88. Chu, B. H.; Kang, B. S.; Ren, F.; Chang, C. Y.; Wang, Y. L.; Pearton, S. J.; Glushakov, A. V.; Dennis, D. M.; Johnson, J. W.; Rajagopal, P.; Roberts, J. C.; Piner, E. L.; Linthicum, K. J., *Appl. Phys. Lett.* **2008,** *93*, 042114/1-042114/3.

89. Shram, N. F.; Netchiporouk, L. I.; Martelet, C.; Jaffrezic-Renault, N.; Bonnet, C.; Cespuglio, R., *Anal. Chem.* **1998,** *70*, 2618-2622.

90. Radoi, A.; Compagnone, D.; Valcarcel, M. A.; Placidi, P.; Materazzi, S.; Moscone, D.; Palleschi, G., *Electrochim. Acta* **2008,** *53*, 2161-2169.

91. Piñero, L. E.; Lebrón, I.; Correa, J.; Díaz, J.; Viera, L.; Arce, R.; García, C.; Oyola, R., *J. Photochem. Photobiol., A* **2012,** *228*, 44-50.

92. Sun, F.; Ma, W.; Xu, L.; Zhu, Y.; Liu, L.; Peng, C.; Wang, L.; Kuang, H.; Xu, C., *TrAC, Trends Anal. Chem.* **2010,** *29*, 1239-1249.

93. Newton, G. L.; Utley, P. R., *J. Anim. Sci* **1978,** *47*, 1338-1344.

94. Kjeldahl, J., *Zeits. Anal. Chem. 22*, 366-82.

95. Brown, C. A.; Jeong, K.-S.; Poppenga, R. H.; Puschner, B.; Miller, D. M.; Ellis, A. E.; Kang, K.-I.; Sum, S.; Cistola, A. M.; Brown, S. A., *J. Vet. Diagn. Invest.* **2007,** *19*, 525-531.

96. China, M.o.H.o.T.P.s.R.o. http://www.moh.gov.cn/publicfiles/business /htmlfiles/wsb/ pmtxwbd/2 00901/38923.htm (accessed on 24/04/2012).

97. Chan, E. Y. Y.; Griffiths, S. M.; Chan, C. W., *The Lancet* **2008,** *372*, 1444-1445.

98. Liao, C.-W.; Chen, Y.-R.; Chang, J.-L.; Zen, J.-M., *Electroanalysis* **2011,** *23*,

573-576.

99. Liu, F.; Yang, X.; Sun, S., *Analyst (Cambridge, U. K.)* **2011,** *136*, 374-378.

100. Jing, W.; Lu, S.; Li, X.; Jiang, X.; Chen, M.; Liang, M.; Tang, X.; Xu, C.; Chen, J., *Chin. J. Chem.* **2011,** *29*, 1601-1605.

101. Liu, Y. T.; Deng, J.; Xiao, X. L.; Ding, L.; Yuan, Y. L.; Li, H.; Li, X. T.; Yan, X. N.; Wang, L. L., *Electrochim. Acta* **2011,** *56*, 4595-4602.

102. Liao, C.-W.; Chen, Y.-R.; Chang, J.-L.; Zen, J.-M., *J. Agric. Food. Chem.* **2011,** *59*, 9782-9787.

103. Li, J.; Chen, Z.; Li, Y., *Anal. Chim. Acta* **2011,** *706*, 255-260.

104. Tsai, T.-H.; Thiagarajan, S.; Chen, S.-M., *J. Agric. Food. Chem.* **2010,** *58*, 4537-4544.

105. Yoshida, J.-i.; Kataoka, K.; Horcajada, R.; Nagaki, A., *Chem. Rev.* **2008,** *108*, 2265-2299.

106. Costentin, C.; Robert, M.; Savéant, J.-M., *Chem. Rev.* **2010,** *110*, PR1-PR40.

107. Birch, A. J.; Rao, G. S., *Advan. Org. Chem.* **1972,** *8*, 1-65.

108. Amatore, C.; Gareil, M.; Savéant, J. M., *J. Electroanal. Chem.* **1984,** *176*, 377-382.

109. Amatore, C.; Savéant, J. M., *J. Electroanal. Chem.* **1980,** *107*, 353-364.

110. Nielson, M. F.; Hammerich, O.; Parker, V. D., *Acta Chem. Scand.* **1986,** *B40*, 101.

111. Nielson, M. F.; Hammerich, O.; Parker, V. D., *Acta Chem. Scand.* **1987,** *B41*, 64.

112. Parker, V. D., *Acta Chem. Scand.* **1981,** *B35*, 373.

113. Guin, P. S.; Das, S.; Mandal, P. C., *Int. J. Electrochem.* **2011,** *2011*.

114. Lehmann, M. W.; Evans, D. H., *J. Phys. Chem. B* **2001,** *105*, 8877-8884.

115. Costentin, C.; Robert, M.; Savéant, J.-M., *J. Am. Chem. Soc.* **2006,** *128*, 8726-8727.

116. Baciocchi, E.; Bietti, M.; Ercolani, G.; Steenken, S., *Tetrahedron* **2003,** *59*, 613-618.

117. Baciocchi, E.; Bietti, M.; Gerini, M. F.; Manduchi, L.; Salamone, M.; Steenken,

S., *Chem. Eur. J.* **2001,** *7*, 1408-1416.

118. Baciocchi, E.; Bietti, M.; Manduchi, L.; Steenken, S., *J. Am. Chem. Soc.* **1999,** *121*, 6624-6629.
119. Baciocchi, E.; Bietti, M.; Steenken, S., *Chem. Eur. J.* **1999,** *5*, 1785-1793.
120. Davies, S. G.; Evans, G. B.; Mortlock, A. A., *Tetrahedron: Asymmetry* **1994,** *5*, 585-606.
121. Davies, S. G.; Mortlock, A. A., *Tetrahedron* **1993,** *49*, 4419-4438.
122. Corey, E. J.; Imwinkelried, R.; Pikul, S.; Xiang, Y. B., *J. Am. Chem. Soc.* **1989,** *111*, 5493-5495.
123. Corey, E. J.; Lee, D.-H.; Sarshar, S., *Tetrahedron: Asymmetry* **1995,** *6*, 3-6.
124. Pikul, S.; Corey, E. J., *Org. Synth.* **1993,** *71*, 22-9.
125. Shimizu, M.; Kamei, M.; Fujisawa, T., *Tetrahedron Lett.* **1995,** *36*, 8607-8610.
126. Hill, J. H. M.; Fogg, T. R.; Guttmann, H., *J. Org. Chem.* **1975,** *40*, 2562-2565.
127. Weiss, M., *J. Am. Chem. Soc.* **1952,** *74*, 5193-5195.
128. Andrieux, C. P.; *Savéant*, J. M., *J. Electroanal. Chem.* **1971,** *33*, 453-461.
129. Fry, A. J.; Reed, R. G., *J. Am. Chem. Soc.* **1969,** *91*, 6448-6451.
130. Koch, R. W.; Dessy, R. E., *J. Org. Chem.* **1982,** *47*, 4452-4459.
131. Kise, N.; Oike, H.; Okazaki, E.; Yoshimoto, M.; Shono, T., *J. Org. Chem.* **1995,** *60*, 3980-3992.
132. Shono, T.; Kise, N.; Shirakawa, E.; Matsumoto, H.; Okazaki, E., *J. Org. Chem.* **1991,** *56*, 3063-3067.
133. Zhou, Y.; Andreou, A.; Biktagirov, E.; Eames, J.; Wadhawan, J., *Electrochem. Commun.* **2010,** *12*, 1493-1497.
134. Pinson, J.; M'Packo, J.-P.; Vinot, N.; Armand, J.; Bassinet, P., *Can. J. Chem.* **1972,** *50*, 1581-1590.
135. Paddon, C. A.; Silvester, D. S.; Bhatti, F. L.; Donohoe, T. J.; Compton, R. G., *Electroanalysis* **2007,** *19*, 11-22.
136. Ammar, F.; Nadjo, L.; Savéant, J. M., *J. Electroanal. Chem.* **1973,** *48*, 146-149.
137. Amatore, C.; *Savéant*, J. M., *J. Electroanal. Chem.* **1977,** *85*, 27-46.
138. Nadjo, L.; Savéant, J. M., *J. Electroanal. Chem.* **1973,** *48*, 113-145.

139. Costentin, C.; Evans, D. H.; Robert, M.; Savéant, J.-M.; Singh, P. S., *J. Am. Chem. Soc.* **2005,** *127*, 12490-12491.
140. Wilke, C. R.; Chang, P., *AIChE J.* **1955,** *1*, 264-270.
141. Evans, D. H.; Lehmann, M. W., *Acta Chem. Scand.* **1999,** *53*, 765-774.
142. Wain, A. J.; Wadhawan, J. D.; Compton, R. G., *ChemPhysChem* **2003,** *4*, 974-982.
143. Friedrich, W., *Vitamins*. Walter de Gruyter: New York, 1988.
144. Voet, D., In *Biochemistry*, John Wiley & Sons: New York, 1990; p 1223.
145. Josic, D.; Hoffer, L.; Buchacher, A., *J. Chromatogr. B* **2003,** *790*, 183-197.
146. Weber, G., *Nutrition* **2001,** *17*, 880-887.
147. Somer, G.; Dogan, M., *Bioelectrochem.* **2008,** *74*, 96-100.
148. Chin, T.; Yeh, S. Y.; Wang, C. M., *J. Electroanal. Chem.* **2003,** *543*, 135-142.
149. Nasiri, H. R.; Panisch, R.; Madej, M. G.; Bats, J. W.; Lancaster, C. R. D.; Schwalbe, H., *Biochim. Biophys. Acta 1787*, 601-608.
150. Wadhawan, J.; Greenman, J.; EI Habbal, M.; Shields, L.; Imrie, C.; Elliott, B. Catheter with a sensing region for redox reactions. PCT/GB2007/050326, 2010.
151. Halls, J. E.; Wright, K. J.; Pickersgill, J. E.; Smith, J. P.; Altalhi, A. A.; Bourne, R. W.; Alaei, P.; Ramakrishnappa, T.; Kelly, S. M.; Wadhawan, J. D., *Electrochim. Acta* **2012,** *70*, 215-227.
152. Park, H.; Park, J.; Shim, Y. B., *J. Electroanal. Chem.* **2001,** *514*, 67-74.
153. Quan, M.; Sanchez, D.; Wasylkiw, M. F.; Smith, D. K., *J. Am. Chem. Soc.* **2007,** *129*, 12847-12856.
154. Chailapakul, O.; Wonsawat, W.; Siangproh, W.; Grudpan, K.; Zhao, Y.; Zhu, Z., *Food Chem.* **2008,** *109*, 876-882.
155. Nohynek, G. J.; Fautz, R.; Benech-Kieffer, F.; Toutain, H., *Food Chem. Toxicol.* **2004,** *42*, 517-543.
156. Donna, L. D.; Maiuolo, L.; Mazzotti, F.; Luca, D. D.; Sindona, G., *Anal. Chem.* **2004,** *74*, 5104-5108.
157. Puoci, F.; Garreffa, C.; Lemma, F.; Muzzalupo, R.; Spizzirri, U. G.; Picci, N.,

Food Chem. **2005,** *93*, 349-353.

158. Wu, L. P.; Li, Y. F.; Huang, C. Z.; Zhang, Q., *Anal. Chem.* **2006,** *78*, 5570-5577.

159. Panizza, M.; Michaud, P. A.; Cerisola, G.; Comninellis, C., *J. Electroanal. Chem.* **2001,** *507*, 206-214.

160. Miller, L. L.; Smith, G. A.; An-Cheng, C.; Qin-Xin, Z., *J. Controlled Release* **1987,** *6*, 293-296.

161. Savéant, J.-M., *J. Phys. Chem. B* **2001,** *105*, 8995-9001.

162. Tinker, J. H.; Michenfelder, J. D., *Anesthesiology* **1976,** *45*, 340-354.

163. Playfair, L., *Philos. T. R. Soc. Lond.* **1849,** *5*, 846.

164. Boedeker, C., *Liebigs. Ann. Chem.* **1861,** *117*, 193.

165. Johnson, C. C., *Proc. Soc. Exp. Biol. Med.* **1928,** *26*, 102.

166. Pereira, F. C.; Zanoni, M. V. B., *Electroanal.* **2007,** *19*, 993-998.

167. Manoharan, P. T.; Hamilton, W. C., *Inorg. Chem.* **1963,** *2*, 1043-1047.

168. Manoharan, P. T.; Gray, H. B., *J. Am. Chem. Soc.* **1965,** *87*, 3340-3348.

169. Bor, G., *J. Inorg. Nucl. Chem.* **1961,** *17*, 174-175.

170. Carapuça, H. M.; Filipe, O. M. S.; Simão, J. E. J.; Fogg, A. G., *J. Electroanal. Chem.* **2000,** *480*, 84-93.

171. Atkins, P. W., *Physical Chemistry*. 5th ed.; Oxford University Press: Oxford, 1994.

172. Barnes, A. S.; Streeter, I.; Compton, R. G., *J. Phys. Chem. C* **2008,** *112*, 8690-8693.

173. Andrieux, C. P.; Delgado, G.; Savaent, J. M., *J. Electroanal. Chem.* **1993,** *348*, 123-139.

174. Andrieux, C. P.; Gallardo, I.; Savaent, J. M.; Su, K. B., *J. Am. Chem. Soc.* **1986,** *108*, 638-647.

175. Andrieux, C. P.; Gelis, L.; Medebielle, M.; Pinson, J.; *Savéant*, J. M., *J. Am. Chem. Soc.* **1990,** *112*, 3509-3520.

176. Andrieux, C. P.; *Savéant*, J. M.; Su, K. B., *J. Phys. Chem.* **1986,** *90*, 3815-3823.

177. Andrieux, C. P.; Savaent, J.-M.; Tallec, J. M.; Tardivel, R.; Tardy, C., *J. Am. Chem. Soc.* **1996,** *118*, 9788-9789.

178. *Savéant*, J. M., *J. Phys. Chem.* **1994,** *98*, 3716-3724.

179. Compton, R. G.; Dryfe, R. A. W.; Eklund, J. C.; Nei, L.; Page, S. D., *Electroanalysis.* **1996,** *8*, 214-217.

180. Compton, R. G.; Dryfe, R. A. W.; Fisher, A. C., *J. Chem. Soc., Perkin Trans. 2* **1994**, 1581-1587.

181. Pinson, J.; Podvorica, F., *Chem. Soc. Rev.* **2005,** *34*, 429-439.

182. Zhong, Y. L.; Loh, K. P.; Midya, A.; Chen, Z.-K., *Chem. Mater.* **2008,** *20*, 3137-3144.

183. O'Neill, M.; Kelly, S. M., *Adv. Mater.* **2011,** *23*, 566-584.

184. Nazarenko, V. G.; Boiko, O. P.; Anisimov, M. I.; Kadashchuk, A. K.; Nastishin, Y. A.; Golovin, A. B.; Lavrentovich, O. D., *Appl. Phys. Lett.* **2010,** *97*, 263305.

185. Zigah, D.; Herrier, C.; Scheres, L.; Giesbers, M.; Fabre, B.; Hapiot, P.; Zuilhof, H., *Angew. Chem. Int. Ed.* **2010,** *49*, 3157-3160.

186. Treadway, C. R.; Hill, M. G.; Barton, J. K., *Chem. Phys.* **2002,** *281*, 409-428.

187. Bykova, V.; Usol'tseva, N.; Ananjeva, G.; Semizikin, A.; Karmanova, T., *Mol. Cryst. Liq. Cryst. Sci. Technol., Sect. A* **1995,** *265*, 651-657.

188. Donnio, B., *Curr. Opin. Colloid Interface Sci.* **2002,** *7*, 371-394.

189. Usol'tseva, N., *Mol. Cryst. Liq. Cryst. Sci. Technol., Sect. A* **1996,** *288*, 201-210.

190. Usoltseva, N. V.; Bykova, V. V., *Mol. Cryst. Liq. Cryst. Sci. Technol., Sect. A* **1992,** *215*, 89-100.

191. Usoltseva, N. V.; Bykova, V. V.; Kormilitsyn, N. M.; Ananieva, G. A.; Maizlish, V. E., *Nuovo Cimento Soc. Ital. Fis., D* **1990,** *12D*, 1237-42.

192. Irvine, J. T. S.; Eggins, B. R.; Grimshaw, J., *J. Electroanal. Chem.* **1989,** *271*, 161-172.

193. Zagal, J. H.; Griveau, S.; Silva, J. F.; Nyokong, T.; Bedioui, F., *Coord. Chem. Rev.* **2010,** *254*, 2755-2791.

194. Abramczyk, H.; Brożek-Płuska, B.; Kurczewski, K.; Kurczewska, M.;

Szymczyk, I.; Krzyczmonik, P.; Błaszczyk, T.; Scholl, H.; Czajkowski, W., *J. Phys. Chem. A* **2006,** *110*, 8627-8636.

195. Evans, L. A.; Thomasson, M. J.; Kelly, S. M.; Wadhawan, J., *J. Phys. Chem. C* **2009,** *113*, 8901-8910.

196. Halls, J. E.; Lawrence, N. S.; Wadhawan, J. D., *J. Phys. Chem. B* **2011,** *115*, 6509-6523.

197. Chami, F.; Wilson, M. R., *J. Am. Chem. Soc.* **2010,** *132*, 7794-7802.

198. OECD, *ICT Applications for the Smart Grid*.

199. APS, Integrating Renewable Electricity on the Grid: A Report by the APS Panel on Public Affairs Society, A. P., Ed. American Physical Society: Washington, 2010.

200. Smar Grids European Platform. http://www.smartgrids.eu (accessed on 11 September 2012).

201. Ponce de León, C.; Frías-Ferrer, A.; González-García, J.; Szánto, D. A.; Walsh, F. C., *J. Power Sources* **2006,** *160*, 716-732.

202. Weber, A.; Mench, M.; Meyers, J.; Ross, P.; Gostick, J.; Liu, Q., *J. Appl. Electrochem.* **2011,** *41*, 1137-1164.

203. Kear, G.; Shah, A. A.; Walsh, F. C., *Int. J. Energy Res.* **2012,** *36*, 1105-1120.

204. Mohamed, M. R.; Sharkh, S. M.; Walsh, F. C. *proceedings of the 5th IEEE vehicle power and propulsion conference*, 2009.

205. Yao, Y.; Zhang, W.; He, B., *Energy Convers. Manage.* **2011,** *52*, 3319-3326.

206. ZBB website. http://www.zbbenergy.com (accessed on 11 September, 2012).

207. Cellenium website. http://vanadiumbattery.com (accessed on 10 September 2012).

208. Abu-Sharkh, S.; Arnold, R. J.; Kohler, J.; Li, R.; Markvart, T.; Ross, J. N.; Steemers, K.; Wilson, P.; Yao, R., *Renewable Sustainable Energy Rev.* **2006,** *10*, 78-127.

209. ABB website. http://www.abb.com (accessed on 12 August 2012).

210. Prudent Energy website. http://www.pdenergy.com (accessed on 11 September 2012).

211. Sumitomo Electric Industries, Ltd. website. http://global-sei.com (accessed on 10 September 2012).

212. RedFlow, Ltd. website. http://www.redflow.com.au (accessed on 11 September 2012).

213. Leung, P. K.; Ponce de León, C.; Low, C. T. J.; Walsh, F. C., *Electrochim. Acta* **2011,** *56*, 2145-2153.

214. Leung, P. K.; Ponce de León, C.; Walsh, F. C., *Electrochem. Commun.* **2011,** *13*, 770-773.

215. Leung, P. K.; Ponce-de-León, C.; Low, C. T. J.; Shah, A. A.; Walsh, F. C., *J. Power Sources* **2011,** *196*, 5174-5185.

216. Leung, P. K.; Ponce-de-León, C.; Low, C. T. J.; Walsh, F. C., *Electrochim. Acta* **2011,** *56*, 6536-6546.

217. Nikiforidis, G.; Berlouis, L.; Hall, D.; Hodgson, D., *J. Power Sources* **2012,** *206*, 497-503.

218. Fedkiw, P. S.; Watts, R. W., *J. Electrochem. Soc.* **1984,** *131*, 701-709.

219. Evans, T. I.; White, R. E., *J. Electrochem. Soc.* **1987,** *134*, 2725-2733.

220. Shah, A. A.; Watt-Smith, M. J.; Walsh, F. C., *Electrochim. Acta* **2008,** *53*, 8087-8100.

221. Scamman, D. P.; Reade, G. W.; Roberts, E. P. L., *J. Power Sources* **2009,** *189*, 1220-1230.

222. Scamman, D. P.; Reade, G. W.; Roberts, E. P. L., *J. Power Sources* **2009,** *189*, 1231-1239.

223. Shah, A. A.; Li, X.; Wills, R. G. A.; Walsh, F. C., *J. Electrochem. Soc.* **2010,** *157*, A589-A599.

224. Rugolo, J.; Aziz, M. J., *Energy Environ. Sci.* **2012,** *5*, 7151-7160.

225. Amatore, C.; Berthou, M.; Hébert, S., *J. Electroanal. Chem.* **1998,** *457*, 191-203.

226. Amatore, C.; Szunerits, S.; Thouin, L.; Warkocz, J.-S., *J. Electroanal. Chem.* **2001,** *500*, 62-70.

227. Amatore, C.; Pebay, C. c.; Thouin, L.; Wang, A.; Warkocz, J. S., *Anal. Chem.*

2010, *82*, 6933-6939.

228. Das, A. K., *Coord. Chem. Rev.* **2001,** *213*, 307-325.

229. Randle, T. H.; Kuhn, A. T., *J. Chem. Soc., Faraday Trans. 1* **1983,** *79*, 1741-56.

230. EL-HALLAG, I. S., *J. Chil. Chem. Soc.* **2010,** *55*, 374-380.

231. Gaiser, L.; Heusler, K. E., *Electrochim. Acta* **1970,** *15*, 161-171.

232. Stein, B., *Met. Finish.* **1985**, 100.

233. Bae, C.; Roberts, E. P. L.; Chakrabarti, M. H.; Saleem, M., *Int. J. Green Energy* **2011,** *8*, 248-264.

234. Chakrabarti, M. H.; Roberts, E. P. L.; Bae, C.; Saleem, M., *Energy Convers. Manage.* **2011,** *52*, 2501-2508.

235. Pell, W. G.; Conway, B. E., *J. Power Sources* **1996,** *63*, 255-266.

236. D. Gernon, M.; Wu, M.; Buszta, T.; Janney, P., *Green Chem.* **1999,** *1*, 127-140.

237. Presser, V.; Dennison, C. R.; Campos, J.; Knehr, K. W.; Kumbur, E. C.; Gogotsi, Y., *Adv. Energy Mater.* **2012,** *2*, 895-902.

238. Halls, J. E.; Wadhawan, J. D., *Energy Environ. Sci.* **2012,** *5*, 6541-6551.

10. APPENDIX

10.1. The derivation of Arrhenius equation from Van't Hoff isochore.

If consider a uni-molecular elementary reaction:

$$\mathrm{A(aq)} \underset{k_b}{\overset{k_f}{\rightleftharpoons}} \mathrm{B(aq)}$$

the equilibrium constant is then given by:

$$\mathrm{K} = \frac{k_f}{k_b}$$

From Van't Hoff Isochore, the temperature dependence of the equilibrium constant (at constant volume) is given by:

$$\frac{\partial lnK}{\partial T} = \frac{\Delta U}{RT^2}$$

where $\Delta \mathrm{U} = E_f - E_b$ (see the explanation of E_f and E_b in Fig. 1.4).

By substituting the equilibrium constant (K) with ratio of rate constants (k_f and k_b), then:

$$\frac{\partial lnk_f}{\partial T} - \frac{\partial lnk_b}{\partial T} = \frac{\Delta U}{RT^2}$$

then by applying the forward and backward change of internal energy, E_f and E_b, then:

$$\frac{\partial lnk_f}{\partial T} = \frac{E_f}{RT^2} + constant$$

$$\frac{\partial lnk_b}{\partial T} = \frac{E_b}{RT^2} + constant$$

by integrating the equations,

$$k_f = A_f exp\left(-E_f/_{RT}\right)$$

$$k_b = A_b exp\left(-E_b/_{RT}\right)$$

with E_f and E_b are the so-called activation energies for forward and backward reactions, respectively, and A_f and A_b are the pre-exponential factors, therefore, in general:

$$k = Ae^{-E_A/RT}$$

where EA is the general activation energy.

10.2. Details of the Pentadiagonal Matrix Algorithm Employed

This method was outlined by I. B. Svir, A. V. Klimenko, R. G. Compton, *Radiotekhnika,* 2001, **118**, 92, and provide corrected expressions are provided here.

Consider the solution of N x N simultaneous equations, described by the matrix equation,

$$[T]\{u\} = \{m\}$$

where [T] is an N x N pentadiagonal matrix where all coefficients are known, $\{u\}$ is a vector of N unknowns, and $\{m\}$ is a vector of N known values. Proceeding via LU decomposition of [T] yields

$$[T] = [T_L][T_U]$$

then next seek a vector $\{f\}$, such that

$$[T_L]\{f\} = \{m\}$$

so that,

$$[T_U]\{u\} = \{f\}$$

and, therefore,

$$[T_U]\{u\} = [T_L]^{-1}\{m\}$$

since

$$\{f\} = [T_L]^{-1}\{m\}$$

Thus,

$$[T_L][T_U]\{u\} = \{m\}$$

as required.

Noting that 1 ≤ j ≤ N and defining,

$$[T] = \begin{bmatrix} a_1 & b_1 & c_1 & 0 & & & & & 0 \\ d_2 & a_2 & b_2 & c_2 & 0 & & & & 0 \\ e_3 & d_3 & a_3 & b_3 & c_3 & 0 & & & 0 \\ & \searrow & & & & \searrow & & & \\ 0 & 0 & e_j & d_j & a_j & b_j & c_j & 0 & 0 \\ & & & \searrow & & & & \searrow & \\ 0 & & & 0 & e_{N-2} & d_{N-2} & a_{N-2} & b_{N-2} & c_{N-2} \\ 0 & & & & 0 & e_{N-1} & d_{N-1} & a_{N-1} & b_{N-1} \\ 0 & & & & & 0 & e_N & d_N & a_N \end{bmatrix}$$

$$[T_L] = \begin{bmatrix} 1 & 0 & & & & & & & 0 \\ z_2 & 1 & 0 & & & & & & 0 \\ \frac{e_3}{x_1} & z_3 & 1 & 0 & & & & & 0 \\ & \searrow & & \searrow & & & & & \\ 0 & & \frac{e_j}{x_{j-2}} & z_j & 1 & 0 & & & 0 \\ & & & \searrow & & \searrow & & & \\ 0 & & & 0 & \frac{e_{N-2}}{x_{N-4}} & z_{N-2} & 1 & 0 & 0 \\ 0 & & & & 0 & \frac{e_{N-1}}{x_{N-3}} & z_{N-1} & 1 & 0 \\ 0 & & & & & 0 & \frac{e_N}{x_{N-2}} & z_N & 1 \end{bmatrix}$$

and

$$[T_u] = \begin{bmatrix} x_1 & y_1 & c_1 & 0 & & & & & 0 \\ 0 & x_2 & y_2 & c_2 & 0 & & & & 0 \\ 0 & 0 & x_3 & y_3 & c_3 & 0 & & & 0 \\ & & & \searrow & & \searrow & & & \\ 0 & & & 0 & x_j & y_j & c_j & 0 & 0 \\ & & & & & \searrow & & \searrow & \\ 0 & & & & & 0 & x_{N-2} & y_{N-2} & c_{N-2} \\ 0 & & & & & & 0 & x_{N-1} & y_{N-1} \\ 0 & & & & & & & 0 & x_N \end{bmatrix}$$

$$\{u\} = \begin{Bmatrix} u_1 \\ u_2 \\ u_3 \\ \downarrow \\ u_j \\ \downarrow \\ u_{N-2} \\ u_{N-1} \\ u_N \end{Bmatrix} \qquad \text{and} \qquad \{m\} = \begin{Bmatrix} m_1 \\ m_2 \\ m_3 \\ \downarrow \\ m_j \\ \downarrow \\ m_{N-2} \\ m_{N-1} \\ m_N \end{Bmatrix}$$

allows the following variables to be defined.

$$x_1 = a_1$$
$$x_2 = a_2 - z_2 y_1$$
$$x_j = a_j - z_j y_{j-1} - \frac{e_j}{x_{j-2}} c_{j-2}$$

$$y_1 = b_1$$
$$y_j = b_j - z_j c_{j-1}$$
$$z_2 = \frac{d_2}{x_1}$$

$$z_i = \frac{d_i - \frac{e_i}{x_{i-2}} y_{i-2}}{x_{i-1}}$$

It thus follows, from forward recursion that,

$$f_1 = m_1$$
$$f_2 = m_2 - z_2 f_1$$
$$f_j = m_j - z_j f_{j-1} - \frac{e_j}{x_{j-2}} f_{j-2}$$

and therefore, the required solution may be found through backward recursion,

$$u_N = \frac{f_N}{x_N}$$
$$u_{N-1} = \frac{f_{N-1} - y_{N-1} u_N}{x_{N-1}}$$
$$u_j = \frac{f_j - y_i u_{j+1} - c_j u_{j+2}}{x_j}$$

10.3. Copy right permissions

ELSEVIER LICENSE
TERMS AND CONDITIONS

Nov 03, 2012

This is a License Agreement between Yan Zhou ("You") and Elsevier ("Elsevier") provided by Copyright Clearance Center ("CCC"). The license consists of your order details, the terms and conditions provided by Elsevier, and the payment terms and conditions.

All payments must be made in full to CCC. For payment instructions, please see information listed at the bottom of this form.

Supplier	Elsevier Limited The Boulevard,Langford Lane Kidlington,Oxford,OX5 1GB,UK
Registered Company Number	1982084
Customer name	Yan Zhou
Customer address	422 Inglemire Lane Hull, HU6 8JQ
License number	3020871211035
License date	Nov 02, 2012
Licensed content publisher	Elsevier
Licensed content publication	Electrochemistry Communications
Licensed content title	Comparison of Birch with electrochemical reduction of 2,3-diphenyl-1,4-diazaspiro[4.5]deca-1,3-diene
Licensed content author	Yan Zhou,Anna Andreou,Eldar Biktagirov,Jason Eames,Jay Wadhawan
Licensed content date	November 2010
Licensed content volume number	12
Licensed content issue number	11
Number of pages	5
Start Page	1493
End Page	1497
Type of Use	reuse in a thesis/dissertation
Portion	full article
Format	both print and electronic
Are you the author of this Elsevier article?	Yes
Will you be translating?	No
Order reference number	
Title of your	Molecular electrochemistry

thesis/dissertation	
Expected completion date	Dec 2012
Estimated size (number of pages)	250
Elsevier VAT number	GB 494 6272 12
Permissions price	0.00 GBP
VAT/Local Sales Tax	0.0 USD / 0.0 GBP
Total	0.00 GBP
Terms and Conditions	

granted in the combination of (i) the license details provided by you and accepted in the course of this licensing transaction, (ii) these terms and conditions and (iii) CCC's Billing and Payment terms and conditions.

8. License Contingent Upon Payment: While you may exercise the rights licensed immediately upon issuance of the license at the end of the licensing process for the transaction, provided that you have disclosed complete and accurate details of your proposed use, no license is finally effective unless and until full payment is received from you (either by publisher or by CCC) as provided in CCC's Billing and Payment terms and conditions. If full payment is not received on a timely basis, then any license preliminarily granted shall be deemed automatically revoked and shall be void as if never granted. Further, in the event that you breach any of these terms and conditions or any of CCC's Billing and Payment terms and conditions, the license is automatically revoked and shall be void as if never granted. Use of materials as described in a revoked license, as well as any use of the materials beyond the scope of an unrevoked license, may constitute copyright infringement and publisher reserves the right to take any and all action to protect its copyright in the materials.

9. Warranties: Publisher makes no representations or warranties with respect to the licensed material.

10. Indemnity: You hereby indemnify and agree to hold harmless publisher and CCC, and their respective officers, directors, employees and agents, from and against any and all claims arising out of your use of the licensed material other than as specifically authorized pursuant to this license.

11. No Transfer of License: This license is personal to you and may not be sublicensed, assigned, or transferred by you to any other person without publisher's written permission.

12. No Amendment Except in Writing: This license may not be amended except in a writing signed by both parties (or, in the case of publisher, by CCC on publisher's behalf).

13. Objection to Contrary Terms: Publisher hereby objects to any terms contained in any purchase order, acknowledgment, check endorsement or other writing prepared by you, which terms are inconsistent with these terms and conditions or CCC's Billing and Payment terms and conditions. These terms and conditions, together with CCC's Billing and Payment terms and conditions (which are incorporated herein), comprise the entire agreement between you and publisher (and CCC) concerning this licensing transaction. In the event of any conflict between your obligations established by these terms and conditions and those established by CCC's Billing and Payment terms and conditions, these terms and conditions shall control.

14. Revocation: Elsevier or Copyright Clearance Center may deny the permissions described in this License at their sole discretion, for any reason or no reason, with a full refund payable to you. Notice of such denial will be made using the contact information provided by you. Failure to receive such notice will not alter or invalidate the denial.

In no event will Elsevier or Copyright Clearance Center be responsible or liable for any costs, expenses or damage incurred by you as a result of a denial of your permission request, other than a refund of the amount(s) paid by you to Elsevier and/or Copyright Clearance Center for denied permissions.

LIMITED LICENSE

The following terms and conditions apply only to specific license types:

15. Translation: This permission is granted for non-exclusive world English rights only unless your license was granted for translation rights. If you licensed translation rights you may only translate this content into the languages you requested. A professional translator must perform all translations and reproduce the content word for word preserving the integrity of the article. If this license is to re-use 1 or 2 figures then permission is granted for non-exclusive world rights in all languages.

16. Website: The following terms and conditions apply to electronic reserve and author websites:
Electronic reserve: If licensed material is to be posted to website, the web site is to be password-protected and made available only to bona fide students registered on a relevant course if:
This license was made in connection with a course,
This permission is granted for 1 year only. You may obtain a license for future website posting,
All content posted to the web site must maintain the copyright information line on the bottom of each image,
A hyper-text must be included to the Homepage of the journal from which you are licensing at http://www.sciencedirect.com/science/journal/xxxxx or the Elsevier homepage for books at http://www.elsevier.com , and
Central Storage: This license does not include permission for a scanned version of the material to be stored in a central repository such as that provided by Heron/XanEdu.

17. Author website for journals with the following additional clauses:

All content posted to the web site must maintain the copyright information line on the bottom of each image, and the permission granted is limited to the personal version of your paper. You are not allowed to download and post the published electronic version of your article (whether PDF or HTML, proof or final version), nor may you scan the printed edition to create an electronic version. A hyper-text must be included to the Homepage of the journal from which you are licensing at http://www.sciencedirect.com/science/journal/xxxxx . As part of our normal production process, you will receive an e-mail notice when your article appears on Elsevier's online service ScienceDirect (www.sciencedirect.com). That e-mail will include the article's Digital Object Identifier (DOI). This number provides the electronic link to the published article and should be included in the posting of your personal version. We ask that you wait until you receive this e-mail and have the DOI to do any posting.

Central Storage: This license does not include permission for a scanned

version of the material to be stored in a central repository such as that provided by Heron/XanEdu.

18. Author website for books with the following additional clauses: Authors are permitted to place a brief summary of their work online only. A hyper-text must be included to the Elsevier homepage at http://www.elsevier.com . All content posted to the web site must maintain the copyright information line on the bottom of each image. You are not allowed to download and post the published electronic version of your chapter, nor may you scan the printed edition to create an electronic version.

Central Storage: This license does not include permission for a scanned version of the material to be stored in a central repository such as that provided by Heron/XanEdu.

19. Website (regular and for author): A hyper-text must be included to the Homepage of the journal from which you are licensing at http://www.sciencedirect.com/science/journal/xxxxx. or for books to the Elsevier homepage at http://www.elsevier.com

20. Thesis/Dissertation: If your license is for use in a thesis/dissertation your thesis may be submitted to your institution in either print or electronic form. Should your thesis be published commercially, please reapply for permission. These requirements include permission for the Library and Archives of Canada to supply single copies, on demand, of the complete thesis and include permission for UMI to supply single copies, on demand, of the complete thesis. Should your thesis be published commercially, please reapply for permission.

21. Other Conditions:

v1.6

If you would like to pay for this license now, please remit this license along with your payment made payable to "COPYRIGHT CLEARANCE CENTER" otherwise you will be invoiced within 48 hours of the license date. Payment should be in the form of a check or money order referencing your account number and this invoice number RLNK500889513. Once you receive your invoice for this order, you may pay your invoice by credit card. Please follow instructions provided at that time.

Make Payment To:
Copyright Clearance Center
Dept 001
P.O. Box 843006
Boston, MA 02284-3006

For suggestions or comments regarding this order, contact RightsLink Customer Support: customercare@copyright.com or +1-877-622-5543 (toll free in the US) or +1-978-646-2777.

Gratis licenses (referencing $0 in the Total field) are free. Please retain this printable license for your reference. No payment is required.

ELSEVIER LICENSE
TERMS AND CONDITIONS

Nov 03, 2012

This is a License Agreement between Yan Zhou ("You") and Elsevier ("Elsevier") provided by Copyright Clearance Center ("CCC"). The license consists of your order details, the terms and conditions provided by Elsevier, and the payment terms and conditions.

All payments must be made in full to CCC. For payment instructions, please see information listed at the bottom of this form.

Supplier	Elsevier Limited The Boulevard,Langford Lane Kidlington,Oxford,OX5 1GB,UK
Registered Company Number	1982084
Customer name	Yan Zhou
Customer address	422 Inglemire Lane Hull, HU6 8JQ
License number	3020871403428
License date	Nov 02, 2012
Licensed content publisher	Elsevier
Licensed content publication	Electrochemistry Communications
Licensed content title	Electrochemistry of organometallic lyotropic chromonic liquid crystals
Licensed content author	Jonathan E. Halls,Richard W. Bourne,Kevin J. Wright,Lee I. Partington,M. Gabriela Tamba,Yan Zhou,Thippeswamy Ramakrishnappa,Georg H. Mehl,Stephen M. Kelly,Jay D. Wadhawan
Licensed content date	June 2012
Licensed content volume number	19
Licensed content issue number	
Number of pages	5
Start Page	50
End Page	54
Type of Use	reuse in a thesis/dissertation
Intended publisher of new work	other
Portion	full article
Format	both print and electronic
Are you the author of this Elsevier article?	Yes
Will you be translating?	No

Order reference number	
Title of your thesis/dissertation	Molecular electrochemistry
Expected completion date	Dec 2012
Estimated size (number of pages)	250
Elsevier VAT number	GB 494 6272 12
Permissions price	0.00 GBP
VAT/Local Sales Tax	0.0 USD / 0.0 GBP
Total	0.00 GBP
Terms and Conditions	

INTRODUCTION

1. The publisher for this copyrighted material is Elsevier. By clicking "accept" in connection with completing this licensing transaction, you agree that the following terms and conditions apply to this transaction (along with the Billing and Payment terms and conditions established by Copyright Clearance Center, Inc. ("CCC"), at the time that you opened your Rightslink account and that are available at any time at http://myaccount.copyright.com).

GENERAL TERMS

2. Elsevier hereby grants you permission to reproduce the aforementioned material subject to the terms and conditions indicated.

3. Acknowledgement: If any part of the material to be used (for example, figures) has appeared in our publication with credit or acknowledgement to another source, permission must also be sought from that source. If such permission is not obtained then that material may not be included in your publication/copies. Suitable acknowledgement to the source must be made, either as a footnote or in a reference list at the end of your publication, as follows:

"Reprinted from Publication title, Vol /edition number, Author(s), Title of article / title of chapter, Pages No., Copyright (Year), with permission from Elsevier [OR APPLICABLE SOCIETY COPYRIGHT OWNER]." Also Lancet special credit - "Reprinted from The Lancet, Vol. number, Author(s), Title of article, Pages No., Copyright (Year), with permission from Elsevier."

4. Reproduction of this material is confined to the purpose and/or media for which permission is hereby given.

5. Altering/Modifying Material: Not Permitted. However figures and illustrations may be altered/adapted minimally to serve your work. Any other abbreviations, additions, deletions and/or any other alterations shall be made only with prior written authorization of Elsevier Ltd. (Please contact Elsevier at permissions@elsevier.com)

6. If the permission fee for the requested use of our material is waived in this instance, please be advised that your future requests for Elsevier

materials may attract a fee.

7. Reservation of Rights: Publisher reserves all rights not specifically granted in the combination of (i) the license details provided by you and accepted in the course of this licensing transaction, (ii) these terms and conditions and (iii) CCC's Billing and Payment terms and conditions.

8. License Contingent Upon Payment: While you may exercise the rights licensed immediately upon issuance of the license at the end of the licensing process for the transaction, provided that you have disclosed complete and accurate details of your proposed use, no license is finally effective unless and until full payment is received from you (either by publisher or by CCC) as provided in CCC's Billing and Payment terms and conditions. If full payment is not received on a timely basis, then any license preliminarily granted shall be deemed automatically revoked and shall be void as if never granted. Further, in the event that you breach any of these terms and conditions or any of CCC's Billing and Payment terms and conditions, the license is automatically revoked and shall be void as if never granted. Use of materials as described in a revoked license, as well as any use of the materials beyond the scope of an unrevoked license, may constitute copyright infringement and publisher reserves the right to take any and all action to protect its copyright in the materials.

9. Warranties: Publisher makes no representations or warranties with respect to the licensed material.

10. Indemnity: You hereby indemnify and agree to hold harmless publisher and CCC, and their respective officers, directors, employees and agents, from and against any and all claims arising out of your use of the licensed material other than as specifically authorized pursuant to this license.

11. No Transfer of License: This license is personal to you and may not be sublicensed, assigned, or transferred by you to any other person without publisher's written permission.

12. No Amendment Except in Writing: This license may not be amended except in a writing signed by both parties (or, in the case of publisher, by CCC on publisher's behalf).

13. Objection to Contrary Terms: Publisher hereby objects to any terms contained in any purchase order, acknowledgment, check endorsement or other writing prepared by you, which terms are inconsistent with these terms and conditions or CCC's Billing and Payment terms and conditions. These terms and conditions, together with CCC's Billing and Payment terms and conditions (which are incorporated herein), comprise the entire agreement between you and publisher (and CCC) concerning this licensing transaction. In the event of any conflict between your obligations established by these terms and conditions and those established by CCC's Billing and Payment terms and conditions, these terms and conditions shall control.

14. Revocation: Elsevier or Copyright Clearance Center may deny the permissions described in this License at their sole discretion, for any

reason or no reason, with a full refund payable to you. Notice of such denial will be made using the contact information provided by you. Failure to receive such notice will not alter or invalidate the denial. In no event will Elsevier or Copyright Clearance Center be responsible or liable for any costs, expenses or damage incurred by you as a result of a denial of your permission request, other than a refund of the amount(s) paid by you to Elsevier and/or Copyright Clearance Center for denied permissions.

LIMITED LICENSE

The following terms and conditions apply only to specific license types:

15. Translation: This permission is granted for non-exclusive world English rights only unless your license was granted for translation rights. If you licensed translation rights you may only translate this content into the languages you requested. A professional translator must perform all translations and reproduce the content word for word preserving the integrity of the article. If this license is to re-use 1 or 2 figures then permission is granted for non-exclusive world rights in all languages.

16. Website: The following terms and conditions apply to electronic reserve and author websites:
Electronic reserve: If licensed material is to be posted to website, the web site is to be password-protected and made available only to bona fide students registered on a relevant course if:
This license was made in connection with a course,
This permission is granted for 1 year only. You may obtain a license for future website posting,
All content posted to the web site must maintain the copyright information line on the bottom of each image,
A hyper-text must be included to the Homepage of the journal from which you are licensing at http://www.sciencedirect.com/science/journal/xxxxx or the Elsevier homepage for books at http://www.elsevier.com , and
Central Storage: This license does not include permission for a scanned version of the material to be stored in a central repository such as that provided by Heron/XanEdu.

17. Author website for journals with the following additional clauses:

All content posted to the web site must maintain the copyright information line on the bottom of each image, and the permission granted is limited to the personal version of your paper. You are not allowed to download and post the published electronic version of your article (whether PDF or HTML, proof or final version), nor may you scan the printed edition to create an electronic version. A hyper-text must be included to the Homepage of the journal from which you are licensing at http://www.sciencedirect.com/science/journal/xxxxx . As part of our normal production process, you will receive an e-mail notice when your article appears on Elsevier's online service ScienceDirect (www.sciencedirect.com). That e-mail will include the article's Digital Object Identifier (DOI). This number provides the electronic link to the published article and should be included in the posting of your personal version. We ask that you wait until you receive this e-mail and have the

DOI to do any posting.

Central Storage: This license does not include permission for a scanned version of the material to be stored in a central repository such as that provided by Heron/XanEdu.

18. Author website for books with the following additional clauses: Authors are permitted to place a brief summary of their work online only. A hyper-text must be included to the Elsevier homepage at http://www.elsevier.com . All content posted to the web site must maintain the copyright information line on the bottom of each image. You are not allowed to download and post the published electronic version of your chapter, nor may you scan the printed edition to create an electronic version.

Central Storage: This license does not include permission for a scanned version of the material to be stored in a central repository such as that provided by Heron/XanEdu.

19. Website (regular and for author): A hyper-text must be included to the Homepage of the journal from which you are licensing at http://www.sciencedirect.com/science/journal/xxxxx. or for books to the Elsevier homepage at http://www.elsevier.com

20. Thesis/Dissertation: If your license is for use in a thesis/dissertation your thesis may be submitted to your institution in either print or electronic form. Should your thesis be published commercially, please reapply for permission. These requirements include permission for the Library and Archives of Canada to supply single copies, on demand, of the complete thesis and include permission for UMI to supply single copies, on demand, of the complete thesis. Should your thesis be published commercially, please reapply for permission.

21. Other Conditions:

v1.6

If you would like to pay for this license now, please remit this license along with your payment made payable to "COPYRIGHT CLEARANCE CENTER" otherwise you will be invoiced within 48 hours of the license date. Payment should be in the form of a check or money order referencing your account number and this invoice number RLNK500889515. Once you receive your invoice for this order, you may pay your invoice by credit card. Please follow instructions provided at that time.

Make Payment To:
Copyright Clearance Center
Dept 001
P.O. Box 843006
Boston, MA 02284-3006

For suggestions or comments regarding this order, contact RightsLink Customer Support: customercare@copyright.com or +1-877-622-5543 (toll free in the US) or +1-978-646-2777.

Gratis licenses (referencing $0 in the Total field) are free. Please retain this printable license for your reference. No payment is required.